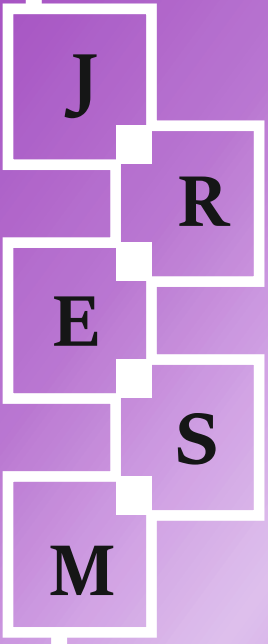




# Research on Engineering Structures & Materials

P-ISSN: 2148-9807 E-ISSN: 2149-4088

Volume 7 Issue 1 February 2021



[www.jresm.org](http://www.jresm.org)

The International Journal of **Research on Engineering Structures and Materials (RESM)** is a peer-reviewed open access journal (p-ISSN: 2148-9807; o-ISSN: 2149-4088) published by MIM Research Group. It is published in February, June, September, and December.

The main objective of RESM is to provide an International academic platform for researchers to share scientific results related to all aspects of mechanical, civil and material engineering areas.

RESM aims the publication of original research articles, reviews, short communications technical reports, and letters to the editor on the latest developments in the related fields.

All expenditures for the publication of the manuscripts are most kindly reimbursed by *MIM Research Group*. Thus, authors do not need to pay for publishing their studies in the journal.

The scope of the journal covers (but not limited to) behavior of structures, machines and mechanical systems, vibration, impact loadings and structural dynamics, mechanics of materials (elasticity, plasticity, fracture mechanics), material science (structure and properties of concrete, metals, ceramics, composites, plastics, wood, etc.), nano-materials performances of new and existing buildings and other structural systems, design of buildings and other structural systems, seismic behavior of buildings and other structural systems, repair and strengthening of structural systems, case studies and failure of structural systems, safety and reliability in structural and material engineering, use of new and innovative materials and techniques in energy systems and mechanical aspects of biological systems (biomechanics and biomimetics).

**The topics covered in JRESM include:**

- Structural Engineering
- Mechanical Engineering
- Material Engineering
- Earthquake Engineering
- Nano-technology
- Energy Systems
- Biomechanics and Biomimetics

**Abstracting and Indexing**

Please visit <http://www.jresm.org> for more information.

**Graphics and Design**

Yunus Demirtaş

[ydemirtas@jresm.net](mailto:ydemirtas@jresm.net)



**RESEARCH on  
ENGINEERING STRUCTURES &  
MATERIALS**



**Published by MIM Research Group**

# RESEARCH on ENGINEERING STRUCTURES & MATERIALS

## Editorial Board

---

<b>Editor in Chief</b>		
Hayri Baytan Özmen	Usak University	Turkey
<b>Editor (Energy, Thermodynamics)</b>		
Canan Kandilli	Usak University	Turkey
<b>Editor (Earthquake Eng., Structural Eng.)</b>		
Michele Barbato	University of California Davis	USA
<b>Editor (Mechanics, Biosystems, Meta-materials)</b>		
Alp Karakoç	Aalto University	Finland
<b>Editor (Applied Mechanics, Manufacturing, Design)</b>		
Faris Tarlochan	Qatar University	Qatar

---

## Editorial Office

---

<b>Publishing Assistant</b>		
Yunus Demirtaş	Eskişehir Technical University	Turkey

---

### Editorial Board Members

---

Farid Abed-Meraim	Arts et Metiers ParisTech	France
P. Anbazhagan	Indian Institute of Science	India
Raffaele Barretta	University of Naples Federico II	Italy
R.S. Beniwal	Council of Scientific and Industrial Research	India
Antonio Caggiano	University of Buenos Aires	Argentina
Noel Challamel	University of South Brittany	France
Abdulkadir Çevik	Gaziantep University	Turkey
J. Paulo Davim	University of Aveiro	Portugal
Hom Nath Dhakal	University of Portsmouth	UK
S. Amir M. Ghannadpour	Shahid Beheshti University	Iran
Ali Goodarzi	Harvard University	USA
Jian Jiang	National Institute of Standards and Technology	USA
Ramazan Karakuzu	Dokuz Eylül University	Turkey
Arkadiusz Kwiecien	Cracow University of Technology	Poland
Stefano Lenci	Universita Politecnica delle Marche	Italy
Yuan Meini	North University of China	China
Stergios A. Mitoulis	University of Surrey	UK
Alaa M. Rashad	Shaqra University	Saudi Arabia
Mohammad Mehdi Rashidi	University of Tongji	China
Pier Paolo Rossi	University of Catania	Italy
Neritan Shkodrani	Polythecnic University of Tirana	Albania
Faris Tarlochan	Qatar University	Qatar
Y.B. Yang	National Taiwan University	Taiwan

### Advisory Board Members

---

Yinusa Amoo Ahmed	University of Lagos	Nigeria
Erkin Akdoğan	Karamanoğlu Mehmetbey University	Turkey
Mustafa Akpolat	Munzur University	Turkey
Sevim Alışır	Ondokuz Mayıs University	Turkey
Saber Alizadeh	Bu-Ali-Sina University	Iran
Danar Altalabani	University of Applied Sciences Karlsruhe	Germany
Mustafa Yasin Aslan	Usak University	Turkey
Huseyin Ersen Balcioglu	Usak University	Turkey
Beyhan Bayhan	Bursa Technical University	Turkey
Emin Bayraktar	Supméca Institute of Mechanics of Paris	France
Mehmet Bulut	Hakkari University	Turkey
Hektor Cullufi	Polytechnic University of Tirana	Albania
Preeta Datta	North Carolina State University	USA
J. Paulo Davim	University of Aveiro	Portugal
Hakan Demir	Iskenderun Technic University	Turkey
Cengiz Görkem Dengiz	Ondokuz Mayıs University	Turkey
Akar Dogan	Munzur University	Turkey
Hany El-Hamshary	Tanta University	Egypt
Engin Emsen	Akdeniz University	Turkey
H. Murat Enginsoy	Usak University	Turkey
Ali Faghidian	Islamic Azad University	Iran
Mohamed Guenfoud	University Larbi Tébessi	Algeria
Mükrimin Şevket Güney	Giresun University	Turkey
Dulce Franco Henriques	Instituto Politécnico de Lisboa	Portugal
Halit Levent Hosgun	Bursa Technical University	Turkey
Mahdi Hosseini	Jawaharlal Nehru Technological University	India

### Advisory Board Members

---

Ercan Isik	Bitlis Eren University	Turkey
Zafer Kaya	Dumlupınar University	Turkey
Ali Koçak	Yildiz Technical University	Turkey
Sedat Kömürcü	İstanbul Technical University	Turkey
Güven Kurtuldu	ETH Zurich	Switzerland
Charles Langston	University of Memphis	USA
Ahmet Meram	KTO Karatay University	Turkey
Süha Orçun Mert	İskenderun Technical University	Turkey
Masoomah Mirrashid	Semnan University	Iran
Jinxu Mo	Yangtze University	China
Kim Hung Mo	University of Malaya	Malaysia
Arunima Nayak	Graphic Era University	India
Mehmet Palanci	Istanbul Arel University	Turkey
Amin Moslami Petrucci	University Amirkabir	Iran
Majid Pouraminian	Islamic Azad University	Iran
Alaa M. Rashad	Building Materials Research and Quality Control Institute	Egypt
Fabio Rizzo	University of Chieti-Pescara	Italy
Behnam Rosti	Shiraz University of Technology	Iran
Tamer Saracyakupoglu	Istanbul Gelisim University	Turkey
Rudimylla Septimio Azeredo	Federal University of Southern and Southeastern Pará	Brazil
Neritan Shkodrani	Polytechnic University of Tirana	Albania
Ramachandran Seshadri	Stony Brook University	USA
Adnan Sozen	Gazi University	Turkey
Brijesh Singh	National Council for Cement & Building Material	India
Hossein Taghipoor	Semnan University	Iran

### Advisory Board Members

---

Anand B. Tapase	Karmaveer Bhaurao Patil College of Engineering	India
Faris Tarlochan	Qatar University	Qatar
Hamide Tekeli	Süleyman Demirel University	Turkey
Dilay Uncu	Manisa Celal Bayar University	Turkey
Abid Ustaoglu	Bartın University	Turkey
Ümit Ünver	Yalova University	Turkey
Gustavo Bosel Wally	Federal University of Rio Grande do Sul	Brazil
Jhair Yacila	Pontificia Universidad Católica del Perú	Peru
Onder Yesil	Usak University	Turkey
Salih Hakan Yetgin	Dumlupınar University	Turkey
Ferhat Yıldırım	Çanakkale Onsekiz Mart University	Turkey
Recep Yurtseven	Pamukkale University	Turkey

## In This Issue

### Editorial Note

1 **Hayri Baytan Ozmen**

A view on how to mitigate earthquake damages in Turkey from a civil engineering perspective

### Research Article

13 **İlker Bekir Topçu, Arda Uzunömeroğlu**

Experimental investigation of utilizing chemical additives and new generation corrosion inhibitors on reinforced concrete

### Research Article

35 **Samson Olalekan Odeyemi, Omolola Titilayo Odeyemi, Adewale George Adeniyi, Zainab Tolu Giwa, Ademola Kamorudeen Salami, Adeyemi Adesina**

Prediction of chloride ingress for palm kernel shell concrete

### Research Article

51 **Anas M. Fares**

The impact of RC shear wall openings at the lateral stiffness of the cantilever shear walls

### Research Article

65 **Ercan Işık, İbrahim Baran Karaşin**

The mutual interaction between the structural footprint and number of floors in steel structures

### Research Article

87 **Stephen John Hardy, Harvir Satsavia**

Experimental low cycle fatigue testing of circular bars with radial through-holes subjected to tension-compression loading

### Research Article

97 **Tanay Karademir**

Micro-mechanical properties of geotextile fibers: measurement and characterization at cold environmental conditions

### Research Article

121 **Baran Sarac**

Influence of sub-glass transition heat-treatment on physical and structural properties of Cu<sub>46</sub>Zr<sub>44</sub>Al<sub>8</sub>Hf<sub>2</sub> metallic glass

Research Article

135 **Güliz Akyüz, Aykut Elmas, Müberra Andaç, Ömer Andaç**

Evaluation of nano sized Mg@BTC metal organic framework as a drug carrier: A long term experimental and predictive theoretical study

Research Article

157 **Salih Hakan Yetgin**

Impact of multi-walled carbon nanotube and graphene oxide on abrasive wear performance of polypropylene

Free access to tables of content, abstracts and full text of papers for web visitors.

Copyright © 2021

Research on Engineering Structures & Materials

MIM Reseach Group Publications

P-ISSN: 2148-9807

E-ISSN: 2149-4088

<http://www.iresm.org>



## ABSTRACTING / INDEXING

The international journal of Research on Engineering Structures and Materials (RESM) is currently Abstracted/Indexed by Asos Indeks, CiteFactor, Cosmos, CrossRef, Directory of Research Journal Indexing, Engineering Journals (ProQuest), EZB Electronic Journal Library, Global Impact Factor, Google Scholar, International Institute of Organized Research (I2OR), International Scientific Indexing (ISI), Materials Science & Engineering Database (ProQuest), Open Academic Journals Index, Publication Forum, Research BibleScientific Indexing Service, Root Indexing, Scopus, Ulakbim TR Index (Tubitak), Universal Impact Factor and under evaluation by many other respected indexes.

Check web site for current indexing info.

# Scopus®





*Editorial Note*

## A view on how to mitigate earthquake damages in Turkey from a civil engineering perspective

Hayri Baytan Ozmen

*Department of Civil Engineering, Usak University, Usak, Turkey*

### Article Info

#### Article history:

Received 13 Nov 2020

Revised 18 Feb 2021

Accepted 18 Feb 2021

#### Keywords:

*Building identifier;*

*Civil engineering education;*

*Disaster management;*

*Proficient engineering;*

### Abstract

Earthquakes are natural events that turns into disasters in our country due to faults made in construction of structures. In order to prevent this, we need to determine solutions and act accordingly. The author wrote this paper to humbly share his knowledge and ideas on the subject with the public and his colleagues and encourage more discussions on the subjects. The mentioned points include views on the common public earthquake debates, main reason of damages being inadequacies in having healthy civil engineering services, the importance of informing and taking into consideration of the feelings of the suffered people, shortages of official damage assessment procedures, the necessity for unique building identifier and a fixed financial aid policy, suggestions on the civil engineering education, and how essential the proficient engineering concept is for robust construction of the structures.

© 2021 MIM Research Group. All rights reserved.

## 1. Introduction

Turkey, especially in the last two decades, has experienced enormous loss of life and property due to the medium and large scale earthquake that caused seismic damage [1, 2]. As a result of the number of damaged buildings and casualties, attention has been focused on the insufficient performance of the structures and the reduction of earthquake damages. The interest in the subject has been renewed with the Aegean Earthquake of October 30, 2020, in which 116 deaths, 1034 injuries and various damages were suffered. Especially, this latest event, in addition to the many resembling others, has initiated the author to contribute to the recent discussions on measures to mitigate seismic damage by sharing his knowledge and evaluations on the subject.

The author has been conducting academic and hands-on studies on seismic evaluation and strengthening of the existing building stock for more than twenty years. He has made 11 research projects supported by national and international organizations (European Union, TUBITAK, AFAD, several universities) and dozens of scientific publications on the subject [3–13].

Apart from these, the author made detailed seismic strength assessment of approximately 200 buildings upon the requests of various public institutions and private parties. He has participated in strengthening studies for half of these. In addition, the author has been found in damage assessment of hundreds of other buildings affected by several earthquakes in Turkey [8, 14–16]. He carried out detailed studies in 225 buildings in Simav region after the 19 May 2011 Simav Earthquake by an invitation from AFAD to assess the feasibility of retrofitting [17, 18].

Corresponding author: [baytan.ozmen@usak.edu.tr](mailto:baytan.ozmen@usak.edu.tr)

[orcid.org/0000-0001-6750-8632](https://orcid.org/0000-0001-6750-8632)

DOI: <http://dx.doi.org/10.17515/resm2020.231ea1113ed>

Res. Eng. Struct. Mat. Vol. 7 Iss. 1 (2021) 1-11

Working on the subject for different levels, having the opportunity to see the many aspects of the matter and being an academician enforces the author to express his thoughts. Author does not claim that the below given ideas are all correct and best versions. He just wants to contribute the discussions to achieve better solutions. The humble views of the author based on his experiences are given below:

## **2. Public discussions on earthquakes**

In our country, although it is off the agenda once in a while, the issue of earthquakes is discussed intensely from time to time due to its frequent occurrence. These discussions focus on when and how large the earthquake will be rather than what we can do against earthquakes, as if we are desperate against them. There are extensive discussions in the press about the magnitude of earthquakes, the type and length of the fault, and where and how long are the faults. Many people in our country has become familiar with many geological terms, and this topic has become one of the daily talks. However, it should be evaluated how much debate has been made about what should be done to reduce earthquake damages and how much we are trying to raise public awareness.

The 2011 Van earthquakes are informative examples in terms of the proximity to the fault and the benefits of earthquake magnitude discussions. The epicenter of the 23 October 2011 earthquake is closer to Van than to Erciş. However, much more destruction took place in Erciş. Muradiye, which is almost the same distance as Erciş from the epicenter of this earthquake and with resembling soil conditions, did not have similar destruction [19]. The earthquake of 23 October 2011 had a 7.2 magnitude, and the 9 November 2011 earthquake was 5.6 magnitude event. The distances of both earthquakes to the center of Van are not very different from each other. However, the 5.6 magnitude earthquake caused 4-5 times more collapse in Van than the first earthquake. It can be said that the structures damaged in the first earthquake collapsed in the second earthquake. However, there are many indications that the effects of the lower magnitude second earthquake in Van are greater [20].

When scientific studies and past earthquakes are examined, it is seen that the magnitude alone is not enough to explain the damaging nature of the earthquake. More than twenty parameters can be counted besides the magnitude related to the evaluation of the destructiveness of earthquakes[21–23]. Therefore, the discussions on "the magnitude of the earthquake will be this" and "the fault here will be broken at this length" are not as useful and primary information as they appear in the public. The provisions in earthquake regulations, if implemented, are in a position to ensure the survival of buildings in almost every earthquake that may occur in our country. Therefore, the issue is not to predict where and how big earthquakes will occur in the country in the future, but to ensure that earthquake regulations are implemented throughout the country.

## **3. Perceptions on reasons of damage**

Unfortunately, the level of awareness regarding the issue is still very low in our country, which has suffered greatly due to the earthquakes. In the public debate, earthquake damages are still attributed to reasons such as low concrete strength, unwashed sand and high number of floors. These are of course important and constitute some of the sources of damage. However, bringing only these issues to the public attention prevents a complete solution and causes a useless consumption of the public energy. Though, common application errors such as reinforcement detailing, insufficient use of lateral reinforcement, faults in manufacture of beam-column joints, deficiencies in lateral load carrying system are among the important causes of damages.

For example, a building with ready-mixed and good strength concrete, built in Erciş in 2011 is severely damaged. The reason for this damage is the use of insufficient lateral reinforcement in the structure, that is, failure to pay attention to engineering principles. There are also design errors related to shear wall locations in the same building [16]. The fact that the errors are attributed to only a few reasons mentioned above constitute an obstacle in creating public opinion and making regulations about the importance of adequate engineering services and the problems related to the training of engineers.

#### **4. Disaster management**

One of the first and most important studies after the earthquake is the determination of the damage status of the buildings. This issue came to the fore a lot in the public after the collapse of Bayram Hotel in 9 November 2011 Van Earthquake. As a result of confusing the damage assessment study conducted right after the earthquake with a general seismic assessment, the personnel who determined the damage state were criticized. In fact, that study was not an evaluation of the seismic performance of the structures and their behavior in future earthquakes, but an examination of the damage they have received in the past earthquake. Since the seismic assessment of the structure is a very detailed and time-consuming study, it is not possible to do it for an entire city after an earthquake. As an example, for an average building, it is normal for just gathering information process to take at least half a day in the building with a team of 7-8 people. In addition, with computer modeling and performance analysis, it is normal for the required time to be several days. Therefore, it is wrong to expect such an assessment from the damage assessment personnel right after an earthquake.

However, it can be said that there are some aspects that require improvement in post-earthquake damage assessment studies:

- Assessment results vary and similar damages can be given different degrees of damage by different teams.
- Important differences can be seen between preliminary damage assessment results and final damage assessment results. In preliminary damage determination, a "severely damaged" structure can be turned into "light damage" by definitive detection or vice versa.
- The negligence of the technical staff who perform damage assessment as a burden and the desire to complete it as soon as possible, negatively affects the effective and efficient work.

These problems make things difficult in all other steps by reducing the public's trust and belief in public authority. It may be helpful to focus on some issues to make damage assessment studies healthier.

##### **4.1 Damage assessment in terms of safety and financial aspects**

Two questions are tried to be answered simultaneously while determining the damage state of the buildings: whether there is heavy damage in the building that will prevent the continuous occupation and to determine the cost level required to repair the damage in the building for possible financial assistance and credit. However, trying to answer these two questions with a single damage level causes problems. For example, in case of widespread wall damage, it may be necessary to increase the level of damage in order to increase the credit/assistance to be given, as the cost of repairing the building will increase. However, structurally, this is not a priority affecting safety. In addition, the fact that significant damage has occurred in a column of the building due to local construction errors seriously endangers the safety of the occupants. However, the repair of the damage may involve low costs due to its local nature. As in these examples, some personnel may

choose to determine the degree of damage according to the extent of the destruction and some personnel according to its significance. Both approaches have justified reasons. For this reason, the author thinks that it will be useful to determine two separate damage level: one indicating the safety status of the building and the other for amount of credit/financial aid to be given.

In addition, it is necessary to consider damage assessment separately on the basis of flats and whole buildings. In fact, it is possible to experience significant wall damage in an apartment located on the ground floor of a building. In this case, significant repair costs will be incurred for this apartment. However, it is possible that no wall and bearing element damage could be found in an apartment on the upper floors of the same building. If we talk about the safety damage status as a reverse situation; in case of severe damage to the columns on the ground floor of the building, it is clear that although there is no damage in the upper floor apartments, the safety damage situation in those apartments should be evaluated as heavy.

The points in the above two paragraphs indicate how complex damage assessment is and why the damage status of structures can change significantly. Damage detection is a parameter that can be handled from four different points of view as the building and apartment level and its economic and safety aspects. It is natural that technical personnel who try to answer all four of these aspects with a single value have difficulties.

#### **4.2 Evaluation of damage status**

The engineers who examine the building may have different opinions about the safety level with regard to the widespread and low and the local and severe level of damage. The fact that people have different engineering views also causes different damage assessment results. By eliminating this kind of subjectivity, certain criteria can be defined for objective damage assessment and all decisions can be made accordingly. The staff can make a determination according to the answers to the questions in the forms they have. If the damage status of the building is determined as a result of a flow chart or scoring prepared according to the answers of certain questions, it will be ensured that all teams reach the same conclusion for the same damage case. Of course, it is important that the number and level of detail of these questions are minimum, taking into account the limited sources of time and labor. However, considering that the structures will not always have the same conditions, it may be inconvenient that the results of these forms are completely binding. In addition to the questions in the form, it may be important to reflect the engineers' specific views on the building. Ensuring that the damage assessment results are objective and independent of personnel, will be beneficial in terms of establishing the trust of the citizens and obtaining healthy damage assessment results.

It is also important to train relevant personnel in order to reduce different and unhealthy damage assessment results. Since engineering education is mostly aimed at new building design, training on these issues is not provided at a sufficient level as a standard. For this reason, the personnel making damage assessment should have received a separate training on this issue.

#### **4.3 Approach to damaged building owners**

Another important feature of the personnel who detects the building damage is conducting the first encounter of the state with citizens who experienced the earthquake. In this respect, it is an important step in showing that the state is interested in them. The author conducted a study on whether moderately damaged buildings in Simav district can be retrofitted after the earthquake of 19 May 2011 [11]. During this study, a survey process requiring 4-5 hours was carried out for each building, including taking core samples and detection of reinforcements in the ground floor. During these procedures, a building owner

said, "You spent so much time and effort. From now on, we will accept whatever you say about the building.". Then, he said the he did not believe the previous damage assessment result as it took only 15 minutes of the previous personnel visited the building.

Citizens generally have a perception that building damage assessment is not done with sufficient care. Due to this understanding, citizens object to public authority at every stage of the administrative and legal procedures. In order to eliminate this negativity and for citizens to cooperate better with the state, it is important for the officials to inform the citizen in the damage assessment process, to explain how the decision was made, even if it was very brief. Regarding damage assessment decisions, besides technical training, providing psychological training to the personnel on this subject may also be considered. This proposal can be seen as a situation that will increase the burden of the personnel who work devotedly under limited resources. However, it is thought that it will be beneficial in terms of reducing the problems that may be experienced in the future.

Likewise, it is important to inform citizens about how the preliminary damage assessment study is carried out. It should be explained that the damage determination is a practice that is performed visually and takes a short time in nature. For this purpose, using the press or a brochure distributed by related staff explaining the procedures can be considered.

Another reason for the objection of the citizens to the damage assessment results is that the damage they have seen and the situation reported by the personnel do not match. It is possible to hear complaints such as "A little damage to my house was given a greater damage while there was so much damage to the house of another person" or vice versa. It has been observed that the reason for this is that the wall damage, which usually covers a larger area, is more credited by the citizens. Buildings with more wall damage are regarded as heavily damaged, and the cracks, which are thought to be at a smaller level, in the structural system elements such as columns and beams are not taken into consideration. It may also be considered that such information can be passed on to citizens by means such as the above mentioned brochure.

#### **4.4 Financial assistance policy to the damaged building owners**

One of the reasons for the lack of adequate dialogue with citizens by technical staff is that citizens try to pressure technical staff about the damage status. Some citizens try to increase the damage status in order to get more financial aid, some try to reduce the damage status in order not to spend money to retrofit their building. This issue stems from the fact that citizens do not fully know the aid and credit policy of the state and a fixed policy has not been implemented on this issue for a long time. In the past years, the monetary aids made after earthquakes and their dependence on the damage limit cause citizens to try to increase the damage status. For example, in the Simav earthquake, a citizen ensured that his slightly damaged structure was converted to moderately damaged, with the expectation that more financial aid would be given. However, as it is concluded that the 3-storey masonry structure cannot be strengthened in the subsequent evaluation, he is in danger of losing his building. However, in case of slight damage, it would have been possible that this result would not have occurred as per the legislation. As in any other uncertainty, the fact that the state's aid/credit policy is not fixed causes citizens to try to affect the damage assessment. In this respect, to whom and how the loans/aids will be given should be set forth as a transparent and unchangeable policy.

Especially after DASK insurance, there have been significant developments in the aid/loan policy and the uncertainty has largely disappeared. However, since this issue is not sufficiently known by the citizens, certain demands may still arise regarding the damage assessment result. Telling the citizen that each damage assessment result has positive and negative aspects and that the best way is to act according to the result of the technical

examination of the building, will also help to overcome such problems. At this point, informing the citizens again comes to the agenda.

## **5. Approach to the people suffered by the earthquake**

As mentioned in the section on damage assessment above, the psychological state of people who have experienced an earthquake is naturally bad and the approach to these people is important. Psychology training should also be considered for all the government personnel working in the earthquake zone. With the training to be provided, it is possible that the staff can come to the fore as an auxiliary element in terms of more effective communication and easier guidance of the public. This will prevent many future problems that may arise.

### **5.1 Morale status of the people in the earthquake zone**

As mentioned in the previous section, the morale of the people in the region where the earthquake was experienced is low and this is the source of many problems. For example, after the 23 October 2011 Van earthquake, many citizens in Ercis, whose houses were not damaged at all, did not enter their homes for a long time due to fear. As statistics show, buildings collapsed and heavily damaged after many earthquakes are around 10% of the total number of buildings. However, with the remaining 90% not entering their buildings, the need for accommodation, food, etc. in the earthquake zone increases roughly 10 times. It is not an easy task to meet the need for shelter for a large city all at once. The necessity, economy, benefit/loss status of aid institutions to be able to fulfill such a request are a separate debate subject, but the considerations that started about the shortage of tents after the Van earthquake are an indication of this situation. This phenomenon is an example of the importance of managing the morale of the people after a disaster.

As the author follows in the press, various entertaining activities for children in the earthquake zone are good examples of services that can be done on the subject. Expecting adults to participate in such activities after the earthquake may not be expected and perhaps not appropriate in terms of morale. But doing these kinds of activities with children is beneficial for their parents to be positively affected.

Although such activities are important, the most important factor that can affect the morale of the people is that the state takes care of them and efforts are made to solve their problems. Of course, it is impossible for people who have experienced an earthquake to be fully satisfied, but it is also important to reduce the degree of dissatisfaction.

Press organizations have a great impact on this issue. In order to attract attention, mostly bad news regarding extreme cases takes place in the press. Although these news are beneficial in terms of raising the motivation to get help from the rest of the country, they negatively affect the morale of the people and the normal order of life in the earthquake region. Press organizations can be asked for help to include positive news especially in the local papers.

## **6. Unique building identity number**

In many processes such as damage detection and gathering information about them, buildings must have a permanent "marker". However, in practice, many difficulties are encountered in identification of the buildings. For example, in the process of collecting information from the building, sometimes all and sometimes some of the information such as the names of the occupants or addresses and plot of the building are used. However, problems are encountered as the information of the same buildings is tried to be accessed in different institutions such as the municipality and public works. The property owners and residents of the buildings, most of which are over 20-30 years old, have mostly changed during this period. There are also differences in address information due to the

change of street and neighborhood titles. The same is true for block and plot numbers. Block numbers change over time for different reasons, and plot numbers can change due to the merging and separation processes.

As a result of this situation, it is not possible to establish contact between the information collected from the field and the information held by public institutions. This situation may cause significant weaknesses in a subject where time is very important such as disaster management operations after an earthquake. For example, in the seismic assessment study conducted by the authors in the Simav district after the earthquake of 19 May 2011, significant time had to be spent on this subject. The information in the building files obtained from the municipality was compared with the individual damage assessment results, and the building information was partially combined. Since the mentioned study covers 225 buildings, it was possible to realize the process. However, it is clear that the problem will become insoluble when a study needs to be carried out on tens of thousands of buildings after an earthquake in big cities.

In order to overcome this problem, the author recommends using an "identification number" for each building plot. This number should be given for new plots with the formation of the plot and should not be changed under any circumstances. A unit in this identification number can be reserved for subdivision operation. In the unallocated plot, this value will be "0". In case of subdivision, this value can be increased by 1-9 for each new plot. Thus, the immutability of the identification number can be achieved. Similar approach can be made for other situations requiring change, if any. Last 2 digits are of the ID number can be reserved for flats in the building. Thus, just like for citizenship number for persons an unchangeable and unique identifier will be created for flats and buildings.

For existing buildings, these values can be assigned by the municipalities, so that all structures can have this unique marker. Thus, the information from all different institutions working on buildings can be collected in a common pool. In this way, significant labor and time will be saved in post-disaster management studies.

## **7. Earthquake resistant construction of buildings**

Earthquakes have turned into disasters due to mistakes made for 20-30 years before it happens. Faults made in 30 years cannot be solved in 5-10 days. Of course, the main point to solve this problem is that the structures should be built earthquake resistant before the earthquake. No post-earthquake study can be considered as effective as building earthquake-resistant structures. Unfortunately, the scenes after the earthquakes in our country reveal that we are not at a sufficient level in this regard. The presence of such high number of damaged buildings after the earthquakes shows that many procedures and people have faults in construction of the building, from workers to engineers, contractors and owners. Issues such as the regulation of the building inspection system, the use of quality materials in buildings, etc. are much discussed in public. Although the author admits that these points are quite important, he wants to draw attention to the issues that he thinks have not been discussed enough, rather than addressing the issues that have been repeated in many occasions.

First of all, the primary reason for the collapse of the structures is not that the structures are made with low strength concrete, un-ribbed reinforcement, sea sand, and lack of shear walls. As partly mentioned above, there are structures that have totally collapsed in Erciş in the earthquake of 23 October 2011 despite being manufactured with high-strength concrete and ribbed steel. Next to these, there are also two-storey mudbrick structures built in accordance with engineering principles and not seriously damaged at all during the earthquake. The primary cause of the damage is structures that have not received adequate

engineering services. For this reason, some suggestions will be presented regarding the development of civil engineering service in our country:

### **7.1 Proficient engineering concept**

Civil engineering is perhaps a branch of engineering where proficient engineering concept is most needed among all others. Because it does not include an auto-control like many other engineering fields. For example, when an electronic engineer is asked to design a circuit, if the circuit in question works, the engineer is successful, if not, the engineer is unsuccessful. In this case, the engineer who cannot make the desired circuit has to improve himself. However, in civil engineering, testing of the work takes place in every 30-40 years by an earthquake for most cases and by this time it is too late. In other words, there is no auto-control in civil engineering for the person to be competent and to improve himself with advancements in the field.

On the contrary, there is a pressure on the civil engineers to relax the rules of earthquake resistant construction. Since being afraid is the work of knowledgeable people, good civil engineers are aware of the danger. However, nobody in the constructions business likes them. Architects are not happy because their design is interfered with when they talk about the deficiencies in the design, the contractor will not be happy because more materials and workmanship is required, the owner will not be satisfied because the house may not be exactly what he wants or it will be more expensive, workers are not satisfied because it is harder to do what they want, and nobody wants to work with this engineers. In this case, although the good engineer has worked harder and improved himself, he is criticized from all parties involved. Since this situation should not be allowed, a system that will protect the engineer who does his job well is necessary. This can be done with expert or proficient engineering concept.

According to the author, engineers should be tested every 5 years and according to the fields they work in. Fields should be separated such as structural engineering, management, construction engineering, geotechnical engineering, hydraulic engineering, etc. Only the ones who are successful in the related exams, can have the license to conduct the engineering services. There should be at least 3 classes such as A, B, C instead of being directly successful or unsuccessful. Those who fall below a certain score should not have license, and others should be authorized for jobs in size according to their grade. Thus, it may be possible to increase the motivation of engineers to have a higher degree. Everyone should have a field of specialization (or if they are successful in the exams, they can have more than one), and accordingly, they should not be accepted as an authorized person in every job that comes their way. Although similar legal regulations have been discussed for many years, they have not been implemented.

Starting with 2008, it was imposed that the engineers who design buildings had to collect a certain score each year by participating in activities such as various courses and scientific meetings. During this period, the author tried to contribute to this process by teaching in some courses and by making scientific presentations. It has been observed that the participating engineers were not satisfied at first because it took their time, but afterwards they were generally satisfied in terms of increasing their knowledge and becoming more capable. However, with the relaxation of the conditions later, this rule became dysfunctional and a very useful and important step in the training of engineers was lost.

### **7.2 Re-organization of civil engineering education**

Civil engineering is a branch of engineering that covers a wide range of topics. Civil engineers work in many fields from computing the durations of traffic lights to water network construction, from determination of building site conditions to design of dams, from highways to construction of skyscrapers. Naturally, not every engineer can be

expected to have in-depth knowledge of each of these subjects. Some of them have very distinct characteristics to each other.

Although civil engineering education varies in every university, the major divisions consist of Structural mechanics, Materials, Construction Management, Mechanics, Hydraulics, Transportation and Geotechnics. Among these departments, there are branches that are closely related to all other branches such as material, mechanics and geotechnics, as well as branches that can be seen far from each other such as structural mechanics and transportation, structural mechanics and hydraulics. Civil engineering, like all engineering branches, is a 4-year department and during this period, all the information about these departments, some related and some unrelated, is given to all students.

However, if proficient engineering is put into practice for the engineers to specialize and become expert in certain branches, as stated above, there will be a discrepancy between the goal and the content of the education. For example, for a student who wants to specialize in building design and construction, the courses regarding the use of water resources, designing traffic lights, etc will be useless. In this case, it will be waste of the resources of both the student and the university.

In fact, this issue, which has become more visible with the emergence of the concept of proficient engineering, is among the problems of civil engineering education. There is little or no other profession with such widespread coverage. In order to solve this problem, dividing civil engineering into other engineering branches and opening different departments for each of them is a difficult and perhaps not a necessary process to carry out in the short term. Instead, it may be a solution to educate the students in divisions that are determined when they begin the university education or after a two-year program of common courses. The related division should be included in the diplomas given at the end of the education and the use of signature rights should be arranged accordingly. In this way, it will be possible to train more competent engineers in each specialization.

## **8. Summary & conclusions**

Earthquakes are natural events that turns into disasters in our country due to faults made in construction of structures. In order to prevent this, we need to determine solutions and act accordingly. The author wrote this paper to humbly share his knowledge and ideas on the subject with the public and his colleagues. The mentioned points may be summarized as follows:

- When discussing about earthquake damages, much of the public energy is wasted on considerations regarding the locations of the faults, timing and magnitude of the next earthquake. However, scientific experiences show that even if we know when, where and how big the next earthquake will be, it has little impact on the mitigation of seismic damage.
- Reasons of building damage are reduced to a few simple points such as low strength concrete, use of unwashed sand and un-ribbed steel, etc. However, the main problem is the insufficient engineering services. Attributing the errors to only a few other reasons constitute an obstacle in creating public opinion and making regulations about the importance of getting adequate engineering service.
- We also have problems on disaster management and controlling the situation after an earthquake. We should take into account the feelings of the people more and inform them more to have their collaboration.
- Official damage assessment after the earthquake should be handled differently in financial-safety aspects and flat-building level. The damage status evaluations

should be independent of the evaluator and more definitive for the property owners.

- Financial aid and loan policies should be clear, fixed and invariable for different earthquakes.
- Morale status in a post-earthquake region may affects the amount of required resources to shelter and organize the suffered people.
- Just like the people, we need unique identity numbers for the buildings to quickly and accurately combine the information from different sources after or before an earthquake.
- Unquestionably, the main solution for preventing earthquake damages is based on building earthquake resistant structures. Civil engineers are the key elements to achieve this goal. Some improvements should be made in civil engineering education. Additionally, proficient engineering concept should be included in related laws and regulations as soon as possible to have healthy civil engineering service.

There is no claim that each of the ideas here is the most correct. We can reach the best solution by sharing ideas and discussing on the matter. Some of the issues mentioned can be seen as difficult to implement and some of them as obvious solutions. However, the author aims to contribute to the formation of public opinion by encouraging the discussions.

## **References**

- [1] Ozmen HB, Yilmaz H, Yildiz H. An acceleration record set for different frequency content, amplitude and site classes. *Res Eng Struct Mater.* 2019; 5(3). <https://doi.org/10.17515/resm2019.116ea0209ds>
- [2] Ozmen HB, Inel M, Meral E, Bucakli M. Vulnerability of low and mid-rise reinforced concrete buildings in Turkey. In: 14th European conference on earthquake engineering. Ohrid, Macedonia; 2010.
- [3] Modeling Non-Linear Behavior of Reinforced Concrete Members, TUBITAK, 105M024, 2005-2008.
- [4] Effect of Recent Earthquake Code Modifications on the Strength and Ductility of Reinforced Concrete Public Buildings, Pamukkale University Scientific Research Unit (PAUBAP), 2006MHF007, 2006-2008.
- [5] Effect of Glass FRP Reinforcement Locations on Flexural Strength and Ductility of Reinforced Concrete Structural Members, Uşak University Scientific Research Unit (UBAP), 2016/TP014, 2016- 2020.
- [6] Evaluation of the Factors Affecting Seismic Performance of Mid and Low-Rise Reinforced Concrete Buildings, TUBITAK, 107M569, 2008-2011.
- [7] Determination of the Structural Properties of the Existing Reinforced Concrete Buildings, Pamukkale University Scientific Research Unit (PAUBAP), 2008FBE005, 2008-2011.
- [8] 2007 October Çameli Earthquake Damaged Masonry Building Inventory, TUBITAK, 108M408, 2008-2009.
- [9] Improving the Quality of Suburban Building Stock, (European Cooperation in the Field of Scientific and Technical Research) COST Project TU 701, 2008-2012.
- [10] Earthquake Science School, TUBİTAK Science and Society Project, 110B072, 2010-2011.

- [11] Evaluation of the Feasibility of Retrofitting the Moderately Damaged Buildings in and around Simav County after 2011 May Simav Earthquake, Prime Ministry Disaster & Emergency Management Presidency (AFAD), 2011-2011.
- [12] Investigation of the Relation between Seismic Damage and Characteristics of the Earthquake Records, Pamukkale University Scientific Research Unit (PAUBAP), 2011BSP024, 2011- 2013.
- [13] Change of Earthquake Ground Motions Depending on Soil Properties, TUBITAK, 215M357, 2015-2019.
- [14] Kumsar H, Özkul M, İnel M, Hançer M, Tama YS, Ozmen HB, et al. 29 october 2007 çameli earthquake pre-examination report. Denizli, Turkey; 2007.
- [15] Inel M, Ozmen HB, Akyol E. Observations on the building damages after 19 May 2011 Simav (Turkey) earthquake. Bull Earthq Eng. 2013; 11(1). <https://doi.org/10.1007/s10518-012-9414-3>
- [16] Ozmen HB, Inel M, Cayci BT. 23 October and 9 November 2011 Van Earthquakes Structural Damage Assessment Report. Denizli, Turkey; 2011.
- [17] Inel M, Un H, Ozmen HB, Akyol E, Cayci BT OG. Investigation of the feasibility of retrofitting the moderately damaged buildings in Simav region and surroundings. Denizli, Turkey.
- [18] Ozmen HB, Inel M, Akyol E, Cayci BT, Un H. Evaluations on the relation of RC building damages with structural parameters after May 19, 2011 Simav (Turkey) earthquake. Nat Hazards. 2014; 71(1). <https://doi.org/10.1007/s11069-013-0900-y>
- [19] Ozmen HB, Inel M, Cayci BT. Engineering implications of the RC building damages after 2011 van earthquakes. Earthq Struct. 2013; 5(3). <https://doi.org/10.12989/eas.2013.5.3.297>
- [20] Disaster and Emergency Management Authority (AFAD). Van Earthquake Report. 2011.
- [21] Kramer SL. Geotechnical Earthquake Engineering. Prentice-Hall, Inc. 1996. 653 p.
- [22] Ozmen HB, Inel M. Damage potential of earthquake records for RC building stock. Earthq Struct. 2016; 10(6). <https://doi.org/10.12989/eas.2016.10.6.1315>
- [23] Ozmen HB. Developing hybrid parameters for measuring damage potential of earthquake records: case for RC building stock. Bull Earthq Eng. 2017; 15(7). <https://doi.org/10.1007/s10518-016-0080-8>

Blank Page



## Experimental investigation of utilizing chemical additives and new generation corrosion inhibitors on reinforced concrete

İlker Bekir Topçu<sup>a</sup>, Arda Uzunömeroğlu<sup>b</sup>

*Department of Civil Engineering, Eskişehir Osmangazi University, Eskişehir, Turkey.*

### Article Info

#### Article history:

Received 29 Sep 2020

Revised 19 Nov 2020

Accepted 25 Nov 2020

#### Keywords:

*Reinforced Concrete;  
Ecological Inhibitors;  
Chemical Additives;  
Corrosion;  
Durability*

### Abstract

Corrosion is the most common structural defect in today's construction industry and therefore requires the most precautionary measures. As a result of corrosion, the repair of the structure causes high costs or is not possible at all. Corrosion inhibitors are the fastest and easiest method to take on corrosion, but many inhibitors used today contain components harmful to the environment and toxic. Today, there is hardly any concrete produced without using any chemical and mineral additives. Researchers are trying to produce less harmful concrete chemicals. In this study, calcium nitrite, which is the most widely used corrosion inhibitor in the market, and ecological boron inhibitor were compared with experimental methods. In addition, the interaction of chemical additives used most in concrete production with these inhibitors was investigated. As a result of experimental studies, it was concluded that the ecological boron inhibitor did not damage the structure of the reinforcement in the concrete and could be used instead of the calcium nitrite inhibitor produced in the market. The electrical resistance, rapid chloride permeability and half-cell potential experiments show that samples containing boron inhibitors gave the best results compared to other samples.

© 2021 MIM Research Group. All rights reserved.

## 1. Introduction

The cost of the material damage by corrosion amounts to millions annually moreover human life and suffering cannot be assessed. In many ways, the term corrosion protection is too narrow to describe the activities of structural scientists dealing with corrosion problems. Therefore, the cost of corrosion can be a higher magnitude than expected.

Rebars are integral component of reinforced concrete structures. High permeable concrete can allow the entrance harmful component that causing corrosion but corrosion is negligible when concrete and rebar are good contact with each other. This is so even when calcium chloride has been used to accelerate the hardening of the concrete [1].

The customary criterion of concrete quality is compressive strength but for the protection of reinforcement and it is more important than the concrete should be sufficiently fluent (low-slump) to envelop the rebar. Even if this involves using more cement than would be necessary merely to provide a given strength. In the concrete mix, high strength is desirable because more durable concrete can prevent the crashing in the concrete surface due to corrosion.

Corrosion causes expansion of steel reinforcement developing high-tensile stresses in the order of 20 MPa to 30 MPa in the surrounding concrete. These stresses are much higher than the tensile strength of concrete, and so cracks are developed in concrete in the vicinity of steel, resulting in the deterioration of reinforced concrete structures. Many countries are faced with

<sup>a</sup>Corresponding author: [ardauzunomeroglu@gmail.com](mailto:ardauzunomeroglu@gmail.com)

<sup>a</sup> [orcid.org/0000-0002-2075-6361](https://orcid.org/0000-0002-2075-6361); <sup>b</sup> [orcid.org/0000-0003-4204-0564](https://orcid.org/0000-0003-4204-0564);

DOI: <http://dx.doi.org/10.17515/resm2020.214st0929>

Res. Eng. Struct. Mat. Vol. 7 Iss. 1 (2021) 13-34

the threat of corrosion, according to researchers. Corrosion is not only the loss of the building but also a formation that endangers human life, social order and economy. In any corroded structures, even the repair of partially-damaged sections involve huge expenditure [2].

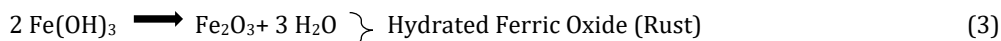
In this study separately from the others, it was investigated that interaction of calcium nitrite inhibitor (most widely used corrosion inhibitor in the market) and other chemical additives, also the effect of new generation ecological boron inhibitor (natural corrosion inhibitor) to the reinforcement, in terms of concrete durability and corrosion process were compared with experimental methods.

## 2. Literature Review

### 2.1. Electrochemical Corrosion

In electrochemical corrosion, all the processes of metal corrosion in the solution of electrolytes showing electrolytic properties such as in the soil and concrete (which can be considered an imperfect electrolyte) or by exposure to the atmosphere. On the other hand, the corrosion of metal at room temperature can normally take place with high velocity only in the presence of moisture; on the other hand, in a dry medium, the attack is very small or non-existent [3].

During the hydration of cement with water, a protective layer is formed in the presence of free lime around the reinforcing bar in concrete. The pH of this layer is about 13. During the service life of the structure, the pH value of this layer is reduced due to the chemical reaction caused by the ingress of moisture, oxygen, chlorides, sulfates and other chemicals present in the environment. During the initial stage of corrosion, rebar becomes the anode of the corrosion cell in which the metal is oxidized to form ferrous ions. The corresponding reaction at the cathode is the reduction of oxygen to produce hydroxyl ions so that the initial corrosion product can be considered to be represented by ferric hydroxide. This rust is a hydroxide of Fe<sub>2</sub>O<sub>3</sub> (ferric oxide) and it precipitates as yellow residue in cavities around the anode. The resulting reactions are given below:



Corrosion in an aqueous medium can be considered as an oxidation-reduction that concerns the metal and which takes place at the metal/solution interface causing the transfer of electrons through the metal and ions through the solution. As oxidation, we mean any phenomenon which causes the removal of electrons from the metal. In such cases, there will be corresponding reduction reactions with the surrounding medium. Therefore, the process takes place by an electro-chemical mechanism so that the metal from the metallic state goes into the solution as hydrated cations through anodic dissolution, or it is changed into a solid compound through anodic oxidation. The anodic process always takes place together with an equivalent cathodic reduction of some constituent in the aqueous electrolyte [4].

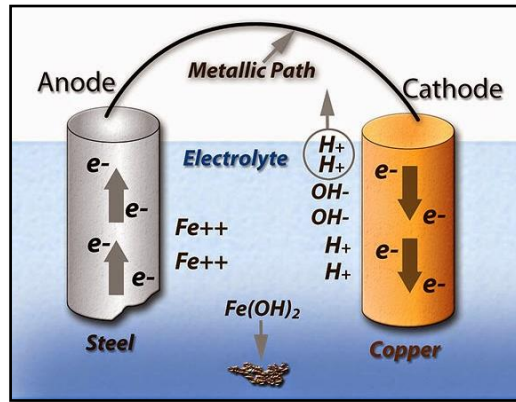


Fig. 1 Basic corrosion cell [5]

As the electrons are formed in the anodic region and are fixed in the cathodic region, a continuous movement of electrons must take place through the metal, and at the same time a movement of anions and cations into the solution. Electron flow is from the anode to the cathode, and the electrons continuously leave the anode and reach the cathode (Fig. 1). As this process continues, the separated electrons damage the anode (reinforcement) over time and consume it (corrosion). In other words, the corrosion process in solution implies:

- Passage of electrons into solution (electrolyte)
- Passage of electrons from the metal (rebar) to an acceptor cathode in the solution
- An ionic current in the solution
- An electronic current on the metal.

The corrosion rate will be controlled by the slowest process in the whole chain. From the definition of electrochemical reactions given below, we can assume that we can find at the corrosion potential a fixed value of corrosion rate. The corrosion rate is electrolytically equivalent to the current rate between the anodes and cathodes of the corrosion cells (Fig. 2).

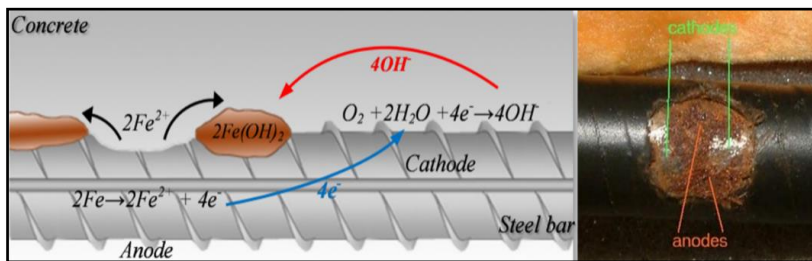


Fig. 2 Electrochemical reaction on rebar [6]

The passage of positive charge from the metal to the medium (at the anode) is always equal to the passage of negative charges from the metal to the medium (at the cathode). This is quite valid, either if cathodes and anodes are made by metals of different characteristics in contact in the medium, or if on the surface of the same metal the anodic or cathodic process takes place at atomic distances. The hardened zones of the metal normally have potential values less noble than the unhardened ones, and consequently, show a greater tendency to dissolve. In the case

of alloys have more than one phase, the different nature of the phases is promoting the formations of local cells [7,8].

## **2.2. Effect of Environmental Conditions**

Water and oxygen are mainly responsible for corrosion initiation. Their presence in concrete depends upon the quality, thickness of the concrete cover around the steel, the temperature, the humidity and the chemical contents in the surrounding environment [9]. Generally, hot and humid climatic environment are major factors responsible for the corrosion of reinforcement in the world. The designers and engineers must seek to change the environment, separate the metal from the environment, or reduce the corrosion reactions.

### *2.2.1. Moisture*

The rate of the electrochemical reaction in a corrosion cell depends upon the moisture content in the vicinity of reinforcement in concrete. The moisture can enter the concrete in several ways, such as; high water/cement ratio, by the concrete surface (outside or inside) or concrete ingredients. Increasing the water ratio of concrete in order to make more workable concrete is very dangerous. Because, when water evaporates and exits, the remaining concrete becomes more permeable. Therefore, the water-cement ratio and the impermeability of concrete play an important role in the corrosion process in concrete structures. From durability consideration, the water-cement ratio is limited in reinforced concrete structures. Similarly, moisture absorption is limited to 5% to 10% depending upon the type of concrete, the importance of the structure and the exposure conditions [10].

### *2.2.2. Chlorides*

The chloride ions are accelerated anode and cathode reaction in the corrosion process. These ions are very easily and rapidly penetrating the deeply of concrete. Chloride ions are depassivated the passive steel and reinforced concrete become more vulnerable against corrosive attacks. They also increase the electrical conductivity of concrete and accelerate the rate of corrosion. Chloride also affects the long-term strength development of concrete and impermeability. Chloride ions at the steel surface cause loss of passivity that provided by the normal alkali protection of free lime. They also reduce the resistivity of concrete. When chloride ions exceed the critical value, rebar is depassivated easily. Corrosion can occur where the chloride content is higher than the critical value [11].

Presence of chloride ions in concrete depends some variable (concrete cover, cement type, condition etc.). It is claimed that the presence of 2-7% calcium chloride does not increase to corrosion of steel when lime water has been used instead of plain water for mixing concrete. However, similar concrete made with plain water in the 2% calcium chloride environment, can cause corrosion. It is similarly claimed that sodium silicate prevents corrosion when calcium chloride is presented in reinforced concrete [12].

### *2.2.3. Oxygen*

The oxygen is existing in concrete in different concentrations and it causes different potentials that consist anode and cathode poles. The corrosion which is quantitatively measured in grams of steel per year depends upon the oxygen flow rate to the reinforcement through the concrete cover [13]. The oxygen flow rate to the rebar depends upon the cover thickness, water-cement ratio and humidity. The oxygen flow rate drops considerably with increasing cover thickness and humidity. The minimum cover thickness for different exposure conditions varies from 13 to 75 mm [14].

## **2.3. Effect of Corrosion on Structures**

Reinforced concrete steels are expected to serve for many years without being corroded. However, with the increase of permeability, high alkali level begins to decrease, with the loss of

alkali passivation, it becomes unable to protect the concrete reinforcement and corrosion formation begins. Corrosion causes volume increase and creates cracks parallel to the reinforcement [15]. Once the concrete cracks, it is completely vulnerable to atmospheric effects, and the structure quickly completes its service life (Fig. 3). Corrosion is not only a visual defect but also a chemical reaction that adversely affects the durability of the concrete.



Fig. 3 Damages caused by reinforcement corrosion in columns and beams [16]

Reinforcement embedded in concrete expands due to corrosion and cracks develop when the stresses caused by the expansion exceed the tensile strength of the concrete. An expansion of about 0.1 mm to 0.2 mm would be sufficient to produce cracks and to damage the concrete cover [17]. These processes depend upon the interaction of the following effects: Chloride content, moisture ratio, loss of resistivity of the concrete, oxygen diffusion, cover thickness, tensile strength, the ratio of cover thickness to rebar diameter, the spacing of the rebars.

#### 2.4. Prevention of Corrosion

Depending upon the stage of corrosion, the cost of repairing the corroded concrete structure is much higher than the initial cost incurred for additional measures taken during construction to prevent corrosion. Therefore, it is a more economical and rational way to take the necessary precautions before the structural member getting corrodes.

##### 2.4.1. Cement

The type of cement used plays a significant part in chloride and sulfate diffusivity in the hardened cement matrix. The risk of corrosion attack decreases, as the thickness of the concrete cover and the ratio of cement to aggregate is increased. The protection provided by Portland and slag cement is good, the environment provided by the slag-cement concrete being less alkaline but more stable. Pozzolan with silica fume reacts with the free lime and form calcium silicate. With this reaction impermeability, density, and strength of the concrete are increasing dramatically.

##### 2.4.2. Aggregates and Water

Aggregates should be washed thoroughly to remove fine dust, silt, clay and sea-salts. Tests for any chloride or sulfate content and for soundness should be conducted on representative samples. The chlorides should not be more than 0.06% in the sand and 0.03% in coarse aggregates. Sulfates in aggregates, (such as  $SO_3$ ) should not exceed 0.4%. The pH value of water should be more than 6. The chloride and sulfate contents should not exceed 500 ppm (0.05%) and 1000 ppm (0.10%) respectively [18].

##### 2.4.3. Concrete Design

For the construction of the concrete structure is always desirable to design low-slump concrete. The mix should be free from segregation and bleeding. Concrete should conform to the followings in order to prevent corrosion:

- The amount of cement in the concrete mix must higher than  $350 \text{ kg/m}^3$
- Water-cement ratio should not be more than 0,50. The water-cement ratio should be as low as possible, because less use of water makes concrete more impermeable.

Commercially-available superplasticizers can be used in quantities appropriate to the mix design so as to increase workability, strength and durability. Corrosion inhibiting mixtures such as calcium nitrate at the rate of  $20 \text{ lt/m}^3$  of concrete may be used to prevent corrosion [19]. It has been determined by the researcher that inadequate utilization of corrosion inhibitors is increases corrosion. In this research, calcium nitrates and ecological (green) inhibitors are compared in order to find the differences between these two additives.

#### 2.4.4. Reinforcement

In reinforced concrete, the use of high-strength deformed rebars with enough spacing is a simple and common way. While doing this, congestion between the reinforcement at any section of the structural member should be avoided.

Nowadays, it is quite common to protect reinforcing bars by galvanizing, especially for use in concrete which is to be exposed in an aggressive atmosphere. In practice, zinc coating is generally done by the hot-dip method. In this method, a thin zinc alloy layer is formed on the rebar surface. There are several advantages that can be gained when using galvanized reinforcing bars. Reinforced concrete can be completely isolated from its surroundings by coating with zinc [20]. However, this is an expensive operation and is rarely carried out properly, and if the cover is insufficient or the concrete mix is of poor quality, it can lead to spalling of the concrete. Some researchers reported that galvanized reinforcement does not resist corrosion long enough to justify the additional cost. Galvanized rebars corrode very rapidly if they are brought into contact with electrochemically passive materials (noble metals such as stainless steel, copper, brass, etc.) so their use is not recommended.

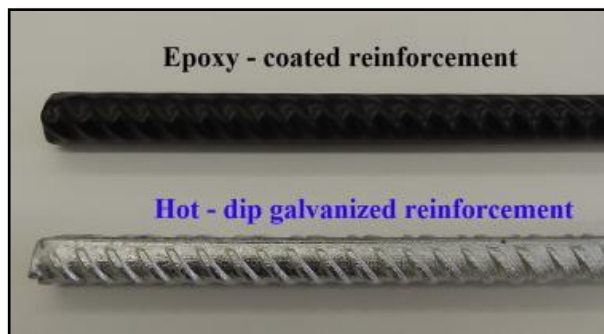


Fig. 4 Epoxy coated and galvanized reinforcements [21]

The adherence of steel and concrete is usually good but it may be weakened by thermal expansion. If extra protection of steel is considered essential, paints have can be used but they are rarely long-lived. Epoxy coatings protect the reinforcement from calcium chloride attack, but some paints of this type cause a lack of bond strength between the steel and the concrete. Reinforcement with epoxy coating has been used for many years in corrosive environments.

Epoxy is a two-component resin. This chemical can be applied to reinforcement by spraying or dipping (Fig. 4). It hardens in a short time after application and adheres well to concrete, steel and wood. Such bars are comparatively more expensive than conventional reinforcement. It is effective in increasing corrosion resistance and is recommended for use in structures with high corrosion risk. Epoxy coatings are also long-lasting and can be used in underwater work.

Bouazaoui et al [22] studied the interfacial shear strength between the steel bar surface and the concrete surface of steel rods that were previously bonded with epoxy resin into concrete using confined pullout test. The yield strength of the steel bar obtained through the test, was 340MPa and the concrete had an average compressive strength of 40MPa at 28 days. While the test continues, the load is gradually increased until the failure occurred in the steel-concrete interface. The author verified that the epoxy coatings significantly improved the shear and tensile stress distribution along with the interface between the steel surface and the concrete surface.

Stainless steel bars are about four times more costly than conventional reinforcement. These steels may be used for exceptional structures that highly require non-magnetic and corrosion-resistant reinforcement [23].

#### 2.4.5. Compaction and Curing

The concrete in the mould should be compacted thoroughly to eliminate honeycombs and voids (Fig. 5). Enough care should be exercised during vibration to ensure that the reinforcement is embedded with a proper bond [24]. Too much vibration leads to bleeding and segregation. Late vibration can be done to eliminate bleed-water film and fissures, if any, under the steel and the coarse aggregate.



Fig. 5 Insufficient implementation of vibration on concrete pouring [25]

The water used for mixing the constituents of the concrete should be a sufficient amount. The exposed area of the concrete to the outside should be protected from drying during the pouring. Because there is a possibility of concrete rapid drying due to the high temperatures. Therefore, concrete must be water cured within about 15 minutes after final finishing to avoid plastic shrinkage cracks. Curing should be continued for seven days so that the concrete attains a strength equal to 70% of its design strength [26]. To keep concrete wet continuously during the curing period; pigments, heavy-duty curing compounds, plastic sheets, waterproof papers and other wet materials may be used.

#### 2.4.6. Concrete Cover

The quality of the concrete and the thickness of the concrete cover is the most important factors to protect the reinforcement from corrosion. Permeability and cracking of the concrete cover will allow easy penetration of aggressive agents such as atmospheric gases, chlorides, sulfates and carbon dioxide. Therefore, where the climate is highly aggressive with a severe atmosphere containing chlorides and other salts, the impermeability and thickness of the concrete cover must be increased (Fig. 6).



Fig. 6 Inadequate use of concrete cover [27]

Depending upon the type of the structural component and exposure conditions, sufficient and recommended thickness of the concrete cover is between 15 to 70 millimeters [28]. Structures are physically inspected to assess corrosion damage. They may be heavily corroded or maybe in the initial stages of corrosion. When the visual inspection shows cracking and spalling with corrosion of steel all along with the member, the member is replaced with a new component.

In some cases, concrete structures can expose intense corrosive effects, the delamination of surface cracks may occur. In such cases, the member is repaired by materials as follows:

- Remove the loose concrete from the surface;
- Rebar should clean from the rust;
- Coating the reinforcement bar with epoxy paint;
- Addition of steel to substitute the loss of reinforcement if necessary;
- Jacketing the surface with cement-based material (Fig. 7);
- Surface of concrete should be coated;



Fig. 7 Retrofitting the corroded reinforced concrete columns with jacketing [29]

In the figure, repairing and strengthening of the concrete cover of reinforced column is shown. Habib et al. repaired the corrosion damage in the reinforced concrete column with the jacketing using fiber reinforcement. With this process reinforced concrete columns can be improved against earthquake [30].

## 2.5. Corrosion Inhibitors

During the working, the structural metals are actually the most critical materials which can suffer from corrosion; a real danger as a result of corrosion to the structures can follow. Protective measures one of which consists of the use of chemical compounds that added in small concentrations to the aggressive environment are able of reducing corrosion of the metal exposed to it. The reaction tendency of the metal is decreased by diminishing the aggressivity of the environment.

Usually, corrosion inhibitors are able to prevent general corrosion, but their action is more difficult against localized corrosion processes. The form of attack represents the greater destruction of material based on the weight of lost metal. However, from the technical points of view, the uniform attack is not the most important, because the life of the metal can be foreseen and the attack can be easily prevented by using corrosion inhibitors [31].

By using corrosion inhibitors, we try to avoid or reduce the corrosion of metallic materials with the addition of chemicals (usually at a low concentration) to corrosive medium. The inhibitors used in structural systems must satisfy the following criteria:

- The cost of a sufficient quantity of inhibitor, and such analytical work as if necessary, must be economic.
- The troubles which may arise should the inhibitor concentration fall, and the likelihood of such a fall should be considered.
- Some inhibitors (cathodic inhibitors) are slowly precipitated either, by decomposition or by reaction with a minor constituent.
- The corrosion inhibitors are toxic liquids that may present a problem in the disposal.
- All the materials should be protected from the threat of corrosion or at least not increasing it [32].

Corrosion inhibitors are chemicals that are harmful to the environment and people. Although they are added to concrete in small amounts, they infiltrate the soil during the perspiration of the concrete and cause environmental pollution. They have lethal effects on animals and carcinogenic effects on humans. The most used and commercial corrosion inhibitor is calcium nitrite. The inhibitor, which is added to the concrete like water during mixing, forms a passive film layer around the reinforcement and protects the reinforcement from corrosion.

Against these toxic effects of corrosion inhibitors, researchers have sought a more ecological inhibitor. As a result of the studies carried out on the boron mine, it has been discovered that some compounds synthesized from this mine protect the metal from corrosion. Turkey has about 74% of the world's boron reserves, so researchers are increasing their work on boron [33]. As a result of our investigation, it was seen that boron inhibitor shows a mixed type inhibitor specification, can't harm nature and people, and it has increased the corrosion resistance of concrete more than other inhibitors (Fig. 8). Boron inhibitor takes its ecological feature from the borane complex it contains and does not contain any other chemicals. However, the exact content cannot be shared. The biggest advantage of this inhibitor is to be used boron reserves are abundant in Turkey.

Gerengi et al. compared the results of boron cation ionic liquids EMITFB (1-ethyl-3-methylimidazolium tetrafluoroborate) inhibitory activity in 0.1M HCl environment with using Electrochemical Impedance Spectroscopy (EIS) and Potentiometric Polarization (TP) methods (This inhibitor is the new generation ecological boron inhibitor and was used in this current study). They have seen that metal surface is disrupted by the action of HCl when St37 metal is exposed to a 0.1 M HCl environment. When the inhibitors are added to the working environment, they observed that the film is formed on the metal surface and the formed film protects the metal against corrosion [34].



Fig. 8 Chemical additives and ecological boron corrosion inhibitor used in this study

Abdulrahman et al. [35] studied the design for a long-life span quality concrete. The main advantage of using calcium nitrite is inhibiting the corrosion process caused by both chloride ions by carbonation and the action of sulfate ions. Depends on the quality of the concrete, nitrates increase the strength gain rate according to the exposure conditions, and the amount of calcium nitrite. Among the side effect of concrete, nitrites accelerate the setting of fresh concrete.

Ryu et al. [36] investigated that use of calcium nitrite-based inhibitors needs greater care in estimating the quantity. Because, when the amount of inhibitor is not sufficient, it will increase the corrosion and damage rapidly the structural member. Thus, it is of utmost importance to define the optimal amount to be added for the inhibitor to work properly.

Okeyini et al. [37], as a result of their physico-chemical analysis on the *Phyllanthus muellerianus* plant, it was understood that *P.muellerianus* has non-toxic, environmentally friendly potentials and protects metal from corrosion. As a result of the researches, they concluded that the components obtained from the leaf of *P.muellerianus*, when used as additives in reinforced concrete samples immersed in a 0.5 M  $H_2SO_4$  environment, reduce the total corrosion of reinforcement in reinforced concrete. As the *P. Muellerianus* concentration used in the test samples increases, the total amount of corrosion decreases.

### 3. Present Experimental Work

Today, there is hardly any concrete produced without using any chemical and mineral additives. In our study, optimal concentration value of inhibitors was determined as  $20 \text{ lt/m}^3$  and this amount kept the concentration of calcium nitrite insufficient amount. In addition, other chemical additives were used at an optimum rate (approximately 2%) in accordance with the standards. The preparation of reinforced and unreinforced samples is shown in Figure 9.



Fig. 9 Preparation of reinforced and unreinforced samples

#### 4. Materials and Methods

##### 4.1. Materials

Concrete samples were prepared with cement, water, aggregate and sand. In this research, CEM I 42.5 R cement was utilized conforming to the TS EN 197-1 [38]. The physical and chemical properties of Type I Portland cement are presented in Table 1. The aggregates are obtained from local sources and the maximum size of coarse aggregate was 12.5 mm and limestone crushed sand was 1.25-5 mm. The reinforced concrete samples were prepared with a 0.50 water-cement ratio and a dosage of cement in the mixture of 350 kg/m<sup>3</sup>. In this research, 16 mm diameter S420 deformed reinforcement steel was used. As a result of the experiments, the yield strength of the steel was 479 MPa and the tensile strength was 602 MPa. These values provide the limits specified in TS 708 [39].

Table 1. Physical and mechanical properties of portland cement

Chemical Composition (%)		CEM I 42.5 R
Physical Properties	Specific Weight	3.11
	Blaine Surface (cm <sup>2</sup> /gr)	3501
	Residue on Sieve - 0.090mm (%)	0.31
	Residue on Sieve - 0.045mm (%)	5.11
	Standard Consistency Water Amount (%)	28.3
	Setting Start Time (min)	180
	Setting Ending Time (min)	270
	Volume Expansion (mm)	1
Mechanical Properties	Compressive Strength - Day 2 (MPa)	23.1
	Compressive Strength - Day 28 (MPa)	49.5

Table 2. Chemical properties of portland cement

	Chemical Composition (%)	CEM I 42.5 R
Chemical Properties	SiO <sub>2</sub>	19.67
	Al <sub>2</sub> O <sub>3</sub>	5.21
	Fe <sub>2</sub> O <sub>3</sub>	2.68
	CaO	63.72
	MgO	3.01
	Na <sub>2</sub> O	0.92
	K <sub>2</sub> O	0.46
	SO <sub>3</sub>	2.13
	MnO	---
	S	---
	Cl <sup>-</sup>	0.006
	Loss of ignition	3.54
Insoluble residue	0.5	
Free CaO	1.85	

Topcu and Karakurt [40] were investigated the properties of rebar within increasing temperatures. Samples were exposed to different temperatures for 3 hours and the pull-out test was examined. 2 types of steel were tested which S220 and S420. All mechanical properties were reduced due to the temperature increase of the steel rebars (Fig. 10).

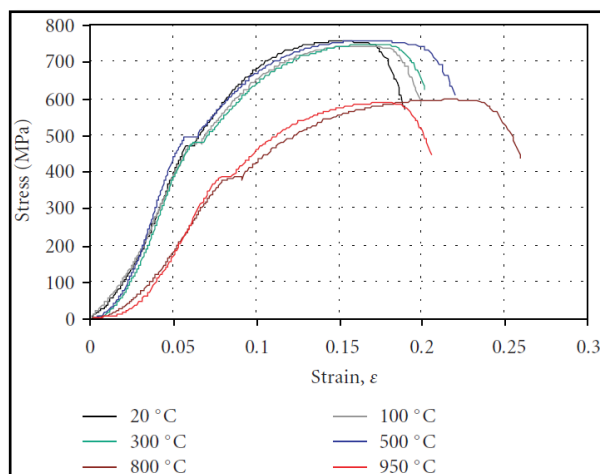


Fig. 10 Stress-strain curve of S420-ribbed steel rebar [40]

Three types of chemical additives were used in our study: set accelerator, set retarder and superplasticizer. In addition, two different corrosion inhibitors were used, namely commercial (calcium nitrite) inhibitor and boron (ecological-green) inhibitor. The additives represented by the series in this study are as follows; CTRL control sample, BORIN boron inhibitor, FERRO calcium nitrite inhibitor, SAK superplasticizer chemical additive, PHIZ setting accelerator chemical additive, and PGEC represents set retarding chemical additive.

## 4.2. Methods

### 4.2.1 Rapid Chloride Permeability Test

The rapid chloride permeability test was applied in accordance with ASTM C 1202 [41] standard. The experiment is carried out on discs obtained by cutting 100x200 mm unreinforced cylinder samples with the help of a concrete cutter. The purpose of this experiment is to see to extent of concrete conducts electricity and to determine the electrical resistance of samples that chlorine ions passing through. The rapid chloride permeability test is shown in Figure 11.



(a)



(b)

Fig 11 Preparation of samples (a), Rapid chloride permeability experiment (b)

Information about the chlorine permeability of concrete is obtained according to the total coulomb values obtained as a result of the experiment. The test samples were kept under curing conditions and the rapid chloride permeability test was carried out on the 28th and 90th day. Tests were carried out on three samples for each mixture kept at the specified curing conditions.

### 4.2.2 Salt Test

The rebars were cut into 150 mm pieces and sent to the laboratory (in airtight bags) for salt testing without being exposed to any chemical effects on their surfaces (to ensure that the test results are not affected). The solution that used for the salt spray test is consists of 5% of NaCl (more than seawater, which is between 1.8% to a max of 3%) and the pH of the solution ranges from 6.5 to 7.2. The exposure zone of the salt test spray chamber is maintained at 35 °C. Salt test applied to rebar samples for 1000 hours according to ASTM D4940 [42] standard. The test is continuous for the duration of the entire test period. Salt test results shown in Figure 12.

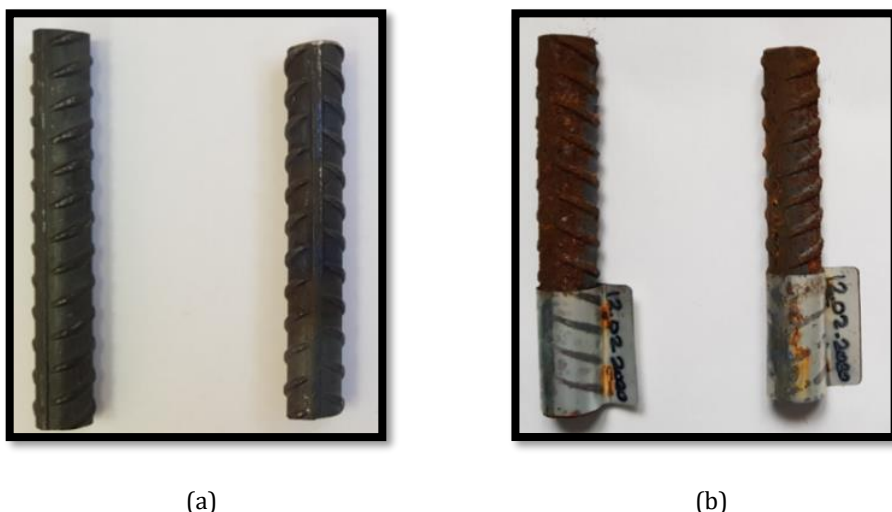


Fig. 12 Structural rebar before salt test (a), after salt test (b)

#### 4.2.3 Electrical Resistivity

This test was carried out on concrete with sample sizes of 100x200 cylinders. Before starting the experiment, two holes were drilled on the cylinders with 50 mm between them and the depth of these holes is 10 mm. The probes of the device were placed in these holes. Before this process, the holes were filled with gel according to ASTM C1876 [43] standard.

An important point to be considered while making these measurements is that the samples must be saturated with water. The surfaces of the samples saturated with water waited until they were dry, and the electrical resistance reading was made with the device after that and an idea about the corrosion status of the produced samples was obtained. The test samples were kept under curing conditions and the electrical resistivity test was carried out on the 28<sup>th</sup> and 90<sup>th</sup> day. Tests were carried out on three samples for each mixture kept at the specified curing conditions.

#### 4.2.4 Half-Cell Potential

The half-cell potential test method, which is based on the principle of instantaneous measurement of the corrosion potential, gives information about the possibility of corrosion in the reinforcement. Half-cell potential is one of the simplest electrochemical measurement methods and can be used in the field, on the structure, or in the laboratory. The potential of the reinforcement in the concrete is determined by establishing the connection of a certain half-cell with the reinforcement. In accordance with ASTM C 876-15 [44] standard, an electrode with a sponge under it is placed on the equipped sample, which is very wet. While the positive pole of the voltmeter is connected to the reinforcement, the cable coming out of the other end of the electrode is connected to the negative pole of the voltmeter. Thus, the circuit is completed and the potential of the reinforcement is measured. As in ASTM C 876-15 standard, copper / copper sulphate (CSE) is used as reference electrode in this study (Fig. 13).

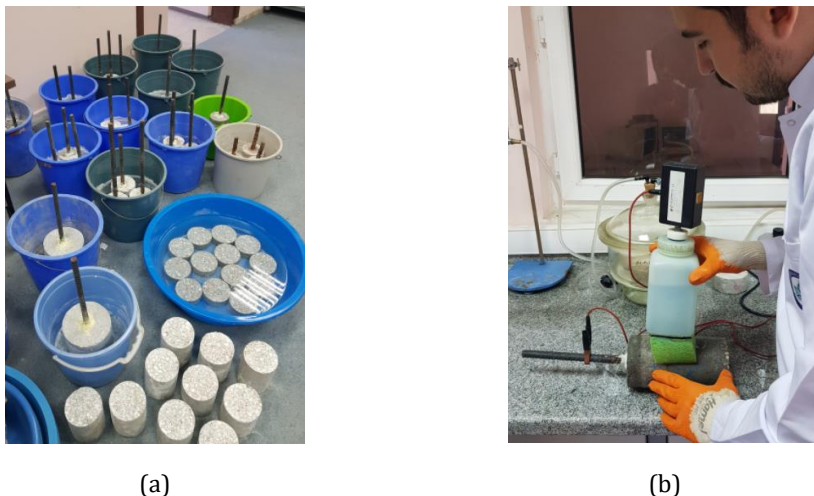


Fig. 13 Curing the test samples (a), Half-cell potential test (b)

Alhozaimy et al. [45], performed laboratory experiments to evaluate half-cell potential, corrosion current, and concrete resistivity over chloride contaminated concrete specimens, to investigate the phenomenon of high corrosion at intersection of steel rebars in the wall footing. They observed that experimental measurements are higher at intersection of steel bars in comparison with the areas between them. Because of the electrical connectivity and poor concrete microstructures, a high corrosion rate is found after the experimental test.

Duong et al. [46], performed half-cell potential and corrosion current density test on concrete specimens to monitor corrosion activity. Corrosion initiation of rebar and carbonation process was observed with different techniques. They observed that with the increase in leaching exposure carbonation depth also increases. It was seen that, fly ash was not only increasing the corrosion resistance but also carbonation and leaching.

## 5. Results and Discussion

Bare rebars were exposed to a salt test to see the corrosion influence on the surface. After the 1000 hours of salt test, we can easily visually analyze the samples. The experimental results show us that, without an alkaline environment created by concrete, rebars are easily getting corroded. Inhibitors used in concrete form a passive film layer around the reinforcement and this layer protects the reinforcement from corrosion. The alkaline environment of the concrete ensures that this film has a more stable structure. Without these two important factors, the reinforcement loses its strength by being corroded very quickly under the influence of chlorine and water.

An impermeable concrete containing inhibitor will last for many years without corrosion, even if exposed to intense chlorine and water effect. Good quality concrete will prevent the corrosive effect from going deeper and protect the steel from the destructive impact of corrosion (especially in the coast region).

Ecological boron inhibitor and calcium nitrite inhibitor were carried out on 100x200 mm samples, respectively, BORIN and FERRO. As seen in Figure 14, according to the half-cell potential of samples, the corrosion amount decreased in both inhibitors compared to the control sample. This is because, due to the nature of the inhibitors, a passive film was formed

around the reinforcement by progressing in the concrete and this layer protected the reinforcement against corrosion.

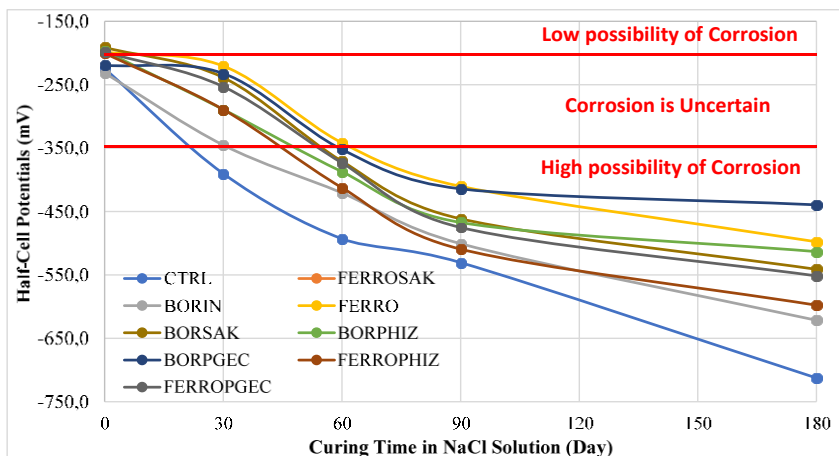


Fig. 14 Half-cell potential results of concrete samples

When we compared the inhibitors among themselves, it was seen that the new generation boron inhibitor slightly reduced the corrosion rate compared to the calcium nitrite inhibitor. This effect increased a little more as time progressed. At the end of 6 months, the boron inhibitor reduced corrosion by 30.1% compared to the control sample, while the calcium nitrite inhibitor reduced it by 14.6%. When we look at the half-cell potential test results, we see that all test samples are corroded. This is because the test chambers used in the experiment contain a high percentage of NaCl.

In such a high chloride environment (this value was chosen to be similar to seawater salt concentration), It is quite natural to start corrosion in samples in a short time. The important thing is, which test sample corroded less as a result of the comparison. After the experiment, the best results were given by an ecological and non-toxic boron corrosion inhibitor among all chemical additive and inhibitor series during the same curing time. Boron corrosion inhibitor gave better results compared to other samples thanks to the natural borane complex it contains.

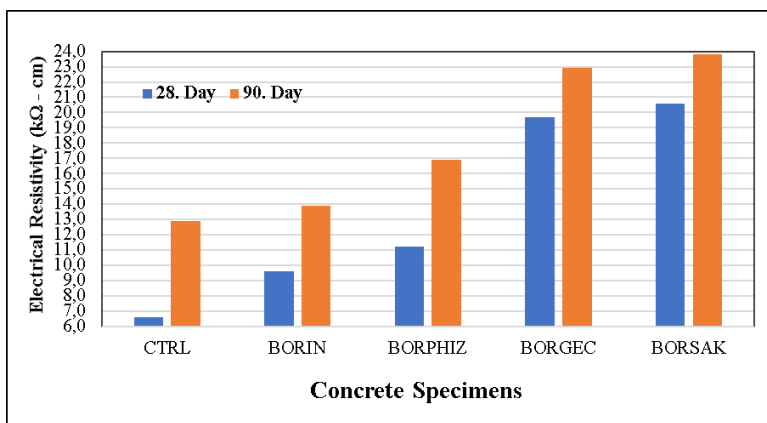


Fig. 15 Electrical resistivity of specimens with boron inhibitor

In the Figure 15, the change of electrical resistance results of concrete with boron inhibitor and chemical additives over time is shown. The combination of boron inhibitors and chemical additives has improved concrete properties. In concrete samples in which set retarder and boron inhibitor were used together, electrical resistance value increased by 19% compared to control samples. In addition, BORSAK series obtained the highest value of these series, 23.8, which is 85% higher than the control series.

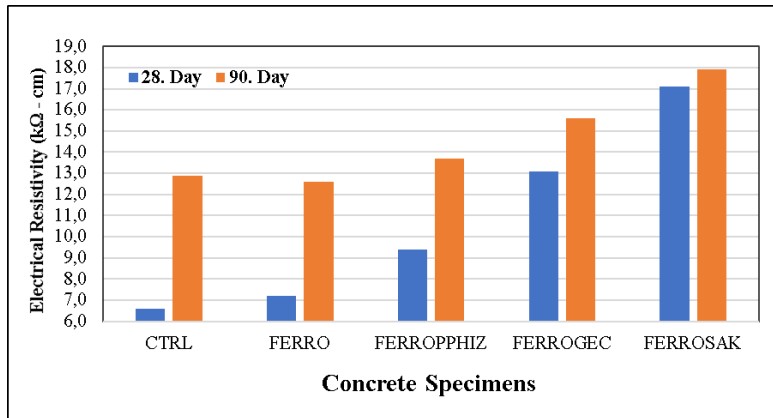


Fig. 16 Electrical resistivity of specimens with calcium nitrate inhibitor

In the Figure 16, the change of electrical resistance results of concretes with calcium nitrite inhibitor and chemical additives over time is shown. When calcium nitrite is used together with other chemical additives in reinforced concrete, it did not damage the internal structure of the cement. It is known as a result of experimental studies that calcium nitrite inhibitor increases the electrical conductivity of concrete due to its nature. However, with the use of other chemical additives, the concrete reached a better consistency, settled in the mold better and the impermeability increased. Electrical resistance values increased with the increase of impermeability.

It is understood from the electrical resistance test results that even if the ecological boron inhibitor was used together with chemical additives, it gave a more positive result (high electrical resistance) than the calcium nitrite inhibitor (harmful and carcinogenic).

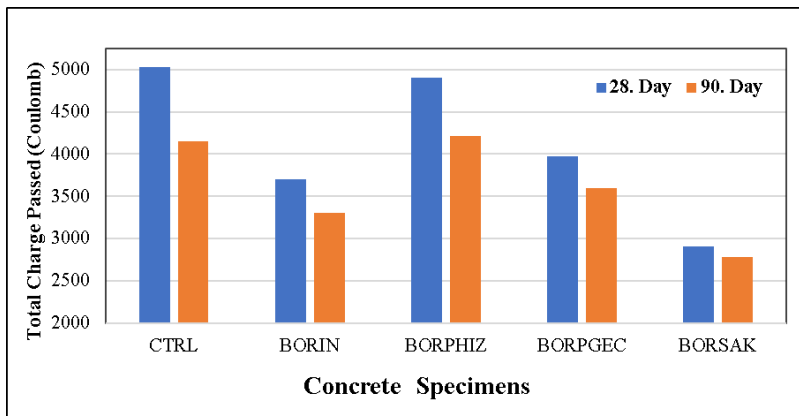


Fig. 17 Rapid chloride permeability of specimens with boron inhibitor

The low electrical resistance value indicates that concrete has a more permeable structure. Therefore, in terms of resistance to corrosion, higher electrical resistance value is desired. However, rapid chloride permeability results are inversely proportional to the results here. High rapid chlorine permeability values indicate that concrete samples are more permeable and will corrode more easily. In other words, lower permeability values are preferred in terms of corrosion resistance.

Values related to chloride ion permeability in concretes containing inhibitors are given above (Fig. 17). The boron inhibitor reduced the chloride permeability of concrete by 45% compared to the control sample. The combined use of boron inhibitor and superplasticizer additive enabled the concrete to settle into the mold better and reduced the permeability. Set accelerator and set retarding additives contain a little chlorine. Therefore, the fast chloride permeability value of the concrete samples where these additives were used was higher. In general, the permeability values of all concrete series using boron inhibitors were lower than the control sample. The longer the curing time, the better the chemical reactions in the cement and the decrease in the chlorine permeability values. The lowest chlorine ion permeability value in these concrete samples belongs to the boron and superplasticizer series with 2779 Coulomb.

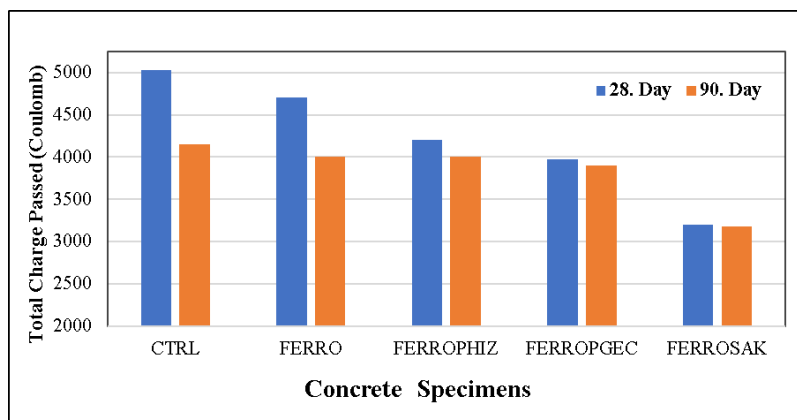


Fig. 18 Rapid chloride permeability of specimens with calcium nitrate inhibitor

When calcium nitrite inhibitor was used alone in the concrete mixture, it slightly affected the chlorine permeability value of the concrete compared to the control sample (Fig. 18). Since calcium nitrite increases the electrical conductivity of concrete, rapid chloride permeability values are not as low as in boron inhibitors. But there is a general decrease in permeability. In particular, the combined use of calcium nitrite and superplasticizers significantly reduced the permeability of concrete by about 38%. The rapid chloride permeability value for this series was determined as 3179 Coulomb.

## 6. Conclusions

The corrosion phenomenon is consisting of so many complex reactions and researchers are keep increasing their study on this field. However, from the case histories of several corrosion-affected structures, it is found that in the majority of cases the corrosion is mainly due to non-observance of specified construction and concreting practice. Therefore, it is necessary to continuing training of the workers on-the-job so that they observe good concreting practice.

Corrosion activity in reinforced-concrete structures primarily depends upon the activation period which is influenced by the interaction of the tensile strength and thickness of the

concrete cover and the penetration of moisture, oxygen, chlorides and toxic components of sulfates, phosphates and nitrates.

Corroded structural members with cracking and spalling of the concrete cover can be repaired by jacketing. Corrosion damage in members with internal cracks and exterior micro-cracks is not visible to the naked eye. The cost of repairs to structures damaged by corrosion is many times more than the additional cost involved in extra care and corrosion-preventive methods adopted in selecting the standard constituent materials, and compacting and curing the concrete. The following preventive measures can be adopted to mitigate corrosion damage in reinforced-concrete structures:

- Use of pozzolana cement blended with 20% of pozzolana materials or ordinary Portland cement,
- Thorough washing of aggregates to eliminate chlorides and other corrosive salts,
- Mixing the concrete with potable water having a pH value not less than 6,
- Designing a low-slump concrete with minimum cement content of 350 kg/m<sup>3</sup> and the maximum water-cement ratio of 0.50,
- Superplasticizers might be used in order to obtain a low water-cement ratio, this will increase the resistivity against corrosion,
- Use of organic and inorganic inhibitors to decrease the corrosion risk,
- Thoroughly compaction of concrete in the molds,
- Curing with water having a pH value not less than 6 for at least seven days until the concrete attains 70% of its design strength and prevent plastic shrinkage cracks,
- Thickness of concrete cover should be smooth and sufficient.

For important structures in an aggressive environment, the concrete cover may be protected with surface-applied inhibitors or coatings with proper thickness.

In this study, the effect of different inhibitors and chemical additives on the corrosion of reinforced concrete steel was investigated. As a result of experimental studies, it was concluded that the ecological boron inhibitor did not damage the structure of the reinforcement in the concrete and could be used instead of the calcium nitrite inhibitor produced in the market. The electrical resistance, rapid chloride permeability and half-cell potential experiments show that samples containing boron inhibitors gave the best results compared to other samples.

As a result of the experimental studies, the half-cell potential values of the samples containing boron inhibitors were found to be 30.1% less. This result is much better than a calcium nitrite inhibitor. The control sample without any chemical additives was the most corroded sample. The best result was obtained from the sample named BORPGEC with boron and set retarder.

When we look at the electrical resistance test results, we see that the electrical resistance of concrete increases with the use of chemical additives. Here, boron and super plasticizer series (BORSAK) gave the best results. Electrical resistance of this series is 85% higher than the control sample. It is known as a result of experimental studies that calcium nitrite inhibitor increases the electrical conductivity of concrete due to its nature. However, with the use of other chemical additives, the concrete reached a better consistency, settled in the mold better and the impermeability increased. Electrical resistance values increased with the increase of impermeability.

In the rapid chlorine permeability test, the series with boron and super plasticizer gave the best result, reducing the chlorine permeability of concrete by 45%. These results are also parallel in calcium nitrite series, but not as good as boron inhibitor. The best result for samples containing calcium nitrite was obtained from the series with calcium nitrite and super plasticizer (FERROSAK), and this series reduced the permeability of concrete by 38% compared to the

control series. The combined use of boron inhibitor and superplasticizer additive enabled the concrete to settle into the mold better and reduced the permeability. Set accelerator and set retarding additives contain a little chlorine that is why this series are a bit higher permeability values than other series.

The boron inhibitor, which will be mass-produced in the future, will provide a significant national income to the country's economy. The boron element has been used by researchers in many fields, and as these researches increase, more efficient properties of the element will emerge.

## References

- [1] Topcu IB, Unal O, Uygunoglu T. Chloride effect in reinforced concrete structures, TCCE İzmir Branch, Concrete Corner, 2005; 124: 36 - 41.
- [2] Topcu IB, Boga AR. Investigation of reinforcement corrosion in fly ash concretes with accelerated method, 3rd National Building Material Congress and Exhibition, 15-17 November 2006, İstanbul.
- [3] Shalabi K, Nazeer AA. Ethoxylates nonionic surfactants as promising environmentally safe inhibitors for corrosion protection of reinforcing steel in 3.5 % NaCl saturated with Ca(OH)<sub>2</sub> solution. Journal of Molecular Structure, 2019; 1195: 863 - 876. <https://doi.org/10.1016/j.molstruc.2019.06.033>
- [4] Quraishi MA, Nayak DK, Kumar R, Kumar V. Corrosion of Reinforced Steel in Concrete and Its Control: An overview. Journal of Steel Structures and Construction, 2017; 3(1): 1-6. <https://doi.org/10.4172/2472-0437.1000124>
- [5] Basic corrosion cell. Received from; 'http://korkappvcoatedconduit.blogspot.com/2014/04/explanation-of-basic-corrosion-cell.html'
- [6] Electrochemical reaction on rebar. Received from; 'https://www.cement.org/learn/concrete-technology/durability/corrosion-of-embedded-materials'
- [7] Yang H, Li W, Liu X, Liu A, Hang P, Ding R, Li T, Zhang Y, Wang W, Xiong C. Preparation of corrosion inhibitor loaded zeolites and corrosion resistance of carbon steel in simulated concrete pore solution. Construction and Building Material, 2019; 225: 90 - 98. <https://doi.org/10.1016/j.conbuildmat.2019.07.141>
- [8] Anitha R, Chitra S, Hemapriya V, Chung IM, Kim SH, Prabakaran M. Implications of eco-addition inhibitor to mitigate corrosion in reinforced steel embedded in concrete. Construction and Building Material, 2019; 213: 246 - 256. <https://doi.org/10.1016/j.conbuildmat.2019.04.046>
- [9] Hossain SMZ, Kareem SA, Al-Shater A, Ezuber H, Hossain MM, Razzak SA. Effects of cinnamaldehyde as an eco-friendly corrosion inhibitor on mild steel in aerated NaCl solutions. Arabian Journal for Science and Engineering, 2020; 45: 229 - 239. <https://doi.org/10.1007/s13369-019-04236-4>
- [10] Lee HS, Ryu HS, Park WJ, Ismail MA. Comparative study on corrosion protection of reinforcing steel by using amino alcohol and lithium nitrite inhibitors. Materials (Basel), 2015; 8: 251 - 269. <https://doi.org/10.3390/ma8010251>
- [11] Deng M, Zhang Y, Li Q. Shear strengthening of RC short columns with ECC jacket: Cyclic behavior tests. Engineering Structures, 2018; 160:535-545. <https://doi.org/10.1016/j.engstruct.2018.01.061>
- [12] Di Carlo F, Meda A. Numerical cyclic behaviour of un-corroded and corroded RC columns reinforced with HPFRC jacket. Composite Structure, 2017; 163:432 - 443. <https://doi.org/10.1016/j.compstruct.2016.12.038>
- [13] Meda A, Mostosi S, Rinaldi Z, Riva P. Corroded RC columns repair and strengthening with high performance fiber reinforced concrete jacket. Materials and Structures, 2016; 49(5):1967-1978. <https://doi.org/10.1617/s11527-015-0627-1>

- [14] Zhang D, Ghoulah Z, Shao Y. Review on carbonation curing of cement-based materials. *Journal of CO2 Utilization*, 2017; 21: 119 - 131. <https://doi.org/10.1016/j.jcou.2017.07.003>
- [15] Song N, Wang Z, Liu Z, Zhou J, Zheng D. Study on improvement of durability for reinforced concrete by surface-painting migrating corrosion inhibitor and engineering application. In: 1st International Conference on New Material and Chemical Industry (NMCi2016). IOP Conference Series: Materials Science and Engineering, 2017. p. 167. <https://doi.org/10.1088/1757-899X/167/1/012072>
- [16] Damages caused by reinforcement corrosion in columns and beams. Received from; 'https://theconstructor.org/structural-engg/methods-of-concrete-column-repair/5833/'
- [17] Ryu HS, Singh JK, Lee H, Ismail MA, Park W. Effect of LiNO<sub>2</sub> inhibitor on corrosion characteristics of steel rebar in saturated Ca(OH)<sub>2</sub> solution containing NaCl: An electrochemical study. *Construction and Building Materials*, 2017; 133(15): 387 - 396. <https://doi.org/10.1016/j.conbuildmat.2016.12.086>
- [18] Shan H, Xu J, Wanga Z, Jiang L, Xu N. Electrochemical chloride removal in reinforced concrete structures: Improvement of effectiveness by simultaneous migration of silicate ion. *Construction and Building Materials*, 2016; 127: 344 - 352. <https://doi.org/10.1016/j.conbuildmat.2016.09.137>
- [19] Pathak RK, Mishra P. Drugs as corrosion inhibitors: A review. *International Journal of Science and Research*, 2016; 5: 671 - 677. <https://doi.org/10.21275/v5i4.NOV162623>
- [20] Shi Z, Lothenbach B, Geiker MR, Kaufmann J, Leemann AS, Ferreira S, Skibsteda J. Experimental studies and thermodynamic modeling of the carbonation of Portland cement, metakaolin and limestone mortars. *Cement and Concrete Rsrch.*, 2016; 88: 60-72. <https://doi.org/10.1016/j.cemconres.2016.06.006>
- [21] Epoxy coated and galvanized reinforcements. Received from; 'https://www.harrissupply solutions.com/epoxy-coated-rebar.html'
- [22] Bouazaoui L, Li A. Analysis of steel/concrete interfacial shear stress by means of pull out test. *International Journal of Adhesion & Adhesives* 28. Elsevier. 2008. pp. 101-108. <https://doi.org/10.1016/j.ijadhadh.2007.02.006>
- [23] Ryu HS, Singh JK, Yang HM, Ismail MA. Evaluation of corrosion resistance properties of N, NO -dimethyl ethanolamine corrosion inhibitor in saturated Ca(OH)<sub>2</sub> solution with different concentrations of chloride ions by electrochemical experiments. *Construction and Building Materials*, 2016; 114: 223 - 231. <https://doi.org/10.1016/j.conbuildmat.2016.03.174>
- [24] Elsener B, Angst U. Corrosion inhibitors for reinforced concrete. *Science and Technology of Concrete Book*, 2016. <https://doi.org/10.1016/B978-0-08-100693-1.00014-X>
- [25] Insufficient implementation of vibration on concrete pouring. Received from; 'https://www.youtube.com/watch?v=SdDEzuYFPcE&ab\_channel=CivilSitevisit'
- [26] Kaur K, Goyal S, Bhattacharjee B, Kumar M. Efficiency of migratory-type organic corrosion inhibitors in carbonated environment. *Journal of Advanced Concrete Technology*, 2016; 14: 548 - 558. <https://doi.org/10.3151/jact.14.548>
- [27] Inadequate use of concrete cover. Received from; 'https://civildigital.com/effects-corrosion-reinforcement-signs-preventive-measures/'
- [28] Elfmarkova V, Spiesz P, Brouwers HJH. Determination of the chloride diffusion coefficient in blended cement mortars. *Cement and Concrete Research*, 2015; 78: 190 -199. <https://doi.org/10.1016/j.cemconres.2015.06.014>
- [29] Habib A, Yildirim U, Eren O. Column repair and strengthening using RC jacketing: a brief State of the art review. *Innovative Infrastructure Solutions*, 2020; 5: 1 - 11. <https://doi.org/10.1007/s41062-020-00329-4>
- [30] Raja PB, Ghoreishiamiri S, Ismail M. Natural corrosion inhibitors for steel reinforcement in concrete - A review. *World Scientific Publishing Company*, 2015; 22: 68 - 75. <https://doi.org/10.1142/S0218625X15500407>
- [31] Diamanti MV, Pérez Rosales EA, Raffaini G, Ganazzoli F, Brenna A, Pedefferri M, Ormellese M. Molecular modelling and electrochemical evaluation of organic inhibitors in concrete. *Corrosion Science*, 2015; 100: 231 - 241. <https://doi.org/10.1016/j.corsci.2015.07.034>

- [32] Larouj M, Lgaza AH, Serrard H, Zarroka H, Bourazmib H, Zarroukc A, Elmidaouia A, Guenbourb A, Boukhrisd S, Ouddaa H. Adsorption properties and inhibition of carbon steel corrosion in hydrochloric acid solution by ethyl 3-hydroxy-8-methyl-4-oxo-6-phenyl-2-(p-toly)-4,6- dihydropyrimido[2,1-b] [1,3]thiazine-7-carboxylate. *Journal of Materials and Environmental Science*, 2015; 6(11): 3251 - 3267.
- [33] Gerengi H, Bilgic H, Sahin HI. Corrosion effect of ecologic inhibitors such as nut shell, pomegranate and savoy cabbage on zinc plate in 5 % NaCl environment. *Düzce University Journal of Forestry*, 2011; 6: 10 - 23.
- [34] Gerengi H, Ugras HI, Yildiz M. Using of ionic liquids containing boron cation as corrosion inhibitor in 0.1 M HCl environment. *Journal of Advanced Technology Sciences*, 2017; 6(1): 11 - 22.
- [35] Abdulrahman AS, Ismail M, Hussain MS. Corrosion inhibitors for steel reinforcement in concrete: A review. *Scientific Research and Essays*, 2011; 6: 4152-4162. <https://doi.org/10.5897/SRE11.1051>
- [36] Ryu HS, Singh JK, Lee H, Park W. An electrochemical study to evaluate the effect of calcium nitrite inhibitor to mitigate the corrosion of reinforcement in sodium chloride contaminated Ca(OH)<sub>2</sub> solution. *Advances in Materials Science and Engineering*, 2017. <https://doi.org/10.1155/2017/6265184>
- [37] Okeniyi OJ, Omotosho OA, Ogunlana OO, Okeniyi ET, Owwoye TF, Ogbiye AS, Ogunlana EO. Investigating prospects of *Phyllanthus muellerianus* as ecofriendly/sustainable material for reducing concrete steel reinforcement corrosion in industrial/microbial environment. *Energy Procedia*, 2015; 74: 1274-1281. <https://doi.org/10.1016/j.egypro.2015.07.772>
- [38] TS EN 197-1, Cement- Part 1: Compositions and conformity criteria for common cements. Turkish Standards, Ankara, 2012.
- [39] TS 708, Steel for the reinforcement of concrete - Reinforcing steel. Turkish Standards, Ankara, 2016.
- [40] Topcu IB, Karakurt C. Properties of Reinforced Concrete Steel Rebars Exposed to High Temperature. *Research Letters in Materials Science*, 2008; Vol. 2008, 1-4. <https://doi.org/10.1155/2008/814137>
- [41] ASTM C1202. Standard Test Method for Electrical Indication of Concrete's Ability to Resist Chloride Ion Penetration. ASTM International. 2019.
- [42] ASTM D4940. Standard Test Method for Conductimetric Analysis of Water-Soluble Ionic Contamination of Blast Cleaning Abrasives. ASTM International. 2020.
- [43] ASTM C 1876. Standard Test Method for Bulk Electrical Resistivity or Bulk Conductivity of Concrete. ASTM International. 2019.
- [44] ASTM C 876 - 15. Standard Test Method for Corrosion Potentials of Uncoated Reinforcing Steel in Concrete. ASTM International. 2015.
- [45] Alhozaimy A, Hussain RR, Al-Zaid R, Negheimish AA. Investigation of severe corrosion observed at intersection points of steel rebar mesh in reinforced concrete construction. *Construction and Building Materials*. 2012; vol. 37, pp. 67-81. <https://doi.org/10.1016/j.conbuildmat.2012.07.011>
- [46] Duong VB, Sahamitmongkol R, Tangtermsirikul S. Effect of leaching on carbonation resistance and steel corrosion of cement-based materials. *Construction and Building Materials*. 2013; vol. 40, pp. 1066-1075. <https://doi.org/10.1016/j.conbuildmat.2012.11.042>



Research Article

## Prediction of chloride ingress for palm kernel shell concrete

Samson Olalekan Odeyemi<sup>\*1,a</sup>, Omolola Titilayo Odeyemi<sup>2,b</sup>, Adewale George Adeniyi<sup>3,c</sup>, Zainab Tolu Giwa<sup>1,d</sup>, Ademola Kamorudeen Salami<sup>1,e</sup>, Adeyemi Adesina<sup>4,f</sup>

<sup>1</sup>Department of Civil & Environmental Engineering, Kwara State University Malete, Nigeria

<sup>2</sup>Department of Science Laboratory Technology, Kwara State Polytechnic, Ilorin, Nigeria

<sup>3</sup>Department of Chemical Engineering, University of Ilorin, Ilorin, Nigeria

<sup>4</sup>Department of Civil Engineering, University of Windsor, Canada

### Article Info

### Abstract

#### Article history:

Received 21 Oct 2020

Revised 14 Dec 2020

Accepted 27 Dec 2020

#### Keywords:

Palm Kernel Shell;  
Chloride ingress;  
Concrete;  
Coarse aggregate;  
Corrosion;  
Chloride

Steel reinforcement corrosion emanating from ingress of chloride into concrete is the key reason for weakening of concrete structures globally. Infiltration of chloride into concrete happens by absorption and diffusion. On the other hand, reinforced concrete containing supplementary materials is more susceptible to corrosion exposure due to its high permeability. In this paper, two concentrations of sodium chloride (NaCl) were applied on concrete containing palm kernel shell as full replacement to granite. Concrete cube specimens of Grade 20 were cast into 150 mm by 150 mm by 150 mm moulds, and their workability were determined by compacting factor and slump tests. The hardened specimens were soaked in sodium chloride (NaCl) solution of 3% and 6% concentration. Spray, Absorption and Compressive strength tests were conducted at 7, 14, 21 and 28 days. Equations were generated by means of the data gotten from the laboratory tests to forecast the chloride penetration depth into the palm kernel shell concrete under the conditions considered in this work. The models generated revealed that absorption affected chloride ingress into the concrete significantly at 6% NaCl concentration. The models also reveal that the cover to reinforcements in Palm Kernel Shell Concrete subjected to chloride attack should be more than what is presently endorsed for reinforced concrete structures.

© 2021 MIM Research Group. All rights reserved.

## 1. Introduction

A key material often utilized in the building industry is concrete [1–5]. Utilizing Palm Kernel Shells (PKS) as a substitute for coarse aggregates in concrete can reduce the rising price of materials used in construction especially in less developed nations of the world and also bring about a reduction in the overall dead weight of the building. Olutoge (2000) [6] examined the physical, compressive strength and fire resistance of concrete made with PKS and the strength fell within the range specified for lightweight concrete.

Itam et. al [7] studied the density of PKS concrete and found out that it varies in the range of 1700 to 2050 kg/m<sup>3</sup> based on the type of sand used and the PKS contents. Generally, when concrete's density is lower than 2000 kg/m<sup>3</sup>, it is categorized as lightweight concrete. Thus, PKS concrete is classified as lightweight concrete [8].

Reinforced concrete (RC) is a composite in which concrete's little tensile strength and ductility are enhanced by the addition of steel reinforcements which have higher tensile

\*Corresponding author: [samson.odeyemi@kwasu.edu.ng](mailto:samson.odeyemi@kwasu.edu.ng)

<sup>a</sup> <https://orcid.org/0000-0001-5217-3403>; <sup>b</sup> <https://orcid.org/0000-0003-4832-885X>;

<sup>c</sup> <https://orcid.org/0000-0001-6615-5361>; <sup>d</sup> <https://orcid.org/0000-0002-4447-2240>;

<sup>e</sup> <https://orcid.org/0000-0003-4787-2618>; <sup>f</sup> <https://orcid.org/0000-0002-7602-3896>

DOI: <http://dx.doi.org/10.17515/resm2020.226st0921>

strength [3]. The steel reinforcements are often entrenched in concrete before the setting of such concrete. The reinforcing arrangements are designed to counteract tensile stresses in regions of the concrete that might cause cracking and subsequently lead to structural failure. RC structures are intended to stay safe and functional over a long period of time. For example, bridges are generally designed to stay safe and functional for a service life of 120 years [9]. However, when these structures are constructed in environments that are high in chloride concentration, the steel reinforcements in them are prone to corrosion from the chloride ions. This poses a challenge to these structures leading to grave economic and safety implications. NaCl is an ionic compound and it is composed of the same amounts of positively and negatively charged sodium and chloride ions respectively [10].

When concrete structures are constructed in highly chloride concentrated environments, chloride ions have the capacity of penetrating through concrete cover into the reinforcing steel [9,11–14]. Corrosion is initiated on the steel at the critical concentration of the chlorides with adequate oxygen and moisture. Corrosion has two implications on the reinforcements: it results in spalling, cracking, and delamination of the concrete leading to the weakening of the bond between the concrete and the reinforcement. Also, this further makes it possible for the chloride ions to infiltrate the steel to cause further corrosion. Additionally, the area of the reinforcement reduces as they corrode, with a resulting reduction in their capacity to carry load [15–18]. Steel corrosion affects structural performance by reducing the effective cross-sectional area of reinforcements, its yield and ultimate strength, elongation rate, bond strength between the steel and concrete, thereby reducing the stiffness and bearing capacity of the structure. These have grave impact on the environment [9,19,20]. Fig. 1 shows the effect of chloride ingress on some steel samples as reported by Adeniyi et. al [11].

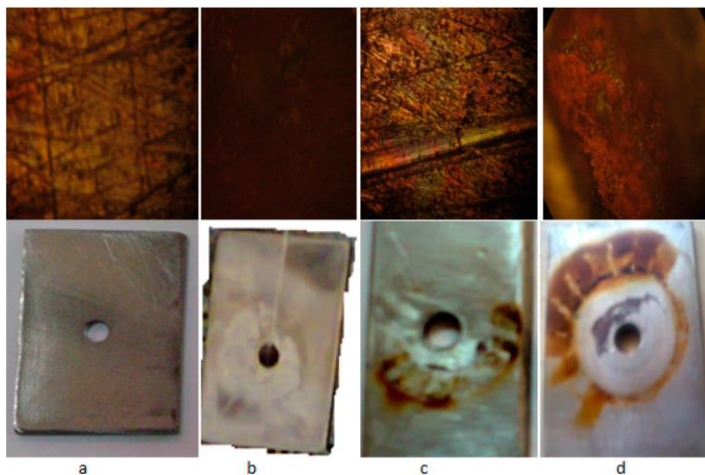


Fig. 1 Photographs and optical micrographs of SS-304 in different chloride environments, (a) as received (b) freshwater (c) brackish and (d) marine after 60 days of immersion [11]

The conveyance of chloride ions into concrete in chloride infested environments can occur by capillary absorption, diffusion and hydrostatic pressure. Absorption occurs by the rising of water in the concrete and this largely affect the level at which chloride ion is taken up. Thus, it impacts the gradient concentration in the concrete. Once there is continuous hydration of the concrete, diffusion process then increases the access of chloride ions through the cover. Permeation arises by water pressure when chloride ion solution is present under an applied hydraulic head on at least a side of the concrete structure

[17,21,22]. Consequently, movement of chloride ions via absorption and pore-liquid, when solutions with chloride ions are sucked into concrete pores, are the two major conveyance mechanisms for chloride ingress in concrete. Diffusion, which is a slow and continuous process, occurs as a result of chloride concentration gradient, once the pore liquid is not allowed evaporate [9,17].

PKS are components of oil palm tree and are predominant in western Africa especially in the riverine areas of Nigeria [23]. They are often regarded as wastes and discarded in the open consequently constituting a nuisance in the environment with little economic benefits. Odeyemi et. al (2019) [3], Dadzie and Yankah (2015) [24] and Olutoge (2010) [25] all stated that the incorporation of PKS in concrete will result in a substantial decrease in the cost of concrete production. The government of Nigeria is promoting the use of local materials in construction to lessen cost. This has resulted in the sourcing and development of substitutes such as non-conventional and agro-based construction materials to achieve the optimum benefits of agricultural wastes [26]. PKS are fibrous carbonaceous and are found in various sizes ranging from 0 – 5 mm, 5 – 10 mm, and 10 -15 mm for small, medium, and large sizes respectively [3]. Fig. 2 shows some samples of PKS.



Fig. 2 Samples of Palm Kernel Shell

The permeability of PKS concrete is high when compared to normal concrete as reported by [27–29] leading to a decline in its durability when exposed to moisture. Therefore, the use of PKS in reinforced concrete structures may lead to early reinforcement corrosion in chloride environment. Therefore, the objectives of this research are: to evaluate the compressive strengths of palm kernel shell concrete when subjected to chloride attack, to determine the consequence of chloride ingress in PKS concrete and to generate numerical models for predicting chloride penetration due to absorption on two different NaCl concentrations.

## 2. Research Methodology

### 2.1. Materials

Materials utilized for this research include Lafarge Elephant brand of Ordinary Portland Cement (Grade 42.5R), Palm Kernel Shell (PKS) obtained from local palm oil industry within Ibadan, Oyo State was used as coarse aggregate. River sand was used as the fine aggregate which conforms to BS EN 12620:2002+A1:2008 [30], potable (drinking) water of pH 7 and Sodium chloride (NaCl) solution which was utilized as the curing medium to

determine the chloride ingress into the concrete. Epoxy resin was employed to coat the concrete to foil evaporation loss and to guarantee that ingress of salt solution is in a single direction. Silver Nitrate ( $\text{AgNO}_3$ ) having a concentration of 0.1M was utilized as the colorimetric solution to estimate the chloride penetration depth.

## 2.2. Method

### 2.2.1 Laboratory Tests

Particle Size Distribution as stipulated in BS EN 933-1:2012 [31] , Specific Gravity and Aggregate Crushing Value tests were conducted on the aggregates, while Slump and Compacting factor tests, both conforming to [32] and [33] respectively, were conducted on the concrete in its fresh state. The proportion of aggregates going through the sieves was plotted against the diameter of the aggregates. Equation 1 was used to compute the Fineness modulus and the Uniformity coefficient, which expresses the grading of the aggregate, was determined from the graph by means of Equation 2.

$$\text{Fineness modulus} = \frac{\text{Total cumulative percentage retained}}{100} \tag{1}$$

$$C_u = \frac{D_{60}}{D_{10}} \tag{2}$$

where:  $C_u$  represents the Uniformity coefficient,  $D_{60}$  denotes the size of aggregates corresponding to 60% fines on the cumulative particle-size distribution curve and  $D_{10}$  denotes the size of aggregates corresponding to 10% fines on the cumulative particle-size distribution curve. If the  $C_u$  of the sample is lower than 4.0 it is inferred that the sample is uniformly graded but if the  $C_u$  of the sample is larger than 4.0, then it is inferred that the sample is well graded [15,34,35]. Also, destructive Compression test which conforms to [36] as shown in Fig. 3 and Chloride penetration evaluation were carried out on hardened concrete.



Fig. 3 Destructive Compression Test on Concrete Samples

### 2.2.2 Concrete Batch, Mixing and Curing

A mix ratio of 1:2:4 for a compressive strength Grade 20 was used, and batching was carried out by weight adopting a water-cement ratio of 0.5. Mixing was done manually as shown in Fig. 4. The specimens were compacted in three different layers; each layer compacted with twenty-five (25) blows with the aid of a tamping rod. The surface of each of the samples was trowel finished to be flat with the top of the concrete mould. The samples were left for 24 hours to ensure setting of the concrete cubes and they were demoulded thereafter. Three cubes from each group were randomly chosen and weighed before immersing in water. This was done to determine the weight gained by each group after each curing regime. The cubes were divided into two groups for curing, that is, curing with clean water and curing with salt water both at 3% and 6% concentration. Curing by immersion was adopted for all the concrete cubes as shown in Fig. 5. The first groups of concrete cube samples were cured in clean water for a period of 28 days so that they can attain their full compressive strength. The weight gained after this time was recorded for each group.



Fig. 4 Mixing of Palm Kernel Shell Concrete



Fig. 5 Curing of Concrete Cubes

### 2.2.3 Chloride Penetration Test on Concrete

The four (4) sides of the second group of samples were treated with epoxy resin. The epoxy resin was applied on the specimens to prevent the loss of water from the sides and to guarantee salt solution is one-directional. Afterwards, the samples were allowed to cure by the drying of the epoxy resin. The concrete cube specimens were then submerged in NaCl solution with a concentration of 3% and 6% NaCl respectively and left in the salt solution for 7, 14, 21 and 28 days as specified by BS 1881-122 [37] in order to generate data for the model.

After each curing time, the specimens were split vertically, and the vertical surface was sprayed with the colorimetric solution and allowed to stay for 5 minutes. This test was done to obtain the depth of chloride penetration using the colorimetric solution. The colorimetric solution used in this research is Silver Nitrate ( $\text{AgNO}_3$ ) solution having a concentration of 0.1 M. The colour of the chloride-contaminated zone changed to light grey colour. The chloride penetration depth was gotten with the aid of a vernier caliper. The colour change agrees with the submission by [38], who also discovered that the duration of colour change is a function of the reaction between chloride and  $\text{AgNO}_3$  on the sprayed surface, to evaluate the depth of chloride penetration.

The model for the chloride ingress in the PKS concrete was generated based on the experimental data obtained from the tests conducted using SPSS software package. The parameters utilized for the model formulation are compressive strength ( $f_{cu}$ ), time ( $t$ ), absorption ( $i$ ) and chloride penetration depth ( $d$ ). The chloride penetration depth was then stated as a function of compressive strength, time and absorption i.e.  $d = f(f_{cu}, t, i)$ .

## 3. Results and Discussions

### 3.1. Properties of Aggregates

The graph of the sieve analysis conducted on the fine aggregates is presented in Fig. 6. The size of the aggregate varies from 0.10 mm to 4.75 mm signifying that the samples are within the group of fine, medium and little coarse sand [15]. This result is within the range specified for fine aggregates. The coefficient of uniformity ( $C_u$ ) is 1.8 which is less than 4 indicating that the fine aggregate is uniformly graded.

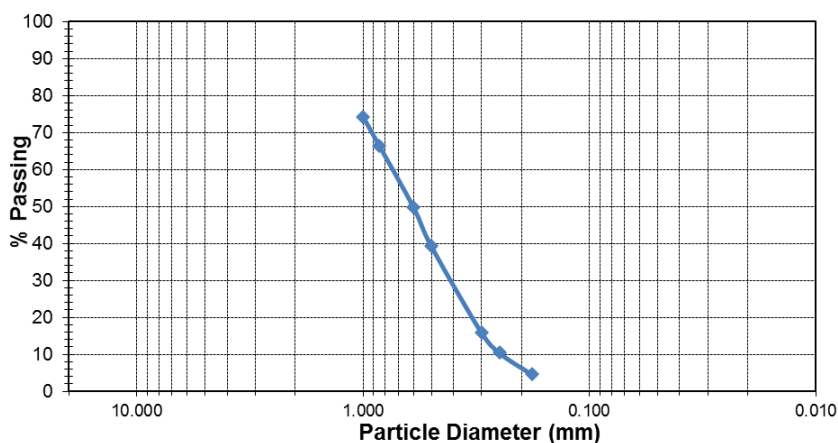


Fig. 6 Particle size distribution (PSD) curve of the fine aggregate

ACI Education Bulletin (2007) [39] specified that Specific gravity for aggregates should be within 2.30 to 2.90. The specific gravity for the fine aggregates in this study is 2.65. This signifies that the fine aggregates are suitable for construction purpose.

The ACV for the coarse aggregate used in this study is 29.8% which is in the range prescribed by BS EN 12620:2002+A1:2008 [30]. This denotes that the aggregate is fit to produce concrete.

### 3.2 Workability of Fresh Concrete

Compacting factor and slump test were utilized in determining the workability of the fresh concrete. From the test carried out, a compacting factor of 0.98 and slump height of 45mm was obtained. The result implies that the concrete is stiff. The results are consistent with the submission of Azunna (2019) [27], Anifowose et al (2017) [40], Ede et al (2016) [41] and Bamigboye et al (2015) [42].

### 3.3 Compressive Strength

The results for the compressive strength test for the cubes cured with water, 3% NaCl, 6% NaCl for 7, 14, 21 and 28 days are presented in Fig. 7. The Figure revealed that samples cured in ordinary potable water has the maximum compressive strength at 28 days compared to the one cured in salt water. The Figure also reveals that the compressive strengths of concrete cubes cured in salt water reduced as the curing days increases. However, concrete cubes cured with 3% NaCl retained its compressive strength when exposed to the salt solution better than the samples in the 6% NaCl solution. The compressive strength results obtained in this research is in tandem with the result obtained by Azunna (2019) [27] and Odeyemi et. al (2019) [3] for PKS concrete.

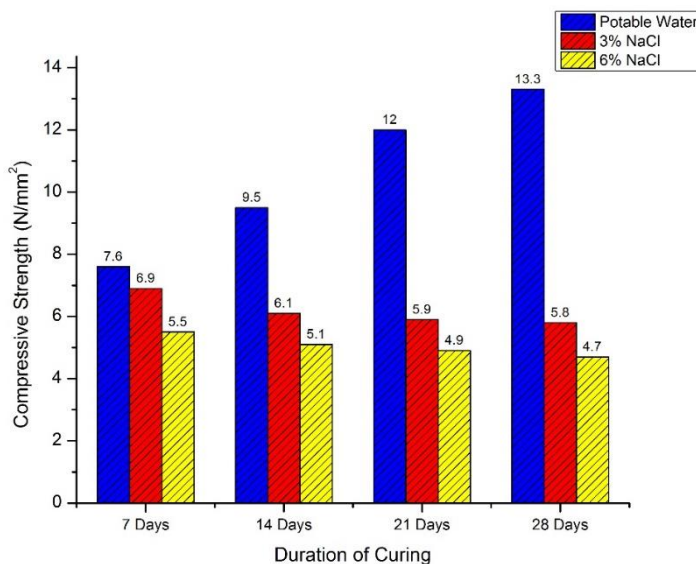


Fig. 7 Average Compressive strength of Concrete Cubes

### 3.4 Water Absorption

Fig. 8 is a presentation of the result of the Absorption tests conducted on concrete cubes at 7, 14, 21 and 28 days in ordinary potable water, 3% NaCl and 6% NaCl solutions. The results show that the chloride concentration of the curing medium increases the water absorption capacity of the concrete cubes. Thus, the samples cured in 6% NaCl solution absorbed more water and salt when compared with other samples. This result is consistent with the findings of Ikumapayi (2019) [9].

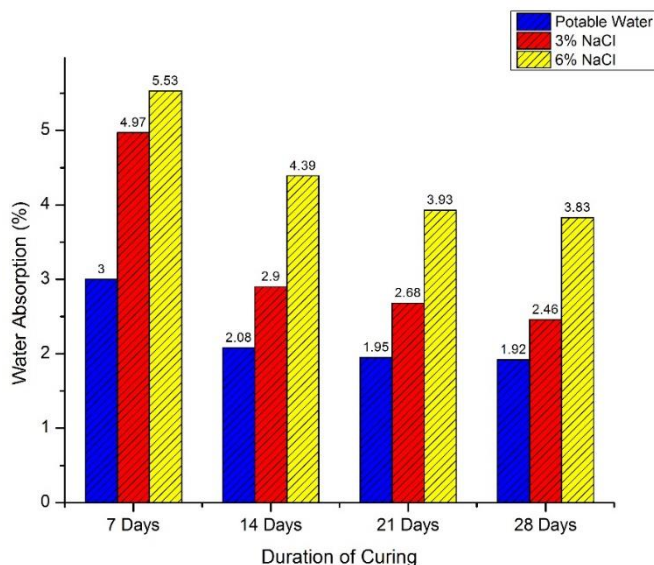


Fig. 8 Water Absorption for concrete cured with water and sodium chloride

### 3.5 Depth of Chloride Penetration

Fig. 9 illustrates the result of the spray test conducted to determine chloride penetration depth on the PKS concrete at 7, 14, 21 and 28 days respectively in sodium chloride solution. It was discovered that as the curing days increase, the depth of chloride penetration also increases. This happened since the depth of chloride penetration is a function of the available pore space in the sample and the concentration of the salt solution. The result shows that concrete cubes cured in 6% saltwater have the highest penetration.

### 3.6 Model for Chloride Penetration Depth

#### 3.6.1 Sodium chloride (3% NaCl)

Tables 1, 2, 3 and 4 show the analysis and results of data gotten from tests conducted on the 3% NaCl solution. The regressions analysis gave an  $R^2$  value of 0.940 which is an indication that there is a good relationship between the chloride penetration depth ( $d$ ) and other parameters i.e. Absorption ( $i$ ), Time ( $t$ ) and Compressive strength ( $f_{cu}$ ).

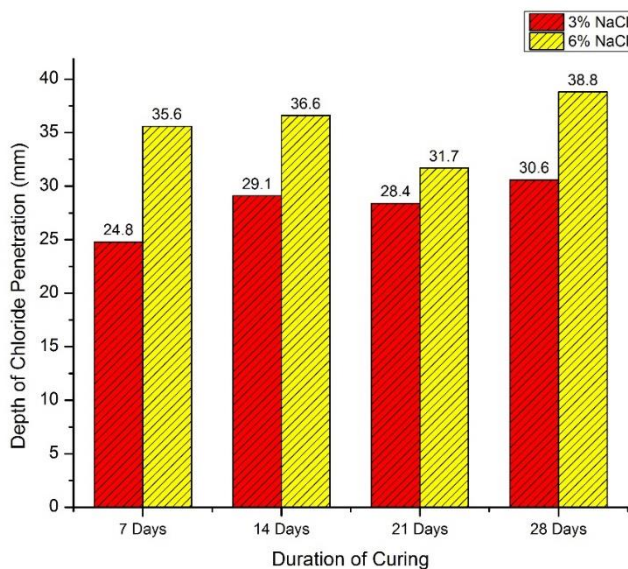


Fig. 9 Depth of chloride penetration in concrete

The level of significance of the values obtained from Table 2 is less than 0.05 which shows that the regression coefficients are statistically significant. Thus, the model for chloride penetration for concrete immersed in 3% Sodium Chloride solution is presented in Equation 3

$$d = 27.776 + 1.682t + 0.19f_{cu} - 1.036i \tag{3}$$

Where d = Chloride penetration depth (mm);  $f_{cu}$  is the characteristic strength  $N/mm^2$ ; t is Time (Age of Concrete coded in multiple of 7 i.e. 7 days = 1, 14 days = 2, 21 days = 3 and 28 days = 4); i – Absorption.

Table 1 Model Summary for 3% Sodium Chloride (NaCl)

Model	R	R Square	Adjusted R Square	Std. Error of the Estimate
1.	0.970	0.940	0.918	0.63882

Table 2 Analysis of Variance

Model	Sum of Squares	df	Mean Square	f	Significance
Regression	51.238	3	17.079	41.852	0.000
1 Residual	3.265	8	0.408		
Total	54.503	11			

Table 3 Coefficients Summary for Sodium Chloride NaCl at 3% Model

Model	Unstandardized Coefficients		Standardized Coefficients	T	Significance	
	B	Standard Error	Beta			
1	Constant	27.776	1.891		14.686	0.000
	t	1.682	0.188	0.882	8.925	0.000
	$f_{cu}$	0.091	0.263	0.035	0.346	0.738
	i	-1.036	0.220	-0.423	-4.698	0.002

Table 4 Regression Summary for Chloride Depth Penetration and Absorption for 3% NaCl Solution

	Coefficients	Standard Error	t Stat	P-value	Lower 95%	Upper 95%	Lower 95.0%	Upper 95.0%
Intercept	29.6328	5.21786	5.67910	0.00020	18.0066	41.25894	18.00667	41.25894
Absorption (%)	1.711101	1.22513	1.39666	0.19273	-1.0187	4.440861	-1.01866	4.440861

Fig. 10 shows that there is no relationship between depths of sodium chloride penetration NaCl (3%) and Absorption for NaCl. This show an approximately constant slope and the R<sup>2</sup>-value is very small which support the model result earlier obtained that it can only explain about 0% of the variation of the data, and also indicate that the depth penetration of sodium chloride do not really depend on the absorption of the salt solution.

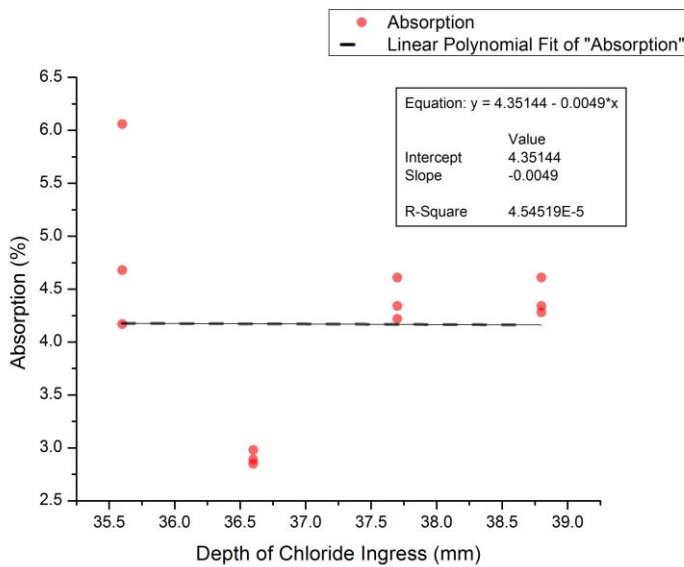


Fig. 10 Chloride Penetration depth against Absorption for 3% NaCl

### 3.7 6% Sodium chloride (NaCl)

Table 5 presents the regression analysis showing the coefficient of correlation  $R^2$  value of 0.989 which implies that there is a high relationship between the chloride penetration depth ( $d$ ) and other parameters considered in the model absorption i.e. ( $i$ ), time ( $t$ ) and compressive strength ( $f_{cu}$ ). Table 6 shows that the regression coefficient is statistically significant. Also, Table 7 and 8 reveals that the significant value for the intercept and time is statistically significant while absorption and compressive strength are not. Thus, the model is presented in Equation 4

$$d = 34.462 + 1.073t + 0.19f_{cu} + 0.019i \tag{4}$$

Where  $d$  = chloride penetration depth (mm);  $F_{cu}$  is the characteristic strength  $N/mm^2$ ;  $t$  is Time (Age of Concrete coded in multiple of 7 i.e. 7 days = 1, 14 days = 2, 21 days = 3 and 28 days = 4);  $i$  - Absorption.

Table 5 Model Summary for 6% Sodium Chloride (NaCl)

Model	R	R Square	Adjusted R Square	Std. Error of the Estimate
2	1.000	0.989	0.973	0.03300

Table 6 Analysis of Variance

Model	Sum of Squares	df	Mean Square	f	Sig
Regression	17.174	3	5.725	5258.253	0.000 <sup>b</sup>
1 Residual	.009	8	0.001		
Total	17.182	11			

Table 7 Coefficients Summary for Sodium Chloride NaCl at 6% Model

Model	Unstandardized Coefficients		Standardized Coefficients	T	Significance	95.0% Confidence Interval for B		
	B	Standard Error	Beta			Lower Bound	Upper Bound	
2	Constant	34.462	0.084		412.204	0.000	34.269	34.655
	t	1.073	0.010	1.002	106.451	0.000	1.049	1.096
	$f_{cu}$	0.005	0.008	0.002	0.186	0.857	-0.017	0.020
	i	0.019	0.010	0.005	0.509	0.624	-0.018	0.028

Table 8 Regression Coefficient for Chloride Depth Penetration and Absorption for 6% NaCl Solution

	Coefficients	Standard Error	t Stat	P-value	Lower 95%	Upper 95%	Lower 95.0%	Upper 95.0%
Intercept	32.01836	3.61004	8.86923	0.0000472	23.9746	40.0620	23.974	40.005
Absorption (%)	1.98375	0.75291	-1.2933	0.2249	-2.6513	0.7038	-2.651	0.7844

Fig. 11 shows that there is a linear relationship between sodium chloride penetration depth and Absorption for 6% NaCl solution. This show an upward movement trend and the R<sup>2</sup> value shows that the variation in the depth of penetration of sodium chloride can be explained at about 17% of its absorption.

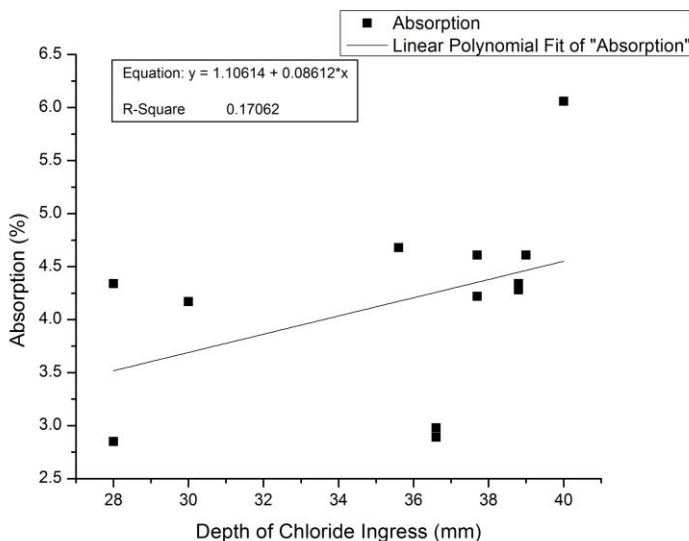


Fig. 11 Chloride Penetration depth against Absorption for 6% NaCl

#### 4. Conclusions

Studies have shown that the corrosion of steel reinforcements resulting from chloride attack is a major cause of weakening of concrete structures globally. Chloride ingress into concrete takes place by absorption and diffusion. Researchers have also discovered that reinforced concrete containing supplementary materials are more susceptible to corrosion exposure due to their high permeability. This research investigated the effect of two concentrations of sodium chloride (NaCl) on concrete containing palm kernel shell as full replacement of granite. Grade 20 concrete were cast into 150 mm by 150 mm by 150 mm cubic moulds, and their workability were determined by compacting factor and slump tests following the relevant international standards. The hardened concrete samples were fully submerged in potable water, sodium chloride (NaCl) solution of 3% and 6% concentration, respectively. Spray, Absorption and Compressive strength tests were conducted at 7, 14, 21 and 28 days. Equations were generated by means of the data gotten from the laboratory tests to forecast the chloride penetration depth into the palm kernel shell concrete for the two (2) chloride concentrations considered in this work. The following conclusions were drawn from the study:

- The absorption of concrete cured in ordinary potable water (control) were found to be less than that of the concrete cured in salt water.
- Absorption, Time and Compressive Strength have a significant influence on the diffusion of chloride ions into the PKS concrete.
- The chloride penetration depth into the PKS concrete increases as the exposure days increases.

- Exposure of PKS concrete to Sodium chloride (NaCl) solution leads to a long-term loss in compressive strength.
- For the Grade 20 concrete utilized for this study, the relationship between chloride penetration depth, age of concrete, compressive strength and absorption is given as:

$$d = 27.776 + 1.682t + 0.19f_{cu} - 1.036i \quad \text{for 3\% NaCl concentration}$$

$$d = 34.462 + 1.073t + 0.19f_{cu} + 0.019i \quad \text{for 6\% NaCl concentration}$$

## References

- [1] Mitchell J. The concrete conundrum. Chem World 2008.
- [2] Odeyemi SO, Atoyebi OD, Ayo EK. Effect of Guinea Corn Husk Ash on the Mechanical Properties of Lateritic Concrete. IOP Conf Ser Earth Environ Sci 2020;445:1-11. <https://doi.org/10.1088/1755-1315/445/1/012034>
- [3] Odeyemi SO, Abdulwahab R, Abdulsalam AA, Anifowose MA. Bond and Flexural Strength Characteristics of Partially Replaced Self-Compacting Palm Kernel Shell Concrete. Malaysian J Civ Eng 2019;31:1-7. <https://doi.org/10.11113/mjce.v31n2.535>
- [4] Anifowose MA, Adeyemi AO, Odeyemi SO, Abdulwahab R, Mudashiru RB. Comparative study of Ikirun and Osogbo Slag on concrete grade 20. Niger J Technol 2019;38:283-8.. <https://doi.org/10.4314/njt.v38i2.2>
- [5] Klyuev SV, Klyuev AV., Abakarov AD, Shorstova ES, Gafarova NG. The effect of particulate reinforcement on strength and deformation characteristics of fine-grained concrete. Mag Civ Eng 2017;75:66-75.
- [6] Olutoge FA. The production of concrete using palm kernel shell as a partial/full substitute for coarse aggregates. 2nd Eng. Conf. Sch. Eng. Technol. F.U.T. Minna, Niger State, Niger., 2000, p. 57-67.
- [7] Itam Z, Beddu S, Mohd Kamal NL, Alam MA, Ayash UI. The Feasibility of Palm Kernel Shell as a Replacement for Coarse Aggregate in Lightweight Concrete. IOP Conf. Ser. Earth Environ. Sci., vol. 32, 2016. <https://doi.org/10.1088/1755-1315/32/1/012040>
- [8] Oyejobi DO, Abdulkadir TS, Yusuf IT, Badiru MJ. Effects of Palm Kernel Shells Sizes and Mix Ratios on Lightweight Concrete. J Res Inf Civ Eng 2012;9.
- [9] Ikumapayi CM. Development of a short time model for predicting chloride ingress into normal and pozzolanic concrete. IOP Conf Ser Mater Sci Eng 2019;640:1-13. <https://doi.org/10.1088/1757-899X/640/1/012113>
- [10] Abalaka AE, Babalaga AD. Effects of Sodium Chloride Solutions on Compressive Strength Development of Concrete Containing Rice Husk Ash. ATBU J Environ Technol 2011;4:33-40.
- [11] Adeniyi AG, Ogunleye OO, Durowoju MO, Odeyemi SO. Modelling stochastic response of type 304 stainless steel (SS-304) crevice corrosion in chloride environments. Indian Chem Eng 2018;0:1-10. doi:10.1080/00194506.2018.1548951. <https://doi.org/10.1080/00194506.2018.1548951>
- [12] Ojoawo SO, Oladejo AM, Olaniyan OS. Effect of Chloride Contaminated Water on the Compressive Strength of Plain Concrete. IOSR J Mech Civ Eng 2014:99-108. <https://doi.org/10.9790/1684-113499108>
- [13] Adeniyi AG, Ogunleye OO, Durowoju MO, Odeyemi SO. Damaging Profile of SS-304 Crevice Corrosion in Chloride Environments. ABUAD J Eng Res Dev 2019;2:11-9.
- [14] Chalhoub C, François R, Carcasses M. Critical chloride threshold values as a function of cement type and steel surface condition. Cem Concr Res 2020;134. <https://doi.org/10.1016/j.cemconres.2020.106086>
- [15] Neville AM. Properties of Concrete. 5th ed. Pearson Education Ltd; 2011.

- [16] Green WK. Steel reinforcement corrosion in concrete - an overview of some fundamentals. *Corros Eng Sci Technol* 2020;289-302. <https://doi.org/10.1080/1478422X.2020.1746039>
- [17] Cao Q, Esmaily M, Liu RL, Birbilis N, Thomas S. Corrosion of mild steel under insulation - the effect of dissolved metal ions. *Corros Eng Sci Technol* 2020;322-30. <https://doi.org/10.1080/1478422X.2020.1734737>
- [18] Cinitha A, Umesha PK, Iyer NR. An overview of corrosion and experimental studies on corroded mild steel compression members. *KSCE J Civ Eng* 2014;18:1735-1744. <https://doi.org/10.1007/s12205-014-0362-0>
- [19] Zeng R, Zhang Y, Zhang X. Analysis on the Mechanical Properties of Corroded Reinforced Concrete. *DEStech Trans Mater Sci Eng* 2018:148-57. <https://doi.org/10.12783/dtmse/msce2016/10462>
- [20] Yusoff M, Abdul Hamid NH, Arshad AK, Mohd Ridzuan AR, Awang H. InCIEC 2015 Proceedings of the International Civil and Infrastructure Engineering Conference. Springer, Singapore; 2015. <https://doi.org/10.1007/978-981-10-0155-0>
- [21] Evans C, Richardson MG. Service Life of Chloride-Contaminated Concrete Structures. *Concrete* 2005:131-7.
- [22] Andrade C. Linear propagation models of deterioration processes of concrete. *Corros Eng Sci Technol* 2020:283-8. <https://doi.org/10.1080/1478422X.2020.1750161>
- [23] Oyedepo OJ, Olanitori LM, Akande SP. Performance of coconut shell ash and palm kernel shell ash as partial replacement for cement in concrete. *J Build Mater Struct* 2015;2:18-24.
- [24] Dadzie DK, Yankah JE. Palm Kernel Shells as a partial replacement for Sand in Sandcrete block production. *Chem Mater Res* 2015;7:61-72.
- [25] Olutoge FA. Investigations On Sawdust And Palm Kernel Shells As Aggregate Replacement. *ARPN J Eng Appl Sci* 2010;5:7-13.
- [26] Mohammed H, Afolabi KO, Umoru LE. Crushed Palm Kernel Shell As a Partial Replacement of Fine Aggregate in Asphaltic Concrete. *Int J Mater Methods Technol* 2014;2:1-5.
- [27] Azunna SU. Compressive strength of concrete with palm kernel shell as a partial replacement for coarse aggregate. *SN Appl Sci* 2019;1:1-10. <https://doi.org/10.1007/s42452-019-0334-6>
- [28] Khankhaje E, Rafieizonooz M, Salim MR, Mirza J, Salmiati, Hussin MW. Comparing the effects of oil palm kernel shell and cockle shell on properties of pervious concrete pavement. *Int J Pavement Res Technol* 2017;10:383-92. doi:10.1016/j.ijprt.2017.05.003. <https://doi.org/10.1016/j.ijprt.2017.05.003>
- [29] Eziefula UG, Opara HE, Anya CU. Mechanical Properties of Palm Kernel Shell Concrete in Comparison With Periwinkle Shell Concrete. *Malaysian J Civ Eng* 2017;29:1-14.
- [30] BS EN 12620:2002+A1:2008. Specification for Aggregates from natural sources for concrete. British Standards, BSI Group Headquarters 389 Chiswick High Road, London, W4 4AL, UK, Standards Policy and Strategy Committee. 2008.
- [31] BS EN 933-1. Tests for Geometrical Properties of Aggregates - Part 1: Determination of Particle Size Distribution - Sieving Method. 2012.
- [32] BS EN 12350-2:2009. Testing Fresh Concrete - Slump Test, British Standards. 2009.
- [33] BS 1881:103. Testing Concrete - Method for Determination of Compacting Factor, British Standards. 1983.
- [34] Shetty MS. Concrete Technology Theory and Practice. S. CHAND & Company Ltd., New-Delhi, India; 2008.
- [35] Bowles JE. Foundation Analysis and Design. The McGraw-Hill Companies, Inc.; 1996.
- [36] BS EN 12390-3:2009. Testing Hardened Concrete - Compressive Strength of Test Specimens, British Standards. 2009.
- [37] BS 1881-122:2011. Testing concrete. Method for determination of water absorption. 2011.

- [38] Kim MY, Yang EI, Yi ST. Application of the colorimetric method to chloride diffusion evaluation in concrete structures. *Constr Build Mater* 2013. <https://doi.org/10.1016/j.conbuildmat.2012.11.084>
- [39] ACI Education Bulletin. Aggregates for Concrete-Materials for Concrete Construction. Developed by Committee E-701, American Concrete Institute, 38800 Country Club Dr, Farmington Hills, Michigan, United States. 2007.
- [40] Anifowose MA, Adebara SA, Odeyemi SO, Olahan AB, Aliyu T. Density, Workability And Compressive Strength Assessment Of Steel Slag In Concrete. *Acta Tech Corviniensis - Bull Eng* 2017;10:63-7.
- [41] Ede AN, Bamigboye GO, Olofinnade OM, Shittu KK. Influence of Portland cement brands and aggregates sizes on the compressive strength of normal concrete. *Mater Sci Forum* 2016;866:78-82. doi:10.4028/www.scientific.net/MSF.866.78. <https://doi.org/10.4028/www.scientific.net/MSF.866.78>
- [42] Bamigboye GO, Ede AN, Egwuatu C, Jolayemi J, Olowu O. Assessment of Compressive Strength of Concrete Produced from Different Brands of Portland Cement. *Civ Environ Res* 2015;7:31-9.

Blank Page



Research Article

## The impact of RC shear wall openings at the lateral stiffness of the cantilever shear walls

Anas M. Fares

Department of Civil Engineering, Necmettin Erbakan University, Konya, Turkey

### Article Info

#### Article history:

Received 16 Aug 2020

Revised 14 Nov 2020

Accepted 15 Nov 2020

#### Keywords:

Lateral displacement;

Openings;

Reinforced concrete;

Shear wall;

Stiffness

### Abstract

Nowadays, Finite Element Method has large impact and huge usage in civil engineering application. It is used in simulating and analyzing civil engineering problem numerically. One of these problems is the openings at shear walls. Shear walls may be used to resist the lateral loads such as wind and earthquake loads. Due to architectural requirements like windows and doors, the shear walls contain openings. In this study, the effect of the window's and the door's openings at reinforced concrete shear walls is studied by using linear elastic analysis at SAP2000 to give a general conceptual sense about opening's effect. It is found that the lateral stiffness is affected by the size of the openings. It can be considered that the window's opening has a small effect on the lateral stiffness and may be neglected if the window's opening area ratio to the total wall side area is up to 3%. Also, when the wall height to length ratio increases, the effect of opening decreases. Moreover, the minimum door opening ratio that converts the solid wall to a frame will be equal to 65% from the total wall area.

© 2021 MIM Research Group. All rights reserved.

## 1. Introduction

Buildings should have sufficient capacity to resist any lateral loads such as earthquake and wind forces. Different lateral resisting systems are used to increase the stiffness capacity; the most common lateral bracing system in the buildings is the reinforced concrete shear wall system. This system has many forms depending on the position and function of walls like core walls, coupled walls, and planar walls. According to Bungale [1], this system is the most appropriate in moderate sized building up to 20 floors. Shear wall system is not preferred in the case of tall buildings, because this system will use a lot of concrete and reinforced steel bars when comparing to other lateral bracing systems like moment resisting frames. The shear wall system is not also preferred in the open spaced structures due to architectural functions.

Due to small drift between floors and good stability in buildings, which will make the buildings more rigid, shear walls offer good performance in resisting lateral loads. Although the internal base shear force in this type of construction is generally more than that of other resisting systems, the capacity of the shear wall system can accept this large force induced by earthquakes. Windows and doors are required to be existed at shear walls due to architectural functions, these openings cause a variation in relative stiffness of wall with openings that extend from that of a solid wall to that of a flexible frame.

The designers are generally ignored the effect of these openings in walls to simplify both modeling and analyzing the structures by using finite element programs. Such choice of neglecting these openings may produce unreal results in seismic design of buildings. So, it

Corresponding author: [anas\\_fares76@yahoo.com](mailto:anas_fares76@yahoo.com)

orcid.org/0000-0003-2804-7364

DOI: <http://dx.doi.org/10.17515/resm2020.208st0816>

Res. Eng. Struct. Mat. Vol. 7 Iss. 1 (2021) 51-63

is thus of prime important to quantify the effect of these openings on the lateral stiffness of buildings.

To conduct this study a literature review is done so as to understand analytical methods or experimental results. The commercial program SAP2000 based on using finite element method is then chosen to be the calculation tool. the linear elastic analysis is performed to give a general conceptual sense about opening's effect. The shear walls are modeled as 2D thin-shell elements. Lateral concentrated loads at the top of shear walls are assigned. The effect of wall height (H) to the wall length (B) is also studied when squared central window openings are existed.

The general objectives of this study are as the following:

- Investigation the effect of the opening's sizes on the lateral stiffness of reinforced concrete shear walls.
- Identifying the maximum ratios of square window openings in the reinforced concrete shear walls to the size of the side wall that can be neglected in modeling the structures for the purpose of simplification.
- Recognizing the minimum opening ratio that converts the behavior of a solid wall to that of a frame, in order to help the designers to make their models as simple and safe as possible.
- To investigate the effect of wall aspect ratio (H/B), wall height (H) to wall length (B), on the stiffness of concrete shear walls with different patterns of openings.

## 2. Literature Review

For many years, the performance of shear wall system has been investigated. The effect of opening size, openings location, openings arrangement and depth have been studied. This section gives brief information collected from many papers and studies, dealing with the behavior of reinforced concrete shear walls with and without openings. Most of these papers are related to experimental and analytical studies of the capacity of shear walls to resist dynamic loads.

Aghayari et al. [2] studied the behavior of coupled shear wall system because most structural design codes have no clear seismic design consideration for base shear, lateral stiffness and period for this system as Aghayari et al. claimed. Aghayari et al. used finite element models built in ANSYS and divided into two categories. First category is the one-floor, two-floor, and three-floor 3D solid models with two-way slabs. The second category is one-floor individual wall with 5m length, 3.5m height, and 0.15m thickness with different central window opening ratios. As a result of their work, corrective coefficients were presented according to the numerical results. They noticed that the empirical formulas in ASCE code for period estimation may not be reliable for real design yet in the case of coupled walls structures. They also noticed that the stiffness of concrete shear walls and fundamental period both are affected by the opening ratio and it is better to use some other structural parameters like relative wall area and opening ratio in the code equations for fundamental period calculations to be more accurate. Based on this work, Aghayari et al. proposed a modification factor to consider the effect of opening ratio on both the lateral stiffness and the fundamental period of individual coupled wall. Multiplication of this factor by the ASCE code empirical formula of period produces more accurate and reliable value.

Sharma et al. [3] analyzed 30-storey building with different opening sizes and shapes at the shear walls, they found that the size of these openings affects the lateral deflection of the building, and the shape of the opening will also affect the drift of the studied building.

The openings produce high local vertical stress and shear strain concentrations around the opening's corners.

Hsiao [4] proposed a new hand calculations method to estimate the rigidity and the lateral deflection of shear walls with openings with an acceptable difference between finite element method and his hand calculations method results. Hsiao method allows the piers of walls at the top to rotate. Hsiao method is divided into 9 steps, where the wall is subdivided into pieces and the equivalent frame method is used to find the deflection of each piece, and then the deflections are combined by a sort of superposition. Hsiao made the following assumptions while deriving his method: (1) The wall is in one floor only (2) A single opening or one layer of multiple openings with the same height elevation (3) The analysis is restricted to linear elastic (4) The foundations are Rigid and no wall deflection due to foundation rotation.

Harini et al. [5] applied numerical finite element method on 7 floors frame-shear wall buildings with openings using linear elastic response spectrum analysis. Harini et al. found that staggered openings exhibited a higher value of period when compared to vertically aligned openings. They also noticed that staggered openings can perform better during seismic action, because cracks propagation in staggered openings is smaller than vertically aligned openings and they will appear at late stage of earthquake.

Sharmin et al. [6] studied the effect of openings in concrete shear walls on the seismic response of structure. They conducted a finite element study by using ETABS program with 6 floors frame-shear wall building by using equivalent static method of earthquake loads. They noticed that the seismic response of the studied structure affected by the size and the location of the opening. the top lateral drift of the building can be reduced thickening the element in the model around the opening of shear wall.

Abbas M [7] conducted study about shear wall with openings by using brick elements. he found that the size of opening play major role in increasing the lateral drift of walls.

Neuenhofer [8] evaluated the accuracy of a simplified hand method proposed by Brandow et al.1997 and Lindeburg et al. 2001 to calculate the lateral deflection of cantilever concrete shear walls with openings due to flexural and shear deformation, where Neuenhofer claimed that this method is used in several design guidelines. Neuenhofer compared these hand method and numerical finite element algorithm on MATLAB at two examples, one for window opening and another for door opening. Neuenhofer found that the lateral stiffness is strongly affected by the vertical location of the opening in the walls, and the hand calculation method doesn't consider this factor. Neuenhofer conducted two parametric studies to find the percentage of error between the hand method and numerical method one for window opening and another for door opening by fixing the wall geometry and change the vertical location of opening. Neuenhofer noticed that the error between hand calculation method and finite element method increases when the vertical location of the opening increase and this error also increases when the opening ratio increases. Thus, Neuenhofer concluded that the Brandow et al. and Lindeburg et al. simplified hand method should be removed from the design guidelines and documents for practicing structural engineering as he claimed.

Kim et al. [9] try to investigate and found a method that may be used in analyzing shear walls with openings. they propose this method by using super elements to model the shear wall.

Balkaya et al. [10] compared the codes formula UBC-97, and Turkish seismic code-98 for estimating the fundamental period of reinforced concrete multi-story shear wall with no opening structures and they found that the equations yielded inaccurate results. They also studied the effect of openings on the lateral stiffness of structure. They performed a

numerical linear elastic modal analysis study using ETABS version 7.22 with 2D shell element on 80 different shear wall buildings in their local region with different openings sizes and locations by using tunnel form techniques with no beams or columns and only using cast in-place walls and slabs with almost the same thickness. In their study, they recommended to use the slab as it is without making any rigid or semi rigid diaphragm assumption in the models. The 80 different buildings were divided into two cases; squared ones with the building long side divided by the short side is less than 1.5, otherwise the buildings are considered as rectangular ones. The final fundamental period results are taken from the first mode of modal analysis. Their proposed equation has a set of factors which affect the period and all of these parameters have numerical coefficients found by non-linear regression. They concluded to use this formula to improve the accuracy when calculate the fundamental period of such structures. Balkaya et al. didn't make any restriction when using their formula like restriction in the number of floors, restriction in the location and sizes of the openings. They also didn't consider the soil-structure interaction in their study. They advised that opening size has to be used in the calculation of the fundamental period and the lateral stiffness, because it plays a major role in the value of drift of structure.

J'aidi [11] studied the rigidity of concrete shear walls with and without openings. He carried out a numerical study using SAP90 to get the results. J'aidi concluded that the rigidity of the solid concrete walls without openings is a function of the wall aspect ratio (height/length) being the most dominated factor, so the walls with the same aspect ratio, same material, and same thickness will have the same rigidity value. J'aidi found numerically that the shear deformation can be neglected when the wall aspect ratio equals to 4. He suggested two patterns for both window and door openings, where the window opening patterns weren't at the center of a studied 3×4m wall. As a result of his study, the small window opening which captured about 2% of the wall area can be neglected, because this percentage of opening reduces the rigidity of the solid wall to about 90%, while 12% window opening area reduces the rigidity to about 50%.

Qaqish et al. [12] investigated the effect of small openings on the behavior of shear walls. They found that when increasing the size of openings, the effect on lateral stiffness will appears clearly.

Mays et al. [13] described a proposed method for the derivation of quasi-static elastic/plastic resistance functions for reinforced concrete wall panels with door and window openings based upon finite element analysis and yield-line theory. This approach is compared with the results of tests on model wall panels. This work has demonstrated that the total ultimate resistance of a panel decreased by up to 60% for openings representing 20% of the panel area. The theory predicted that up to 37% of the residual capacity could then be lost by the incorporation of blast-resistant openings. Stiffening the edges of openings by placing reinforcement equal in quantity to that which has been interrupted adjacent to the opening appears to be beneficial.

Yanez et al. [14] conducted a study on the effect of square opening at concrete walls on the seismic behavior. different sizes and arrangements of openings studied under reversed cyclic loading. It was concluded that the stiffness of walls is dependent on the size of the openings not on their horizontal locations. It was suggested that if the opening area to the side wall area is up to 10%, the effect on lateral stiffness can be neglected.

Lin et al. [15] studied the ultimate strength of concrete walls with openings under lateral load by conducting a finite element analysis and experimental study. The experimental tests conducted by different wall samples with different sizes of opening and multi patterns of reinforcing around the opening. The test results indicated that the shear strength contributed by diagonal reinforcement around opening reached 40% of its yield

strength, while the shear strength contributed by rectangular arrangement reached 20% of its yield strength. The stiffness of walls also affected by the depth of opening.

### 3. Central Window Opening and Opening Ratio ( $R_o$ ): Analyzing and results

The openings at shear walls in the reality are either doors or windows. In this section, the effect of central window opening on the wall stiffness will be studied because these openings cause a variation in lateral stiffness that extends from that of a solid wall to that of a frame as shown in Fig.1.

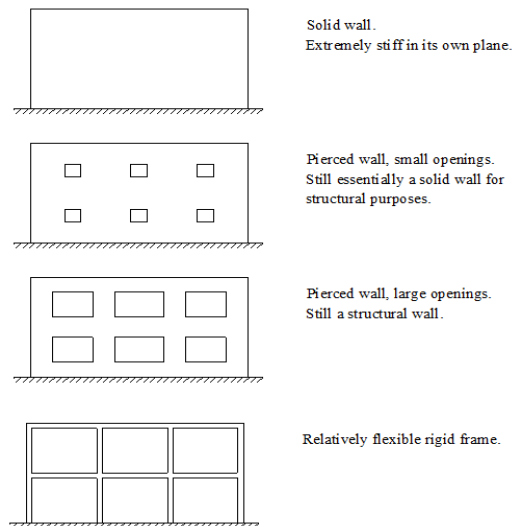


Fig. 1 Transition in a monolithic planer construction, from a solid wall to a flexible, moment resisting frame [16]

The openings at walls affect the total stiffness of the structure and may reduce it which leads to a decrease in the lateral stiffness of structure. In the following study, the wall thickness, aspect ratio ( $H/B$ ), and wall concrete material are assumed to be fixed and the wall opening ratio is the only parameter to be varied.

A 3×3m 2D planer cantilever wall is modeled with concrete compressive strength  $f_c$  equals to 24MPa, the thickness of the wall equals to 0.2m, and top shear load equals to 1000kN. These parameters are to evaluate the effect of different central window and door openings in the next sections. Fig. 2 shows model number C-W12 with dimensions as modeled at SAP2000. A deflection of each case is tabulated then the relationship between opening ratios in the wall and the corresponding change in stiffness are shown in graphs.

17 central squared window openings of varying sizes are suggested. In this section the largest ratio of central window opening in a wall whose effect on the lateral stiffness is small and can be neglected will be identified. The results of the average lateral deflection of the top points ( $\Delta$ ), the lateral stiffness ( $K$ ), and the stiffness ratio ( $R_s$ ) are tabulated in Table 1.

For the naming of the models, C refers to the concrete wall and W refers to window opening. The stiffness ratio ( $R_s$ ) is defined as the ratio of the lateral stiffness of a wall with opening divided by the lateral stiffness of the same wall without openings. The opening ratio ( $R_o$ ) represents the opening area in the wall divided by the total wall side area. The lateral stiffness ( $K$ ) is founded by dividing the lateral load ( $P$ ) onto the average lateral deflection of the top points ( $\Delta$ ) for each case.

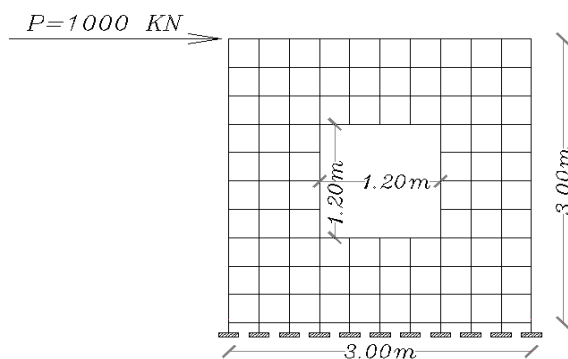


Fig. 2 C-W12 3×3m cantilever wall model with central window opening

Table 1. Results of window opening models with a 3×3m wall

Model number	Opening size (m)	Opening ratio, $R_o$ (%)	Top displacement, $\Delta$ (mm)	Stiffness, K ( $10^4$ kN/m)	Stiffness ratio, $R_s$ (%)
C-W0	0.00	0.00	1.47	67.89	100
C-W3	0.3×0.3	1.00	1.52	65.79	96.90
C-W4	0.4×0.4	1.87	1.52	65.70	96.78
C-W5	0.5×0.5	2.78	1.55	64.52	95.03
C-W6	0.6×0.6	4.00	1.66	60.24	88.73
C-W7	0.7×0.7	5.44	1.76	56.81	83.69
C-W8	0.8×0.8	7.11	1.86	53.76	79.19
C-W9	0.9×0.9	9.00	2.00	50.00	73.65
C-W10	1 × 1	11.11	2.21	45.24	66.65
C-W11	1.1×1.1	13.44	2.54	39.37	57.99
C-W12	1.2×1.2	16.00	2.84	35.21	51.87
C-W13	1.3×1.3	18.78	3.28	30.49	44.91
C-W14	1.4×1.4	21.78	3.90	25.64	37.77
C-W15	1.5×1.5	25.00	4.66	21.45	31.61
C-W16	1.6×1.6	28.44	5.66	17.66	26.02
C-W17	1.7×1.7	32.11	7.16	13.96	20.57
C-W18	1.8×1.8	36.00	9.05	11.05	16.27

### 3.1 Discussion of Results

Fig. 3 shows the relationship between  $R_s$  and  $R_o$  as expected. Increasing the size of opening will decrease the stiffness of the wall. If 5% reduction in the wall lateral stiffness is considered negligible, then the opening area in the wall give such a reduction in stiffness equals 3% of the total wall side area. Thus, central window opening can be neglected in modeling the walls when its area ratio to total wall side area is up to 3%. In the common practice the 3% opening area appears in the bathroom window openings. Typical squared window opening of size 1.30×1.30m which is commonly used in practice reduces the stiffness of 3×3m solid wall to about 50%. The rapid drop in stiffness can be noticed when using large opening ratios. When the opening ratio is around 17% from the total wall area, the wall will lose 50% of it is stiffness.

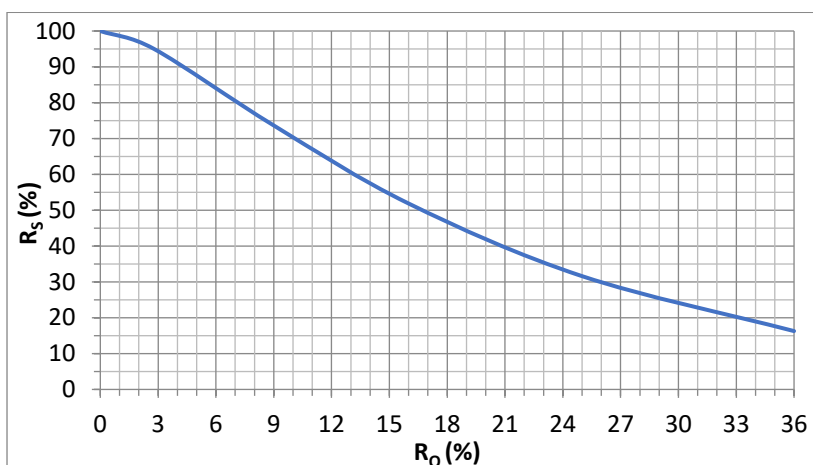


Fig. 3 Squared windows opening ratio versus stiffness ratio of 3×3m wall

#### 4. Effect of Wall (H/B) Ratio with Central Openings on The Lateral Displacement

35 cases for the same previous wall length, thickness and material are taken to study the effect of wall height and multiple openings on the top lateral displacement. 1000kN lateral load is applied on the top of the wall at each floor level where floor height is assumed to be 3m, and then the results of top displacement ( $\Delta$ ), and displacement ratio ( $R_D$ ) which is defined as the ratio of the lateral top displacement of a wall with opening divided by the lateral displacement of the same wall without openings are tabulated in Table 2. For the naming of the models, C-W refers to concrete wall and window opening respectively, then the first number and the second number refers to the opening ratio and (H/B) respectively. Fig 4 shows a schematic drawing for C-W12,2.

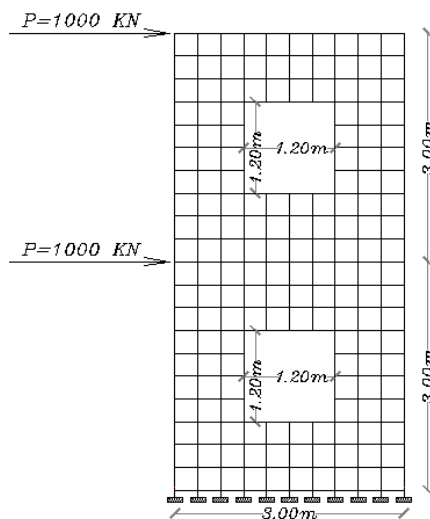


Fig. 4 C-W12,2 model with boundary conditions and applied lateral loads

Table 2. lateral displacement results on different wall heights and central opening sizes

Model number	H/B (m)	Opening size (m)	Total opening ratio, $R_o$ (%)	Top displacement, $\Delta$ (mm)	Displacement Ratio, $R_D$
C-W0,2	2	0.00	0.00	10.92	1.00
C-W3,2	2	0.3×0.3	1	11.00	1.01
C-W6,2	2	0.6×0.6	4	11.52	1.05
C-W9,2	2	0.9×0.9	9	12.60	1.15
C-W12,2	2	1.2×1.2	16	15.30	1.40
C-W15,2	2	1.5×1.5	25	21.21	1.94
C-W18,2	2	1.8×1.8	36	35.15	3.22
C-W0,3	3	0.00	0.00	42.67	1.00
C-W3,3	3	0.3×0.3	1	42.78	1.00
C-W6,3	3	0.6×0.6	4	43.86	1.03
C-W9,3	3	0.9×0.9	9	46.21	1.08
C-W12,3	3	1.2×1.2	16	52.22	1.22
C-W15,3	3	1.5×1.5	25	65.94	1.55
C-W18,3	3	1.8×1.8	36	95.93	2.25
C-W0,6	6	0.00	0.00	531.00	1.00
C-W3,6	6	0.3×0.3	1	532.30	1.00
C-W6,6	6	0.6×0.6	4	536.95	1.01
C-W9,6	6	0.9×0.9	9	548.85	1.03
C-W12,6	6	1.2×1.2	16	581.63	1.10
C-W15,6	6	1.5×1.5	25	654.95	1.23
C-W18,6	6	1.8×1.8	36	809.32	1.52
C-W0,9	9	0.00	0.00	2487.50	1.00
C-W3,9	9	0.3×0.3	1	2488.11	1.00
C-W6,9	9	0.6×0.6	4	2501.2	1.01
C-W9,9	9	0.9×0.9	9	2539.54	1.02
C-W12,9	9	1.2×1.2	16	2650.85	1.07
C-W15,9	9	1.5×1.5	25	2901.55	1.17
C-W18,9	9	1.8×1.8	36	3399.91	1.37
C-W0,12	12	0.00	0.00	7562.73	1.00
C-W3,12	12	0.3×0.3	1	7562.87	1.00
C-W6,12	12	0.6×0.6	4	7593.03	1.00
C-W9,12	12	0.9×0.9	9	7690.39	1.02
C-W12,12	12	1.2×1.2	16	7982.19	1.06
C-W15,12	12	1.5×1.5	25	8640.97	1.14
C-W18,12	12	1.8×1.8	36	9908.36	1.321

#### 4.1 Discussion of Results

Fig 5. shows the relationship between the displacement ratios versus opening ratios for different wall H/B ratio. From this figure, the increase in H/B shall reduce effect of openings. The reduction in RD will be in a rapid form when the wall aspect ratio is small, where the effect of shear deformation contribution is significant compared with large aspect ratio.

The effect for the same  $R_o$  on the lateral displacement becomes smaller as the height of the building increases. This effect appears more clearly for low number of floors. The lateral deflection and the stiffness of the concrete shear wall with opening depend on the wall H/B ratio. If H/B increases, then the deflection mode becomes dominated by flexure. Thus, the

area of the wall is not the dominant factor in the lateral deflection, but rather the moment of inertia. Reducing the central area of the wall by increasing the central  $R_0$  will reduce the wall moment of inertia by a small value, but it is reducing the shear area of the wall by large value. It can also be seen that 3%  $R_0$  still gives negligible reduction in the lateral stiffness of walls with different  $H/B$  ratios, where all values of  $R_D$  are less than 1.05 for  $H/B$  greater than 1.

To find out the maximum  $R_0$  that can be neglected, a threshold of 5% increase in  $R_D$  will be accepted as a negligible difference. From Figure 3.9 the value of  $R_0$  that can be neglected safely is 4.00%, 6.00%, 11.00%, 14.00% and 15.00% for  $H/B$  equals to 2, 3, 6, 9 and 12 respectively.

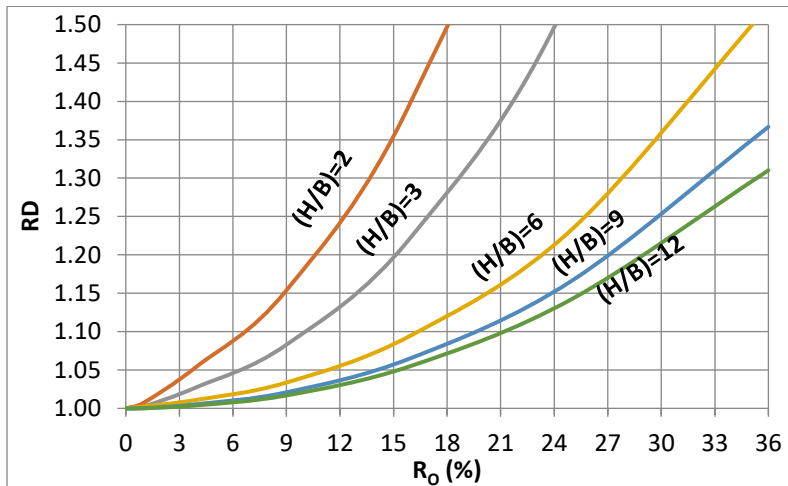


Fig. 5 Displacement ratio  $R_D$  versus opening ratio  $R_0$  for different floor heights in shear wall with multiple openings

Moreover, if the engineer models the wall with opening as a solid wall for simplification issues, then the result of the lateral displacement must be modified by using lateral displacement modifiers. For the common central window opening of  $1.30 \times 1.30\text{m}$ , the top lateral displacement modifiers are 1.50, 1.30, 1.10, 1.09 and 1.07 for  $H/B$  equals to 2, 3, 6, 9 and 12 respectively. Multiplying these values with the top lateral displacement of concrete shear walls with no openings will give the top lateral displacement of the walls with central  $1.3 \times 1.30\text{m}$  window opening.

### 5. Door Opening: Analyzing and results

In this section, the effect of door opening in a wall on the lateral stiffness will be studied using 4 door openings of varying sizes that are suggested as shown in Fig.7. This figure shows the wall model at the left and its equivalent frame model at the right with dimensions. These models will be named as C-D followed by the dimension of the opening, where C and D refer to concrete wall with door opening.

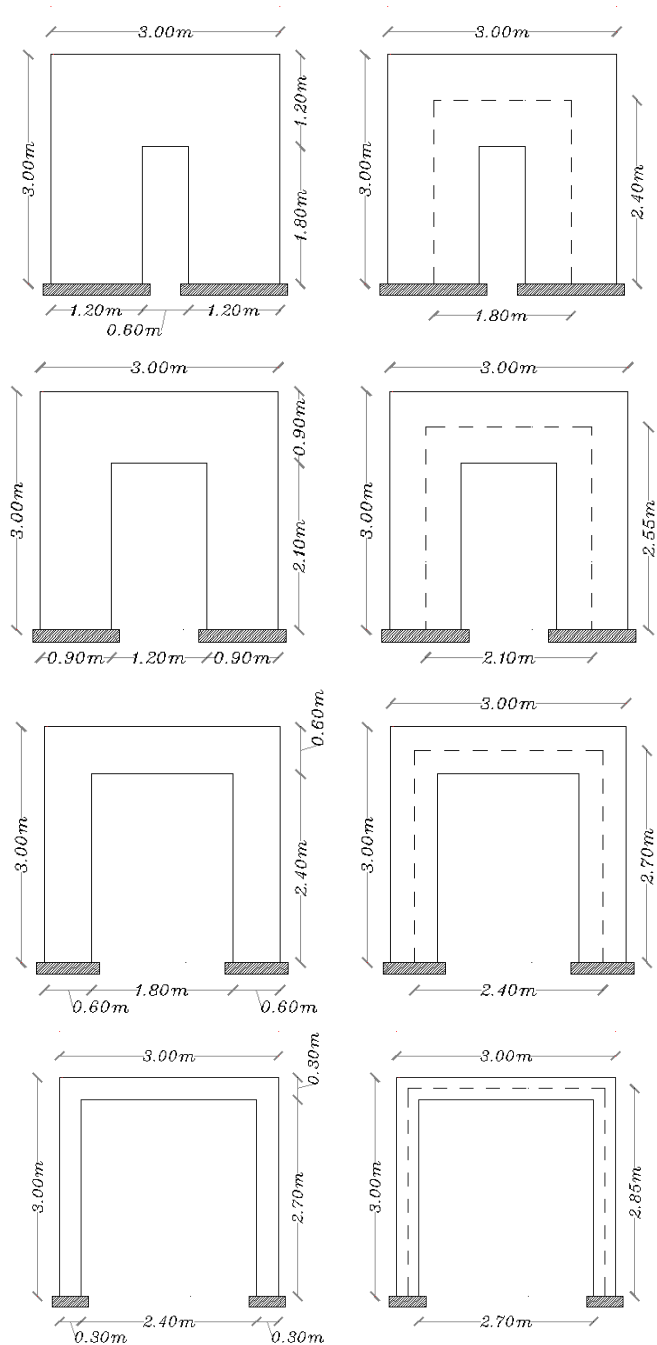


Fig. 7 C-D6,18/ C-D12,21/ C-D18-24/ C-D24-27 solid wall and its equivalent frame model from left to right respectively

The results of the total lateral deflection ( $\Delta$ ) from 2D wall, total deflection from 1D beam equivalent frame model, both flexural deflection ( $\Delta_f$ ) and shear deflection ( $\Delta_s$ ) from the equivalent frame model, the lateral stiffness ( $K$ ), and the stiffness ratio ( $RS$ ) are tabulated in Table 3 and they are drawn in Fig. 8.

The reason why both shear and flexural deflection are gutted from the equivalent frame model is because SAP2000 doesn't clarify the contribution of both shear and flexure deformation and gives only the total deflection of the 2D area element.

Table 3. Results of door opening models with a 3×3m wall from SAP2000

Model number	Opening size (m)	$\Delta_{2D}$ area total (mm)	$\Delta_{1D}$ beam total (mm)	$\Delta_s$ (mm)	$\Delta_f$ (mm)	Stiffness, K ( $10^4$ kN/m)	Stiffness Ratio, $R_s$ (%)
C-D6,18	0.6×1.8	2.37	2.37	0.95	1.42	42.19	62.02
C-D12,21	1.2×2.1	4.75	4.94	1.24	3.70	21.05	30.95
C-D18,24	1.8×2.4	15.72	16.18	1.98	14.20	6.36	9.35
C-D24,27	2.4×2.7	135.02	136.30	4.13	132.17	0.74	1.09

### 5.1 Discussion of Results

Fig. 8 shows the relationship between  $R_s$  and  $R_o$ , where it has the same trend in the case of window opening. Increasing the size of opening will decrease the stiffness of the wall as expected and as shown previously. When the door opening ratio is 17% from the total wall area, the wall will lose almost 50% of its stiffness and this ratio is the same as in the case of window opening. The typical door opening of 1.00×2.00m which is commonly used in practice and represents 22.22% of RO in a wall of 3.00×3.00m will result in a loss of the stiffness of this wall to about 60%.

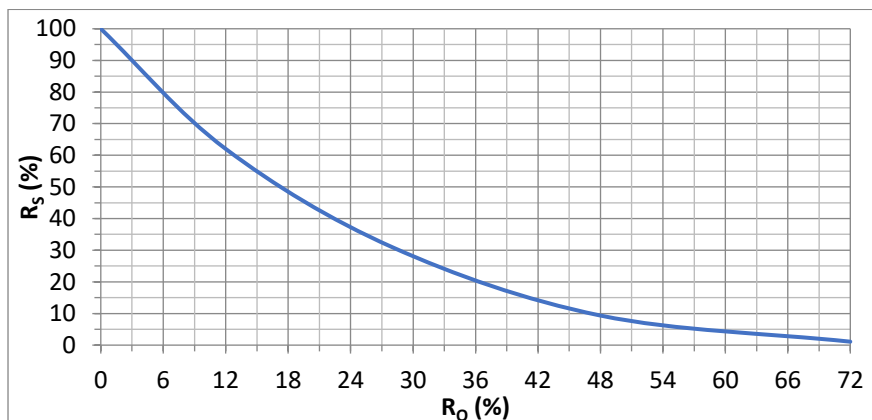


Fig. 8 Door opening ratio versus stiffness ratio of 3×3m wall

Fig.9 shows the contributions of both shear and flexural deflections from the total deflection results drawn by using results listed in Table 3. Assuming a 5% of shear deformation contribution to be considered negligible, the minimum door opening ratio that converts the solid wall to a frame shall be equal to 65% from the total wall area, and from Fig.8 this ratio makes  $R_s$  of the wall equal to 2.90%.

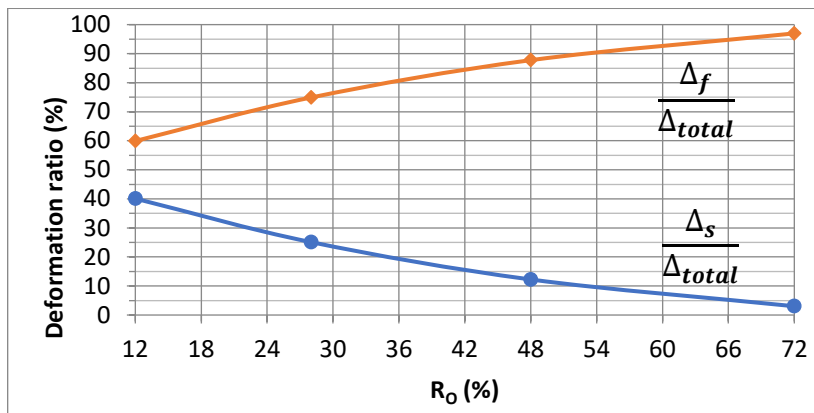


Fig. 9 Relative contribution of shear and flexure deformation to total wall with door opening deformation in a 3x3m wall

## 6. Conclusions

In this study, the modeling and behavior of individual concrete shear walls with openings are discussed. These openings are both central squared windows and door openings. A matrix of parameters that is expected to have an effect on the lateral stiffness of the wall is searched. This matrix includes a wall aspect ratio (H/B), opening type, and opening ratio  $R_o$ . The effect of opening on the lateral deflection of the wall is discussed in both conditions: in central opening and in multiple central openings with different wall heights. The main findings and conclusions can be summarized as the following:

- The opening size plays major role on the lateral displacement and stiffness of reinforced concrete shear walls.
- Increasing the size of opening at shear walls will increase the lateral displacement, and thus reduce the lateral stiffness of structure.
- It is found that the maximum window opening at concrete shear walls that could be neglected in modeling, due to simplification, will be up to 3% from the total wall area when 5% of the stiffness ratio RS reduction can be accepted.
- It is concluded that, in multiple wall aspect ratios, H/B, with central window opening in concrete shear walls, it is noticed that increasing the wall aspect ratio H/B will decrease the effect of openings in the lateral deflection and stiffness of the concrete shear wall and this is because the deflection mode of the wall becomes dominated by flexure.
- It is found that, 65% of the door opening will convert a solid wall to a frame in its behavior when 5% difference due to shear deformation contribution may be considered negligible.
- It is found that, a typical door in a common practice with dimensions of 1.00x2.00m decreases a 3x3m solid wall stiffness by 60%.

## References

- [1] Taranath BS. Reinforced Concrete Design of Tall Buildings. CRC Press. Taylor & Francis Group, 2010. <https://doi.org/10.1201/9781439804810>
- [2] Aghayari R, Ashrafy M, Roudsari M. Estimation of the Base Shear and Fundamental Period of Low-Rise Reinforced Concrete Coupled Shear Wall Structures. Asian Journal of Civil Engineering, 2017; 18 (7).

- [3] Ruchi S, Jignesh A. Effects of opening in shear walls of 30- storey building. JOURNAL OF MATERIALS AND ENGINEERING STRUCTURES, 2015;2: 44-55.
- [4] Hsiao KJ. Hand- Calculated Procedure for Rigidity Computation of Shear Walls with Openings. ASCE Journal of Structural Engineering, 2014; 19(4). [https://doi.org/10.1061/\(ASCE\)SC.1943-5576.0000210](https://doi.org/10.1061/(ASCE)SC.1943-5576.0000210)
- [5] Harini AT, Kumar GS. Behavior of R.C. Shear Wall with Staggered Openings under Seismic Loads. International Journal for Research in Emerging Science and Technology, 2014; 2(3).
- [6] Sharmin RC, Rahman MA, Islam MJ, Das AK. Effect of Openings in Shear Wall on Seismic Response of Structure. International Journal of computer applications, 2012; 59 (1): 10-13. <https://doi.org/10.5120/9511-3901>
- [7] Abbas MH. Analysis of Shear Wall with Openings using Brick Element. European Journal of Scientific Research, 2011;51 (3): 359-371.
- [8] Neuenhofer, A. Lateral Stiffness of Shear Walls with Openings. ASCE Journal of Structural Engineering, 2006; 132 (11): 1846-1851. [https://doi.org/10.1061/\(ASCE\)0733-9445\(2006\)132:11\(1846\)](https://doi.org/10.1061/(ASCE)0733-9445(2006)132:11(1846))
- [9] Kim HS, Lee DG. Analysis of shear wall with openings using super elements, Engineering Structures, 2003; 25: 981-991. [https://doi.org/10.1016/S0141-0296\(03\)00041-5](https://doi.org/10.1016/S0141-0296(03)00041-5)
- [10] Balkaya C, Kalkan E. Estimation of Fundamental Period of Shear-Wall Dominate Building Structures. The Journal of Earthquake Engineering and Structural Dynamics, 2003; 32 (7): 985-998. <https://doi.org/10.1002/eqe.258>
- [11] J'aidi YT. Rigidity of Reinforced Concrete Shear Walls and Effect of Openings. Master thesis. An-Najah National University, 2002.
- [12] Qaqish S, Daqqaq F. Effect of horizontal forces on shear walls with small openings. Technical Services and Studies-University of Jordan. Jordan, 2000.
- [13] Mays GC, Hetherington JG, Rose TA. Resistance-Deflection Functions for Concrete Wall Panels with Openings. Journal of Structural Engineering, 1998; 124 (5): 579-587. [https://doi.org/10.1061/\(ASCE\)0733-9445\(1998\)124:5\(579\)](https://doi.org/10.1061/(ASCE)0733-9445(1998)124:5(579))
- [14] Yanez FV, Park R, Paulay T. Seismic behavior of walls with irregular openings. Earthquake Engineering. Tenth World Conference, Balkema, Rotterdam, 1992.
- [15] Lin CY, Kuo CL. Behavior of shear wall with openings. Proceedings of Ninth world Conference on Earthquake Engineering. Tokyo-Kyoto, Japan, IV:535-540, 1988.
- [16] Ambrose J, Vergun D. Simplified Building Design for Wind and Earthquake Forces. Third Edition, John Willey & Sons INC, 1995.

Blank Page



## The mutual interaction between the structural footprint and number of floors in steel structures

Ercan Işık<sup>1,a</sup>, İbrahim Baran Karaşın<sup>2,b,\*</sup>

<sup>1</sup>Bitlis Eren University, Faculty of Engineering and Architecture, Civil Engineering Dept. Bitlis Turkey.

<sup>2</sup>Dicle University, Faculty of Engineering, Civil Engineering Dept. Diyarbakır- Turkey.

### Article Info

#### Article history:

Received 10 Mar 2020

Revised 04 Jun 2020

Accepted 16 Jul 2020

#### Keywords:

Steel;

Footprint;

Number of floor;

Cost;

Pushover;

Material model.

### Abstract

Structural dimensions and number of floors are some of the factors affecting the building behaviour under the earthquake effects. In this study, the structural footprint and the number of floors were selected as a variable. For this purpose, a steel structure model with fixed dimensions and properties of load-bearing system elements was selected. The structural footprint was selected as the first variable and then five different structure models were created. The structural footprint was changed by setting each axial clearance in both directions. Each axial clearance was increased by 0.5m in each structure model. Three different number of floors as to be 5, 6 and 7 floors were selected as the second variable. Eigenvalue and pushover analyses were performed for each model and each number of floors. As a result of the analyses, the target displacement values for period, frequency, cumulative participation mass ratio, base shear force, settlement, stiffness and degree of damage were acquired separately. As the structural footprint and number of the floors increase, while the period, settlement and the target displacement values increased, on the contrary, there was a decrease in participation mass ratio, base shear forces and stiffness values. In the study, cost comparisons of building construction were also made considering the change in the total structural area and the number of floors. The criterion of safety and economy was ignored due to increase both in the number of floors and the footprint. This study emphasizes the importance of avoiding the unnecessary structural dimensions via optimum design principles. As structural footprint area and number of floors increase, period values increase, stiffness and seismic capacity values decrease. As the number of floors and footprint area increases, the total building area increases, so the approximate building cost has also increased.

© 2021 MIM Research Group. All rights reserved.

## 1. Introduction

There are several parameters that can adversely affect the building behaviour under the vertical and horizontal loads. It is possible to gather most of these parameters under the structural characteristics. Structural characteristics are provided by the application of engineering principles in the design and evaluation of structures. Structural characteristics may positively/adversely affect the building behaviour and particularly earthquake response [1, 5]. The total number of stories is one of the important factors determining the degree of damage caused by an earthquake. There is a direct relationship between the number of floors and earthquake damages. The increase in the amount of damage is

\*Corresponding author: [barankarasin@gmail.com](mailto:barankarasin@gmail.com)

<sup>a</sup>orcid.org/0000-0001-8057-065X; <sup>b</sup>orcid.org/0000-0001-5990-1215;

DOI: <http://dx.doi.org/10.17515/resm2020.184st0310>

Res. Eng. Struct. Mat. Vol. 7 Iss. 1 (2021) 65-86

unavoidable for the structures having negligent structural characteristics in the design and period [6,7].

There are three main elements in the design and evaluation of structural systems as to be load, material and dimensional conditions. The concept of dimension figures the load-bearing systems, non-load bearing systems and other structural characteristics in three dimensions. The two-way length values forming the total structural area take an important place in the concept of dimension. Dimensions, stated as width and length, can be calculated as the sum of the axial clearances forming the load-bearing system and consoles outside the axle. The total structural area was effective in all the stages of structural calculation, as well as in terms of cost. The structural area may be determined larger than adequate due to some reasons. This determination has some effects both in structural calculations and in economic terms.

There are different studies with the effect of the number of floors on the building performance, and different types of analysis have been taken into account for different parameters [8-10]. The results obtained from these studies do not overlap exactly [10]. A great number of design variables were affect to the construction costs. The most important design variables that affect the total cost of the structure; shape and complexity of buildings plan, number and height of floors and service requirements of the building [11-13]. Most of the studies to examine the relationship between them are related to reinforced concrete structures. In some of these studies, it was determined that the increase in the number of floors increased the cost of the building [14, 15]. In some studies, they said that with the increase in the number of floors, the unit cost will decrease and then increase again, that is, a U-shaped relationship [16, 17].

Within the scope of this study, both the number of floors and the axial clearance that forms the structural footprint were selected as variables for steel structure model. Three different values were considered in terms of number of floors as to be 5, 6 and 7 floors. In terms of structural footprint, on the other hand, five different models were selected where the axial clearance values were same in both X and Y axis. 4m, 4.5m, 5m, 5.5m and 6m were selected as the axial clearance values. The structural footprint of the steel structure model was changed with the changing axial clearance values. Analyses were performed by enabling the interaction between the changing number of floors and the structural footprints reciprocally. Eigenvalue analyses were performed by using the steel structure models with five different structural footprints for each number of floors. The target displacement values for base shear force, settlement, stiffness and degree of damage were acquired separately for each structural model by using pushover analysis. All results were compared for both structural footprints and number of floors change. Cost accounts were carried out in order to reveal the relationship of these two variables between the building construction costs. Proposals were made after evaluating the analysis results.

In the first part of the study, information was given about the types of analysis used in the selected building constructions. The structural characteristics of the selected steel structure were presented in the next step. Information was provided about the different building models considered in the study and the results were compared. In the final part of the study, the way how the construction costs were calculated was explained, and cost values were compared for all models used.

Both structural analysis and economic comparisons in reinforced concrete structures are available in the literature. No such publication was found in steel structures. Two different parameters selected within the scope of the study are both important in terms of building cost and earthquake effects. All conceivable values related to the variables considered in

the study were obtained. Both the behaviour under the effects of earthquake and cost calculations was obtained in detail for steel structures. This shows that, this study can be used in both the scientific and construction sectors.

## 2. Methodology

Firstly, eigenvalue analyses were performed to the structural models for each variable used in this study. Mode shapes and natural frequency for any structure can be acquired by eigenvalue analysis. Material properties always remain constant via calculation. Briefly, it can be considered as a shear elastic structural analysis. The section can be symbolized with material sectional properties such as torsional constant, moment of inertia, modulus of elasticity and modulus of stiffness. Eigenvalue analysis was used to obtain the period, frequency, participation modal factors, effective modal masses and their percentage values related to the structure [18-20]. Another analysis used for all steel structure models selected within the scope of the study was pushover analysis. Pushover analysis is widely used for the structural performances in a potential earthquake. Pushover analysis captures the nonlinear structural behaviour effectively and hence can trace the structural behaviour progressively up to failure. Pushover analysis can provide the most effective measure of global structural behaviour in terms of base shear capacity and displacement ductility of the structure. A capacity curve obtained via pushover analysis represents the relationship between the base shear force and the displacement of the roof. The base shear was normalized by structure seismic weight, while the roof level displacement was normalized by building height to represent the shear strength coefficient and roof displacement drift, respectively [21-23]. A typical example of idealised capacity curve is shown in Figure 1.

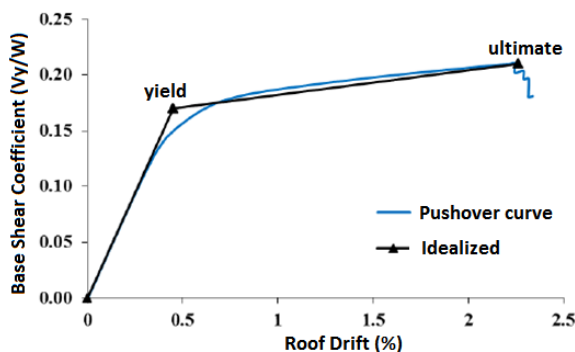


Fig 1. Typical pushover and idealized capacity curves [24]

## 3. Properties of the Examined Building Models

Within the scope of the study, a steel structure model having different number of floors and structural footprints was selected. The structure was selected symmetrically in both X and Y axes. The analyses were performed with the academic licensed Seismostruct software. ZE selection was made in the software used for the structural basic soil class. It was considered IV class as the structural important class and 5% as the damping ratio.

Mathematical models are used for describing the stress-strain relationship for any material. The material model plays a very important role in the seismic structural analyses

[25]. Calculations were made for steel model selected as Menegotto-Pinto steel model (stl\_mp) [26] in this study. This model, proposed by Menegotto and Pinto, is widely used to simulate the cyclic response of steel structures and steel bars of reinforced concrete structures [27]. The stress-strain relationship for this steel model was given in Figure 2.

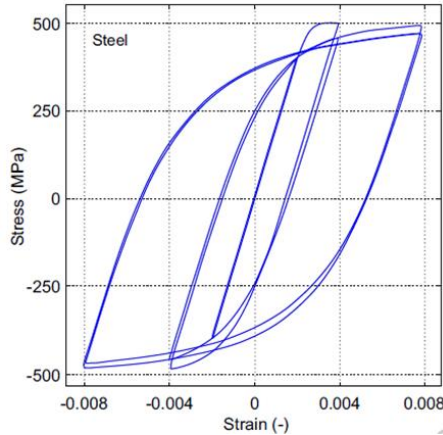


Fig 2. Stress-strain relation for Menegotto-Pinto steel model [20]

In the selected steel structure model, I300 bars were considered. In order to make comparisons in structural models, these bars were taken into consideration in all columns and beams in all structural models. The cross-sectional representation and the dimensions of the selected profile are shown in Figure 3.

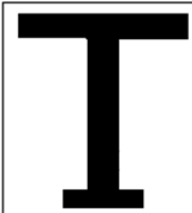
	Sections dimensions (m)	
	Bottom flange width	0.100
	Bottom flange thickness	0.010
	Top flange width	0.200
	Top flange thickness	0.015
	Web height	0.300
	Web thickness	0.015

Fig 3. Size and type of cross section of structural elements

Each axial clearances (a, b) forming the footprint, the first parameter considered within the scope of the study, took different values. Figure 4 shows the formwork plan of steel structure considered in the study.

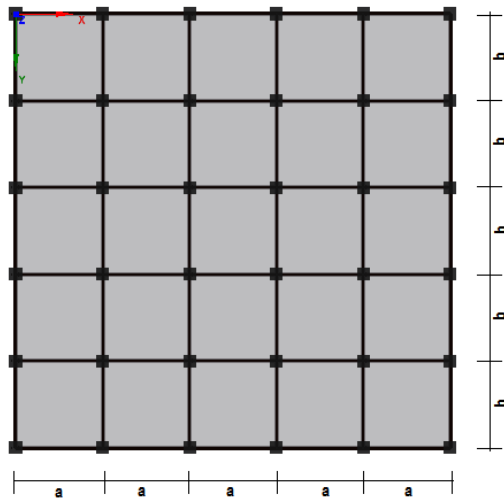


Fig 4. Floor formwork plan of steel structure model

Number of floors were kept constant and  $a$  and  $b$  values for footprint were selected as variables. For the values for  $a$  and  $b$ , five different cases were considered. Considered structural dimensions are given in Table 1.

Table 1. Considered structural dimensions for models

Model No	$a$ (m)	$b$ (m)	Footprint area (m <sup>2</sup> )
Model 1	4.0	4.0	400
Model 2	4.5	4.5	506.25
Model 3	5.0	5.0	625
Model 4	5.5	5.5	756.25
Model 5	6.0	6.0	900

Figure 5 shows the 3-D structure models patterned by software in case of considering the different numbers of floors.

#### 4. The Results of Analysis

Firstly, it was carried out by considering the different floor numbers. The results were obtained for five different structure models separately which were created by considering the five different footprints for each number of floors. Table 2 shows the comparison of values for periods and frequencies acquired via Eigenvalue analysis results for five-storey steel structure.

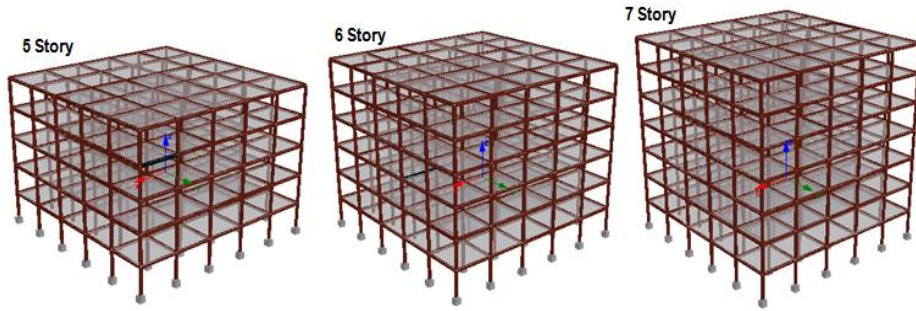


Fig 5. 3-D Models for steel structures with different numbers of floors

Figure 6 shows the 2-D structure models patterned for the selected numbers of floors, and the loads applied to the structure.

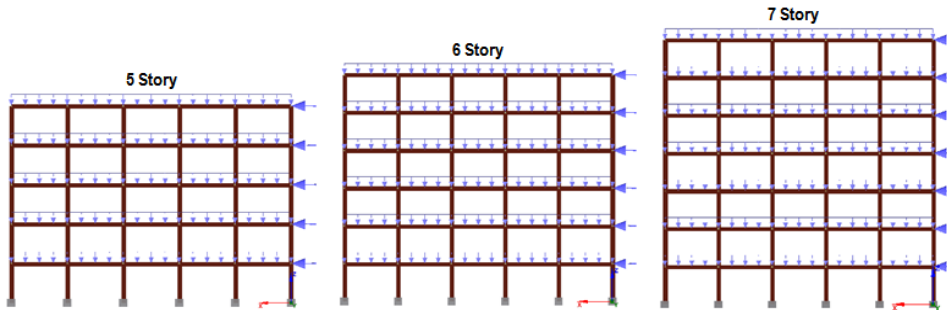


Fig 6. 2-D structure models for different numbers of floors and the applied loads

Table 2. The comparison of periods and frequencies for different footprints for 5-story

Mode	Period (sec)					Frequency (Hertz)				
	Model 1	Model 2	Model 3	Model 4	Model 5	Model 1	Model 2	Model 3	Model 4	Model 5
1	0.5957	0.6263	0.6562	0.6854	0.7141	1.6788	1.5967	1.5239	1.4589	1.4004
2	0.3149	0.3370	0.3590	0.3807	0.4023	3.1755	2.9669	2.7856	2.6266	2.4860
3	0.2537	0.2728	0.2919	0.3109	0.3299	3.9423	3.6655	3.4256	3.2160	3.0312
4	0.2028	0.2130	0.2229	0.2326	0.2420	4.9301	4.6946	4.4860	4.2996	4.1317
5	0.1273	0.1334	0.1394	0.1451	0.1508	7.8553	7.4945	7.1752	6.8901	6.6333
6	0.1026	0.1094	0.1160	0.1226	0.1291	9.7479	9.1441	8.6176	8.1545	7.7440
7	0.0981	0.1026	0.1069	0.1111	0.1151	10.189	9.7465	9.3544	9.0039	8.6881
8	0.0855	0.0891	0.0934	0.0990	0.1046	11.701	11.217	10.710	10.099	9.5599
9	0.0819	0.0877	0.0927	0.0961	0.0994	12.209	11.407	10.788	10.404	10.058
10	0.0470	0.0499	0.0527	0.0555	0.0583	21.296	20.048	18.963	18.008	17.161

Cumulative mass percentages acquired via Eigenvalue analyses are given in Table 3.

Table 3. The acquired cumulative mass ratios for 5-story (%)

Mode	Cumulative Mass Ratio (%)									
	U <sub>x</sub>					U <sub>y</sub>				
	Model 1	Model 2	Model 3	Model 4	Model 5	Model 1	Model 2	Model 3	Model 4	Model 5
1	0.00	0.00	0.00	0.00	0.00	87.33	87.25	87.18	87.10	87.03
2	0.00	0.00	0.00	0.00	0.00	87.33	87.25	87.18	87.10	87.03
3	83.80	83.58	83.36	83.15	82.95	87.33	87.25	87.18	87.10	87.03
4	83.80	83.58	83.36	83.15	82.95	96.33	96.27	96.22	96.16	96.11
5	83.80	83.58	83.36	83.15	82.95	98.95	98.93	98.90	98.88	98.85
6	83.80	83.58	83.36	83.15	82.95	98.95	98.93	98.90	98.88	98.85
7	83.80	83.58	83.36	83.15	82.95	99.81	99.81	99.80	99.79	99.79
8	83.80	83.58	93.67	93.51	93.37	100.0	100.0	99.80	99.79	99.79
9	94.03	93.84	93.67	93.51	93.37	100.0	100.0	100.0	100.0	100.0
10	97.82	97.73	97.64	97.56	97.48	100.0	100.0	100.0	100.0	100.0

Base shear forces were calculated separately for each number of floors and each structure model. The settlement on the idealized curve at the moment of flow ( $d_y$ ) was selected as settlement values. The values for elastic stiffness ( $K_{elas}$ ) and effective stiffness ( $K_{eff}$ ) were calculated separately. The target displacements for the damage of structure can also be calculated. Three different cases were defined for damages in software as follows: non-collapsing (NC), severe damage (SD) and damage limitation (DL). These values were calculated for all models by Seismostruct software [20]. Table 4 shows the comparison of all values on X-axis as result of structural calculations.

Table 4. Acquired result for different 5-storey structural models

Model	Base Shear (kN)	$K_{elas}$	$K_{eff}$	$d_y$	DL	SD	NC
1	10129.84	54439.42	50487.68	0.2006	0.0170082	0.0218187	0.03782
2	10036.24	51245.38	47776.49	0.2101	0.0195205	0.0250415	0.043413
3	9915.62	48377.97	45351.85	0.2186	0.0221865	0.0284615	0.049342
4	9774.18	45799.5	43185.76	0.2263	0.0249964	0.0320662	0.055591
5	9617.92	43473.34	41195.64	0.2335	0.027977	0.0358898	0.062220

Figure 7 shows the comparison of pushover curves for the structural models having different footprints in terms of the selected 5-storey.

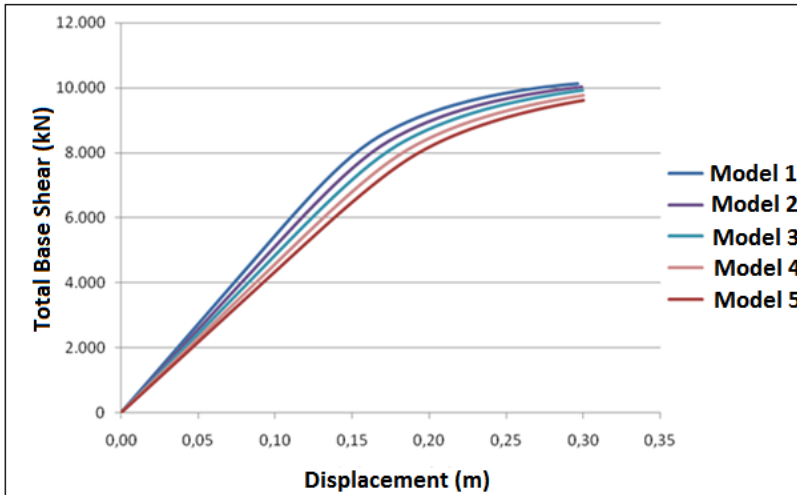


Fig 7. The comparison of pushover curves for 5-story for different structural models

The comparison of values for period and frequency obtained via eigenvalue analysis in terms of six-storey steel structure is given in Table 5.

Table 5. The comparison of period and frequency for different footprints of 6-story

Mode	Period (sec)					Frequency (Hertz)				
	Model 1	Model 2	Model 3	Model 4	Model 5	Model 1	Model 2	Model 3	Model 4	Model 5
1	0.7086	0.7448	0.7802	0.8149	0.8489	1.4113	1.3426	1.2817	1.2271	1.1780
2	0.3789	0.4055	0.4320	0.4583	0.4843	2.6393	2.4659	2.3148	2.1822	2.0648
3	0.3058	0.3289	0.3520	0.3751	0.3981	3.2699	3.0403	2.8408	2.6661	2.5121
4	0.2396	0.2516	0.2634	0.2749	0.2861	4.1736	3.9738	3.7966	3.6380	3.4950
5	0.1480	0.1553	0.1623	0.1692	0.1758	6.7555	6.4402	6.1610	5.9115	5.6867
6	0.1112	0.1164	0.1214	0.1263	0.1311	8.9921	8.5902	8.2342	7.9159	7.6292
7	0.0993	0.1064	0.1135	0.1205	0.1275	10.072	9.3989	8.8125	8.2983	7.8440
8	0.0932	0.0973	0.1013	0.1052	0.1089	10.734	10.276	9.8708	9.5077	9.1803
9	0.0844	0.0881	0.0915	0.0949	0.0981	11.843	11.357	10.925	10.538	10.190
10	0.0570	0.0608	0.0645	0.0681	0.0717	17.537	16.451	15.507	14.679	13.947

Cumulative mass percentages obtained via eigenvalue analyses for six-story is given in Table 6.

**Table 6. Cumulative mass percentages for 6-story (%)**

Mode	Cumulative Mass Ratios (%)									
	Ux					Uy				
	Model 1	Model 2	Model 3	Model 4	Model 5	Model 1	Model 2	Model 3	Model 4	Model 5
1	0.00	0.00	0.00	0.00	0.00	86.33	86.27	86.21	86.15	86.09
2	0.00	0.00	0.00	0.00	0.00	86.33	86.27	86.21	86.15	86.09
3	83.11	82.94	82.77	82.59	82.42	86.33	86.27	86.21	86.15	86.09
4	83.11	82.94	82.77	82.59	82.42	95.49	95.44	95.38	95.33	95.28
5	83.11	82.94	82.77	82.59	82.42	98.36	98.33	98.30	98.27	98.24
6	83.11	82.94	82.77	82.59	82.42	99.49	99.48	99.46	99.45	99.44
7	93.18	93.01	92.84	92.69	92.54	99.49	99.48	99.46	99.45	99.44
8	93.18	93.01	92.84	92.69	92.54	99.91	99.90	99.90	99.90	99.89
9	93.18	93.01	92.84	92.69	92.54	100.00	100.00	100.00	100.00	100.00
10	96.95	96.84	96.73	96.63	96.54	100.00	100.00	100.00	100.00	100.00

Table 7 shows the comparison of all the values obtained in X direction as a result of structural calculations for six-story.

**Table 7. The results regarding different structural models for 6-story**

Model	Base						
	Shear (kN)	K_elas	K-eff	dy	DL	SD	NC
1	9973.31	45173.69	42057.11	0.2371	0.0244309	0.0313408	0.0543339
2	9927.44	42495.9	39590.28	0.2508	0.028191	0.0361643	0.0626961
3	9785.38	40077.23	37677.5	0.2597	0.0319625	0.0410026	0.071084
4	9642.14	37893.41	35832.92	0.2691	0.036059	0.0462577	0.0801945
5	9487.23	35917.72	34121.58	0.278	0.0404328	0.0518685	0.0899217

The comparison of pushover curves for structure models with different footprints in terms of six-story structure is given in Figure 8.

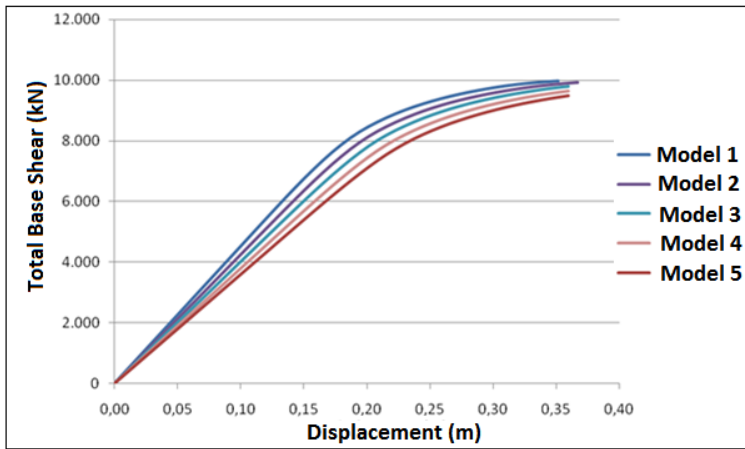


Fig 8. The comparison of pushover curves for 6-story

The comparison of values for period and frequency obtained via eigenvalue analysis in terms of seven-story steel structure is given in Table 8.

Table 8. The comparison of period and frequency for different footprints of 7-story

Mode	Period (sec)					Frequency (Hertz)				
	Model 1	Model 2	Model 3	Model 4	Model 5	Model 1	Model 2	Model 3	Model 4	Model 5
1	0.8218	0.8636	0.9045	0.9446	0.9840	1.2169	1.1579	1.1055	1.0586	1.0163
2	0.4431	0.4742	0.5052	0.5359	0.5665	2.2567	2.1086	1.9794	1.8659	1.7653
3	0.3583	0.3853	0.4124	0.4394	0.4664	2.7907	2.5953	2.4250	2.2757	2.1439
4	0.2767	0.2907	0.3042	0.3175	0.3306	3.6135	3.4405	3.2869	3.1493	3.0251
5	0.1694	0.1777	0.1859	0.1938	0.2016	5.9042	5.6259	5.3793	5.1588	4.9601
6	0.1254	0.1552	0.1371	0.1428	0.1842	7.9773	6.4442	7.2918	7.0037	5.4280
7	0.1168	0.1313	0.1337	0.1421	0.1505	8.5601	7.6139	7.4776	7.0352	6.6442
8	0.1027	0.1253	0.1119	0.1163	0.1483	9.7395	7.9815	8.9345	8.5962	6.7441
9	0.0902	0.1074	0.0980	0.1017	0.1206	11.087	9.3127	10.205	9.8347	8.2913
10	0.0838	0.0942	0.0908	0.0941	0.1053	11.935	10.620	11.013	10.624	9.5003

Cumulative mass percentages obtained via eigenvalue analyses for seven-story is given in Table 9.

**Table 9. Cumulative mass percentages for 7-story (%)**

Mode	Cumulative Mass (%)									
	Ux					Uy				
	Model 1	Model 2	Model 3	Model 4	Model 5	Model 1	Model 2	Model 3	Model 4	Model 5
1	0.00	0.00	0.00	0.00	0.00	85.59	85.55	85.50	85.45	85.39
2	0.00	0.00	0.00	0.00	0.00	85.59	85.55	85.50	85.45	85.39
3	82.62	82.49	82.35	82.21	82.07	85.59	85.55	85.50	85.45	85.39
4	82.62	82.49	82.35	82.21	82.07	94.84	94.79	94.73	94.68	94.64
5	82.62	82.49	82.35	82.21	82.07	97.85	97.81	97.78	97.74	97.71
6	82.62	82.49	82.35	82.21	82.07	99.14	97.81	99.10	99.08	97.71
7	92.60	82.49	92.27	92.13	91.99	99.14	99.12	99.10	99.08	97.71
8	92.60	92.43	92.27	92.13	91.99	99.72	99.12	99.70	99.70	99.06
9	92.60	92.43	92.27	92.13	91.99	99.95	99.71	99.94	99.94	99.69
10	92.60	92.43	92.27	92.13	91.99	100.00	99.95	100.00	100.00	99.94

Table 10 shows the comparison of all the values obtained in X direction as a result of structural calculations for seven-storey.

**Table 10. The results regarding different models for 7-story**

Model	Base Shear (kN)	K_elas	K-eff	dy	DL	SD	NC
1	9804.68	38497.59	36142.38	0.2713	0.033095	0.042455	0.073602
2	9752.97	36215.03	33998.07	0.2869	0.038224	0.049035	0.085009
3	9650.17	34138.44	32132.03	0.3003	0.043647	0.055992	0.09707
4	9507.19	32254.17	30578.88	0.3109	0.049216	0.063136	0.109455
5	9350.52	30543.45	29085.36	0.3215	0.055255	0.070883	0.122886

The comparison of pushover curves for structure models with different footprints in terms of seven-story structure is given in Figure 9.

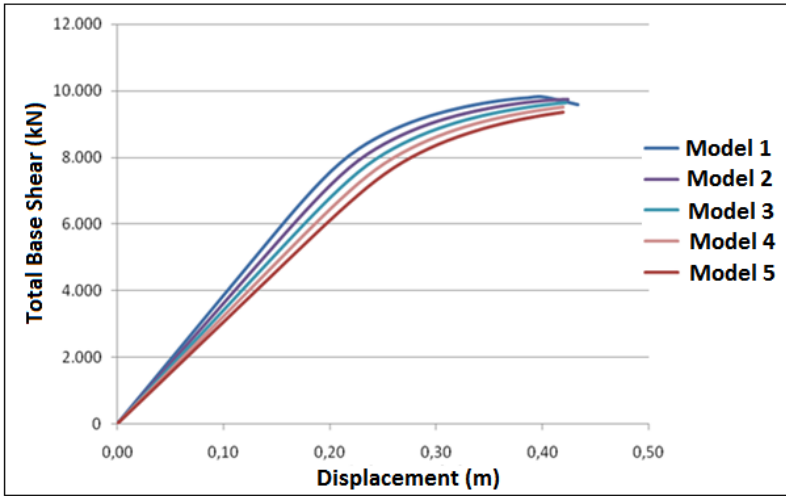


Fig 9. The comparison of pushover curves for 7-storey having different footprints

Additional comparisons for each steel structure model with same footprints but different number of floors were performed separately. The comparison of pushover curves for the changing numbers of floors in terms of Model 1 is given in Figure 10.

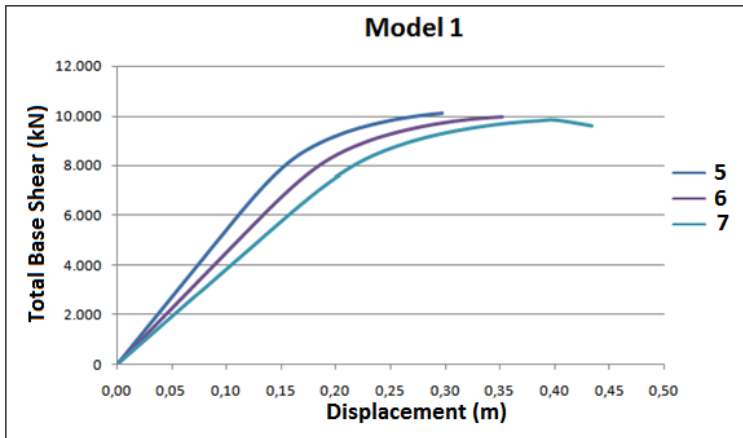


Fig 10. The comparison of pushover curves for Model 1 having different numbers of floors but same footprints.

The change of obtained values in terms of number of floors is given in Table 11.

Table 11a. The comparison of result values for structure models having different footprints in terms of change in number of floors

Model	Base Shear (kN)			K <sub>elas</sub>		
	5 Story	6 Story	7 Story	5 Story	6 Story	7 Story
1	10129.8	9973.3	9804.6	54439.4	45173.6	38497.5
2	10036.2	9927.4	9752.9	51245.3	42495.9	36215.0
3	9915.6	9785.3	9650.1	48377.9	40077.2	34138.4
4	9774.1	9642.1	9507.1	45799.5	37893.4	32254.1
5	9617.9	9487.2	9350.5	43473.3	35917.7	30543.4

Table 11b. The comparison of result values for structure models having different footprints in terms of change in number of floors

Model	K <sub>eff</sub>			dy		
	5 Story	6 Story	7 Story	5 Story	6 Story	7 Story
1	50487.6	42057.1	36142.3	0.200	0.237	0.271
2	47776.4	39590.2	33998.0	0.210	0.250	0.286
3	45351.8	37677.5	32132.0	0.218	0.259	0.300
4	43185.7	35832.9	30578.8	0.226	0.269	0.310
5	41195.6	34121.5	29085.3	0.233	0.278	0.321

The whole comparison of pushover curves for Model 2, Model 3, Model 4 and Model 5 having different numbers of floors but same footprints is given in Figure 11.

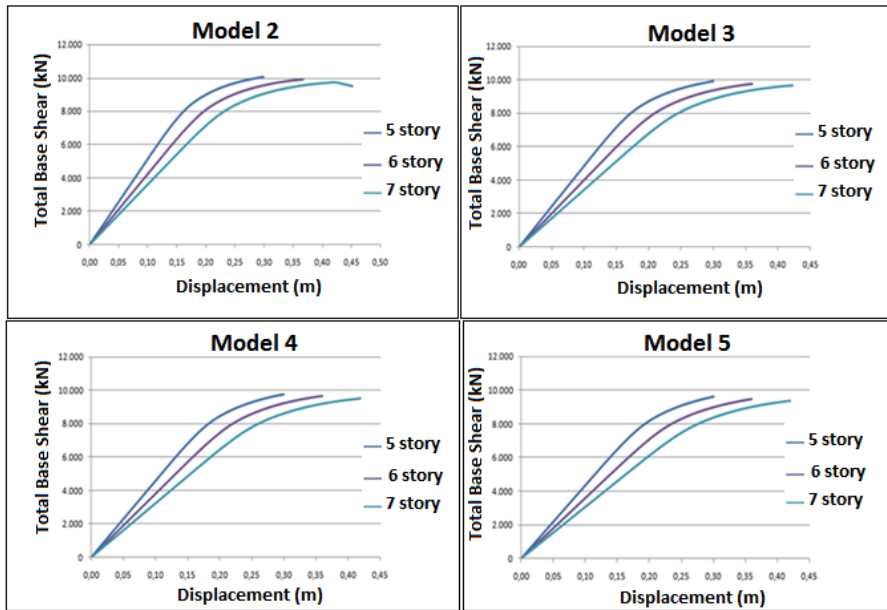


Fig 11. The comparison of pushover curves models having different numbers of floors but same footprints

The change of target displacement values as performance criteria in terms of footprints and number of floors obtained via software is given in Table 12.

Table 12. The comparison of target displacement values

Model	DL			SD			NC		
	5 Story	6 Story	7 Story	5 Story	6 Story	7 Story	5 Story	6 Story	7 Story
1	0.017	0.0244	0.0330	0.0218	0.0313	0.0424	0.0378	0.0543	0.0736
2	0.019	0.0281	0.0382	0.0250	0.0361	0.0490	0.0434	0.0627	0.0850
3	0.022	0.0319	0.0435	0.0284	0.0410	0.0559	0.0493	0.0710	0.0970
4	0.025	0.0360	0.0492	0.0320	0.0462	0.0631	0.0555	0.0801	0.1094
5	0.027	0.0404	0.0552	0.0358	0.05187	0.07088	0.06222	0.08992	0.12289

The comparison of period values obtained for all the number of floors and structure models having different footprints is given in Table 13.

**Table 13. The comparison of period values for all the structure models**

Mode	Period (sec)														
	Model 1			Model 2			Model 3			Model 4			Model 5		
	5	6	7	5	6	7	5	6	7	5	6	7	5	6	7
1	0.595	0.708	0.821	0.626	0.744	0.863	0.656	0.780	0.904	0.685	0.814	0.944	0.714	0.848	0.984
2	0.314	0.378	0.443	0.337	0.405	0.474	0.359	0.432	0.505	0.380	0.458	0.535	0.402	0.484	0.566
3	0.253	0.305	0.358	0.272	0.328	0.385	0.291	0.352	0.412	0.310	0.375	0.439	0.329	0.398	0.466
4	0.202	0.239	0.276	0.213	0.251	0.290	0.222	0.263	0.304	0.232	0.274	0.317	0.242	0.286	0.330
5	0.127	0.148	0.169	0.133	0.155	0.177	0.139	0.162	0.185	0.145	0.169	0.193	0.150	0.175	0.201
6	0.102	0.111	0.125	0.109	0.116	0.155	0.116	0.121	0.137	0.122	0.126	0.142	0.129	0.131	0.184
7	0.098	0.099	0.116	0.102	0.106	0.131	0.106	0.113	0.133	0.111	0.120	0.142	0.115	0.127	0.150
8	0.085	0.093	0.102	0.089	0.097	0.125	0.093	0.101	0.111	0.099	0.105	0.116	0.104	0.108	0.148
9	0.081	0.084	0.090	0.087	0.088	0.107	0.092	0.091	0.098	0.096	0.094	0.101	0.099	0.098	0.120
10	0.047	0.057	0.083	0.049	0.060	0.094	0.052	0.064	0.090	0.055	0.068	0.094	0.058	0.071	0.105

The comparison in percentage of cumulative participation mass ratios in X direction obtained via eigenvalue analyses and values considered within the scope of the study is given in Table 14. The comparison in percentage of cumulative participation mass ratios in Y direction is given in Table 15.

**Table 14. The comparison of cumulative participation mass ratios in X direction**

Mode	Cumulative Mass (%) ( $U_x$ )														
	Model 1			Model 2			Model 3			Model 4			Model 5		
	5	6	7	5	6	7	5	6	7	5	6	7	5	6	7
1	0.00	0.00	0.00	0.00	0.00	0.00	0.00	0.00	0.00	0.00	0.00	0.00	0.00	0.00	0.00
2	0.00	0.00	0.00	0.00	0.00	0.00	0.00	0.00	0.00	0.00	0.00	0.00	0.00	0.00	0.00
3	83.8	83.1	82.6	83.5	82.9	82.4	83.3	82.7	82.3	83.1	82.5	82.2	82.9	82.4	82.0
4	83.8	83.1	82.6	83.5	82.9	82.4	83.3	82.7	82.3	83.1	82.5	82.2	82.9	82.4	82.0
5	83.8	83.1	82.6	83.5	82.9	82.4	83.3	82.7	82.3	83.1	82.5	82.2	82.9	82.4	82.0
6	83.8	83.1	82.6	83.5	82.9	82.4	83.3	82.7	82.3	83.1	82.5	82.2	82.9	82.4	82.0
7	83.8	93.1	92.6	83.5	93.0	82.4	83.3	92.8	92.2	83.1	92.6	92.1	82.9	92.5	91.9
8	83.8	93.1	92.6	83.5	93.0	92.4	93.6	92.8	92.2	93.5	92.6	92.1	93.3	92.5	91.9
9	94.0	93.1	92.6	93.8	93.0	92.4	93.6	92.8	92.2	93.5	92.6	92.1	93.3	92.5	91.9
10	97.8	96.9	92.6	97.7	96.8	92.4	97.6	96.7	92.2	97.5	96.6	92.1	97.4	96.5	91.9

**Table 15. The comparison of cumulative participation mass ratios in Y direction**

Mode	Cumulative Mass (%) ( $U_y$ )														
	Model 1			Model 2			Model 3			Model 4			Model 5		
	5	6	7	5	6	7	5	6	7	5	6	7	5	6	7
1	87.3	86.3	85.5	87.2	86.2	85.5	87.1	86.2	85.5	87.1	86.1	85.4	87.0	86.0	85.3
2	87.3	86.3	85.5	87.2	86.2	85.5	87.1	86.2	85.5	87.1	86.1	85.4	87.0	86.0	85.3
3	87.3	86.3	85.5	87.2	86.2	85.5	87.1	86.2	85.5	87.1	86.1	85.4	87.0	86.0	85.3
4	96.3	95.4	94.8	96.2	95.4	94.7	96.2	95.3	94.7	96.1	95.3	94.6	96.1	95.2	94.6
5	98.9	98.3	97.8	98.9	98.3	97.8	98.9	98.3	97.7	98.8	98.2	97.7	98.8	98.2	97.7
6	98.9	99.4	99.1	98.9	99.4	97.8	98.9	99.4	99.1	98.8	99.4	99.0	98.8	99.4	97.7
7	99.8	99.4	99.1	99.8	99.4	99.1	99.8	99.4	99.1	99.7	99.4	99.0	99.7	99.4	97.7
8	100	99.9	99.7	100.	99.9	99.1	99.8	99.9	99.7	99.7	99.9	99.7	99.7	99.8	99.0
9	100	100	99.9	100	100	99.7	100	100	99.9	100	100	99.9	100	100	99.6
10	100	100	100	100	100	99.9	100	100	100	100	100	100	100	100	99.9

When making comparisons, in the first stage, footprints were kept constant. Table 16 shows the percentages of changes for different parameters resulting from changing of footprints. When calculating the percentage of changes, Model 1 having the smallest footprint was selected as a reference. Percentage of changes of each model according to Model 1 was calculated separately. The maximum period value was considered as the period value. Since negligible differences among the percentages of changes in terms of the values for non-collapsing (NC), severe damage (SD) and damage limitation (DL), the percentages of change in these three conditions were calculated only for DL. Comparison of all results obtained via pushover analyses is shown in Table 16.

Table 16. Comparison of all the result values for different footprints (%)

Parameter	Story Number	Model 1	Model 2	Model 3	Model 4	Model 5
Period (sec)	5	0	5.14	10.16	15.07	19.88
	6	0	5.12	10.17	15.01	19.81
	7	0	5.09	10.07	14.95	19.74
Total Base Shear (kN)	5	0	0.92	2.11	3.51	5.05
	6	0	0.46	1.88	3.32	4.87
	7	0	0.42	1.58	3.03	4.63
K_Elas	5	0	5.87	11.13	15.87	20.14
	6	0	5.93	11.28	16.12	20.49
	7	0	5.93	11.32	16.22	20.57
K_eff	5	0	5.37	10.17	14.46	18.40
	6	0	5.87	10.41	14.80	18.87
	7	0	5.93	11.10	15.39	19.53
dy (m)	5	0	4.74	8.97	12.81	16.40
	6	0	5.78	9.53	13.50	17.25
	7	0	5.85	10.68	14.60	18.50
DL - SD - NC	5	0	14.82	30.47	47.00	64.53
	6	0	15.40	30.82	47.61	65.49
	7	0	15.50	31.88	48.62	66.97

In the second stage of comparisons, the change in the number of floors was examined. Percentages of changes obtained as a result of differentiation of the number of floors are given in Table 17.

In the study, economic differences were also revealed by considering footprints and the number of floors. For this reason, the unit price determined for finding the approximate costs of structures in Turkey were used. According to “The Bulletin on the Approximate Unit Costs of Structures for 2019 to be used in the Account of Architectural and Engineering Fees” which was published in the Official Gazette by the Ministry of Environment and Urbanization [28], cost of structures in IV. Class Structures – Group A is 1270 TL/m<sup>2</sup>. According to the currency values provided by the Turkish Central Bank, this value is approximately 225\$/m<sup>2</sup> today. Structural damage-led financial losses were estimated by multiplying total damaged constructional area and unit cost. Cost calculations for different structure models and number of floors are given in Table 18.

Table 17. Comparison of result values in terms of change in the number of floors (%)

Parameter	Model	5 Story	6 Story	7 Story
Period (sec)	Model 1	0	18.95	37.96
	Model 2	0	18.92	37.89
	Model 3	0	18.90	37.84
	Model 4	0	18.89	37.82
	Model 5	0	18.88	37.80
Total Base Shear (kN)	Model 1	0	1.54	3.21
	Model 2	0	1.49	2.83
	Model 3	0	1.37	2.78
	Model 4	0	1.35	2.73
	Model 5	0	1.35	2.67
K_Elas	Model 1	0	17.02	29.28
	Model 2	0	17.07	29.33
	Model 3	0	17.16	29.43
	Model 4	0	17.26	29.57
	Model 5	0	17.38	29.74
K_eff	Model 1	0	16.69	28.41
	Model 2	0	17.13	28.84
	Model 3	0	17.43	29.15
	Model 4	0	17.52	29.20
	Model 5	0	17.67	29.40
dy (m)	Model 1	0	18.20	35.24
	Model 2	0	18.37	36.55
	Model 3	0	18.80	37.37
	Model 4	0	18.91	37.38
	Model 5	0	19.19	37.68
DL - SD - NC	Model 1	0	43.62	94.53
	Model 2	0	43.92	95.80
	Model 3	0	44.02	96.71
	Model 4	0	44.24	96.88
	Model 5	0	44.49	97.46

Table 18. Cost values for the selected steel structure having different footprints and number of floors

Model	Total Construction Area (m <sup>2</sup> )			Unit Cost (\$/m <sup>2</sup> )	Total Cost (\$)		
	5 Storey	6 Storey	7 Storey		5 Storey	6 Storey	7 Storey
Model 1	2000	2400	2800	225	450000	540000	630000
Model 2	2531.25	3037.5	3543.75	225	569531.25	683437.5	797343.75
Model 3	3125	3750	4375	225	703125	843750	984375
Model 4	3781.25	4537.5	5293.75	225	850781.25	1020937.5	1191093.8
Model 5	4500	5400	6300	225	1012500	1215000	1417500

For cost comparisons between the models, the number of floors and total constructional area were selected as two different variables. When comparing the number of floors, the five-storey steel structure was chosen as the Model 1 reference structure with the lowest total construction area for the total construction area. The cost change rates calculated according to the selected reference structures are given in Table 19.

Table 19. Percentage of change of number of floors and footprints on cost (%)

	Model	Footprint Area			Storey Number		
		5 Story	6 Story	7 Story	5 Story	6 Story	7 Story
Total Cost Change (%)	Model 1	0	0	0	0	20	40
	Model 2	26.55	26.55	26.55	0	20	40
	Model 3	56.25	56.25	56.25	0	20	40
	Model 4	89.05	89.05	89.05	0	20	40
	Model 5	125	125	125	0	20	40

The mutual interaction of two different variables was taken into consideration in the study. As the structural footprint area decreased, the structure became more rigid. Consequently, the period value increased as the base area increased and seismic capacity decreased. As the number of floors increases, the period value increases, the stiffness value and seismic capacity decrease. The increase in the floor area and number of floors caused the structure to be less rigid. The total construction area increased since the increase of these two values, the approximate cost of the building also increased.

Cost comparisons were made only according to the total constructional area. It is obvious that the difference will be greater with the addition of other costs other than electricity, machinery and construction.

## 5. Conclusions

In structural analysis, the structural dimensions and the number of floors ensue as important factors. The structural dimensions and the total number of floors in the structure can take different values due to different reasons. Within the scope of this study, considering the number of floors and changes in structural dimensions, two different structural analyses were performed. The comparison of the values obtained as a result of

the analyses is given in the study. In this study, level of change in the structure cost calculations of these two variables was also calculated.

In the study, it was seen that as the footprints and numbers of floors of structure increased, period values increased, too. Period values increased approximately equal in terms of change of footprints for all different numbers of floors. This also applies to the number of floors. The period value increased by 5% for each footprint change, while the period value increased by 19% for each increase of the number of floors. As the footprints and number of floors decreased, the cumulative mass participation percentages obtained in both X and Y directions increased.

Among the results of the analysis used in the study, the smallest percentages of change were obtained at the base shear force. As the number of floors and footprints of the structure increased, the base shear forces decreased. One of the parameters obtained as a result of the analysis is the stiffness values. Both the elastic and effective stiffness values decreased naturally with the increase in the number of floors and the footprints. The percentages of stiffness change in increase of both number of floors and footprints were equal.

As a result of the analyses, the greatest percentages of change were observed at the target displacements predicted for the structure. Target displacement values for the settlement at the moment of flow (dy), non-collapsing (NC), severe damage (SD) and damage limitation (DL) increased depending on the footprints and number of floors. The increase in target displacements in terms of performance criteria reveals the direct relationship between the damage occurring in the earthquake and the number of floors.

Only construction costs were considered in the cost calculations. As the footprints and the number of floors increased, the building cost also increased. Cost increased by 20% for each increase in the number of the floors. As the footprints increased, the cost change occurred as much as the percentage of footprints changes. However, in the study, while the cost calculations were made, no cost calculations were made for electricity, machinery and similar works.

The importance of structural dimensions and number of floors were mentioned within the scope of the study. Unnecessary increase in dimensions and number of floors adversely affects both cost and structural analysis.

In addition to these parameters used in this study, models in which plan shape, element size and layout are taken into consideration can be developed. The height of the floors, several number of floors, the local soil conditions, the importance of the building and the seismicity conditions of the region where the building will be built will also change the structural analysis and cost values. The increase in the circumference in the buildings increases the facade area in the models of the same height, which also affects the facade insulation and exterior wall costs, which are the secondary construction costs. Construction cost has been calculated approximately. Using the unit prices for detailed cost analysis results will make the results more valuable.

## **References**

- [1] Ferraioli, M. (2016). Dynamic increase factor for pushdown analysis of seismically designed steel moment-resisting frames. *International Journal of Steel Structures*, 16(3), 857-875. <https://doi.org/10.1007/s13296-015-0056-6>

- [2] Işık, E. 2016. Consistency of the rapid assessment method for reinforced concrete buildings. *Earthquakes and Structures*, 11(5), 873-885. <https://doi.org/10.12989/eas.2016.11.5.873>
- [3] Yakut, A. 2004. Preliminary seismic performance assessment procedure for existing RC buildings. *Engineering Structures*, 26(10), 1447-1461. <https://doi.org/10.1016/j.engstruct.2004.05.011>
- [4] Šipoš, T. K., Hadzima-Nyarko, M. 2017. Rapid seismic risk assessment. *International Journal of Disaster Risk Reduction*, 24, 348-360. <https://doi.org/10.1016/j.ijdrr.2017.06.025>
- [5] Hadzima-Nyarko, M., KalmanSipos, T. 2017. Insights from existing earthquake loss assessment research in Croatia. *Earthquakes and Structures*, 13(4), 365-375.
- [6] Sucuoğlu, H. 2007. A screening procedure for seismic risk assessment in urban building stocks. Sixth National Conference on Earthquake Engineering, Istanbul, Turkey. <https://doi.org/10.1193/1.2720931>
- [7] Şengezer, B.S. 1999. The damage distribution during March 13, 1992 Erzincan earthquake. YT U. Press Release Center, 13.
- [8] Özdemir, M., Işık, E., Ülker, M. 2016. Performance evaluation of reinforced concrete buildings with different story numbers. *BEU Journal of Science*, 5(2), 183-190.
- [9] Korkmaz, K.A., Düzgün, M. 2006. Statik artımsal itme analizinde kullanılan yük dağılımlarının değerlendirilmesi. *Teknik Dergi*, 17(82), 3873-3878.
- [10] Sezer, F., Gençoğlu, M., Celep, Z. 2007. Betonarme binaların deprem güvenliğinin değerlendirilmesinde deprem yönetmeliği 2007 de kurallarına örnekle kıyaslamalı bir bakış. *Altıncı Ulusal Deprem Mühendisliği Konferansı, İstanbul, Turkey*.
- [11] İlerisoy, Z.Y., Tuna, M.E. 2011. Effects of plane dimensions and number of storeys on the cost of rectangular-plane buildings constructed with tunnel Form Megaron, 13(4), 559-568.
- [12] Safiki, A., Solikin, M., Sahid, M.N. 2015. Cost implications of building design plans: a literature review analysis, *The 2nd International Conference on Engineering Technology and Industrial Application (ICETEA-2015)*, Indonesia.
- [13] Saidu, İ., Alumbugu, P.O., Abdulazeez, A., Ola-Awo, W.A., 2015. Assessment of the effect of plan shapes on cost of institutional buildings in Nigeria, *International Refereed Journal of Engineering and Science (IRJES)*, 4(3), 39-50.
- [14] Ferry, D.J., Brandon P.S. 2007. *Cost planning of building*, 9th Edition, Oxford: Wiley-Blackwell.
- [15] Tregenza P. 1972. Association between building height and cost. *Architects Journal Information Library*, 11,1031-1032.
- [16] Çıracı, M. 1996. Konutlarda maliyet tahmini için bir model, T.C. Başbakanlık Toplu Konut İdaresi Başkanlığı, Konut Araştırma Dizisi-6, Ankara.
- [17] Türkel, E.B., Ergen, E. 2016. "Tünel kalıp sistemi kullanılan betonarme yüksek yapılarda, yükseklik ve kat alanı ile maliyet arasındaki ilişki". *Pamukkale Üniversitesi Mühendislik Bilimleri Dergisi*, 22(6), 418-426.
- [18] Antoniou, S., Pinho, R. 2003. *Seismostruct - Seismic Analysis program by Seismosoft*. Technical manual and user manual.
- [19] Kutanis, M., Boru, E. O., Işık, E. 2017. Alternative instrumentation schemes for the structural identification of the reinforced concrete field test structure by ambient vibration measurements. *KSCCE Journal of Civil Engineering*, 21(5), 1793-1801. <https://doi.org/10.1007/s12205-016-0758-0>
- [20] SeismoStruct v6.5 2013. A computer program for static and dynamic nonlinear analysis of framed structures. Seismosoft.

- [21] Estêvão, J. M., Oliveira, C. S. 2015. A new analysis method for structural failure evaluation. *Engineering Failure Analysis*, 56, 573-584. <https://doi.org/10.1016/j.engfailanal.2014.08.009>
- [22] Ademovic, N., Hrasnica, M., Oliveira, D.V. 2013. Pushover analysis and failure pattern of a typical masonry residential building in Bosnia and Herzegovina. *Engineering Structures*, 50, 13-29. <https://doi.org/10.1016/j.engstruct.2012.11.031>
- [23] Chopra, A.K., Goel, R.K. 2002. A modal pushover analysis procedure for estimating seismic demands for buildings. *Earthquake Engineering & Structural Dynamics*, 31(3), 561-582. <https://doi.org/10.1002/eqe.144>
- [24] Inel, M., Meral, E. 2016. Seismic performance of RC buildings subjected to past earthquakes in Turkey. *Earthquakes and Structures*, 11(3), 483-503. <https://doi.org/10.12989/eas.2016.11.3.483>
- [25] Işık, E., Özdemir, M. 2017. Performance based assessment of steel frame structures by different material models. *International Journal of Steel Structures*, 17(3), 1021-1031. <https://doi.org/10.1007/s13296-017-9013-x>
- [26] Menegotto, M. 1973. Method of analysis for cyclically loaded RC plane frames including changes in geometry and non-elastic behavior of elements under combined normal force and bending. In *Proc. of IABSE symposium on resistance and ultimate deformability of structures acted on by well-defined repeated loads* (pp. 15-22).
- [27] Bosco, M., Ferrara, E., Ghersi, A., Marino, E. M., Rossi, P. P. 2016. Improvement of the model proposed by Menegotto and Pinto for steel. *Engineering Structures*, 124, 442-456. <https://doi.org/10.1016/j.engstruct.2016.06.037>
- [28] <http://www.resmigazete.gov.tr/eskiler/2019/03/20190316-12.htm>, (Last accessed August 2019)



Research Article

## Experimental low cycle fatigue testing of circular bars with radial through-holes subjected to tension-compression loading

Stephen John Hardy<sup>\*,1,a</sup>, Harvir Satsavia<sup>2,b</sup>

<sup>1</sup> College of Engineering, Swansea University, Bay Campus, Swansea, UK

<sup>2</sup> Redstone Rail, Royal Leamington Spa, UK

### Article Info

#### Article history:

Received 20 Aug 2020

Revised 6 Nov 2020

Accepted 23 Oct 2020

#### Keywords:

Low cycle fatigue;

Experimental work;

Circular bars;

Radial holes;

Tension-compression

### Abstract

The aim of this experimental testing was to assess how the introduction of features such as holes into a component under severe variable loading can result in low cycle fatigue (LCF) behaviour. Circular bars with a range of radial through-hole diameters were subjected to severe cyclic axial loading until failure occurred. Relationships between the hole diameter, the loading and the number of cycles to failure are shown graphically. Results are also presented using the elastic stress concentration factor ( $K_t$ ) as the independent variable. Although not strictly applicable in situations where significant plasticity occurs, such as in LCF behaviour, further planned studies might show how  $K_t$  can be used as a guide for similar components and loadings with other types of notches. Low cycle fatigue lives in the range 161 to 5280 cycles, for the largest hole/highest load and the smallest hole/lowest load combinations respectively, were observed. The lower value is approaching the ultra-low cycle fatigue (ULCF) regime. In the worst case, the introduction of a radial hole resulted in an average fatigue life reduction factor of more than two orders of magnitude.

© 2021 MIM Research Group. All rights reserved.

## 1. Introduction

Geometric discontinuities such as shoulders, holes, grooves, threads, etc. induce local high (above average) stresses. These stress raisers are generally termed 'notches'. In a variable loading regime, Fatigue Crack Initiation (FCI) and subsequent propagation can occur at the roots of these notches. Since most engineering components contain notches of some form or another, design assessment methods for these components must take account of any such stress raisers. Many instances of mechanical failure can be attributed to inadequate design in the region of a discontinuity. It has been estimated that up to 90% of all structural failures have fatigue as the root cause of failure [1]. An early example is the fatigue failure of railway axles, which became a problem in the middle of the 19th century and drew attention to the effects of cyclic loading. It was the first instance in which components had been exposed to millions of cycles at differing stress levels thus causing fatigue defects.

Although a component may satisfy static design considerations, High Cycle Fatigue (HCF) can occur under low to moderate variable loading. This can take many cycles, typically  $10^6$  or more. However, under moderate to high variable loading, notches are likely sites for plastic deformation and fatigue failure can occur in significantly fewer cycles e.g.  $10^4$  or less. This is referred to as Low Cycle Fatigue (LCF) and the LCF behaviour of notched components is a complex problem, which has been modelled extensively and remains of great interest. From an analytical viewpoint, LCF life predictions are based on a local strain

\*Corresponding author: [s.j.hardy@swansea.ac.uk](mailto:s.j.hardy@swansea.ac.uk)

<sup>a</sup> orcid.org/0000-0003-3899-9174; <sup>b</sup> orcid.org/0000-0002-0615-9069

DOI: <http://dx.doi.org/10.17515/resm2020.210me0820>

Res. Eng. Struct. Mat. Vol. 7 Iss. 1 (2021) 87-95

approach, e.g. Dowling et al [2] and Topper and Gowda [3], using experimental fatigue data from simple uniaxial un-notched specimen tests. A useful review of life prediction techniques is provided by Agrawal et al [4]. They consider smooth and notched specimens at both room and elevated temperature. Although the authors focus on predictive techniques, they acknowledge the importance of experimental testing to support these predictive techniques. Although powerful computation methods, such as finite element analysis, can be used to predict LCF life, there is still a considered need for experimental data to support the predictions.

In this paper, the experimental LCF testing of circular bars with radial through-holes subjected to cyclic axial loading is described and the effects of hole size and loading level are quantified and compared with un-notched specimens. Gowhari-Anaraki et al [5] have previously described experimental LCF testing of notched circular shafts in bending, where the effect of external notches is quantified and the fatigue lives are compared with estimates using the simple notch stress-strain conversion rules (Neuber, linear). Recently, Dundulis et al [6] have carried out low cycle fatigue testing on plain circular bars made from P91 steel subjected to strain controlled high temperature axial loading. Unlike the work reported here, where specific stress concentration features generate high local levels of total strain range, low cycle fatigue is induced by the high level of bulk total strain range (up to 1%) being applied. The authors demonstrate good comparison between the experimental results and those estimated using the Manson-Coffin-Basquin equation. Recently, Beesley et al [7] have proposed an analytical method for predicting shakedown, ratchetting and crack initiation loads of notched components using a circular bar with scalloped edges containing a chamfered through-hole. They plan to carry out experimental testing to determine the LCF life of these components. As yet, this work has not been reported but will be of significant interest to the authors of this paper.

## 2. Experimental Components and Testing Method

Low cycle fatigue testing was undertaken using a Zwick HA 250kN hydraulic fatigue testing machine, as shown in Figure 1. Tensile specimens with a gauge diameter of 12 mm were manufactured from M20, EN8 steel screwed bar. Typical material properties for tempered EN8 are shown in Table 1.

Table 1 Typical tempered EN8 material properties

Young's Modulus (GPa)	Poisson's Ratio	Yield Stress (MPa)	UTS (MPa)	%age Elongation	0.2% Proof Stress (MPa)	Brinell Hardness	KCV Impact Toughness (J)
190	0.3	465	700-850	16	450	201-255	28

Four types of specimen were tested:

1. A plain fatigue specimen, machined from the screwed bar, nominal diameter = 12 mm (see Fig. 2);
2. As specimen 1 with a central 2.4 mm diameter radial through-hole;
3. As specimen 1 with a central 4.2 mm diameter radial through-hole;
4. As specimen 1 with a central 6.0 mm diameter radial through-hole.

A tensile test was carried out on each type of specimen in order to estimate the load at which plastic deformation began from which an approximate 'yield load' was determined.

For the fatigue testing, fully reversed sine wave loading at 1 Hz was carried out at 80%, 75%, 70%, 65% and 60% of this 'yield load'.



Fig. 1 Zwick HA 250kN hydraulic fatigue testing machine



Fig. 2 Fatigue specimens and original screwed bar

### 3. Experimental Results

Initial tensile testing of specimen types 1, 2, 3 and 4 produced 'yield loads' of 53, 40, 32 and 22 kN respectively. These values were then used for the fatigue tests.

The results of the fatigue tests are shown in Table 2. For the plain specimen, the fatigue lives for 65% and 60% of the 'yield load' are in the transition region between LCF and HCF, and these tests were not repeated. For all other tests, the fatigue lives are within the LCF region. The value in brackets after the average value is a measure of the repeatability and is obtained by the Equation 1:

$$\% \text{ discrepancy} = \frac{(\text{higher } N_f - \text{lower } N_f)}{\text{average } N_f} \times 100 \quad (1)$$

With a few notable exceptions, the test-to-test discrepancies are within reasonable bounds for experimental testing. The number of cycles to failure for the bar with the 6 mm diameter hole and a load of 80% of the 'yield load' is approaching a region referred to as Ultra-Low Cycle Fatigue (ULCF), which is often set at  $N_f < 100$  cycles [8].

Table 2 Fatigue Test Results

Percentage of yield load	Test Specimens							
	Plain Bar		2.4 mm diameter hole		4.2 mm diameter hole		6.0 mm diameter hole	
Number of cycles to failure ( $N_f$ )								
	Test 1	Test 2	Test 1	Test 2	Test 1	Test 2	Test 1	Test 2
80%	331	416	283	291	222	252	161	175
	Average = 373.5 (23%) (Load = 42.4 kN)		Average = 287 (3%) (Load = 32.0 kN)		Average = 237 (13%) (Load = 25.6 kN)		Average = 168 (8%) (Load = 17.6 kN)	
	Test 1	Test 2	Test 1	Test 2	Test 1	Test 2	Test 1	Test 2
75%	1041	949	466	754	330	215	244	224
	Average = 995 (9%) (Load = 39.75 kN)		Average = 610 (47%) (Load = 30.0 kN)		Average = 272.5 (42%) (Load = 24.0 kN)		Average = 234 (9%) (Load = 16.5 kN)	
	Test 1	Test 2	Test 1	Test 2	Test 1	Test 2	Test 1	Test 2
70%	5048	5028	1902	1453	361	305	240	335
	Average = 5038 (0.4%) (Load = 37.1 kN)		Average = 1677.5 (27%) (Load = 28.0 kN)		Average = 333 (17%) (Load = 22.4 kN)		Average = 287.5 (33%) (Load = 15.4 kN)	
	Test 1	Test 2	Test 1	Test 2	Test 1	Test 2	Test 1	Test 2
65%	22631	-	2748	2337	589	497	404	284
	Average = 22631 (-) (Load = 34.45 kN)		Average = 2542.5 (16%) (Load = 26.0 kN)		Average = 543 (17%) (Load = 20.8 kN)		Average = 344 (35%) (Load = 14.3 kN)	
	Test 1	Test 2	Test 1	Test 2	Test 1	Test 2	Test 1	Test 2
60%	57211	-	5280	3750	787	1136	648	404
	Average = 57211 (-) (Load = 31.8 kN)		Average = 4515 (34%) (Load = 24.0 kN)		Average = 961.5 (36%) (Load = 19.2 kN)		Average = 526 (46%) (Load = 13.2 kN)	
	Test 1	Test 2	Test 1	Test 2	Test 1	Test 2	Test 1	Test 2

The results are also presented in graphical form in Figures 3 and 4 for % 'yield load' against  $\log_{10} N_f$  and load against  $\log_{10} N_f$  respectively. From Figure 3:

- Trends of increasing  $N_f$  with reducing % 'yield load' are as expected;
- There is a small degree of overlap for the 75% 'yield load' results but they are within reasonable expectations of experimental discrepancy;
- Although in the transition region, the three highest  $N_f$  results for the plain specimen appear to follow the general trend;
- The results appear to converge as 'yield load' increases, including the results for the plain specimen;
- As expected, the specimen with the 6 mm hole has the lowest  $N_f$  values and the plain specimen has the highest  $N_f$  values. and from Figure 4:
- Again, the trends are clear but, in this case, the overlap for the 75% 'yield load' is not apparent here.

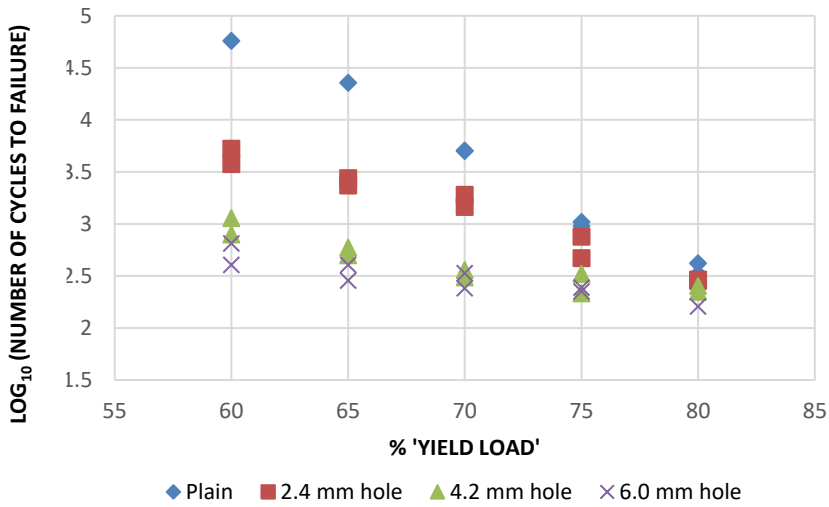


Fig. 3 The variation of Log<sub>10</sub> N<sub>f</sub> against % 'Yield Load'

The variation of log<sub>10</sub> N<sub>f</sub> with hole size is shown in Figure 5 for all tests and the range of loads considered. These results are also presented against elastic stress concentration factor, K<sub>t</sub>, in Figure 6. Figure 5 can be used to enable interpolation for hole sizes between those considered in the experiments. Although not strictly applicable in situations where significant plasticity occurs, such as in LCF behaviour, further planned studies might show how K<sub>t</sub> can be used as a 'guide' for similar components and loadings with other types of notches.

The variation of log<sub>10</sub> (N<sub>fu</sub>/N<sub>fn</sub>) with K<sub>t</sub>, where N<sub>fu</sub> is the average number of cycles to failure from Tests 1 and 2 for the un-notched (plain) specimen and N<sub>fn</sub> is the average number of cycles to failure from Tests 1 and 2 for the notched (holed) specimen at the same load, is shown in Figure 7. The results show a reduction factor in N<sub>f</sub> of between 1.3 and 12.7 for the 2.4 mm diameter hole, between 1.6 and 59.5 for the 4.2 mm diameter hole and between 2.2 and 108.8 for the 6.0 mm diameter hole.

Finally, Figures 8 and 9 are examples of failed specimens. In all cases, fatigue crack initiation starts at the inside surface of the hole followed by varying degrees of crack propagation (shiny, granular regions) until brittle fracture (dull regions with a fibrous appearance) occurs at the point where the remaining cross-section is unable to withstand the load.

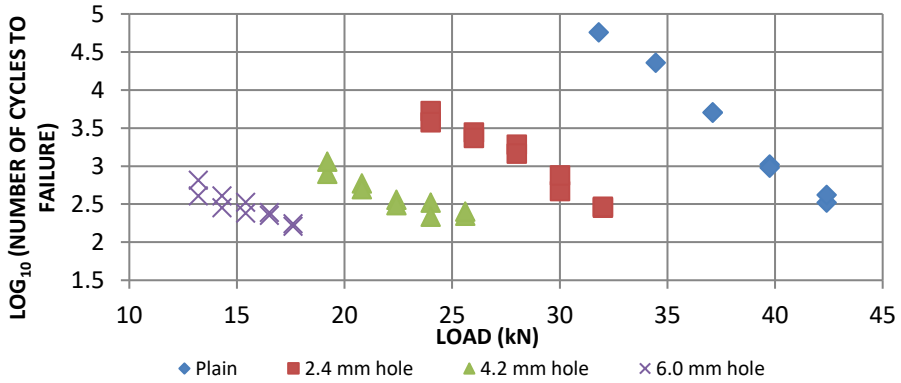


Fig. 4 The variation of  $\text{Log}_{10} N_f$  against Load

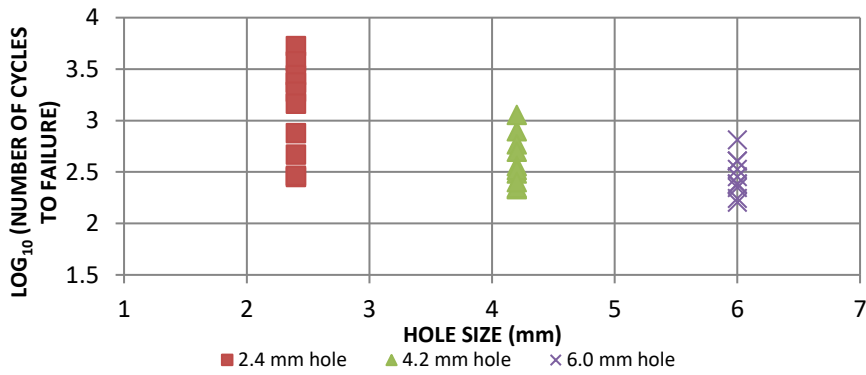


Fig. 5 The variation of  $\text{Log}_{10} N_f$  against Hole Size for the range of loads (increasing load  $\downarrow$ )

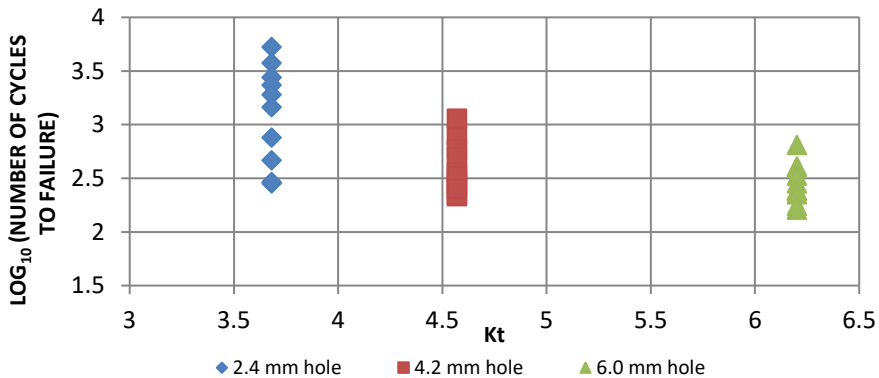


Fig. 6 The variation of  $\text{Log}_{10} N_f$  against  $K_t$  for the range of loads (increasing load  $\downarrow$ )

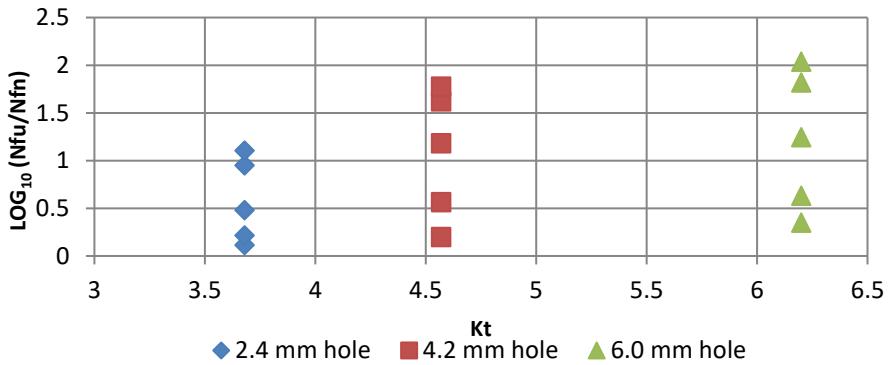


Fig. 7 The variation of  $\text{Log}_{10}(N_{fu}/N_m)$  against  $K_t$  (increasing load ↓)



Fig. 8 Examples of failed specimens for a load of 80% of the 'Yield Load'

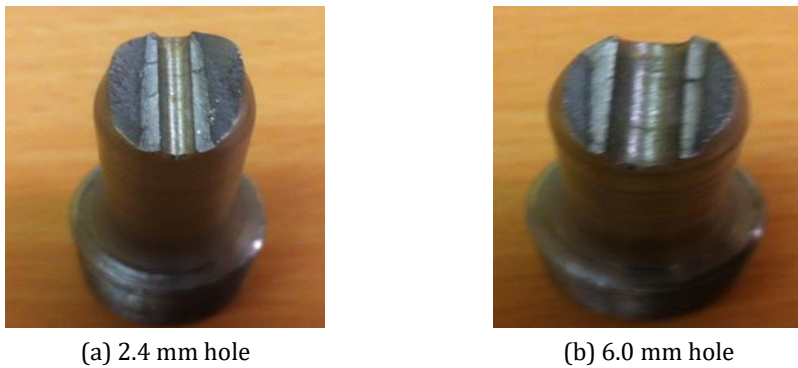


Fig. 9 Enlarged views of failed specimens for a load of 80% of the 'Yield Load'

#### 4. Discussion

With the availability of affordable high-power computers, access to finite element analysis to model highly complex problems such as fatigue and to generate very accurate predictions has revolutionised the design process. Nevertheless, there is a danger in relying totally on such predictive techniques. This is particularly true when modelling the elastic-plastic properties of materials in a variable/cyclic loading regime, such as in low

cycle fatigue. The need for physical evidence to support numerical predictions is, therefore, highly desirable (even essential).

Experimental testing can be very expensive, both in time and resources. This is particularly true for high cycle fatigue testing, where individual tests can run for several months. Low cycle fatigue tests, on the other hand, take far less time to complete and, for reasons explained above, provide valuable evidence to support the design process for components operating in a potentially low cycle fatigue loading regime.

Whereas numerical predictions are 'right-first-time', experimental testing is subject to variability for otherwise identical tests. Care must be taken to minimise this variation. With a few notable exceptions, the experimental results presented in this paper show good repeatability and can instil a reasonable degree of confidence in those results.

The presence of notches such as holes, shoulders, grooves etc. result in a significant increase in the local stress and these stress raisers can, under fatigue loading conditions, result in low cycle fatigue even at moderate loading. A fundamental understanding of the effects of these notches on fatigue behaviour, using simple components, is vitally important to the designer, who needs to be aware that the introduction of a notch will reduce the fatigue life and can well change a high cycle fatigue problem to one of low cycle fatigue, the more complex modelling of which has been previously discussed. It is worth noting that holes are sometimes introduced at a later stage and a new design assessment must be undertaken.

This paper examines the effects of stress raisers in simple components subjected to a fatigue loading regime, in this example plain circular bars/shafts with radial through-holes subjected to cyclic axial loading. Three different hole sizes, namely 2.4 mm, 4.2 mm and 6.0 mm diameter, were drilled into a 12 mm diameter gauge section of EN8 screwed bar. Tests were carried out at loads of 80%, 75%, 70%, 65% and 60% of the 'yield load' (defined as the load at which non-linear material behaviour just starts). Similar tests were also performed on plain bars in order to compare and quantify the effects of the introduction of the holes.

Apart from a few anomalies, both the repeatability and consistency of the results are within acceptable bounds. For a given load level, the least number of cycles to failure corresponds to the largest hole size, as expected.

Figures 3, 4 and 5 can be interpolated for values between the loads and hole sizes considered here. Furthermore, results for other notch types can be added to Figures 6 and 7 to see if the elastic stress concentration factor,  $K_t$ , can be used as a simple normalising parameter, bearing in mind that  $K_t$  is only directly applicable for elastic conditions and LCF can be associated with significant plasticity.

## 5. Conclusions

The results have confirmed known qualitative information and have quantified this information for plain bars with radial through-holes subjected to axial tension-compression low cycle fatigue loading. The main conclusions from the work are:

- The introduction of a hole has reduced the fatigue life of the bar. In the worst case, the introduction of a 6 mm diameter hole for a load of 60% of the 'yield load' has reduced the fatigue life by more than two orders of magnitude, Furthermore, whereas the plain bar was in the transition region between LCF and HCF, the hole has brought the fatigue behaviour well within the LCF regime. The smallest reduction in fatigue life observed, for a 2.4 mm diameter hole and a load of 80% of the 'yield load', is a factor of 1.3. This is an interesting result which might not be obvious at first sight but it must be

remembered that the fatigue life of the plain bar has also reduced significantly at this very high load.

- For any given % 'yield load', the larger the hole the greater the reduction in fatigue life. The greatest reductions are seen at the 60% 'yield load' (as explained above) and the level of reduction depends significantly on the hole size. The higher the load, the less the effect of the hole size itself.
- The smaller the hole, the greater the effect of the actual load on the fatigue life. For the 2.4 mm diameter hole,  $\log_{10} N_f = 2.4 \rightarrow 3.8$  over the range of loads and for the 6.0 mm diameter hole,  $\log_{10} N_f = 2.2 \rightarrow 2.8$ .
- The number of cycles to failure for the largest hole together with the highest load is approaching the ultra-low cycle fatigue regime.

### Abbreviations

FCI	Fatigue Crack Initiation
HCF	High Cycle Fatigue
LCF	Low Cycle Fatigue
$N_f$	Number of cycles to failure
ULCF	Ultra-Low Cycle Fatigue

### References

- [1] Sachs NW. Practical plant failure analysis: a guide to understanding machinery deterioration and improving equipment reliability, 2<sup>nd</sup> edition, Boca Raton CRC Press Taylor and Francis Group, 2019, ISBN 13:978 - 1 - 138 - 32411 - 4.
- [2] Dowling NE, Brose WR, Wilson WK. Notched member fatigue life prediction by the local strain approach. *Advances in Engineering*, 1977, 6: 55-84.
- [3] Topper TH, Gowda CVBG. Local stress/strain approach to fatigue analysis and design. ASME Design engineering conference and show, Paper 70-DE-24, Chicago, 1970.
- [4] Agrawal R, Uddanwadiker R, Padole P. Low cycle fatigue life prediction. *Int J Emerging Engineering Research and Technology*, 2014, 2(4): 5-15.
- [5] Gowhari-Anaraki AR, Hardy SJ, Pipelzadeh MK. Experimental and analytical fatigue data for notched shafts in bending. *Jurnal Kejuruteraan (University Kebangsaan Malaysia)*, 2003, 15: 15-31.
- [6] Dundulis G, Janulionis R, Grybenas A, Makarevicius V, Dundulis R. Numerical and experimental investigation of low cycle fatigue behaviour in P91 steel. *Eng Failure Analysis*, 2017, 79: 285-295. <https://doi.org/10.1016/j.engfailanal.2017.05.001>
- [7] Beesley R, Chen H, Hughes M. A novel simulation for the design of a low cycle fatigue experimental testing programme. *Computers and Structures*, 2017, 178: 105-118. <https://doi.org/10.1016/j.compstruc.2016.09.004>
- [8] Pereira JCR, de Jesus AMP, Xavier J, Fernandes AA. Ultra low-cycle fatigue behaviour of a structural steel. *Eng Structures*, 2014, 60: 214-222. <https://doi.org/10.1016/j.engstruct.2013.12.039>

Blank Page



Research Article

## Micro-mechanical properties of geotextile fibers: measurement and characterization at cold environmental conditions

Tanay Karademir

Department of Civil Engineering, Istanbul Bilgi University, Istanbul, Turkey

### Article Info

#### Article history:

Received 21 Apr 2020

Revised 15 Jun 2020

Accepted 10 July 2020

#### Keywords:

Polypropylene Fibers;  
Geotextiles;  
Mechanical Properties;  
Ambient Conditions;  
Cold Temperatures

### Abstract

One of the most important properties of a fabric (geotextile) and also one of the focus areas of the current research study is its tensile strength, and thus, mechanical properties (modulus, resilience, strength, toughness). To this end, the mechanical properties of the geotextiles must properly be evaluated at the “macro-scale” as well as at the “micro-scale” as they are fibrous synthetic materials including polymeric fibers as well as significant volume of void space. As being a polymer, the mechanical behavior of the geotextile micro-fibers is highly dependent on the ambient conditions including particularly the temperature. In light of this, the tensile behavior of geotextile single micro-fibers was characterized by performing micro-mechanical tensile tests at “micro-scale” level at different cold temperature conditions using Dynamic Thermo-Mechanical Analyzer (DMA) to measure the developed “micro-scale” tensile stress – strain behavior of geotextile micro-fibers. The results examined from the influence of micro-mechanical properties of polymeric fibers on the observed temperature dependent stress-strain curve were used to determine the modulus of elasticity ( $E$ ), modulus of resilience ( $U_R$ ), ultimate tensile strength ( $T_{max}$ ), amount of plastic strain ( $\epsilon_p$ ), toughness ( $U_T$ ), rupture strength ( $T_R$ ) for the polypropylene (PP) micro-fiber of needle-punched nonwoven (NPNW) geotextile and the variation in those important mechanical properties with a change in ambient temperature conditions. The experimental results show that the mechanical properties of the PP fibers do not remain constant within the common range of cold temperatures ( $-10\text{ }^\circ\text{C} - 21\text{ }^\circ\text{C}$ ) found in typical civil engineering applications such that the temperature change was found to be an important factor affecting the PP fiber micro-mechanical properties such as modulus, strength, toughness and plastic elongation. Therefore, the test results provide an index of behavior at “micro-scale” level for the polymeric geotextile single fibers at cold temperature conditions.

© 2021 MIM Research Group. All rights reserved.

## 1. Introduction and Background

Temperature has a significant effect on the mechanical properties of polymers, such as modulus, tensile strength, toughness and hardness. Polymers soften and eventually flow as they are heated while they harden when cooled [1, 2]. Therefore, it is important to know the limiting temperatures at which polymer components can still be loaded with moderate deformations [3]. One of the most important properties of a fabric (geotextile) and also one of the focus areas of the current research study is its tensile strength, and thus, mechanical properties (modulus, resilience, strength, toughness). Most geotextile applications have been developed by relying on those engineering properties [4]. This is attributed to the fact that many geosynthetic applications using geotextiles are designed to complement the relatively low tensile capacity of soils [5]. To this end, tensile stress-strain (or: tensile force-displacement) test that is one of the common mechanical test types extensively used for polymeric materials (geotextiles) will comprehensively be examined in the paper.

Corresponding author: [tanay.karademir@bilgi.edu.tr](mailto:tanay.karademir@bilgi.edu.tr)

<https://orcid.org/0000-0002-9689-2140>;

DOI: <http://dx.doi.org/10.17515/resm2020.190ma0421>

Res. Eng. Struct. Mat. Vol. 7 Iss. 1 (2021) 97-120

Temperature has a significant effect on tensile properties of polymers [6, 7]. Since polymers are anisotropic materials and highly sensitive to both temperature change and strain rate [3, 8]. As temperature decreases in a polymeric material, a gradual contraction of the material occurs, resulting in less free volume as well as strengthening of the bonding forces which form the polymer structure and constitute the network of polymer chains holding the material together [3, 9]. Further, the tensile behavior of a polymer is strongly related to the state of the material which is dependent on its temperature. Polymers (Oriented Crystal Fiber, Glassy) are brittle at the lowest temperatures. As the temperature decreases, they become more “tough”, until they reach brittle-ductile transition below which polymers become sufficiently brittle that they can exhibit rupture (break) at relatively small strains. Further decrease in temperature leads to a glassy-like behavior [8, 10]. As the operating temperature range (typically  $-10\text{ }^{\circ}\text{C}$  to  $40\text{ }^{\circ}\text{C}$ ) in the field for PP geotextile is limited to temperatures much lower than  $T_m$  and higher than  $T_g$ , geotextile single fibers manufactured from this polymeric material is expected to exhibit temperature dependent “stiffness” and “ductile elasto-plastic” tensile behavior [6, 9]. Moreover, the type of behavior a polymeric material shows (brittle versus ductile) when tested depends on the strain rate of extension in tensile tests. For example, if extremely high strain rates are used, a polymer can exhibit brittle behavior at almost any temperature [4, 7]. Since geotextiles are made from polymeric materials, it is well known that their behavior can be affected by test conditioning such as ambient temperature, and the rate of extension or contraction in tension or compression tests, respectively such that there is an important aspect of fibrous materials (e.g. geotextiles) which must always be considered when fabrics are tested in tension mode.

In the earlier research works, the geotextiles being a very common polymer-based material utilized in a wide range of infrastructural applications were tested and the mechanical properties were characterized at macro scale only. On the other hand, the geotextile is a nonwoven fibrous material (fabric) that contains micro-fibers and significant amount of void (pore) space. For this reason, macro-scale characterization and response observed in the past could be deemed as incomplete since unable to provide a comprehensive understanding and sufficient insight to the micro-mechanical properties of geotextile fibers at micro-state and their measurement and characterization at cold environmental conditions (cold temperatures). To this end, the research work presented in the paper will provide a different perspective onto the topic in light of the reasons discussed in detail as follows: The geotextiles can exhibit different tensile stress-strain behavior as well as show favorable versus adverse response to varied test conditions such as temperature and strain rate variations when tested at the “macro-scale” level versus when tested at the “micro-scale” level. This is due to the heterogeneous internal structural formation of the fibrous materials (geotextiles) such that the total deformation under extension or contraction loading is the cumulative result of fiber deformation and internal structural rearrangement of the geotextile for which the initial elasto-plastic type deformation is strongly temperature and strain rate dependent, while the long-term rearrangement type deformation is not [11, 12].

## **2. Characterization of Micro-Mechanical Properties of Geotextile Fibers**

### **2.1. Fabric Characteristics used in Testing Program**

The tested micro-fibers were extracted from a staple fiber polypropylene (PP) needle-punched nonwoven (NPNW) type geotextile. NPNW geotextiles consist of spatially curved fibers that are often assumed to be randomly oriented and isotropically distributed [12, 13].

## 2.2. Experimental Device: Dynamic Thermo-Mechanical Analyzer (DMA)

Dynamic Thermo-Mechanical Analyzer (DMA) (Figure 1) was first used to measure micro-mechanical properties (tensile behavior or the developed “micro-scale” stress-strain response) of geotextile fibers.



Fig. 1 Computer Automated Dynamic Thermo-Mechanical Analyzer (Entire System)

## 2.3. Consistency and Accuracy of Measurements

Among several modes of operations (e.g. Multi-Frequency, Multi-Stress–Strain, Creep Stress–Relaxation, Isostrain) (Figure 2) that the DMA provides, the Controlled Strain Rate mode (Figure 2b) was used to measure tensile properties and to investigate the development of tensile stress versus strain relationships of single geotextile fibers at different cold temperatures. In this mode of operation, strain is ramped at a constant rate while the temperature is held constant. As such, the micro-scale tests were conducted at constant rate of elongation at micro-state (controlled strain rate mode: Figure 3) over the range of cold temperatures from  $-10\text{ }^{\circ}\text{C}$  to  $21\text{ }^{\circ}\text{C}$  with  $5\text{ }^{\circ}\text{C}$  increments between different test temperatures to observe the repeatability of the developed tensile force-extension behavior as well as to see the reproducibility of fiber tensile strength response at every test temperature.

In particular, Figure 3 demonstrates that the experimental set-up has high capability and robust performance in applying accurate strain controlled extensional tension on micro-fibers during the entire course of the tests from the initiation to the end at all test temperatures even at cold ambient temperature condition of  $-10\text{ }^{\circ}\text{C}$ . Further, as seen in Figure 3 that the tensile tests for the entire range of cold test temperatures performed using Controlled Strain Mode in which Strain over Stress Ratio increases linearly with a constant rate with respect to time (Figure 2b) among the alternative testing and characterization modes as shown in Figure 2 verifies that the system has advanced as well as robust control and accurate, consistent measurements on the whole tested micro-fiber specimens during the experiments at all cold test temperatures. Since, the four different tests at each test temperature demonstrates similar response and consistent behavior which confirms the reproducibility of micro-fiber tensile strength at every test temperature and the repeatability of the developed tensile force – extension behavior for the tested micro-fibers (Figure 3).

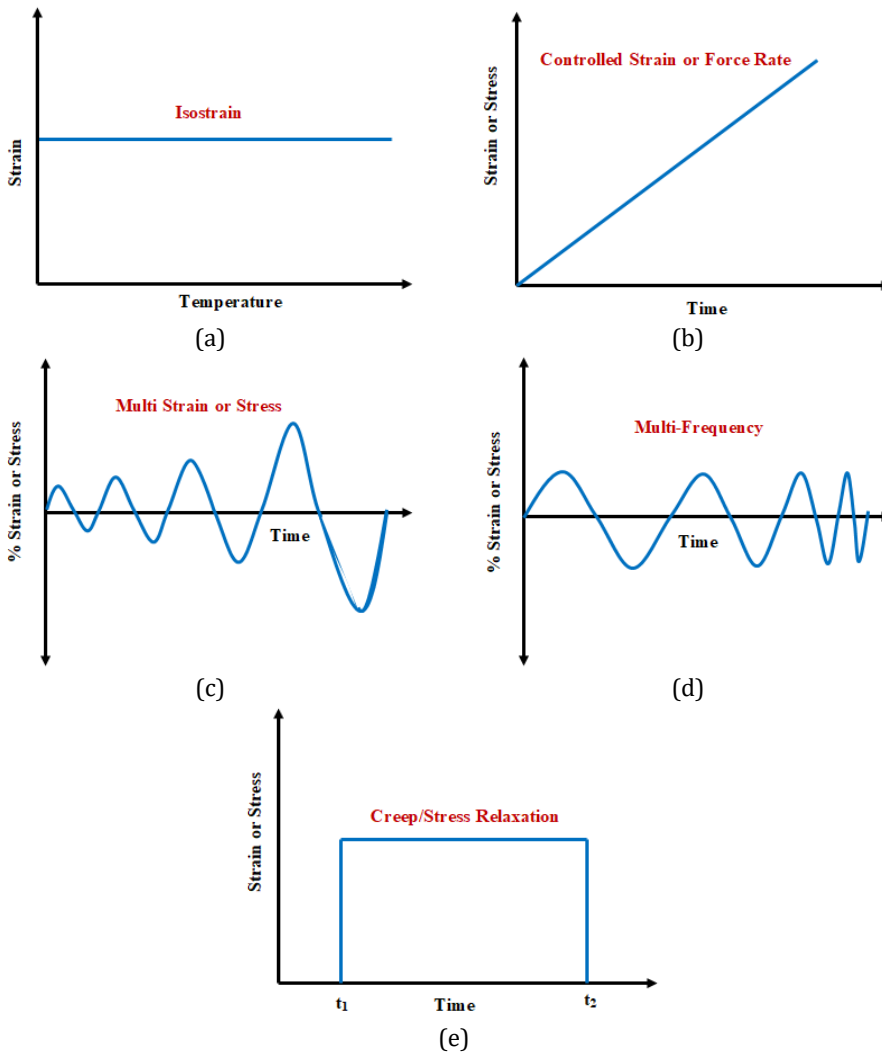


Fig. 2 Different Modes of Micro-Mechanical Testing and Characterization

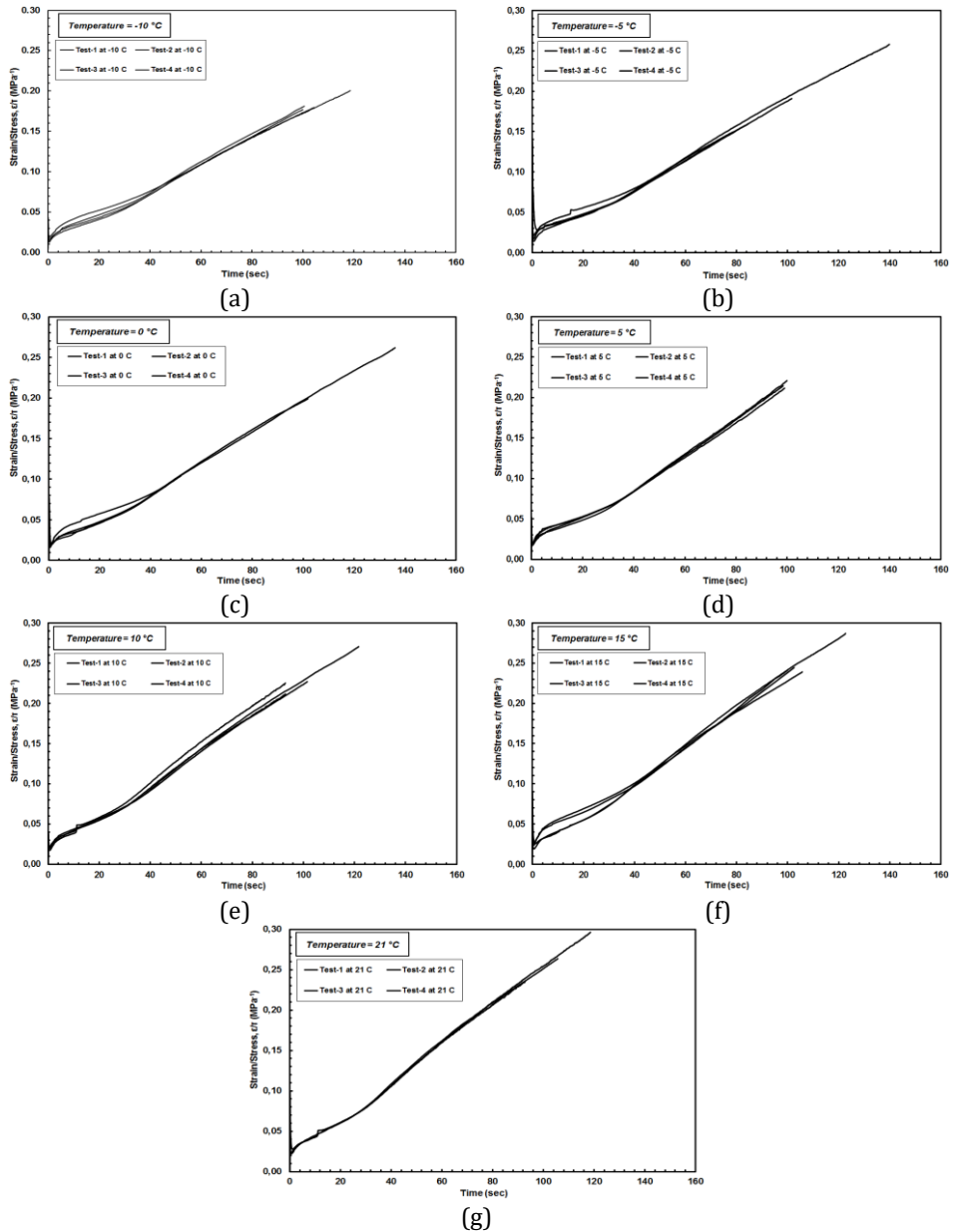


Fig. 3 Controlled Strain Rate Mode of Testing for Micro-Fibers at Different Ambient Conditions

#### 2.4. Characterization Technique: Test Method, Sample Preparation and Experimental Procedures

The micro-fiber specimens (Figure 4) tested to failure using a constant-rate-of uniaxial extension (CRE) type tensile testing of a predetermined gage length and rate of extension at different cold temperatures were extracted from geotextile samples selected randomly from the big roll of the textile fabric. After preparation, the fiber test specimens were placed and conditioned between two smooth clamp fixtures (with flat jaws for gripping the fiber specimens) of the Dynamic-Thermo-Mechanical Analyzer (DMA). The distance

between the clamps was adjusted to obtain the selected nominal gage length of 12.5 mm. The fiber which was glued on the paper tab was gripped with a set of stationary jaws by removing slack without stretching the specimen and then, the axial alignment of the fiber must be ensured by carefully controlling the paper tab and the fiber tension kit. After moving the grips to ensure that the specimen was axially aligned straight, the paper tab was cut gently at the middle points of either side. Before initiating the experiment to measure tensile properties and to investigate the development of tensile force versus elongation curve of PP fibers at cold temperature conditions, the oven was closed and the temperature was decreased down to the target test temperature through the controller software of the system. Subsequently, the test was initiated and the PP fiber specimens were stretched in tension and ruptured using a constant-rate-of extension (CRE) type tensile test in which the rate of extension (extension speed) was set as a constant value of 0.125 mm/s for fiber specimens having an average diameter of 0.035 mm (35  $\mu\text{m}$ ) to provide proper rate of elongation for the gage length (net measurement length of the fiber) of 12.5 mm selected. This strain rate was determined based on initial specimen length,  $L$ ; [ $d\epsilon/dt=(L/100)$ ] and intentionally used to observe the entire deformation behavior - consisting of i) elastic elongation; and ii) inelastic deformation of fiber polymeric materials under tension until the rupture takes place. After breaking the specimen, the tension clamp was returned to its original position (starting condition) and all remains of the failed specimen were removed from the clamp faces.

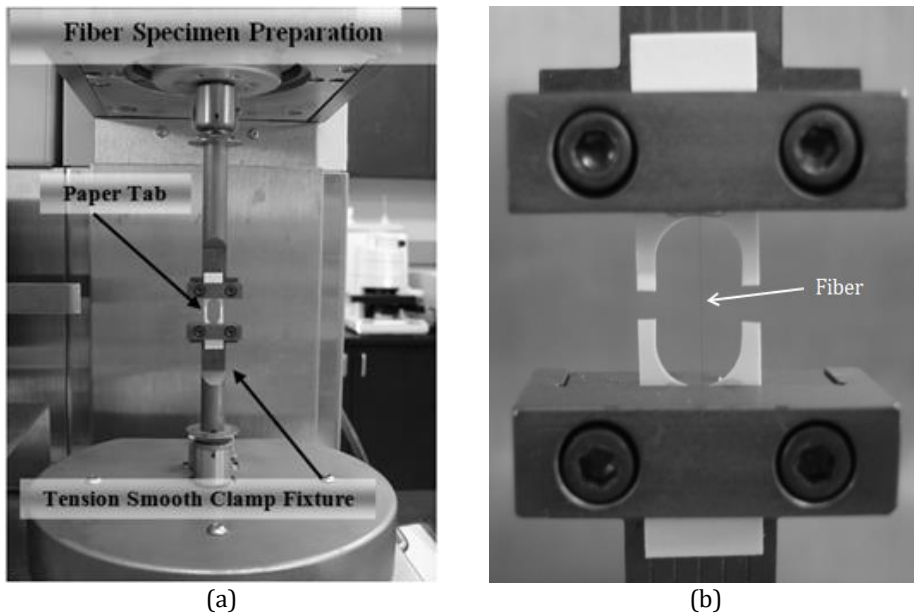


Fig. 4 The PP Micro-Fiber Test Specimen Placement and Conditioning

The area correction for the tested single geotextile specimens during the experiments were automatically performed by the controller software of the DMA as follows. After moving the grips to ensure that the specimen was axially aligned straight, the exact diameter of the specimen was measured and the value of which was entered into controller program so that the program during elongation was able to automatically compute the tensile stress by using the current cross-sectional area of the specimen detected by the digital camera system during extension of the specimen and comparing this value with the initial cross-sectional area. Therefore, the tensile stresses measured were the corrected values based

on elongation of the specimen and the resulting contraction occurred in the area detected by the integrated camera system.

### 3. Micro-Scale Mechanical Behavior and Response of Fibers

#### 3.1. Introduction and Scope

The tensile stress – strain curves at different cold temperatures for polypropylene (PP) micro-fibers are presented in Figure 5. The tensional elongation behavior of micro-fibers within the entire range of ambient temperatures tested (-10 °C to 21 °C) comprised of elasto-and-predominantly-plastic response comparing the amount of strain exhibited during the course of plastic elongation relative to that of displayed throughout elastic elongation (Figure 5).

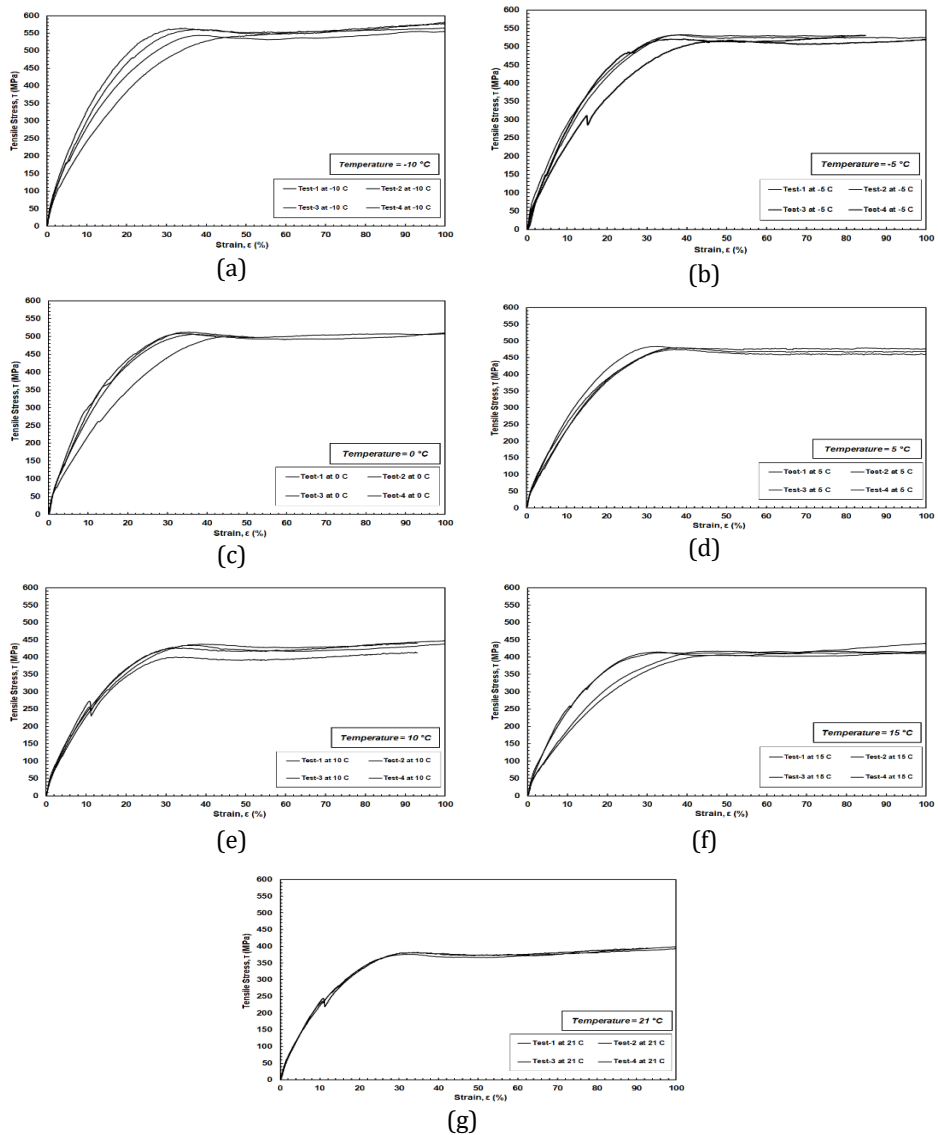


Fig. 5 Tensile Stress – Strain Curves at Different Temperatures for Polypropylene Micro-Fibers tested at Constant Rate of Elongation at Micro-State

Moreover, the tensile stress versus axial strain curves at different temperatures demonstrate that there occurs a dramatic (very sharp) increase in tensile stress within a small strain (elongation) of the fiber, and thereafter, the rate of increase in tensile stress becomes gradual at a slower rate prior to yielding transforming to plastic response after elastic elongation. Furthermore, as seen in Figure 5, during plastic elongation, tensile stress remained approximately constant although the elongation of the specimen continued, however, the specimens were not able to withstand additional tensile stress. Based on observations made on post-test micro-fiber specimens after the experiments were completed, it was seen that the failure (rupture point) took place at different locations of the sample gauge length with some being close to the middle of the specimen, whereas, others were closer to either end (up or down) where the tension break rupture occurred in the upper or lower portion of the fiber specimens.

### **3.2. Shape and Development of Stress versus Strain/Stress Curves at Different Temperatures and Elasto-Perfectly-Plastic Behavior**

Micro-mechanical uniaxial tensile tests on the micro-fibers performed under a “constant rate” of extension loading at test temperatures ranging from -10 °C up to 21 °C with 5 °C increments between different test temperatures displayed predominantly inelastic response exhibited over a relatively large strain intervals as compared to that of elastic response mobilized over a very limited strain intervals (Figure 6). The shapes of stress versus strain/stress curves for all the tests performed on micro-fiber specimens at various cold temperatures were in good agreement, and indicated that plastic elongation behavior (nonlinear elasto-perfectly plastic form) occurs in polypropylene fibers under tensile load prior to failure or rupture of the fibers. The strain over stress ratio at the onset of the tests reads about 0.1 MPa<sup>-1</sup>, and then, with an initial slight (insubstantial) increase in tensile stress, this ratio reduces to 0.02 MPa<sup>-1</sup> within a very small time interval of measurement. Later, stress increases linearly and dramatically with respect to strain over stress ratio at a constant positive slope ( $Slope = [Stress/(Strain/Stress)] = Stress^2/Strain$ ) within a very short time interval of measurements which indicates that, at this stage of the tensile tests, the square of stress is directly proportional to strain through a linear (1st order) relationship. Finally, beyond a strain over stress ratio of 0.07-0.08 MPa<sup>-1</sup>, the stress remains approximately constant displaying a slope of zero ( $Slope = Stress^2/Strain$ ) demonstrating that the tensile stress measured for the rest of the test progress remains more or less constant that is an indication of perfectly plastic behavior as such the strain increases at a constant rate of elongation implying true plastic behavior of micro-fibers prior to rupture at about 0.25 MPa<sup>-1</sup> strain over stress ratio. Although the elastic stage lasts within a relatively short interval of the strain/stress of 0.06 MPa<sup>-1</sup>, the plastic stage progresses at a much larger interval of the strain/stress of 0.17 MPa<sup>-1</sup>. To this end, it is seen that the elongation of micro-fibers under tension over the entire range of test temperatures from -10 °C to 21 °C is predominantly comprised of permanent plastic straining along with a minor and limited amount of temporary elastic deformation.

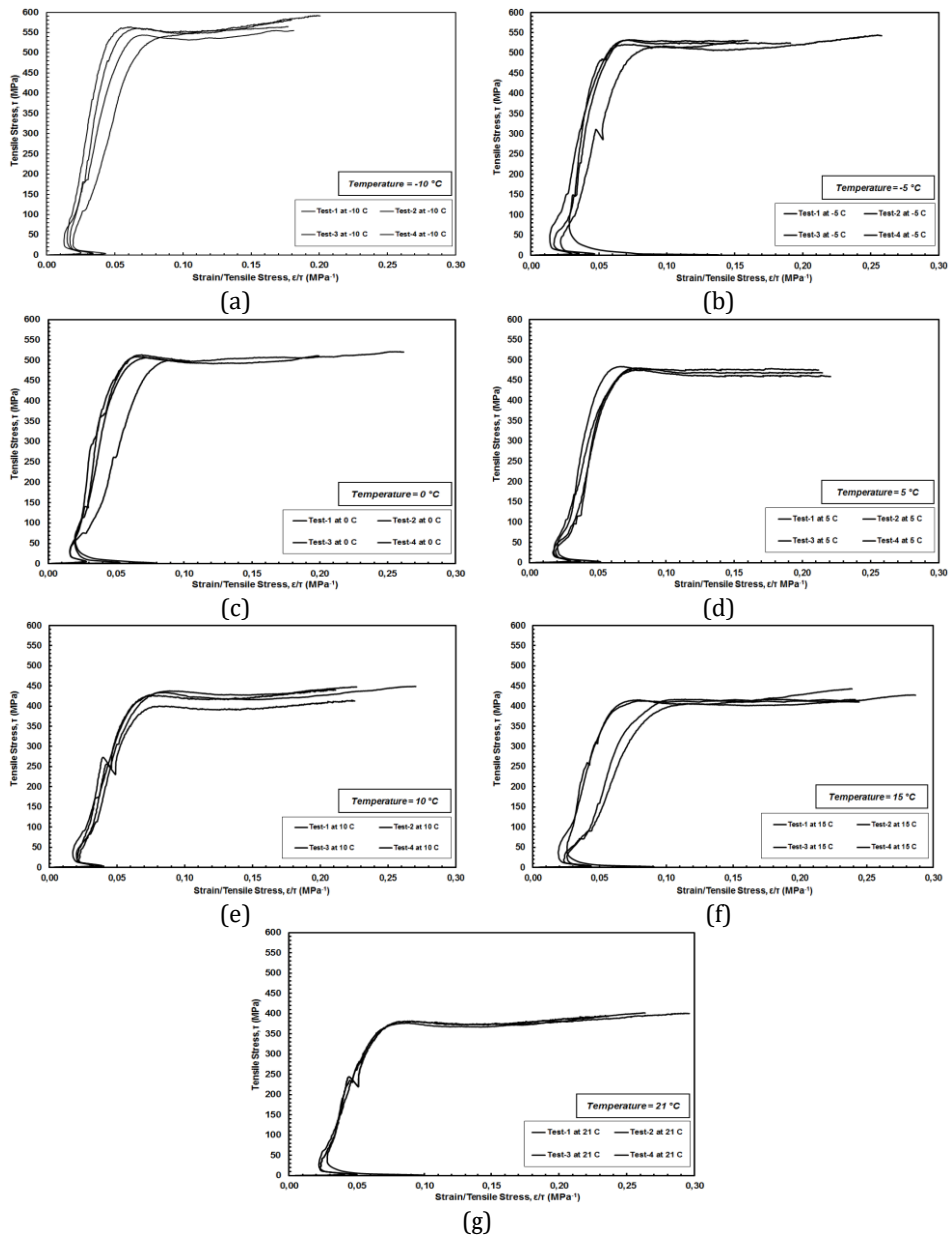


Fig. 6 Tensile Stress – Strain/Stress Curves at Different Ambient Temperatures

Further, the tensile stress versus strain/stress curves at different cold temperatures presented in Figure 6 are descriptive and provide an opportunity in illustration for a detailed view and helps us see obviously the different stages of elasto-perfectly-plastic behavior and fiber yielding stage in demonstrating the details of transformation of the behavior from elastic to plastic. Moreover, Figures 5 and 6 verify the accuracy and consistency of the measurements for the mechanical properties of the micro-fibers tested at different cold temperatures from the proximity of the curves in the replicate tests at the same test temperature.

### 3.3. Assessment of Ductility and Brittleness for the Material Tested

There is an apparent trend which can be observed in the series of graphs in both Figures 5 and 6 of the tensile stress versus strain and/or strain/stress failure envelopes, respectively, for polypropylene fiber specimens growing with a decrease in temperature such that the size of the area under the curve enlarges which is an indication of greater energy absorbed by the fiber during tensile deformation under the load. As such, for the tested polymeric fibers, the tensile stress – strain curves from colder temperature tests fall outside of the failure envelope of that defined by the warmer temperature tests. This variation in tensile stress versus strain response shows the influence of temperature on the PP micro-fibers at micro-state. Furthermore, the fibers are highly ductile with majority of the fibers experiencing a large amount of plastic deformation before rupture (Figures 5 and 6). Brittle tension rupture for the specimens was not observed for the temperature range tested (-10 °C to 21 °C). Brittle failure modes generally occur under glass transition temperature ( $T_g$ ) of polymeric material as the nature of bonding between the molecules of polymers is based on ambient temperature.

Furthermore, Figure 7 demonstrates stress over strain ratio with respect to strain in the tensile tests at different cold temperatures. The purposeful use and illustrative explanation of Figure 7 is such that the stress to strain ratio, at all test temperatures, escalates very fast within only 1% strain of elongation, and arrives to a very sharp point peak (indication of elastic elongation), and thereafter, drops off exponentially, and finally reaches to approximately constant values at about 40% strain of elongation after which remains asymptotically until fiber rupture. The slope of the curves in Figure 7 represents the proportion of tensile stress to the square of strain [ $Slope = \{Stress/Strain\}/Strain = [Stress/(Strain)^2]$ ]. A very rapid increase in the stress to strain ratio at the onset of the tests within only 1% axial strain with increasing nonlinear slope of the curves at this stage demonstrates that the measured tensile stress ramps up very quickly at a much higher rate than the  $(strain^2)$ . This is attributed to enhanced resilience of the polypropylene micro-fibers exhibited at elastic stage of elongation under the application of tensile elongation instantly within very small range of longitudinal strains less than 2% that testifies the development of immediate elastic response as soon as the fiber has been tensioned extensionally where the linear increase of stress over strain ratio at a constant rate with respect to axial strain verifies and demonstrates the development of elastic response. Thereafter, the exponential decrease after the “sharp point peak” displayed in the curves in Figure 7 reveals that the rate of increase in tensile stress at elastic stage begins to decrease gradually indicating the behavior is transforming from elastic to plastic nature by passing through a transition zone up until 40% of tensile elongation. This stage of the tensile response was portrayed as a logarithmic increase behavior with a decreasing rate of increase in the tensile stress versus axial strain curves shown in Figure 5 as a mid-phase in between elastic and plastic stages of the tests. Additionally, a relatively lower rate of decrement in the curves (Figure 7) displayed at post-peak stage compared to those exhibited in pre-peak stage is another indication for the mid-phase which develops between elastic and plastic stages under tensile elongation of the fibers. As such, although the tensile stress arrives to peak within 1% of longitudinal elongation, drops off from the peak and reaches to plastic stage by undergoing 39% of additional elongation after the peak (Figure 7). Further, the asymptotic behaviors observed in the curves in Figure 7 at which the stress to strain ratio remains almost constant after 40% of tensile elongation until the rupture of the fiber at about 100% elongation point out the occurrence of plastic deformation where inconsequential change is seen in tensile stress with increasing axial strain throughout an interval of significant amount of elongation prior to fiber break. Consequently, three distinct parts, within the entire range of ambient test temperatures, are seen in tensile force versus elongation response of the micro-fibers including a

predominant plastic stage occurred during or mobilized over 60% fraction of the total axial elongation developed in the fibers under tension, verifying that the micro-fibers are capable of withstanding greater extent of plastic elongation. This denotes that a ductile response with a predominant plastic phase has been observed for tensile stress versus strain behavior of the micro-PP-fibers regardless of ambient temperature tested. Additionally, as the temperature increases, the amount of plastic axial elongation exhibited by the micro-fibers becomes larger. This is associated with material hardness as the polymeric micro-fibers inherently become softer, and hence, more ductile when ambient temperature increases resulting in greater flexibility.

Moreover, as compared to the warmer test temperatures above 0 °C, there occurs a slight variation in the values of tensile stresses measured in the different replicate tests at the same ambient conditions for the micro-fibers particularly when the ambient test temperature becomes colder much below 0 °C. This is associated with the inherent material properties of polymeric PP-fibers such that the firmness of the micro-fibers as per micro-mechanical stability in exhibiting identical tensile strength response in the replicate tests at the same ambient conditions becomes less consistent with a further decrease in ambient temperature especially below 0 °C (Figures 6 and 7).

#### **3.4. Fiber Micro-Mechanical Properties and Stages of Force-Displacement Failure Envelopes**

Tensile stress versus strain/stress curves at different temperatures presented in Figure 6 clearly illustrated different stages of elasto-plastic behavior and yielding stages of the tested micro-fibers in demonstrating the mechanisms for the transformation of the tensile behavior from elastic to plastic passing through the two yielding stages including initial and ultimate yielding of the fibers under tensile elongation. In this perspective, Figure 8 presents the mean tensile stress versus strain/stress curves as a function of the temperature starting from the standard room temperature of 21 °C down to the ambient cold temperature condition of -10 °C. These mean curves are descriptive in emphasizing that the micro-fibers resulted in a similar trend of tensile stress versus axial strain response at all test temperatures such that the tensile stress – strain/stress curves have a nonlinear elasto-perfectly-plastic form regardless of the ambient temperature tested. The mean curves shown in Figure 8 provided an opportunity in illustration for a detailed view and helping to see clearly the different stages of elasto-perfectly-plastic behavior and fiber yielding stage in depicting the details of transformation of the behavior from elastic to plastic. Additionally, the curves demonstrate that there occurs a dramatic, very sharp increase in tensile stress within a small strain of the fiber, and thereafter, the rate of increase in tensile stress becomes gradual at a slower rate prior to yielding, and thus, transforming to plastic response after elastic elongation.

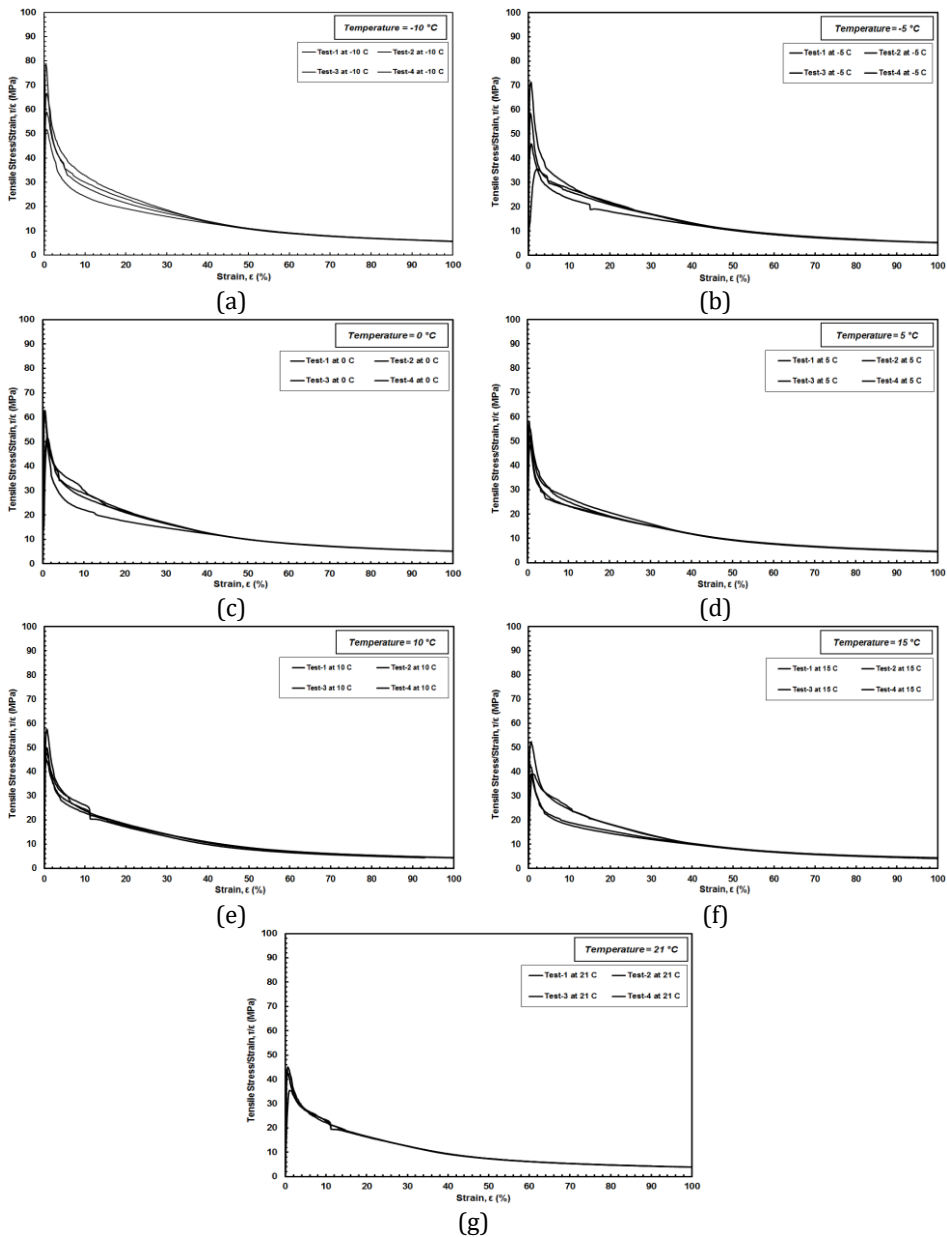


Fig. 7 Assessment of Ductility and Brittleness for Tensile Elongation Response of the PP Micro-Fibers

As demonstrated in Figure 8, the general pattern in tensile stress –strain/stress behavior of polypropylene fibers in the tension tests at different ambient cold temperatures ranging from 21 °C down to -10 °C can visually be portrayed in three segments: i) strain/stress ratios start about  $0.05 \text{ MPa}^{-1}$  and proceed to left on the graph space with a steady rise at a very low (minimal) slope, and thereafter, the curves undergo initial yielding at a strain over stress ratio of  $0.015 \text{ MPa}^{-1}$  as well as they change direction by progressing to slightly right on the graph space, and then; ii) tensile stress increases dramatically within a relatively

small range of  $0.04 \text{ MPa}^{-1}$  strain over stress ratio, and finally; iii) the curves exhibit ultimate yielding stage and level off, remains more or less constant at greater strain over stress ratios displaying perfectly-plastic response with a nearly constant resistances after ultimate yielding stage prior to fiber rupture. Moreover, the curves at all test temperatures reached rupture failure at axial elongations from 100% to 120%. Consequently, it is noted that a transition dominant tensile behavior (Figures 6 and 8) was observed for the PP-micro-fibers at colder temperatures than the room temperature ( $\leq 21 \text{ }^\circ\text{C}$ ) including; i) elastic stage developing from initiation of the test up to initial yielding, ii) elastic stage continuing and displaying a gradual decrease in the rate of increase in tensile stress with increasing strain from initial yielding to ultimate yielding, iii) plastic stage mobilizing after ultimate yielding until fiber rupture being the predominant mechanism for the examined tensile response of the micro-fibers over the entire test temperatures ranging from  $-10 \text{ }^\circ\text{C}$  to  $21 \text{ }^\circ\text{C}$ . In summary, the uniaxial tensile stress versus axial strain behavior of the fibers at different ambient temperatures tested consists of elastic straining, transition zone and predominant plastic deformation (Figure 8). That is to say, tensile stress ramps up dramatically within very small axial extensional displacements at a range of  $0.04 \text{ MPa}^{-1}$  strain over stress ratio, and then, it remains almost constant during inelastic deformation of the polymeric material after passing through yielding deformation. The inelastic portions of the stress versus strain/stress curves are essentially parallel at all test temperatures.

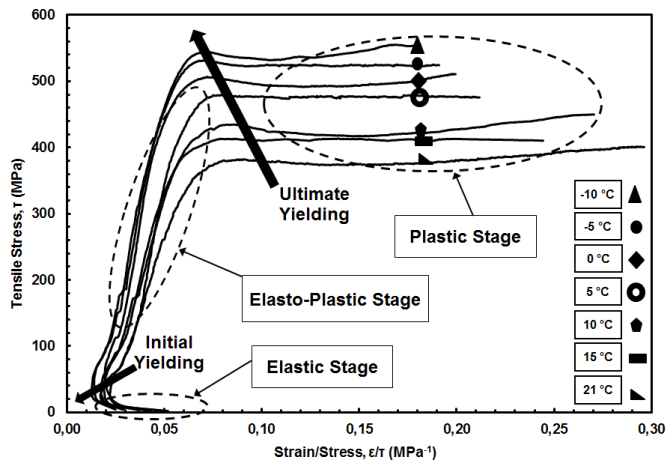


Fig. 8 Different Phases of Elasto-Perfectly-Plastic Behavior and Fiber Yielding Stage

To sum up, as evident from Figures 5 through 8, the force – displacement curves underwent a relatively short elastic deformation stage as compared to a longer plastic deformation phase. As such, all the micro-fiber specimens tested experienced greater amount of strains prior to failure by proceeding through all three main phases of elasto-plastic deformation including elastic, yielding and plastic zones. In this perspective as per the polymer material properties of the micro-fibers, the tensile force versus axial elongation behavior, in principle, can be divided into three separate zones, depending on the molecular response of the polymer to the level of applied strain [6–8]; i) Within Zone I, the response to load is instantaneous and elastic, since the deformations are recoverable upon load removal; ii) Deformations within Zone II are still recoverable, but not instantaneously. Time dependent response within Zone II usually is generally associated with visco-elastic behavior; iii) Within Zone III, the material exhibits an inelastic response

in that the deformations are irrecoverable upon load removal and response within this region is related to plastic behavior in which strains consist plastic components. In terms of physico-chemical considerations, the stretching of inter-atomic bonds occurs in Zone I when going through elastic elongation. Throughout the transition zone (Zone II), polymer molecular chains get straightened. Lastly, the relative displacement of molecules in the polymer takes place in Zone III during plastic deformation.

### 3.5. Modulus of Elasticity, E

The observed tensile stress versus axial strain behavior of PP fiber specimens indicated that the fibers become stronger and stiffer as temperature decreases under the application of tensile load. The initial elastic portion of stress – strain curves rotates “counter-clockwise” demonstrating an increase in stiffness; hence, elasticity modulus with decreasing temperature. As such, the result of micro-scale tensile tests on the PP fibers disclosed and presented that the modulus of elasticity increased at an increasing rate incrementally as the ambient temperature decreased. Figure 9a shows the change of elasticity modulus as a function of temperature. The values of the modulus of elasticity have been calculated from initial linear portions of the stress versus strain curves. The mean diameter of a single fiber under zero tensile load is 35  $\mu\text{m}$  (0.035 mm) which constitutes an average cross sectional area of  $9.62 \times 10^{-10} \text{ m}^2$  ( $9.62 \times 10^{-4} \text{ mm}^2$ ). When the measured tensile forces on the order of 35 to 55 gram-force at various temperatures are divided by the small cross-sectional area of the fiber; then, the resulting elasticity modulus values were in the order of tens of MPa.

It is evident from Figure 9a that the PP fiber modulus is inversely proportional to temperature. The maximum stiffness for all the tests conducted in this study was obtained at the lowest ambient temperature (-10 °C). As such, the fibers produced from polymers were stiffer and firmer at colder temperature conditions and became relaxed and more flexible at warmer temperatures such as the room temperature (21 °C). Consequently, in the tests at lower temperatures, the fibers underwent less deformation as compared to those of at higher ambient temperatures before proceeding through transition deformations or yielding from elastic type to plastic type elongations. A regression analysis performed on the experimental data based on second-order polynomial fit provided a good quadratic increase model with a high “coefficient of determination” of 0.9815. The closeness of fit between the regression curve and the test data indicates that a good correlation between the temperature and the modulus of the fibers exists (Figure 9a). The empirical relationship (Equation 1) between fiber modulus and temperature was developed based on the results of micro-scale tensile tests at different ambient temperatures and could be utilized as a mathematical empirical relationship to relate elasticity modulus to temperature change in which Young’s modulus values follow a nonlinear pattern with decreasing temperature for the PP fibers extracted from NPNW geotextiles.

$$E \text{ (MPa)} = 0.0396x[T(^{\circ}\text{C})]^2 - 1.5724x[T(^{\circ}\text{C})] + 49.752 \quad (1)$$

where, E : Modulus of elasticity (MPa), T : Temperature (°C)

### 3.6. Modulus of Resilience, U<sub>R</sub>

Resilience is defined as the ability of a material to absorb energy when deformed elastically, and release that energy upon unloading [6, 7, 14, and 15]. As seen from the results of experimental program at different cold temperature conditions, tensile stress versus axial strain curves had a similar form with a sharp increase prior to arriving in the transition zone and ultimately experiencing plastic deformation at all temperatures tested

(Figure 5). In light of this, resilience for the fibers can be determined based on the concept of being the maximum energy that they absorb under tension within the elastic limit without creating a permanent distortion before the transition zone (yielding stage) of stress – strain curves. Therefore, the modulus of resilience for the PP fibers tested at various temperatures was calculated by integrating tensile stress with respect to axial strain – that is basically the area underneath of the stress – strain curves – from zero up to the elastic limit so as to obtain the elastic deformation energy per volume of the test specimen, referring to resilience, until at a point where the first departure from linearity occurs. In terms of physical considerations, the elastic deformation energy under tensile elongation per volume of the test specimen describing the modulus of resilience is basically observed during elastic straining wherein the developed deformations are instantaneously recoverable. The modulus of resilience ( $U_R$ ) for the PP fibers increased exponentially as the ambient temperature decreased (Figure 9b). It means that the area under tensile stress versus axial strain curves until elastic limit, that is the elastic deformation energy per volume of test specimen, enlarges with an increasing rate with decreasing temperature. The modulus of resilience was smallest at room temperature (21 °C) and displayed an increase at colder temperatures (<21 °C). As such, the maximum energy required and absorbed per unit volume of the PP fibers without creating a permanent plastic deformation (elongation) becomes greater with a decrease in the ambient temperature.

Moreover, the rate of increase for the modulus of resilience ( $U_R$ ) became greater over the range of ambient temperatures particularly between 5 °C and -10 °C as compared to that of the range of ambient temperatures between 20 °C and 5 °C. As such, the  $U_R$  displays an increase at a lower rate from 20 °C down to 5 °C, whereas the  $U_R$  exhibits a raise at a higher rate from 5 °C down to -10 °C. Besides, the exponential model developed provides a higher coefficient of determination value ( $R^2$ ) in comparison to that of the linear regression fit. For this reason, the exponential model obtained has been thought of a better regression fit both in precisely displaying the overall behavior (the change or variation of  $U_R$  with decreasing temperature) and in accurately demonstrating a closer proximity between intermittent test data and continuous regression curve that resulted in attaining a larger value of  $R^2$  closer to 1. To this end, the obtained empirical relationship between modulus of resilience and temperature (exponentially increasing behavior of  $U_R$  as a function of temperature) is given in Equation 2 (CoD = 0.9832):

$$U_R \text{ (J/m}^3\text{)} = (1 \times 10^8) \times e^{-0.018 \times [T \text{ (}^\circ\text{C)}]} \quad (2)$$

where,  $U_R$  : Modulus of resilience (J/m<sup>3</sup>), T : Temperature (°C)

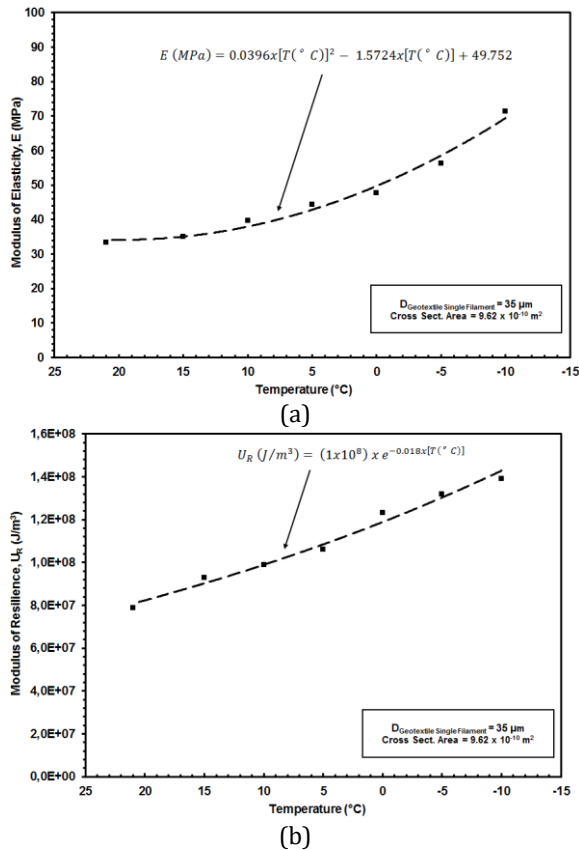


Fig. 9 Elastic Stage Mechanical Properties of the Micro-Fibers and Temperature:  
 (a) Modulus of Elasticity (E); (b) Modulus of Resilience ( $U_R$ )

### 3.7. Tensile Strength, $\tau_{\text{max}}$

One of the most important mechanical properties of polymeric materials is its tensile strength under tensional elongation that shows indestructibility of the material employed in the field. Since a polymer type (PP) is used as a base material to produce geotextile micro-fibers, they do not maintain and sustain tensile strength and robustness properties with temperature change to which most geotechnical engineering applications are exposed. It was observed as a result of micro-scale tensile tests on the PP micro-fibers that tensile strength, ( $\tau_{\text{max}}$ ) increased as the ambient temperature decreased with greater tensile strength under tension measured at lower cold temperature conditions (Figure 10a). The resulting values of tensile strength measured were on the order of hundreds of MPa. The PP micro-fibers at cold temperatures were stronger and resistant but became weaker and less strong at higher warm temperatures due to polymer material properties changing with temperature and the bonding strength of polypropylene molecules strongly dependent on the ambient temperature conditions. However, this is only the micro-level response of the fibers extracted from a geotextile fabric. At global state (macro-level), depending on fiber processing type and fabric manufacturing method, temperature might have minor influence on tensile properties of geotextile fabric sheet [11–13] due to internal structural formation which is generated through fiber-fiber interlocking (bonding), nature of inner voids, and ability of fibers for rearrangement under external forces.

As seen from Figure 10a, there is an inverse proportion in between tensile strength of the PP micro-fibers and temperature in which they possess higher tensile strength values at lower temperatures due to more intact chemical composition and stronger bonding type of base polymer molecules (polypropylene) of the fiber at cooler temperatures resulting from the material physico-chemical properties. Further, several different types of regression analysis such as linear, exponential, polynomial were performed on the micro-mechanical tensile test data. The linear regression provided the best correlation between tensile strength and temperature such that a very good fit between intermittent test data and continuous regression curve for which a higher coefficient of determination (CoD) of 0.9807 was obtained as compared to that of polynomial or exponential regression models that resulted in lower CoD values. For single PP fibers extracted from NPNW geotextile and stretched axially (elongation) under tensile force at micro-state at several temperatures, the empirical relationship developed through regression analysis of micro-tensile test data to relate the change in tensile strength to the variation in ambient temperature is given as follows:

$$T_{max} (MPa) = -5.3817x[T(^{\circ}C)] + 503.27 \quad (3)$$

where,  $T_{max}$  : Tensile strength (MPa), T : Temperature ( $^{\circ}C$ )

### 3.8. Rupture Strength, $\tau_R$

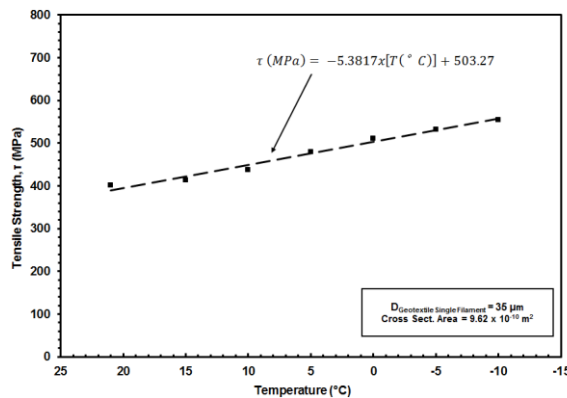
The tensile stress versus axial strain curves showing force versus elongation response of the micro-fibers, regardless of ambient temperature tested, underwent a relatively short elastic deformation stage as compared to a much longer plastic deformation phase (Figures 5 and 8). That is to say, almost all the fiber specimens experienced larger strains (axial elongations) prior to failure by progressing through all three main phases including elastic stage, transition zone, and plastic deformation (Figure 8), typical for elasto-plastic behavior, prior to exhibiting failure (break) that is called the rupture of the PP micro-fibers under tensional elongation. In the micro-scale tensile tests at various temperatures, the tensile force increased rapidly in a very sharp manner within very small axial strains during elastic stage, then, it remains almost constant during inelastic and irrecoverable deformation of the polymeric material after passing through yielding stage, consequently resulted in inelastic portions of the stress-strain curves being essentially parallel (Figures 5 and 6). This shows that the sturdiness of the PP fibers maintained and sustained more or less same with a minor trivial strength loss after experiencing maximum tensile stress (tensile strength) as tensile elongation continued to larger axial strains. Similar to the tensile strength ( $T_{max}$ ) that increased with decreasing temperature, the rupture strength ( $\tau_R$ ) increased with a decrease in temperature such that the higher rupture strength under tensional elongation has been measured at lower cold temperature conditions (Figure 10b).

A linearly increasing behavior was observed for which the empirical relationship attained based on the regression of intermittent experimental data is given in Equation 4 for the rupture strength ( $\tau_R$ ) as a function of temperature. A high coefficient of determination (CoD = 0.9836) obtained from the regression analysis in between the discontinuous test data and the resulting continuous regression line shows that the best correlation between rupture strength ( $\tau_R$ ) and temperature with a very good fit is the linear (1<sup>st</sup> order) relationship as follows:

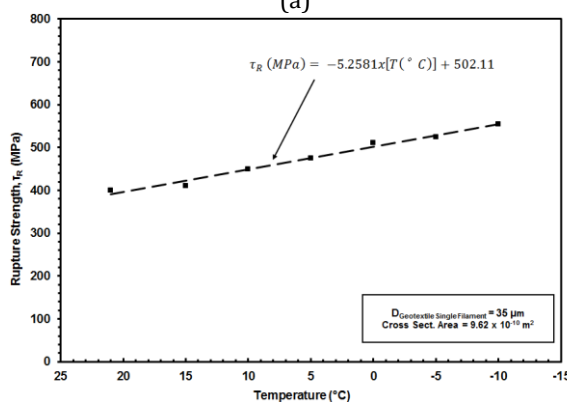
$$T_R (MPa) = -5.2581x[T(^{\circ}C)] + 502.11 \quad (4)$$

where,  $\tau_R$  : Rupture strength (MPa), T : Temperature ( $^{\circ}C$ )

Furthermore, Figure 10a presents the change of mean tensile strength – that is the average of the *maximum* tensile stress measured at every four replicate tests at each test temperature – with a variation in the ambient temperature. On the other hand, Figure 10b shows the change of mean rupture strength – that is the average of the tensile stress at *failure* or *break* of the micro-fibers measured at every four replicate tests at each test temperature – with a variation in the ambient temperature. Since, at each ambient temperature, the four replicate tests were performed to demonstrate similar response and consistent behavior which confirms the reproducibility of the tensile strength of the PP micro-fiber at every test temperature and the repeatability of the developed tensile stress – axial strain behavior for the tested fibers at micro-state. Furthermore, Figure 10b verifies that the PP micro-fibers exhibited *elastic-perfectly-plastic* response over the entire range of test temperatures as the tensile strength measured was very similar to the rupture strength at break at every micro-tensile tests. The onset of plastic deformation has been determined by analyzing the experimental data after ultimate yielding (Figure 8) in the tests based on variation in the measured values of tensile stress for the condition being within 5 percentile (5 %). Figures 6 and 8 were generated, accordingly, on this purpose to demonstrate a better illustration and definite borders in the plots between different test stages including elastic, elasto-plastic and plastic.



(a)



(b)

Fig. 10 Tensile and Rupture Strength of the Micro-Fibers and Temperature:

(a) Tensile Strength ( $\tau_{max}$ ); (b) Rupture Strength ( $\tau_R$ )

### 3.9. Amount of Plastic Strain, $\varepsilon_p$

The PP micro-fibers exhibited higher values of modulus of resilience at colder temperature conditions while they displayed lower strains prior to yielding until elastic limit as well as, most importantly, lower extent of plastic strains ( $\varepsilon_p$ ) before the rupture. This is attributed to the improvement of the stiffness properties of polymeric fiber with a decrease in the ambient temperature. Figure 11a shows the change in the value of plastic strain ( $\varepsilon_p$ ) as a function of temperature. The polymeric fiber became more brittle and its capacity to sustain plastic deformation under tension diminished and experienced less permanent strains or plastic deformations by encountering the rupture – that is the occurrence of failure – at smaller tensile elongations at colder temperature conditions. A linearly decreasing behavior was observed for the plastic strain ( $\varepsilon_p$ ) exhibited by the polymeric-micro-fibers in the tests with a decrease in the ambient temperature. The empirical relationship obtained for the plastic strain as a function of temperature is given in Equation 5 with a high value of coefficient of determination (CoD = 0.9932):

$$\varepsilon_p (\%) = 0.21x[T(^{\circ}C)] + 64.88 \quad (5)$$

where,  $\varepsilon_p$  : Amount of plastic strain (%), T : Temperature ( $^{\circ}C$ )

### 3.10. Toughness, $U_T$

Toughness can be defined as the ability of a material to absorb energy and experience full range of deformation both elastically and plastically during tensional elongation without rupturing [3, 7, 8]. Therefore, toughness, in physical meaning, can describe the amount of total energy per unit volume that a material can absorb before rupturing, and hence, toughness can be a proper measure for a polymeric material (PP micro-fiber) at what degree (severity) it shows a resistance against rupture when stressed. As such, toughness requires a balance of strength and ductility such that a material should be capable of withstanding both high stresses and high strains. The PP micro-fibers are highly ductile with the majority of the tested fibers experiencing a large amount of plastic deformation before the failure (breaking). For example, some of the fibers were able to elongate up to a maximum strain of more than 120% that resulted in a high energy absorption level. This is attributed to greater toughness properties of the micro-fibers signifying how much energy capacity they have to absorb before rupturing that is relevant to durability and long-term performance, while their strength implies only how much load resistance capacity they have to support and sustain over lifetime prior to failure. Further, the energy ingested (consumed) until rupture (toughness) under tensile force and elongation is essentially irreversible due to typical nature of the force-elongation behavior of the micro-fibers being predominantly plastic as opposed to resilience for which the energy absorbed is reversible such that the energy is released back upon unloading the material.

For the tested PP micro-fibers at different ambient temperatures, toughness ( $U_T$ ) was determined by integrating the area under the stress-strain curves so as to find the total energy of mechanical deformation, including elastic, elasto-plastic and plastic, per unit volume under tensile elongation up to the point of failure that will extend the understanding for the ability of the PP fibers at cold temperature conditions in absorbing mechanical energy. Toughness for the micro-fibers increased linearly with decreasing temperature (Figure 11b). This verifies that the area under the tensile stress versus axial strain curve enlarges with a decrease in the ambient temperature. Among several different types of regression analyses such as linear, exponential, polynomial performed on the computed values of toughness at different temperatures, the linear regression provided the best correlation between toughness and temperature with a higher coefficient of

determination (CoD) of 0.9839 much closer to 1 (Figure 11b). Therefore, it is noted that tensile toughness for the PP micro-fibers is a function of ambient temperature such that the energy absorbed per unit volume of the fibers rises when the ambient temperature becomes colder. The resulted empirical relationship (Equation 6) between toughness and temperatures is as follows:

$$U_T \text{ (J/m}^3\text{)} = -5 \times 10^6 [T(\text{ }^\circ\text{C})] + 4 \times 10^8 \tag{6}$$

where,  $U_T$  : Toughness (J/m<sup>3</sup>), T : Temperature (°C)

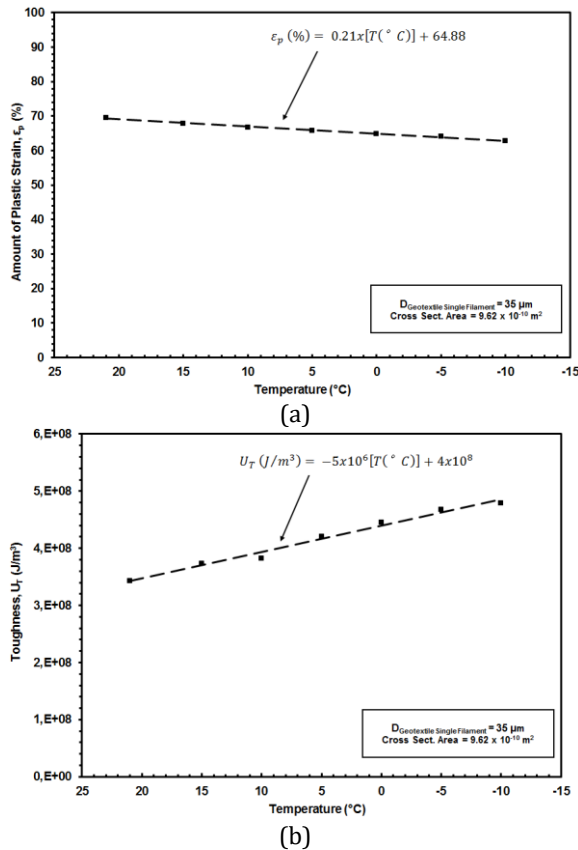


Fig. 11 Plastic Stage Mechanical Properties of the Micro-Fibers and Temperature:

(a) Amount of Plastic Strain ( $\epsilon_p$ ); (b) Toughness ( $U_T$ )

#### 4. Further Discussion on Experimental Findings

Based on the experimental findings of the study, the micro-mechanical properties of the PP fibers do not remain constant within the range of cold temperatures (-10 °C < T < 20 °C) encountered in typical infrastructural applications such that the ambient temperature change was found to be an important factor in affecting the polymeric fiber mechanical properties such as modulus, strength, toughness, ductility and most importantly, elastic (reversible) and plastic (irreversible) energy absorption of the micro-fibers under tensile elongation and their variation with ambient temperature. The amount of elastic energy absorption relative to the total magnitude of energy absorption (including elastic and

plastic) for the PP micro-fibers under tensile loading increases with decreasing temperature (Figure 12). This is attributed to the polymer characteristics of micro-fibers such that the resilience of the PP fibers at micro-state enhances as a result of a decrease in the ambient temperature. As such, the micro-fibers were able to absorb more energy while loaded under tensile elongation within the elastic limit without creating a permanent yielding before the transition zone – that is the elastic-to-plastic transformation – prior to exhibiting permanent deformations in plastic nature as seen from the stress versus strain envelopes (curves). As such, the amount of reversible energy during elastic elongation of the fibers under tensile force becomes greater as temperature decreases (Figure 12a) and this is associated with elastic properties of the PP micro-fibers becoming intensified (improved) at lower temperatures.

Moreover, the amount of plastic energy absorption relative to the total magnitude of energy absorbed by the micro-fibers prior to rupture (break) under tensile elongation decreases with decreasing ambient temperature (Figure 12b). This shows that the PP fibers become less ductile and losing from their flexibility properties at colder temperatures resulting in observing ruptures – that is fiber breakage – at smaller elongations (i.e. strains) when subjected to tensile loads. This could influence the durability properties of the fibers, and hence, the survivability and longevity properties of the geotextile fabric sheets made from the PP micro-fibers tested in the study when employed in the field for infrastructural applications exposed to cold temperature conditions. Furthermore, the capacity of a material in terms of the capability for plastic energy absorption is associated with its compliance properties, whereas, the ability of a polymeric material regarding elastic energy absorption is related to its resilience properties. Therefore, the ductility versus brittleness properties of the PP micro-fibers such as their characteristics being ductile or brittle is strongly ambient temperature dependent at micro-state in light of the experimental findings (Figures 12a and 12b).

Figure 12c shows that the ratio of plastic energy absorption with respect to elastic energy absorption decreases as the ambient temperature decreases from 21 °C down to -10 °C. In this perspective, it is noted that the PP micro-fibers become more resilient but less compliant due to a decrease in the ambient environmental temperature that should be considered by the design engineers in assessing the mechanical and durability properties of the geotextile fabrics at different ambient temperatures that is produced from these PP micro-fibers when employed in the infrastructural facilities subjected to varied environmental conditions including temperature. Additionally, the fiber strength can be considered as the major factor controlling geotextile micro-scale mechanical properties, and hence, its macro-scale mechanical response such as tensile strength being the primary function of a geotextile fabric sheets utilized in the civil engineering applications. To this end, the global (“macro-scale”) tensile response of nonwoven geotextiles, due to their fibrous inherent characteristics, is the summation of elastic elongations, inelastic (plastic) deformations in the micro-fibers as well as deformations due to the rearrangement of inherent internal structure including void space [12] which is not sensitive to temperature change [11, 13] in contrast to the elasto-plastic deformations of the polymeric micro-fibers under stress which is highly sensitive to the changes in the ambient conditions such as temperature as presented in the paper from the results of experimental program at micro-state. Therefore, a contradictory response was observed for the micro-fibers extracted from geotextile fabric sheets when tested at the “micro-scale” level - reported in the paper - as opposed to the response inferred from tests at the “macro-scale” level - published earlier by Andrawes et al. [11]. This primarily results from fibrous geotextile inherent characteristics having different “micro-structure” and “macro-structure” properties.

Moreover, the sudden change observed at a temperature of 0 °C to 5 °C is attributed to physico-chemical properties of the PP fibers such that the stretching of inter-atomic bonds

occurs when going through elastic elongation becomes lower as temperature decreases below 0 °C resulting in polymer molecular chains getting less straightened. On the other hand, as temperature increases above 5 °C, the relative displacement of molecules in the polymer takes place considerably during plastic deformation. For these reasons, there occurs a conversion in the behavior below 0 °C and above 5 °C such that at ambient temperatures particularly below 0 °C, the ratio of elastic energy absorption with respect to total energy absorption prior to rupture gets higher suddenly. On the other hand, at ambient temperatures particularly above 5 °C, the ratio of plastic energy absorption with respect to total energy absorption prior to rupture gets higher instantly.

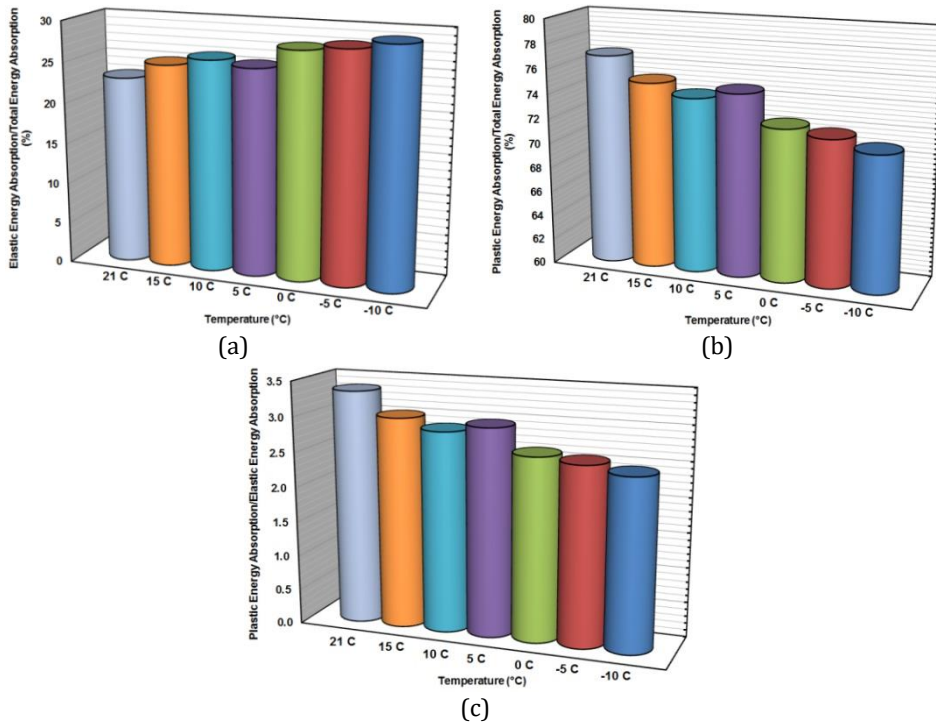


Fig. 12 Comparison of Elastic and Plastic Energy Absorption of the Micro-Fibers and their Variation with Ambient Temperature: (a) Elastic/Total (%) vs. Temperature; (b) Plastic/Total (%) vs. Temperature; (c) Plastic/Elastic vs. Temperature

## 5. Conclusions

The micro-fibers are used to manufacture nonwoven geotextile fabrics. Despite this fact, the previous studies were generally interested in mechanical and durability properties of geotextile fabrics at macro-state (global-scale). However, this study has been intended to provide unique as well as innovative aspect and carried out particularly for investigating the micro-mechanical properties of the fibers at micro-state and exploring the experimental methodology for their extensive characterization in the laboratory. In light of the information and the supplementary discussions provided throughout the paper regarding the influence of mechanical properties of the polymeric micro-fibers on the observed temperature dependent tensile stress versus axial strain behavior, the micro-mechanical response of the PP fibers were characterized by performing micro-scale mechanical tensile tests for which the testing method was adapted to a specialized

computer automated dynamic mechanical system called DMA. The results of the experimental program were used to determine the modulus of elasticity ( $E$ ), modulus of resilience ( $U_R$ ), ultimate tensile strength ( $T_{max}$ ), amount of plastic strain ( $\epsilon_p$ ), toughness ( $U_T$ ), rupture strength ( $T_R$ ) for the PP fibers extracted from NPNW geotextiles, and additionally, to investigate the variation of those important mechanical properties for a polymeric fiber with a decrease in the ambient temperature. Various test temperatures between  $-10\text{ }^\circ\text{C}$  and  $21\text{ }^\circ\text{C}$  were chosen to simulate the cold temperature range expected in the field for infrastructural applications in which the geotextile fabric sheets produced from the PP micro-fibers are employed.

The major impacts of cold temperatures on micro-mechanical properties of the polymeric fibers were the enhancement in ultimate tensile strength and the increase in material stiffness – due to molecular bonding strength of polymeric fibers – which resulted in the increment of amount of total energy absorbed (toughness) prior to rupture (failure) under tensile elongations. As such, the instantaneous temperature-dependent modulus for the range of test temperatures such as typical of geotechnical practice increased in a quadratic form showing that the PP micro-fibers at cooler temperatures are stiffer than that of at warmer ambient temperatures. Further, the enhancement of the PP fiber stiffness with decreasing temperature is attributed to the polymer material properties such that the polymeric fiber becomes harder and its capacity to sustain plastic deformation under tension is improved. The change in those mechanical properties of the PP micro-fibers is a function of ambient temperature variation.

The PP fiber specimens experienced the same failure mode such that they exhibited significant ductility under tensile elongation within the entire range of test temperatures from  $-10\text{ }^\circ\text{C}$  to  $21\text{ }^\circ\text{C}$ . Further, a similar trend for tensile stress versus axial strain response at all test temperatures was observed for the PP micro-fibers such that the tensile stress – axial strain curves have a nonlinear elasto-perfectly plastic form. The general pattern in stress-strain response of polypropylene fibers in the tension tests was visually portrayed in two segments: i) sharp increase to a maximum; then, ii) leveling off at higher strain levels such that the micro-fibers exhibited nearly constant resistances after yielding until they reached rupture at elongations between 100% and 120% axial strains. The elastic portion of the curves, before experiencing yield, develops with a relatively constant rate of change in tensile stress with respect to axial strain. Additionally, the resulting tensile stress versus axial strain curves for lower temperature tests are located on the upper part of the stress-strain space compared with that of the higher temperature tests. This shows that the tension failure envelopes grew (enlarged) as the ambient temperature decreased

## References

- [1] Nielsen LE., Mechanical properties of polymers and composites. Vol. 1, 2, Marcel Dekker Inc., NY, USA, 1974.
- [2] Painter PC, Coleman MM. Fundamentals of polymer science. 2nd Edition, CRC press, Boca Raton, FL, USA, 1997.
- [3] Zhai Z, Jiang B, Drummer D. "Temperature-dependent response of quasi-unidirectional E-glass fabric reinforced polypropylene composites under off-axis tensile loading," Composites Part B, Vol. 148, No. 4, 2018, pp. 180-187. <https://doi.org/10.1016/j.compositesb.2018.04.058>
- [4] Li J-H, Hsieh J-C, Lou C-W, Hsieh C-T, Pan Y-J, Hsing W-H, Lin J-H. "Needle punched thermally-bonded eco-friendly nonwoven geotextiles: Functional Properties," Materials Letters, Vol. 183, No. 6, 2016, pp. 77-80. <https://doi.org/10.1016/j.matlet.2016.07.074>

- [5] Mitchell JK, Seed RB, Seed HB. "Kettleman Hills Waste Landfill Slope Failure. I: Liner System Properties," *Journal of Geotechnical Engineering*, Vol. 116, No. 4, 1990, pp. 647-668. [https://doi.org/10.1061/\(ASCE\)0733-9410\(1990\)116:4\(647\)](https://doi.org/10.1061/(ASCE)0733-9410(1990)116:4(647))
- [6] Nielsen LE, Landel RF. *Mechanical Properties of Polymers and Composites*. Marcel Dekker, Inc., New York, NY, USA, 1994.
- [7] Dowling NE. *Mechanical behavior of materials*. 3rd Edition, Pearson Prentice Hall, Upper Saddle River, NJ, USA, 2007, 912p.
- [8] Youssefi M, Safaie B. "The study on the mechanical properties of multi-walled carbon nanotube/polypropylene fibers," *Journal of Institution of Engineers, India Series E*, Vol. 99, No. 1, 2018, pp. 37-42. <https://doi.org/10.1007/s40034-017-0110-3>
- [9] Stein RS, Powers J. *Topics in Polymer Physics*. Imperial College Press, London, UK, 2006, 414p. <https://doi.org/10.1142/p302>
- [10] Daniels C. *Polymers: Structure and Properties*. Technomic Publishing Company, Inc., Lancaster, PA, USA, 1989.
- [11] Andrawes KZ, McGown A, Kabir Md. H. "Uniaxial Strength Testing of Woven and Nonwoven Geotextiles," *Geotextiles and Geomembranes*, Vol. 3, No. 1, 1984, pp. 41-56. [https://doi.org/10.1016/0266-1144\(84\)90004-9](https://doi.org/10.1016/0266-1144(84)90004-9)
- [12] Kobler J, Schneider M, Ospald F, Andra H, Muller R. "Fiber orientation interpolation for the multiscale analysis of short fiber reinforced composite parts," *Computational Mechanics*, Vol. 61, No. 4, 2018, pp. 729-750. <https://doi.org/10.1007/s00466-017-1478-0>
- [13] Kumar NS, Shabaridharan K, Perumalraj R, Ilango, V. "Study on cross directional tensile properties of bamboo-/polypropylene-blended needle-punched non-woven fabrics," *Journal of Industrial Textiles*, Vol. 47, No. 6, 2018, pp. 1342-1356. <https://doi.org/10.1177/1528083717690611>
- [14] Osswald T, Menges G, *Material Science of Polymers for Engineers*. Hanser/Gardner Publications, Cincinnati, Ohio, USA, 1995.
- [15] Lunenschloss J, Albrecht W. *Non-Woven Bonded Fabrics*. J. Translation editor: Hock, Ellis Horwood, 1985, 549p.



Research Article

## Influence of sub-glass transition heat-treatment on physical and structural properties of $\text{Cu}_{46}\text{Zr}_{44}\text{Al}_8\text{Hf}_2$ metallic glass

Baran Sarac

*Erich Schmid Institute of Materials Science, Austrian Academy of Sciences, 8700 Leoben, Austria*

### Article Info

#### Article history:

Received 11 Aug 2020

Revised 24 Sep 2020

Accepted 28 Sep 2020

#### Keywords:

*Metallic glass;*  
*Heat-treatment;*  
*Dynamic mechanical analysis;*  
*Differential scanning calorimetry;*  
*Residual stress;*  
*X-ray diffraction*

### Abstract

The metastability of metallic glasses (MGs) can be altered via post-heat treatment around its glass transition temperature  $T_g$ . Here, the influence of the short-term heat treatment slightly below the glass transition on the thermal, thermomechanical, and structural properties are investigated. The water-cooled copper mold casting is used to produce the  $\text{Cu}_{46}\text{Zr}_{44}\text{Al}_8\text{Hf}_2$  MGs under argon gas. Heat treatment was performed by continuous heating at 20 °C/min to 400 °C, followed by immediate cooling. Samples were characterized by differential scanning calorimetry (DSC) and dynamic mechanical analysis (DMA) via continuously heating through its  $T_g$  and  $T_x$  (crystallization temperature) and by X-ray diffraction (XRD) in Bragg-Brentano ( $\theta - 2\theta$ ) geometry. Main findings observed are (1) an increase in the thermal stability,  $T_x - T_g$ , registered by DMA and DSC, (2) a remarkable drop of the relaxation enthalpy in the DSC trace calculated from the change in specific heat before  $T_g$ , (3) appearance of a third broad peak after heat-treatment in XRD, and (4) steady profile of  $E'$  below  $T_g$  correlated to the  $\beta$ -relaxation in DMA. The unexpected increase in  $\Delta T$  is linked to the release of the residual stresses accumulated during fast-quenching of the molten ingot down to room temperature. This stress can be estimated as 240 MPa on the outer surface and 100 MPa in the center of the cast CuZr-MG plates, which can be eliminated by the introduced heat-treatment method. Overall, this study suggests a direct and practical way to enhance the thermal stability and high strength retention of CuZr-based metallic glasses at elevated temperatures.

© 2021 MIM Research Group. All rights reserved.

## 1. Introduction

The thermodynamic behavior of complex alloy systems can reveal additional information such as mechanical damping, vibration-induced phase transformations and sensitive defect investigation compared to the conventional static-type characterization [1-7]. The instantaneously reversible elasticity, time-delayed viscoelasticity and time-dependent irreversible viscoplasticity are investigated experimentally and theoretically by applying a small vibrational load, which can be done at constant frequency or a range of frequencies during continuous heating or isothermal treatment [8-13]. Dynamic mechanical analysis (DMA) is nowadays used to identify the changes in the storage  $E'$  and loss  $E''$  moduli as a function of the glass transition and crystallization events of amorphous metallic alloys so-called (bulk) metallic glasses (B)MGs [14-24].

The transition of the metastable glasses to a stable configuration is called physical aging or structural relaxation by the annihilation of excess free volume [25], while isoconfigurational glassy state dynamics obey the Arrhenius behavior [26, 27]. The relaxation phenomenon has two major components: main ( $\alpha$ ) and secondary ( $\beta$  or excess wing) [28, 29]. The  $\alpha$  relaxation is mainly linked to the cooperative motion of atoms or

Corresponding author: [baran.sarac@oeaw.ac.at](mailto:baran.sarac@oeaw.ac.at)

[orcid.org/0000-0002-0130-3914](https://orcid.org/0000-0002-0130-3914);

DOI: <http://dx.doi.org/10.17515/resm2020.205ma0811>

Res. Eng. Struct. Mat. Vol. 7 Iss. 1 (2021) 121-134

molecules in the liquid, whereas the secondary relaxation can be described as the local noncooperative motion of molecules or atoms [30, 31]. Some metallic glass classes show a prominent  $\beta$ -relaxation peak [32, 33], whereas others do not show a pronounced secondary peak but an excess wing of the  $\alpha$  relaxation peak [29, 34, 35].

In the class of metallic glass, CuZr-MGs exhibit appealing glass-forming ability with cooling rates down to 10 K/s, allowing them to be cast into mm-thick samples [36]. They possess higher yield strength (up to 2.5 GPa [37, 38]) close to the theoretical limit, up to 2.6% elastic strain at room temperature [39, 40], and acceptable fracture toughness of up to 100 MPa m<sup>-1/2</sup> [41]. Recent investigations on the isothermal annealing of BMGs below the glass-transition temperature  $T_g$  revealed the pronounced changes in terms of mechanical and thermal properties due to the structural relaxation, and in turn, the annihilation of free volume stored in MGs upon casting [42-55]. Among them, Li *et al.* has shown that although no pronounced changes are observed for the DSC trace, annealing close to sub- $T_g$  for a long duration can lead to brittle behaviour with nearly-zero fracture energy [43]. The long-term thermal annealing at temperatures below  $T_g$  for Zr-containing metallic glasses was proven to originate from the temporary structural relaxation with an additional endotherm in the glass transition region, which can be fully reversed by the subsequent heat treatment for a short term above  $T_g$  [42]. Thus, the endotherm observed in differential scanning calorimetry (DSC) right after  $T_g$  is accounted for by the time-dependent relaxation process during sub- $T_g$  annealing. Another study from the same group has shown that the difference between the fictive (determined from calorimetry) and critical fictive (determined from annealing and 3-point bend test) temperatures defines their mechanical behaviour and its sensitivity to rate of cooling and annealing conditions [56]. In addition to the annihilation of free volume, phase devitrification can be also observed for the Zr<sub>57</sub>Ti<sub>8</sub>Nb<sub>2.5</sub>Cu<sub>13.9</sub>Ni<sub>11.1</sub>Al<sub>7.5</sub> [57] and Zr<sub>55</sub>Cu<sub>30</sub>Al<sub>10</sub>Ni<sub>5</sub> [58] alloys depending on the isothermal treatment temperature and time.

It has been confirmed in the literature that the sub- $T_g$  annealing induced structural reordering of Cu and Zr atoms leads to limited diffusion on the nanometer-scale registered by the synchrotron X-ray diffraction (XRD), which eventually results in considerable compressive plasticity [58-60]. This improvement was linked to the chosen heat treatment path: continuous heating to the desired sub- $T_g$ , wait for several minutes until the temperature is stabilized, followed by rapid cooling to the desired temperature. For the Zr<sub>35</sub>Ti<sub>30</sub>Cu<sub>7.5</sub>Be<sub>27.5</sub> with larger glass forming ability, our group has proven that the mechanical properties of the 2D honeycombs [46] and periodic heterostructures [45] do not alter for long-term isothermal heat treatment (18 h and below) even if the sub- $T_g$  annealing is performed only 25 °C below its glass transition.

The influence of sub- $T_g$  annealing on CuZr-based metallic glasses was also studied in detail by our group. In the first study, Cu<sub>46</sub>Zr<sub>44</sub>Al<sub>8</sub>Hf<sub>2</sub> composition was used, and various characterizations including DSC, dilatometry, 3-point bend-test, parallel-plate rheometry, XRD and transmission electron microscopy was conducted on a range of heat-treated samples below and above its  $T_g$  [49]. In the second article, by using the same material, we have analysed the differences in the atomic configuration on the optimized sample (heat-treated at 400 °C) and the as-cast state using reciprocal and real space analysis with the data acquired from the synchrotron XRD measurements [61].

Here, we present that the thermomechanical, thermophysical and structural properties of Cu<sub>46</sub>Zr<sub>44</sub>Al<sub>8</sub>Hf<sub>2</sub> metallic glasses are altered by continuous heating and subsequent cooling treatment. Thin sheets prepared from the mm-sized cast plate were subjected to  $\mu$ m-scale oscillating displacements in a 3-point bending mode.  $E'$ ,  $E''$  and  $\tan\delta$  values, particularly

around the supercooled liquid region and sub-glass transition were compared to the as-cast state sample. The structural properties of each sample were characterized by XRD, whereas the continuous heating traces of the standard DSC were comparatively evaluated. The modifications are linked to the residual stresses imposed during casting and their release via the post-heat treatment process.

## 2. Material and Method

The master alloy of  $\text{Cu}_{46}\text{Zr}_{44}\text{Al}_8\text{Hf}_2$  was prepared from elements with purity higher than 99.99% by arc-melting (Edmund Bühler GmbH) in an argon atmosphere purified by Ti getter. The master alloys were heated above the liquidus temperature three times to homogenize the ingot. The water-cooled copper mold casting into plate shape with  $75 \times 10 \times 1 \text{ mm}^3$  was conducted under the Ar atmosphere using an in-situ suction casting device attached to Edmund Bühler Arc Melter. Part of the rods was inserted in the TA Discovery Hybrid Rheometer DHR-3 and brought to  $400 \text{ }^\circ\text{C}$  at a heating rate of  $20 \text{ }^\circ\text{C}/\text{min}$  under  $\text{N}_2$  atmosphere. After a lag time of 5 seconds, samples were immediately cooled to  $150 \text{ }^\circ\text{C}$  at a cooling rate of  $50 \text{ }^\circ\text{C}/\text{min}$  and subsequently water-quenched to room temperature. All the samples were ground and polished, where the final samples were  $8.0 \pm 1.0 \text{ mm}$  in length and  $4.5 \pm 0.3 \text{ mm}$  in width with a thickness of  $0.50 \pm 0.05 \text{ mm}$ . Differential scanning calorimetry (DSC) measurements were performed with a Mettler Toledo DSC 3+ under Ar atmosphere at a constant heating rate of  $20 \text{ }^\circ\text{C}/\text{min}$  with  $20.0 \pm 0.5 \text{ g}$  polished samples. Dynamic mechanical analysis (DMA) was performed in three-point bending mode using a TA Discovery Hybrid Rheometer DHR-3 in the temperature range  $50 \text{ }^\circ\text{C} - 600 \text{ }^\circ\text{C}$  with a heating and cooling rate of  $10 \text{ }^\circ\text{C}/\text{min}$  and a frequency of  $1 \text{ Hz}$  for a  $20 \text{ }\mu\text{m}$  oscillation displacement which generates the oscillation stress. A constant preload of  $25 \text{ N}$  was applied. Nitrogen was used as purging gas during the experiments. The samples were examined by X-ray diffraction (XRD) in Bragg-Brentano ( $\theta$ - $2\theta$ ) geometry using a Bruker D2Phaser diffractometer with  $\text{Co K}\alpha$  radiation ( $\lambda = 1.7089 \text{ \AA}$ ) using a step size of  $0.02$ .

## 3. Results

Since the temperature stabilization can be precisely controlled and rapidly satisfied in the DMA furnace, the samples were cooled immediately after heating (with a lag time of 5 seconds). This procedure is different from the previous heat treatment studies performed in a standard calibrated furnace, where 5 minutes of isothermal heat treatment was applied both for temperature stabilization and atomic reconfiguration [49]. Figure 1 compares the as-cast sample with the heat-treated sample at  $400 \text{ }^\circ\text{C}$  for 5 minutes. The first broad amorphous X-ray diffraction maximum does not visibly change upon heat treatment, whereas the second broad maximum shifts slightly towards a larger  $2\theta$  (Table 1). In amorphous structures, X-rays are scattered in many directions yielding a broad diffraction peak distributed in a wide range of  $2\theta$  instead of high intensity narrower peaks [62]. The first and second broad amorphous X-ray diffraction maximum,  $Q_1 = 1.36 \text{ \AA}^{-1}$  and  $Q_2 = 2.35 \text{ \AA}^{-1}$ , respectively, is defined by the configuration of the nearest neighbor shell atoms. A detailed synchrotron XRD analysis using the same composition was performed by our group, which indicates the probabilities of the most abundant atomic pairs, Zr-Cu, followed by Cu-Cu and Zr-Zr, respectively [61]. A third peak for the heat-treated sample at  $101^\circ$  with  $Q_3 = 5.42 \text{ \AA}^{-1}$  emerges due to the reconfiguration of these atomic pairs within the amorphous clusters. Thus, compared to our previous XRD findings [49, 61], the heat treatment environment and time for heat treatment seems to influence the type of medium-to-long-range order changes.

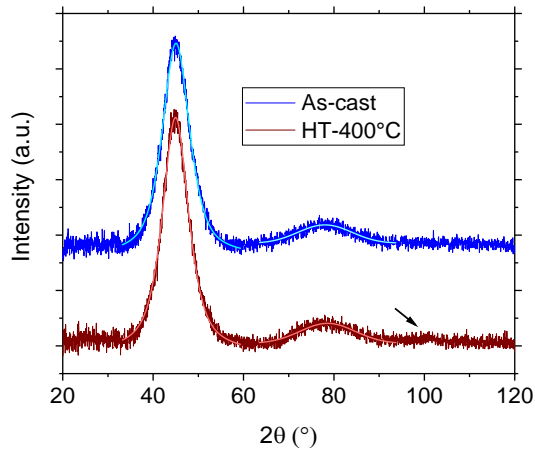


Fig. 1 X-ray diffraction patterns of the as-cast (blue) and heat-treated at 400 °C (wine). The black arrow indicates the small hump observed for the HT-400°C sample. Pseudo-Voigt fitting (Cyan and light red colors) was applied to find the peak positions.

The DSC traces of the as-cast and HT-400°C samples in Figure 2 registered the slight shift in  $T_g$  towards smaller temperatures (by 5 °C). On the other hand, no change is observed for the crystallization temperature ( $T_x = 510$  °C). Thus, the supercooled liquid region (SCLR),  $\Delta T = T_x - T_g$ , becomes larger with the short-term sub- $T_g$  heat treatment, confirming the existence of structural modifications observed in the XRD diffractogram. The relaxation enthalpy before the relaxation endotherm,  $\Delta H_{relax}$ , shows a pronounced decrease as well as the change in the shape of the area, i.e. for the HT-400°C sample, specific heat ( $c_p$ ) does not drop during relaxation as in the case for the as-cast samples. Thus, similar to our previous study, the stored free-volume in the metallic glass during casting is partially consumed by this heat treatment process without a significant degree of change in  $T_g$  and  $T_x$  [60].

Since the temperature stabilization can be precisely controlled and rapidly satisfied in the DMA furnace, the samples were cooled immediately after heating (with a lag time of 5 seconds). Figure 3 shows the before and after DMA measurement image of the representative as-cast sample. The metallic shiny and flat samples deform in the SCLR due to the dramatic drop in viscosity by roughly an order of magnitude per every 20 °C increase [63-65]. As a result, the samples were bent  $\sim 90^\circ$  under small amounts of applied loads (25 N), while the surface was oxidized and became black.

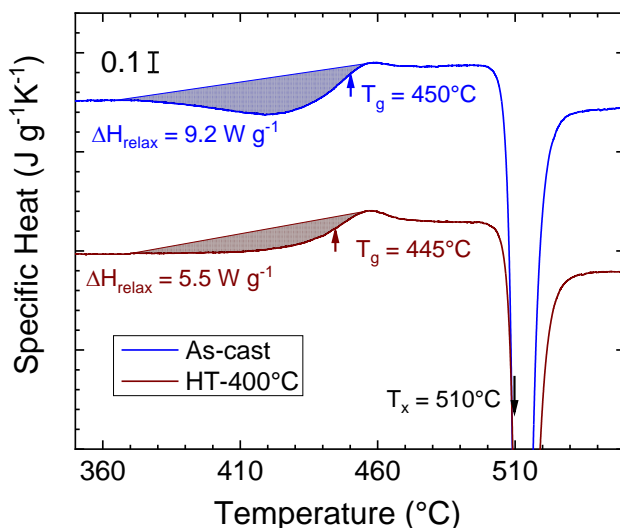


Fig. 2 Specific heat calculated from the DSC traces as a function of temperature for the as-cast (blue) and HT-400°C (wine) samples.  $T_{g\text{as-cast}} = 450 \pm 2^\circ\text{C}$ ,  $T_{g\text{HT-400}^\circ\text{C}} = 445 \pm 2^\circ\text{C}$ ,  $T_x = 510 \pm 2^\circ\text{C}$ ,  $\Delta H_{\text{relaxas-cast}} = 9.2 \pm 0.5 \text{ W g}^{-1}$ , and  $\Delta H_{\text{relaxHT-400}^\circ\text{C}} = 5.5 \pm 0.5 \text{ W g}^{-1}$ .

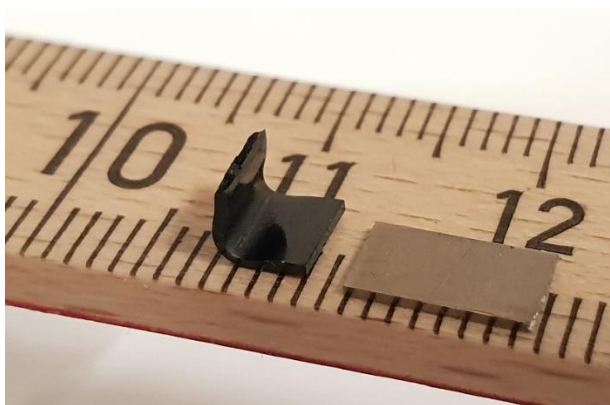
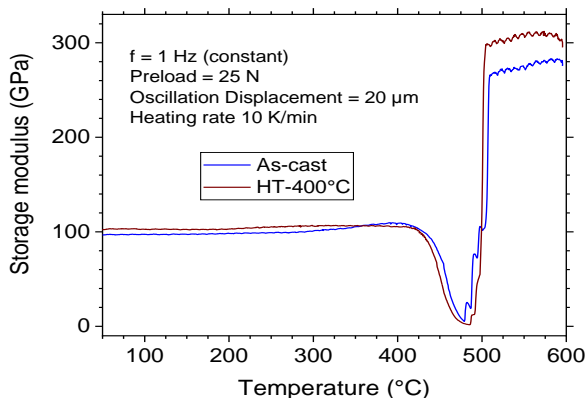


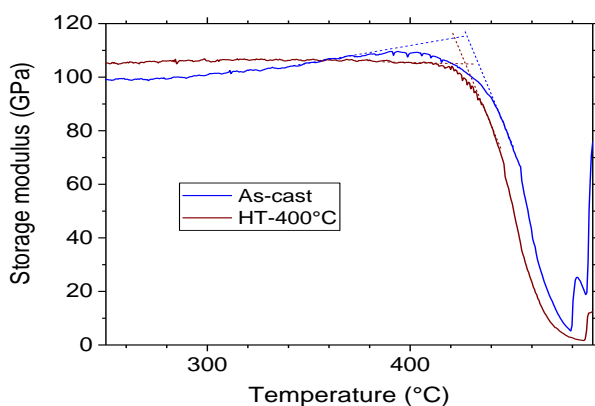
Fig. 3 CuZr-based MG samples prepared for the three-point bending test. The flat, metallic gray sample (right) is the representative as-cast state sample—the sample bends during continuous heating in its SCLR under a small static load (left).

The deformation profiles of the as-cast and HT-400°C samples are displayed in Figure 4a. A relatively constant storage modulus is observed for both samples until 275 °C. After this temperature, the as-cast state sample stiffens by the rise of the storage modulus  $E'$  from 99 GPa to 110 GPa. On the other hand, no remarkable change of the  $E' = 105 \text{ GPa}$  for the HT-400°C is observed. This is because of the increase in  $E'$  below  $T_g$  related to  $\beta$ -transition disappears after the sub- $T_g$  heat treatment. The  $T_g$  determined from the  $E'$  onset (intersection of the dashed lines in Figure 4b) yields the values of 427 and 415 °C for the

as-cast and HT-400°C, respectively. Since the  $T_g$  determined from the  $E'$  onset being related to mechanical failure, it can be concluded that the sub- $T_g$  annealing causes embrittlement, which can lead to early catastrophic failure, as reported in [42, 45, 46, 56]. After full crystallization, the storage modulus immediately exceeds the storage modulus of the initial states.



(a)

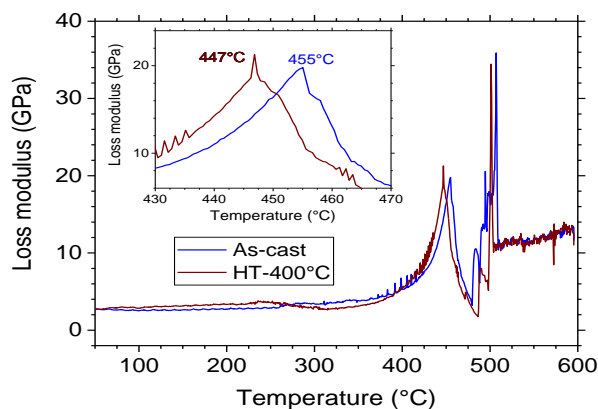


(b)

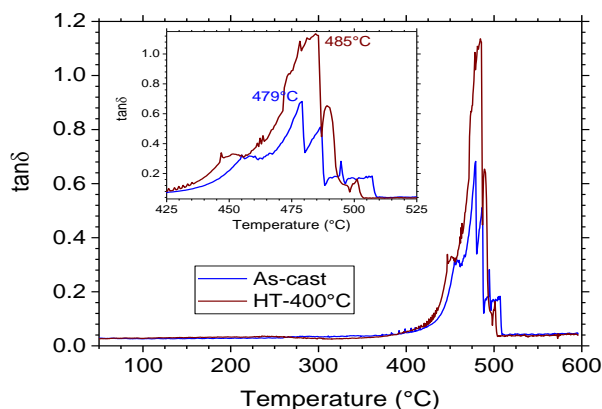
Fig. 4 (a) Overview and (b) magnified traces of the storage modulus ( $E'$ ) vs. temperature ( $T$ ) of the MG determined from three-point bending, under continuous heating at a heating rate of 10 °C/min and a frequency of 1 Hz between 50°C and 600 °C. The temperature accuracy is within  $\pm 2$  °C.

Figure 5a depicts the loss modulus,  $E''$ , as a function of temperature.  $T_g$  values determined from the  $E''$  peaks are 455 °C and 447 °C for the as-cast and HT-400°C samples, respectively. This peak corresponds to the temperatures where the viscous drop already begins, and thus, is more closely related to the physical property changes obtained from the differential scanning calorimetry (c.f. Figure 2). Compared to  $E'$  and  $E''$ ,  $\tan\delta = E''/E'$  shows the peak at the highest temperature; for the as-cast and HT-400°C samples, these values are 479°C and 485°C, respectively. This point corresponds to the bottom points at the  $E'$  vs.  $T$  graph in Figure 4b, indicating the full crystallization,  $T_x$ . The extent of the SCLR

is larger for the heat-treated sample, corroborating our DSC results. It is known that the height and shape of the  $\tan\delta$  peak change systematically with amorphous content.  $\tan\delta_{\max}$  for the HT-400°C is 1.14, much higher than the 0.68; moreover, it is slightly broader than the as-cast state sample. The summary of the findings of the DSC, DMA and XRD studies are given in Table 1.



(a)



(b)

Fig. 5 (a) The loss modulus ( $E''$ ) and (b)  $\tan\delta$  vs. temperature ( $T$ ) of the MG determined from three-point bending, under continuous heating at a heating rate of 10 °C/min and a frequency of 1 Hz between 50 °C and 600 °C. The temperature accuracy is within  $\pm 2$  °C.

Our findings hint that the as-cast state sample might have residual stresses imposed upon casting, which can arrest the free volume in MGs. On the other hand, the post-heat treatment releases these stresses and contributes to the free volume. The residual stresses imposed on the sample upon quenching and the influence of post-heat treatment on the stress release are shown in the discussion part.

Table 1. Comparison of DSC, DMA and XRD data of the as-cast and heat-treated samples. Note that the temperature accuracy for the DSC and DMA measurements is within  $\pm 2$  °C, and the enthalpy of relaxation is within  $\pm 0.5$  W g<sup>-1</sup>; the storage and loss modulus is within  $\pm 3$  GPa, and XRD accuracy is within  $\pm 0.02$ °.

DSC	$T_g$ (°C)	$T_x$ (°C)	$\Delta T$ (°C)	$\Delta H_{relax}$ (W g <sup>-1</sup> )
As-cast	450	510	60	9.2
HT-400°C	445	510	65	5.5
DMA	$T_g(E'_{onset})$ (°C)	$T_g(E''_{peak})$ (°C)	$T_x(tan\delta_{peak})$ (°C)	$\Delta T'$ (°C)
As-cast	427	455	479	52
HT-400°C	415	447	485	70
DMA	$\Delta T'$ (°C)	$E' @ 275$ °C	$E'_{onset}$	$\tan\delta$
As-cast	24	99	110	0.68
HT-400°C	38	105	105	1.14
XRD	1 <sup>st</sup> peak (°)	2 <sup>nd</sup> peak (°)	3 <sup>rd</sup> peak (°)	
As-cast	45.06	78.02	N/A	
HT-400°C	44.96	78.60	101.02	

#### 4. Discussion

The cooling rate of a plate can be estimated from the finite element modeling of the BMG ingots fabricated by the copper mold casting, where the obtained cooling rates of samples were in a linear agreement with the variation of sample diameter [66]. For the plate geometry, the equation to obtain the cooling rate  $R$  was slightly modified as:

$$R = 15800 / (\sqrt{4 * (w * t) / \pi})^{1.92} \quad (1)$$

where  $w$  and  $t$  are the width and thickness of the cast plate, respectively. For  $t = 1$  mm and  $w = 10$  mm, the cooling rate can be estimated as  $R \sim 1375$  °C/s. For metallic glasses, a remarkable slow-down is viscosity, and in turn, the atomic mobility is observed due to the decrease in the number of metastable configurations that glass can be present [67]. For this reason, we can estimate the heat transfer coefficient  $h$  from the cooling rate at  $T_g$  by:

$$h = \frac{R * V * c_p * \rho}{S * (T_g - T_f)} \quad (2)$$

where  $V = L * w * t$  is the volume of the cast rod ( $L = 75$  mm length of the rod),  $c_p$  the specific heat and  $\rho$  the density of the BMG,  $S = 2(L * w + w * t + L * t)$  the surface area and  $T_f = 298$  K the final temperature of the cast rod, respectively.  $c_p$  and  $\rho$  are determined by the continuous heating curve of a similar CuZrAl-based BMG and Archimedes' method as  $c_p \sim 450$  J kg<sup>-1</sup> °C<sup>-1</sup> and  $\rho = 6970$  kg m<sup>-3</sup>, respectively [68].  $T_g = 700$  K is selected from the  $E'$  onset in Fig. 4b to reflect the mechanical property changes. Inserting these values into the equation (2) yields  $h \sim 4820$  W m<sup>-2</sup> K<sup>-1</sup>. From the correlation between the hoop stress vs  $h$  in Fig. 6 of ref. [69] the compressive ( $\sigma_{cres}$ , outer region) and tensile ( $\sigma_{tres}$ , center region) residual stresses can be estimated as  $\sigma_{cres} = 240$  MPa and  $\sigma_{tres} = 100$  MPa. The mold material, i.e. whether it is stainless steel or copper, has a negligible influence on the RT stress state of the as-cast BMG rod. This is mainly because the metallic mold is

elastic throughout the casting process, and the residual stresses in as-cast BMGs are hardly influenced by the mold material and its shape (maximum by 3%) [69]. Hence, the elastic stresses are relaxed after removing the mold, leaving only the residual stress in the cast-BMG.

From our previous dilatometry measurements for the same composition, the thermal expansion coefficient can be retrieved as  $\alpha = 1.124 \times 10^{-5} \text{ K}^{-1}$  [49]. Hence, the continuous heating to 400 °C from RT creates counter stress according to:

$$\sigma_{xx} = E(x) * \alpha(x) * \Delta T \quad (3)$$

where  $x$  is an arbitrary direction showing linearity,  $E = 97 \text{ GPa}$  (obtained from the DMA data) and  $\Delta T = 375 \text{ K}$ . If we assume an isotropic stress annihilation, then  $\sigma = 410 \text{ MPa}$ . Assuming that a further stress release is possible while temperature stabilization and subsequent rapid quenching to minimize any post-shrinkage, the considered BMG is fully released from the residual stresses.

The complete annihilation of the residual stresses is also reflected in the thermal, thermomechanical and structural properties of the considered CuZr-based MG. As expected, the sample structurally relaxes after the sub- $T_g$  heat treatment, as revealed by the drop in the relaxation enthalpy and  $T_g$  registered in Fig. 2. This special heat treatment, on the contrary to general heat treatment processes of MGs around and above  $T_g$ , increases the thermal stability of the alloy ( $\Delta T$ ), which can be linked to the percolation of locally favoured clusters within the amorphous matrix which does not lead to observable crystallinity [70]. This change in local scale is also reflected in the new peak at  $101^\circ$  (corresponding to  $d = 1.09 \text{ \AA}$ ) observed by the XRD study in Fig. 1. The release of the residual stresses results in a plateau with a relatively constant storage modulus of 105 MPa compared to the remarkable stiffening effect observed for the as-cast sample (Fig. 4 and Table 1). Moreover, this stress release yields a significant decrease in  $T_g$  measured both from the  $E'_{onset}$  and  $E''_{peak}$  and increase in  $T_x$  measured from the  $\tan\delta_{peak}$ , which in turn increases the  $\Delta T$ .

## 5. Conclusions

In this contribution, direct evidence is provided that the thermomechanical properties of CuZr-based MGs under sinusoidal oscillating stress being altered by continuous heating to 50 °C below  $T_g$ , and rapidly cooled to room temperature after temperature balance. The findings clearly indicate that the sub- $T_g$  heat treatment modifies the short-to-medium range ordering in metallic glass corroborated with the appearance of the 3<sup>rd</sup> broad hump in XRD. The sub- $T_g$  heat treatment accounts for the stress release which alters the thermomechanical and thermophysical properties. In this regard, the heat-treated sample has high thermal stability and stiffness retention at elevated temperatures.

The key novelties are: (1) This study is a continuous heating and cooling type heat treatment process without having a relatively long term (~5 min) heat treatment. (2) This is the first time in the literature that influence of the sinusoidal oscillating stress applied via DMA on the thermomechanical properties has been assessed for the heat-treated CuZr-based metallic glasses. (3) This study links the correlation between thermophysical, thermomechanical and structural properties via the adopted heat treatment and the correlated release of the residual stresses.

The metallic shiny and flat samples are bent  $\sim 90^\circ$  under small amounts of applied static load (25 N) and oscillation displacement (20  $\mu\text{m}$ ), and the surface becomes oxidized during dynamic mechanical analysis (DMA) three-point bending experiment. The broad,

amorphous peaks for the as-cast sample do not differ after the heat treatment; however, a small third broad peak at 101° emerges. The differential scanning calorimetry (DSC) traces indicate an increase in  $T_g$  by 5 °C after heat-treatment. The enthalpy of relaxation  $\Delta H_{\text{relax}}$ , on the other hand, decreases significantly from 9.2 W g<sup>-1</sup> to 5.5 W g<sup>-1</sup>, confirming the changes in the configurational state. DMA performed in the three-point bending mode reveals that  $E'$  shows a steady profile after sub- $T_g$  annealing. The  $T_g$  and crystallization temperature  $T_x$  determined from the onset of the decrease in the loss modulus  $E''$  and the peak positions of  $\tan \delta$ , respectively, suggests that  $T_g$  and  $\Delta T$  are larger for the HT-400°C sample in line with the DSC findings. On the other hand,  $T_g$  measured from the onset of the storage modulus  $E'$ , indicating the sudden changes in the mechanical properties, is 12 °C larger for the as-cast state sample. The crystallization temperature  $T_x$  of the HT-400°C sample determined from the  $\tan \delta$  is 6 °C higher, confirming a remarkable difference between the supercooled liquid regions (cf.  $\Delta T = 54$  °C for as-cast and  $\Delta T = 72$  °C for HT-400 °C samples). The unusual increase affirmed by the DSC and DMA analyses is accounted for by the residual stresses imposed on the sample during rapid quenching. The mathematical estimations to find these cumulative stresses yield 240 MPa and 100 MPa on the outer surface and center of the cast plate, respectively. Due to the linear expansion of the cast plates upon continuous heating, the residual stresses can be fully released by the subsequent sub- $T_g$  heat-treatment.

### Acknowledgement

The author thanks Mr. Amir Rezvan, who has prepared the samples and heat-treated the MG for the 3-point bending test. The author gratefully acknowledges the financial support of the Austrian Science Fund (FWF) under project grant I3937-N36 (PI: Baran Sarac).

### References

- [1] Liao GY, Chen B, Meng QK, Wang MJ, Zhao XQ. Strain glass in defect-containing ferroelastic Ti44Ni51Nb5 alloy. *Rare Metals*. 2015; 34: 829 - 832. <https://doi.org/10.1007/s12598-014-0229-z>
- [2] Prasad DS, Ebenezer NS, Shoba C, Pujari SR. Effect of nickel electroplating on the mechanical damping and storage modulus of metal matrix composites. *Mater Res Express*. 2018; 5: 116409. <https://doi.org/10.1088/2053-1591/aadf0b>
- [3] Kim JT, Soprunyuk V, Chawake N, Zheng YH, Spieckermann F, Hong SH, et al. Outstanding strengthening behavior and dynamic mechanical properties of in-situ Al-Al3Ni composites by Cu addition. *Composites, Part B*. 2020; 189: 107891. <https://doi.org/10.1016/j.compositesb.2020.107891>
- [4] Junker P, Kochmann DM. Damage-induced mechanical damping in phase-transforming composites materials. *Int J Solids Struct*. 2017; 113: 132 - 146. <https://doi.org/10.1016/j.ijsolstr.2017.01.040>
- [5] Jin XJ, Liu JY, Jin MJ. Martensitic transformation and precursor phenomena in Au7Cu5Al4 alloys. *J Alloys Compd*. 2013; 577: S155 - S158. <https://doi.org/10.1016/j.jallcom.2012.04.072>
- [6] Salva HR, Fabietti LM, Ghilarducci AA, Urreta SE. Mechanical damping in nanostructured Nd60Fe30Al10 magnetic alloys. *J Alloys Compd*. 2010; 495: 420 - 422. <https://doi.org/10.1016/j.jallcom.2009.10.012>
- [7] Wu SK, Chang SH, Chou TY, Tong S. Low-frequency damping properties of dual-phase Mg-xLi-0.5Zn alloys. *J Alloys Compd*. 2008; 465: 210 - 215. <https://doi.org/10.1016/j.jallcom.2007.10.134>
- [8] Pelletier JM, Perez J, Duffrene L. Mechanical response of an oxide glass to mechanical loading-shear and volume relaxation effects: physical analysis. *Acta Mater*. 2000; 48: 1397 - 1408. [https://doi.org/10.1016/S1359-6454\(99\)00387-0](https://doi.org/10.1016/S1359-6454(99)00387-0)

- [9] Wang Q, Pelletier JM, Blandin JJ. Thermal stability of cerium-based bulk metallic glasses. Influence of iron addition. *J Alloys Compd.* 2010; 504: 357 - 361. <https://doi.org/10.1016/j.jallcom.2010.05.070>
- [10] Jeong HT, Fleury E, Kim WT, Kim DH, Hono K. Study on the mechanical relaxations of a Zr<sub>36</sub>Ti<sub>24</sub>Be<sub>40</sub> amorphous alloy by time-temperature superposition principle. *J Phys Soc Jpn.* 2004; 73: 3192 - 3197. <https://doi.org/10.1143/JPSJ.73.3192>
- [11] Ulutan D, Sima M, Özel T. Prediction of Machining Induced Surface Integrity Using Elastic-Viscoplastic Simulations and Temperature-Dependent Flow Softening Material Models in Titanium and Nickel-Based Alloys. *Adv Mater Res.* 2011; 223: 401 - 410. <https://doi.org/10.4028/www.scientific.net/AMR.223.401>
- [12] Wang J, Xu Y, Zhang W, Moumni Z. A damage-based elastic-viscoplastic constitutive model for amorphous glassy polycarbonate polymers. *Mater Des.* 2016; 97: 519 - 531. <https://doi.org/10.1016/j.matdes.2016.02.118>
- [13] Asadian H, Shelesh-Nezhad K. Simulation of dynamic mechanical and viscoelastic behavior in polymer/clay nanocomposites. *Polym Compos.* 2020; 41: 817 - 823. <https://doi.org/10.1002/pc.25412>
- [14] Wang WH. Dynamic relaxations and relaxation-property relationships in metallic glasses. *Prog Mater Sci.* 2019; 106: 100561. <https://doi.org/10.1016/j.pmatsci.2019.03.006>
- [15] Datye A, Ketkaew J, Schroers J, Schwarz UD. Effect of the fictive temperature on the modulus, hardness, yield strength, dynamic mechanical and creep response of Zr<sub>44</sub>Ti<sub>11</sub>Cu<sub>10</sub>Ni<sub>10</sub>Be<sub>25</sub> metallic glasses. *J Alloys Compd.* 2020; 819: 152979. <https://doi.org/10.1016/j.jallcom.2019.152979>
- [16] Qiao JC, Chen YH, Casalini R, Pelletier JM, Yao Y. Main  $\alpha$  relaxation and slow  $\beta$  relaxation processes in a La<sub>30</sub>Ce<sub>30</sub>Al<sub>15</sub>Co<sub>25</sub> metallic glass. *J Mater Sci Technol.* 2019; 35: 982 - 986. <https://doi.org/10.1016/j.jmst.2018.12.003>
- [17] Sergiienko RA, Shcheretskyi OA, Zadorozhnyy VY, Verkhovliuk AM, Louzguine-Luzgin DV. Investigation of Zr<sub>55</sub>Cu<sub>30</sub>Al<sub>10</sub>Ni<sub>5</sub> bulk amorphous alloy crystallization. *J Alloys Compd.* 2019; 791: 477 - 482. <https://doi.org/10.1016/j.jallcom.2019.03.270>
- [18] Louzguine-Luzgin DV, Zadorozhnyy MY, Ketov SV, Jiang J, Golovin IS, Aronin AS. Influence of cyclic loading on the structure and double-stage structure relaxation behavior of a Zr-Cu-Fe-Al metallic glass. *Mater Sci Eng, A.* 2019; 742: 526 - 531. <https://doi.org/10.1016/j.msea.2018.11.031>
- [19] Ruta B, Pineda E, Evenson Z. Relaxation processes and physical aging in metallic glasses. *J Phys: Condens Matter.* 2017; 29: 503002. <https://doi.org/10.1088/1361-648X/aa9964>
- [20] Qiao JC, Wang Q, Pelletier JM, Yao Y. Relaxation of Ni-free Ti<sub>40</sub>Zr<sub>10</sub>Cu<sub>36</sub>Pd<sub>14</sub> bulk metallic glass under mechanical stress. *Intermetallics.* 2018; 102: 6 - 10. <https://doi.org/10.1016/j.intermet.2018.08.009>
- [21] Qiao JC, Cong J, Wang Q, Pelletier JM, Yao Y. Effects of iron addition on the dynamic mechanical relaxation of Zr<sub>55</sub>Cu<sub>30</sub>Ni<sub>5</sub>Al<sub>10</sub> bulk metallic glasses. *J Alloys Compd.* 2018; 749: 262 - 267. <https://doi.org/10.1016/j.jallcom.2018.03.285>
- [22] Frey M, Busch R, Possart W, Gallino I. On the thermodynamics, kinetics, and sub-T<sub>g</sub> relaxations of Mg-based bulk metallic glasses. *Acta Mater.* 2018; 155: 117 - 127. <https://doi.org/10.1016/j.actamat.2018.05.063>
- [23] Yamada R, Tanaka N, Guo W, Saida J. Crystallization behavior of thermally rejuvenated Zr<sub>50</sub>Cu<sub>40</sub>Al<sub>10</sub> metallic glass. *Mater Trans.* 2017; 58: 1463 - 1468. <https://doi.org/10.2320/matertrans.MAW201703>
- [24] Sarac B, Spieckermann F, Rezvan A, Gammer C, Krämer L, Kim JT, et al. Annealing-assisted high-pressure torsion in Zr<sub>55</sub>Cu<sub>30</sub>Al<sub>10</sub>Ni<sub>5</sub> metallic glass. *J Alloys Compd.* 2019; 784: 1323 - 1333. <https://doi.org/10.1016/j.jallcom.2019.01.063>

- [25] Yavari AR, Le Moulec A, Inoue A, Nishiyama N, Lupu N, Matsubara E, et al. Excess free volume in metallic glasses measured by X-ray diffraction. *Acta Mater.* 2005; 53: 1611 - 1619. <https://doi.org/10.1016/j.actamat.2004.12.011>
- [26] Ruta B, Chushkin Y, Monaco G, Cipelletti L, Giordano VM, Pineda E, et al. Relaxation dynamics and aging in structural glasses. *AIP Conf Proc.* 2013; 1518: 181 - 188. <https://doi.org/10.1063/1.4794566>
- [27] Jakse N, Pasturel A. Coupling between dynamic slowing down and chemical heterogeneity in a metallic undercooled liquid. *Phys Rev B.* 2017; 95: 144210. <https://doi.org/10.1103/PhysRevB.95.144210>
- [28] Yu HB, Wang WH, Samwer K. The  $\beta$  relaxation in metallic glasses: an overview. *Mater Today.* 2013; 16: 183 - 191. <https://doi.org/10.1016/j.mattod.2013.05.002>
- [29] Qiao JC, Casalini R, Pelletier JM. Main ( $\alpha$ ) relaxation and excess wing in Zr<sub>50</sub>Cu<sub>40</sub>Al<sub>10</sub> bulk metallic glass investigated by mechanical spectroscopy. *J Non-Cryst Solids.* 2015; 407: 106 - 109. <https://doi.org/10.1016/j.jnoncrsol.2014.08.009>
- [30] Dyre JC. Colloquium: The glass transition and elastic models of glass-forming liquids. *Rev Mod Phys.* 2006; 78: 953 - 972. <https://doi.org/10.1103/RevModPhys.78.953>
- [31] Angell CA, Ngai KL, McKenna GB, McMillan PF, Martin SW. Relaxation in glassforming liquids and amorphous solids. *J Appl Phys.* 2000; 88: 3113 - 3157. <https://doi.org/10.1063/1.1286035>
- [32] Liu XF, Zhang B, Wen P, Wang WH. The slow  $\beta$ -relaxation observed in Ce-based bulk metallic glass-forming supercooled liquid. *J Non-Cryst Solids.* 2006; 352: 4013 - 4016. <https://doi.org/10.1016/j.jnoncrsol.2006.08.006>
- [33] Wang Z, Yu HB, Wen P, Bai HY, Wang WH. Pronounced slow  $\beta$ -relaxation in La-based bulk metallic glasses. *J Phys: Condens Matter.* 2011; 23: 142202. <https://doi.org/10.1088/0953-8984/23/14/142202>
- [34] Hachenberg J, Samwer K. Indications for a slow  $\beta$ -relaxation in a fragile metallic glass. *J Non-Cryst Solids.* 2006; 352: 5110 - 5113. <https://doi.org/10.1016/j.jnoncrsol.2006.01.143>
- [35] Zhao ZF, Wen P, Shek CH, Wang WH. Measurements of slow  $\beta$ -relaxations in metallic glasses and supercooled liquids. *Phys Rev B.* 2007; 75: 174201. <https://doi.org/10.1103/PhysRevB.75.174201>
- [36] Groza JR, Shackelford JF. *Materials Processing Handbook.* CRC Press, Boca Raton, FL, USA, 2007. <https://doi.org/10.1201/9780849332166>
- [37] Inoue A, Zhang T, Kurosaka K, Zhang W. High-strength Cu-based bulk glassy alloys in Cu-Zr-Ti-Be system. *Mater Trans.* 2001; 42: 1800 - 1804. <https://doi.org/10.2320/matertrans.42.1800>
- [38] Tian L, Cheng YQ, Shan ZW, Li J, Wang CC, Han XD, et al. Approaching the ideal elastic limit of metallic glasses. *Nat Commun.* 2012; 3: 609. <https://doi.org/10.1038/ncomms1619>
- [39] Shan ZW, Li J, Cheng YQ, Minor AM, Asif SAS, Warren OL, et al. Plastic flow and failure resistance of metallic glass: Insight from in situ compression of nanopillars. *Phys Rev B.* 2008; 77: 155419. <https://doi.org/10.1103/PhysRevB.77.155419>
- [40] Guo H, Yan PF, Wang YB, Tan J, Zhang ZF, Sui ML, et al. Tensile ductility and necking of metallic glass. *Nat Mater.* 2007; 6: 735 - 739. <https://doi.org/10.1038/nmat1984>
- [41] Ashby MF, Greer AL. Metallic glasses as structural materials. *Scr Mater.* 2006; 54: 321 - 326. <https://doi.org/10.1016/j.scriptamat.2005.09.051>
- [42] Kumar G, Rector D, Conner RD, Schroers J. Embrittlement of Zr-based bulk metallic glasses. *Acta Mater.* 2009; 57: 3572 - 3583. <https://doi.org/10.1016/j.actamat.2009.04.016>
- [43] Li WD, Gao YF, Bei HB. On the correlation between microscopic structural heterogeneity and embrittlement behavior in metallic glasses. *Sci Rep.* 2015; 5: 14786. <https://doi.org/10.1038/srep14786>

- [44] Schuh CA, Hufnagel TC, Ramamurty U. Overview No.144 - Mechanical behavior of amorphous alloys. *Acta Mater.* 2007; 55: 4067 - 4109. <https://doi.org/10.1016/j.actamat.2007.01.052>
- [45] Sarac B, Schroers J. Designing tensile ductility in metallic glasses. *Nat Commun.* 2013; 4: 2158. <https://doi.org/10.1038/ncomms3158>
- [46] Sarac B, Ketkaew J, Popnoe DO, Schroers J. Honeycomb Structures of Bulk Metallic Glasses. *Adv Funct Mater.* 2012; 22: 3161 - 3169. <https://doi.org/10.1002/adfm.201200539>
- [47] Wei R, Wang XL, Yang S, Jiang F, He L. Formation of CuZr-based bulk metallic glass composites containing nanometer-scale B2-CuZr phase through sub-Tg annealing. *J Alloys Compd.* 2014; 617: 699 - 706. <https://doi.org/10.1016/j.jallcom.2014.08.045>
- [48] Wei R, Yang S, Chang Y, Li YF, Zhang CJ, He L. Mechanical property degradation of a CuZr-based bulk metallic glass composite induced by sub-Tg annealing. *Mater Design.* 2014; 56: 128 - 138. <https://doi.org/10.1016/j.matdes.2013.11.001>
- [49] Sarac B, Zhang L, Kosiba K, Pauly S, Stoica M, Eckert J. Towards the Better: Intrinsic Property Amelioration in Bulk Metallic Glasses. *Sci Rep.* 2016; 6: 27271. <https://doi.org/10.1038/srep27271>
- [50] Murali P, Ramamurty U. Embrittlement of a bulk metallic glass due to sub-Tg annealing. *Acta Mater.* 2005; 53: 1467 - 1478. <https://doi.org/10.1016/j.actamat.2004.11.040>
- [51] Hayat F, Yin J, Tabassum A, Hou H, Lan S, Feng T. Effects of cooling rate and sub-Tg annealing on Ni80P20 metallic glass: A molecular dynamic (MD) study. *Comput Mater Sci.* 2020; 179: 109681. <https://doi.org/10.1016/j.commatsci.2020.109681>
- [52] Zhang P, Maldonis JJ, Besser MF, Kramer MJ, Voyles PM. Medium-range structure and glass forming ability in Zr-Cu-Al bulk metallic glasses. *Acta Mater.* 2016; 109: 103 - 114. <https://doi.org/10.1016/j.actamat.2016.02.006>
- [53] Kosiba K, Pauly S. Inductive flash-annealing of bulk metallic glasses. *Sci Rep.* 2017; 7: 2151. <https://doi.org/10.1038/s41598-017-02376-x>
- [54] Haruyama O, Yoshikawa K, Yamazaki Y, Yokoyama Y, Egami T. Comparison of Structural Relaxation Behavior in As-Cast and Pre-Annealed Zr-Based Bulk Metallic Glasses Just below Glass Transition. *Mater Trans.* 2015; 56: 648 - 654. <https://doi.org/10.2320/matertrans.M2015023>
- [55] Song M, Liao XZ, He YH. Effect of sub-T-g annealing on the mechanical properties of a ZrAlNiCuNb bulk metallic glass. *Phil Mag Lett.* 2011; 91: 713 - 723. <https://doi.org/10.1080/09500839.2011.609842>
- [56] Kumar G, Neibecker P, Liu YH, Schroers J. Critical fictive temperature for plasticity in metallic glasses. *Nat Commun.* 2013; 4: 1536. <https://doi.org/10.1038/ncomms2546>
- [57] Scudino S, Kuhn U, Schultz L, Nagahama D, Hono K, Eckert J. Microstructure evolution upon devitrification and crystallization kinetics of Zr<sub>57</sub>Ti<sub>8</sub>Nb<sub>2.5</sub>Cu<sub>13.9</sub>Ni<sub>11.1</sub>Al<sub>7.5</sub> melt-spun glassy ribbon. *J Appl Phys.* 2004; 95: 3397 - 3403. <https://doi.org/10.1063/1.1652244>
- [58] Van Steenberge N, Concustell A, Sort J, Das J, Mattern N, Gebert A, et al. Microstructural inhomogeneities introduced in a Zr-based bulk metallic glass upon low-temperature annealing. *Mater Sci Eng, A.* 2008; 491: 124 - 130. <https://doi.org/10.1016/j.msea.2008.01.083>
- [59] Stoica M, Van Steenberge N, Bednarčík J, Mattern N, Franz H, Eckert J. Changes in short-range order of Zr<sub>55</sub>Cu<sub>30</sub>Al<sub>10</sub>Ni<sub>5</sub> and Zr<sub>55</sub>Cu<sub>20</sub>Al<sub>10</sub>Ni<sub>10</sub>Ti<sub>5</sub> BMGs upon annealing. *J Alloys Compd.* 2010; 506: 85 - 87. <https://doi.org/10.1016/j.jallcom.2010.07.001>
- [60] Hajlaoui K, Benameur T, Vaughan G, Yavari AR. Thermal expansion and indentation-induced free volume in Zr-based metallic glasses measured by real-time diffraction using synchrotron radiation. *Scr Mater.* 2004; 51: 843 - 848. <https://doi.org/10.1016/j.scriptamat.2004.07.008>

- [61] Sarac B, Bernasconi A, Wright J, Stoica M, Spieckermann F, Mühlbacher M, et al. Structural modifications in sub-T<sub>g</sub> annealed CuZr-based metallic glass Mater Sci Eng. A. 2017; 707: 245 - 252. <https://doi.org/10.1016/j.msea.2017.09.013>
- [62] Cullity BD. Diffraction I: Directions of Diffracted Beams. 2nd ed: Addison-Wesley Publishing Company Inc., Reading, MA, USA, 1978.
- [63] Busch R, Schroers J, Wang WH. Thermodynamics and kinetics of bulk metallic glass. Mrs Bull. 2007; 32: 620-623. <https://doi.org/10.1557/mrs2007.122>
- [64] Schroers J. The superplastic forming of bulk metallic glasses. JOM. 2005; 57: 35 - 39. <https://doi.org/10.1007/s11837-005-0093-2>
- [65] Sarac B, Kumar G, Hodges T, Ding SY, Desai A, Schroers J. Three-Dimensional Shell Fabrication Using Blow Molding of Bulk Metallic Glass. J Microelectromech Syst. 2011; 20: 28 - 36. <https://doi.org/10.1109/JMEMS.2010.2090495>
- [66] Yang GN, Shao Y, Yao KF, Chen SQ. A study of cooling process in bulk metallic glasses fabrication. Aip Adv. 2015; 5: 117111 <https://doi.org/10.1063/1.4935440>
- [67] Debenedetti PG, Stillinger FH. Supercooled liquids and the glass transition. Nature. 2001; 410: 259 - 267. <https://doi.org/10.1038/35065704>
- [68] Wu K, Li R, Zhang T. Crystallization and thermophysical properties of Cu<sub>46</sub>Zr<sub>47</sub>Al<sub>6</sub>Co<sub>1</sub> bulk metallic glass. Aip Adv. 2013; 3: 112115. <https://doi.org/10.1063/1.4832235>
- [69] Aydiner CC, Üstündag E. Residual stresses in a bulk metallic glass cylinder induced by thermal tempering. Mech Mater. 2005; 37: 201 - 212. <https://doi.org/10.1016/j.mechmat.2004.03.001>
- [70] Wu ZW, Li FX, Huo CW, Li MZ, Wang WH, Liu KX. Critical scaling of icosahedral medium-range order in CuZr metallic glass-forming liquids. Sci Rep. 2016; 6: 35967. <https://doi.org/10.1038/srep35967>



Research Article

## Evaluation of nano sized Mg@BTC metal organic framework as a drug carrier: A long term experimental and predictive theoretical study

Güliz Akyüz<sup>1,a</sup>, Aykut Elmas<sup>\*1,b</sup>, Müberra Andaç<sup>1,2,c</sup>, Ömer Andaç<sup>1,2,d</sup>

<sup>1</sup>Department of Nanoscience and Nanotechnology, Ondokuz Mayıs University, Samsun, Turkey

<sup>2</sup>Department of Chemistry, Ondokuz Mayıs University, Samsun, Turkey

### Article Info

#### Article history:

Received 13 Jun 2020

Revised 25 Oct 2020

Accepted 27 Oct 2020

#### Keywords:

Long term release;

Nano sized Mg@BTC;

Drug carrier;

Model fit tests;

Slow release

### Abstract

Metal Organic Frameworks (MOFs) have found wide applications as a drug carrier in nanotherapeutics because of adjustable pore-sizes, controllable structural properties, large surface area and high pore volume. In this work, nanosized Mg@BTC is synthesized by electrochemical method and used as a new drug carrier for ibuprofen. The ibuprofen (IB) is loaded to the Mg@BTC 1:1 ratio with the amount of %99.8. The release of ibuprofen from nanocarrier has been observed experimentally for long term. After 100.5 hours, the release ratio yields 36 %. The ibuprofen has been tested at  $40 \pm 0.5$  °C. System showed a rapid release after 100 hours, the release ratio yields 72.29 %. The release profile of IB loaded Mg@BTC is tested by using model depended mathematical models to get observation and prediction of the release. Zero Order Model, First Order Model, Higuchi Model, Peppas Model and Hixon Model functions are fitted to the release profiles. Watson's U Squared Method is used to test the fit strength of the models. Observation from the release profiles, it is seemed Peppas Model yields the best results. Also, thermodynamic analysis has been studied.

© 2021 MIM Research Group. All rights reserved.

## 1. Introduction

Porous materials with high surface area have always attracted attention for nanotechnological applications. The various molecular structures, properties and promising applications are some of the main reasons of this attention. Metal organic frameworks (MOFs) can be considered as one of the most popular porous materials. As a short description, MOFs are self-assembly, branched and high porosity crystalline polymers which possess metal ions with organic linkers. Examples of some common linkers are oxalic acid, terephthalic acid, trimesic acid, adamantane-1,3,5,7-tetracarboxylic acid, fumaric acid, 4,5-imidazolecarboxylic acid, 1,4-butanedicarboxylic acid, 4,6-dihydroxy benzene-1,2,5-trisulfonic acid, biphenyl-4,4-dicarboxylic acid, 2,5-dihydroxyterephthalic acid, 6,6-dichloro-4,4-di(pyridin-4-yl)-1,1-binaphthyl-2,2-diol, 6-naphthalenedicarboxylic acid and 1,3,5-benzenetribenzoic acid respectively [1].

Besides, various combinations of metals and ligands or method types can be used for obtaining different MOFs. Some of the synthesis methods are hydro-thermal method, microwave and ultrasonic methods, electrochemical synthesis, mechanochemical synthesis, diffusion method, solvent evaporation and ionothermal synthesis respectively [1-3].

\*Corresponding author: [aykutdiamond@gmail.com](mailto:aykutdiamond@gmail.com)

<sup>a</sup>orcid.org/0000-0002-3522-9716; <sup>b</sup>orcid.org/0000-0002-7721-4088; <sup>c</sup>orcid.org/0000-0001-7262-9762;

<sup>d</sup>orcid.org/0000-0003-3641-9690

DOI: <http://dx.doi.org/10.17515/resm2020.199na0613>

Res. Eng. Struct. Mat. Vol. 7 Iss. 1 (2021) 135-156

MOF's non-toxic activity is related to synthesis method and chemicals which are used in the process. Obtaining biocompatible MOFs with green synthesis methods which support to eliminate the use of toxic chemicals is possible. Electrochemical and sonochemical methods are developed for this purpose [3, 4].

MOFs should have minimal toxic effects when they enter the body system. Some metals are highly toxic like chromium. But some of them present in the body with less toxicity and large quantities. Such as; iron, calcium, copper, zinc, manganese. Their oral lethal dose is below 50 (LD50) in the body [1].

Metal organic frameworks have been applied on several fields [5-10]. Major applications of MOFs are light emitting devices [11, 12] and sensors [3, 11], gas storage [13, 14], magnets [15, 16], catalysts [17, 18] and drug delivery [1-3, 19-21].

In recent years, MOF based therapies have started to attract attention. Many strategies have developed in order to increase the effect of conventional therapeutics. Many drawbacks of small molecule drugs can be controlled by the use of new developments of drug delivery. MOFs have a very important role in the controlled drug release due to their pore size, shape, structure and chemical properties, adjustable structure, a large surface area and large pore sizes. Thus, the encapsulation of different types of drugs have been studied.

Vasconcelos et al. [22] prepared Zn@BDC and doxorubicin loaded into structure (DOX@Zn@BDC). The drug delivery system showed slower release and studies of cytotoxicity showed good results for the system developed with antineoplastic doxorubicin. Abbasia and Rizvandia [2] investigated the release properties of rifampicin from Cu@BTC nanoparticles. Furthermore, Lestari et al. [3] studied on Zn@BTC and investigated its ability in loading and slow release of ibuprofen. Ibuprofen is a propionic acid derivative and a nonsteroid anti-inflammatory drug. It is used for anti-inflammatory, antipyretic, and analgesic effects. It has been used in the treatment of osteoarthritis, rheumatoid arthritis, gout, mild and moderate pains [23, 24].

In this study, nano sized Mg@BTC were synthesized and first time used as a drug carrier. For synthesis and functionalized of Mg@BTC, electrochemical method was used which supports to eliminate the use of toxic chemicals. Besides, evaluation of Mg@BTC for controlled release of ibuprofen was observed for long term up to 100 hours at different temperature conditions contrary to many studies.

Also, a predictive research has taken place in the consideration of mathematical modeling of drug release profile. The reason of the testing the system with models is to predict the release behavior of the drug and generate more effective experiments for avoiding waste of time and money. Mathematical models can represent different types of kinetics of drug release profile depending on the system. In this work, five models are chosen. Zero Order Model and First Order Model are derived from the reaction kinetics of the chemistry [25]. They are very popular in the field. In addition to these models, the Higuchi Model [26], Peppas Model [27], and Hixon Model [28] are also chosen to for the testing because of their strength between the all other models. All of the three models are used for testing the results of long term drug release profile of the MOF both which described below.

After the fitting procedure, numerical comparison of the models is generated. It is chosen the Watson's U-Squared test [29] for the convenience of the system and the results are compared via the computer software.

Also, thermodynamic parameters has been generated by using Arrhenius equation, Eyring equation and Gibbs free energy equation [30].

## 2. Experimental

### 2.1. Materials and methods

Methanol (99%), NaCl (99%), KCl (99%), Na<sub>2</sub>HPO<sub>4</sub> (99%), KH<sub>2</sub>PO<sub>4</sub> (99%), NaOH, HCl, tween 20, benzene-1,3,5-tri-carboxylic acid (H<sub>3</sub>BTC, 99%), n-hexane (99%), tetrabutylammoniumtetrafluoroborate (TBATFB, 99%) were purchased from Sigma Aldrich. Na-ibuprofen (99%) was provided commercially by Adeka. The phosphate buffer saline (PBS) solution was prepared according to procedure [31]. Magnesium metal plates were used as the electrodes. The synthesized [Mg@BTC] and ibu@[Mg@BTC] were characterized using X-ray diffraction spectroscopy (XRD) (Rigaku Smart lab). Concentration of loaded and released ibuprofen was analyzed using UV-Vis spectroscopy (Thermo scientific evolution 220, PCCU1). The FTIR spectra (PerkinElmer, Spectrum two, USA) of the samples were recorded with an infrared spectrometer to characterize the MOF and, it was recorded in a range of 400–4000 cm<sup>-1</sup> using spectrometer. The surface morphology and particles sizes of the samples were carried out using high resolution scanning electron microscopy (SEM) (JEOL-JSM-7001F). The energy dispersive spectrometry (EDS) analysis as also studied. Atomic force microscope (AFM) (NT-MDT NEXT, Russia) was used to determine the morphology of MOF. All measurements were performed at room temperature.

### 2.2. Electro-chemical synthesis of [Mg@BTC]

Electro-chemical synthesis of [Mg@BTC] was studied according to the procedure previously described [3]. Two plates of magnesium metal were used as electrodes and activated by polishing using sandpaper. Plates initial masses were respectively 0,6969 g and 0,6782 g. The ligand H<sub>3</sub>BTC (5.25 g) and the electrolyte tetrabutylammoniumtetrafluoro-borate (TBATFB) (4.11 g) were dissolved in the methanol (250 mL) and stirred for 15 min. The magnesium plates were placed inside the electrochemical cell. Electrolysis was verified using an ambient temperature under a voltage of 3 V 9.5 mA for 4 hours. The white precipitate that resulted from the reaction was washed three times with methanol and dried at room temperature for 24 h and further activated at 120 °C for 48 hours.

### 2.3. In vitro loading ibuprofen into [Mg@BTC] and release study

The mass variation of loaded ibuprofen into [Mg@BTC] are in ratio 1:1 (g/g). Ibuprofen (0.1525 g) was dissolved in 10 mL of n-hexane, then [Mg@BTC] (0.1525 g) was added and stirred for 72 h at an ambient temperature. The suspension was then centrifuged, washed with n-hexane and the remaining filtrate were analyzed using UV-Vis spectroscopy to determine the rest of the unloaded ibuprofen. The precipitate was dried at room temperature for 24 h and then called as ibu@[Mg@BTC] and placed in 25 mL of phosphate buffer saline (PBS) containing tween 20 (0.5% v/v) at physiological pH, temperature of 36 ± 0.5 °C and stirred constantly for time intervals 0.25, 0.5, 1, 1.5, 2.25, 3, 4, 4, 5, 7, 9, 24, 30, 48, 54, 72, 100.5 h. 2.5 mL of solution from each buffer was harvested overtime with subsequent replacement of equal volume of fresh buffer at the different time interval.

Moreover, release study was tested by high temperature condition (40 ± 0.5 °C). The same experimental conditions were maintained with temperature of 36 ± 0.5 °C and the temperature of the experimental system was set at 40 ± 0.5 °C. Equal volume of samples were collected for different time intervals 0.25, 0.5, 1, 1.5, 2.25, 3, 4, 4, 5, 7, 9, 24, 30, 48, 54, 72, 100.5 h. The release of the ibuprofen was then quantified by measuring its absorbance using absorption spectroscopy at 228 nm and the concentration of the released ibuprofen calculated with the aid of a standard curve.

For the all fitting procedure of the models, graphical representations and thermodynamic calculations, The Wolfram Mathematica software is used. Also, Watson's U-Squared method is chosen for the quantitative strength test of the fit functions [29]. The model functions are defined by the user for suitable data set. But for the graphical representation, model fitting and testing method, build-in functions are preferred to use because of the effective user interference.

### 3. Result and Discussion

FTIR spectroscopy was carried out to the identification of structure analysis of Mg@BTC. The spectra of the synthesized Mg@BTC powder was recorded. The spectrum of the powder is illustrated in Fig. 1. The bond formation between the tricarboxylic acid and the magnesium metal ions were observed from the significant shift of carbonyl (C=O) peak from carboxylate at 1700-1400  $\text{cm}^{-1}$ . This shift corresponded to the formation of coordination bonding in Mg@BTC as shown in Fig. 1. Besides, absorption peaks in the 1100-900  $\text{cm}^{-1}$  band was observed due to the vibration of the C-O bond in the carboxylate group [4, 32]. Since there is no broad peak centered at around 3300  $\text{cm}^{-1}$ , Mg@BTC does not contain water

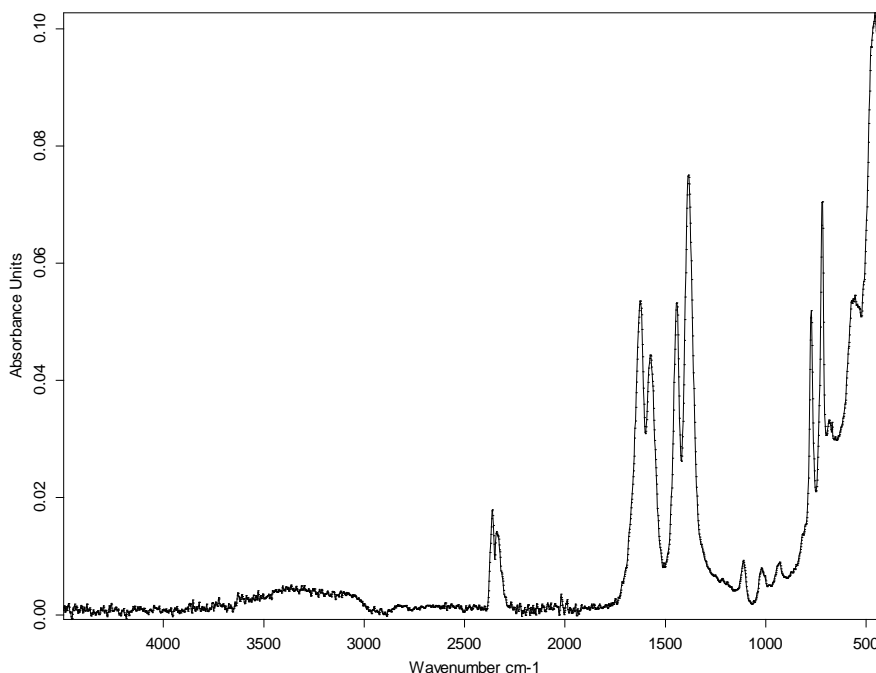


Fig. 1 FTR spectra of Mg@BTC.

The thermal decomposition of Mg@BTC was shown in Fig. 2. In general, three steps of mass loss process were observed [4]. In the first stage, the loss of water molecules at temperatures up to 20-80 °C. Approximately 3% mass loss was observed. 16.43% mass loss was detected after the releasing of the methanol from the structure at temperatures up to 80-550 °C. Besides, 50.57 % mass loss was observed at temperatures up to 550 °C-655 °C. The final mass of Mg@BTC was 29 % at 888 °C.

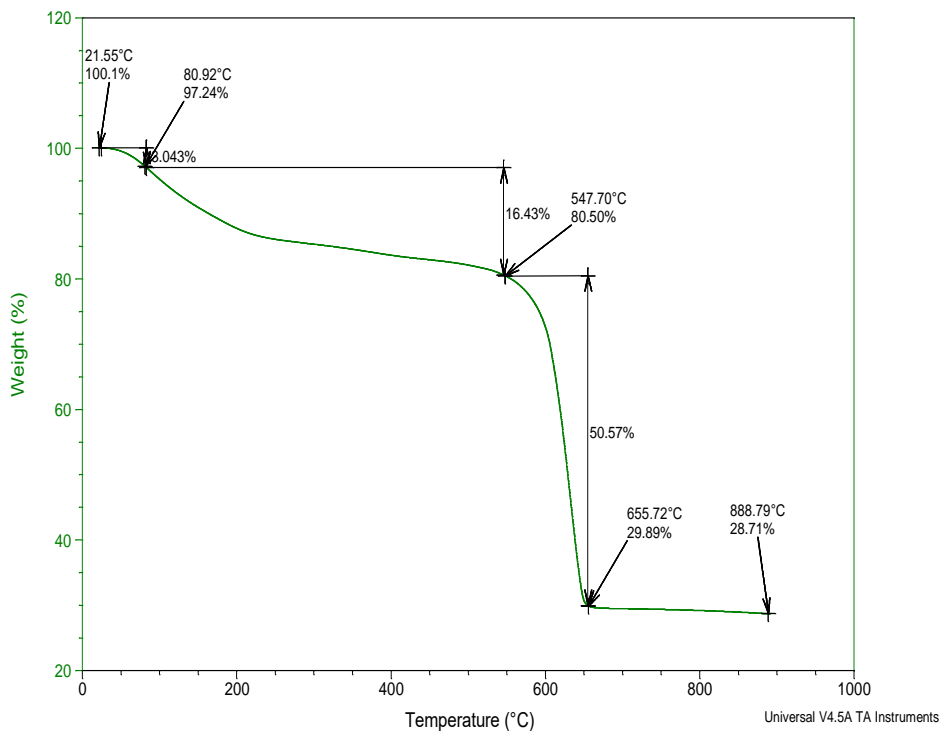


Fig. 2. TGA curve of Mg@BTC.

The crystal structures of all the synthesized Mg@BTC were confirmed by powder X-ray diffraction (XRD) using a Rigaku Smart lab. Diffraction patterns were collected at a scan rate of  $2^\circ \text{ min}^{-1}$  at  $0.02^\circ$  steps from  $10$  to  $80^\circ$  two theta.

In our study, solvent-free 3D Mg@BTC was obtained owing to the synthesis in methanol. However, indexing could not be performed due to the low crystallinity of the structure. The powder XRD diffraction patterns were given in Fig. 3. The X-ray diffraction pattern of the Mg@BTC is similar to that reported previously study of Bella et al. [33].

SEM images of nano sized Mg@BTC are given in Fig 4, Fig 5, Fig. 6 and Fig. 7. Powder samples are attached to the carbon band. When the morphology of Mg@BTC is examined, Mg@BTC particles are filamentous in shape and their sizes vary in the range of 30-90 nm. SEM images in Fig 4, Fig 5, Fig. 6 and Fig. 7 are in good agreement with EDS results of Mg@BTC which are shown in Fig. 8 and Fig. 9. The chemical composition of Mg@BTC was investigated via EDS, and EDS mapping analysis and spectrum are shown in Fig. 8 and Fig. 9. EDS mapping analysis and spectrum of Mg@BTC confirms the nanoparticles in which Mg, C, and O are present.

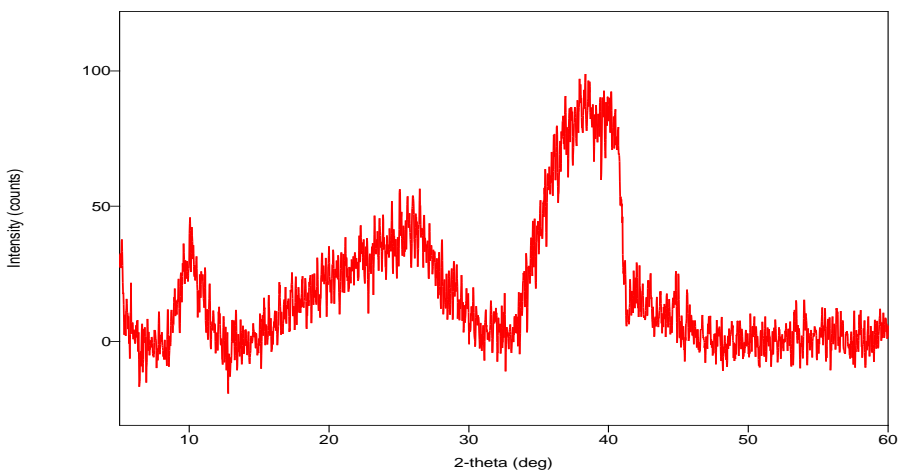


Fig. 3 XRD diffraction pattern of nano sized Mg@BTC

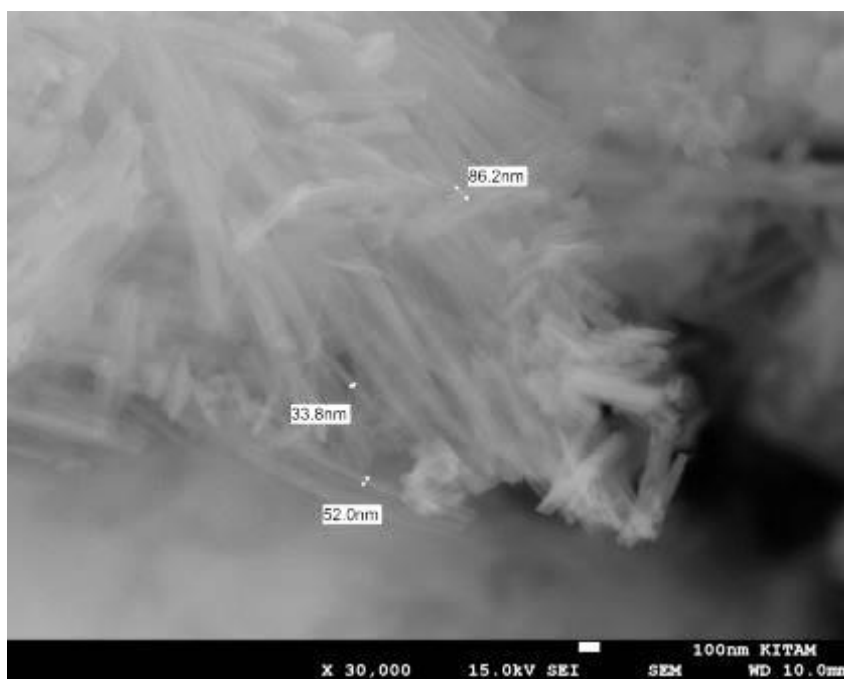


Fig. 4 SEM images of Mg@BTC

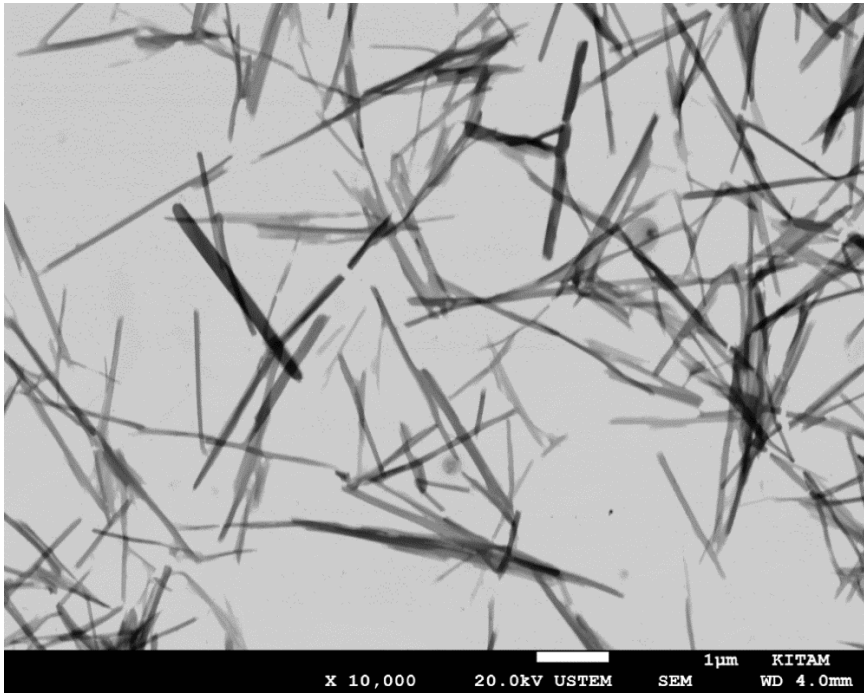


Fig. 5.- SEM images of Mg@BTC

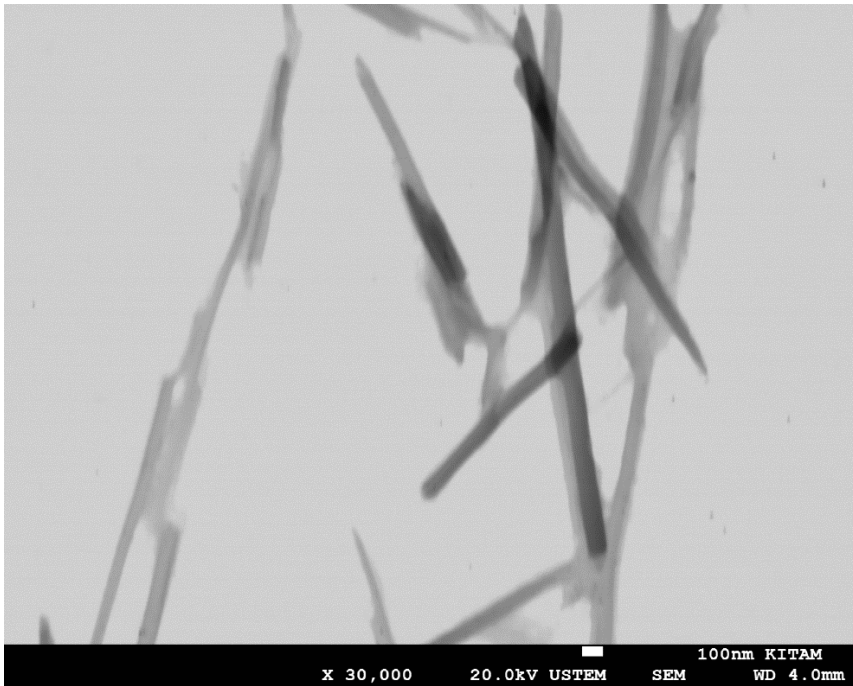


Fig. 6 SEM images of Mg@BTC.

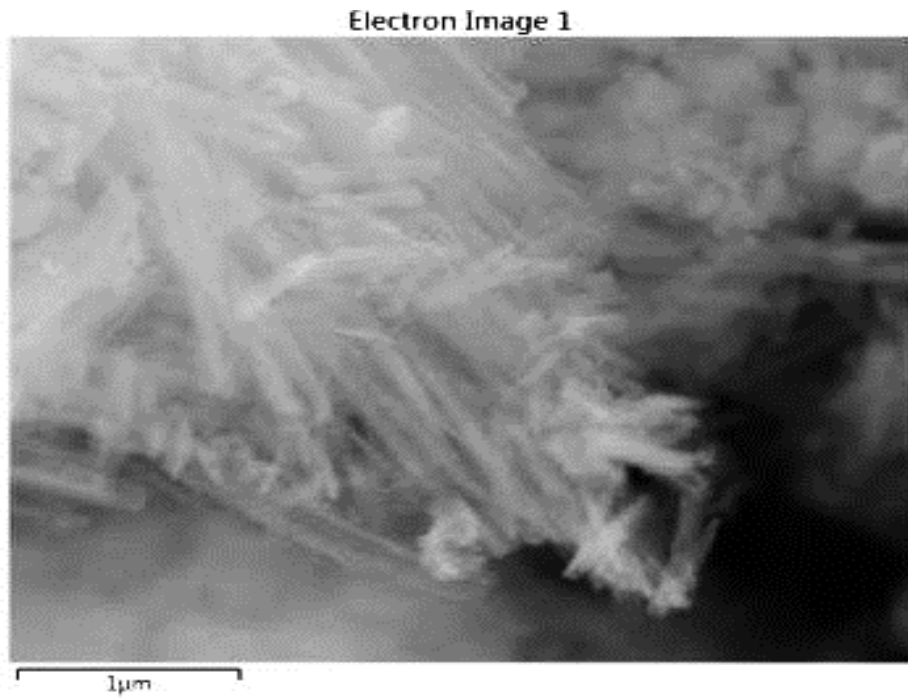


Fig. 7 SEM images of Mg@BTC.

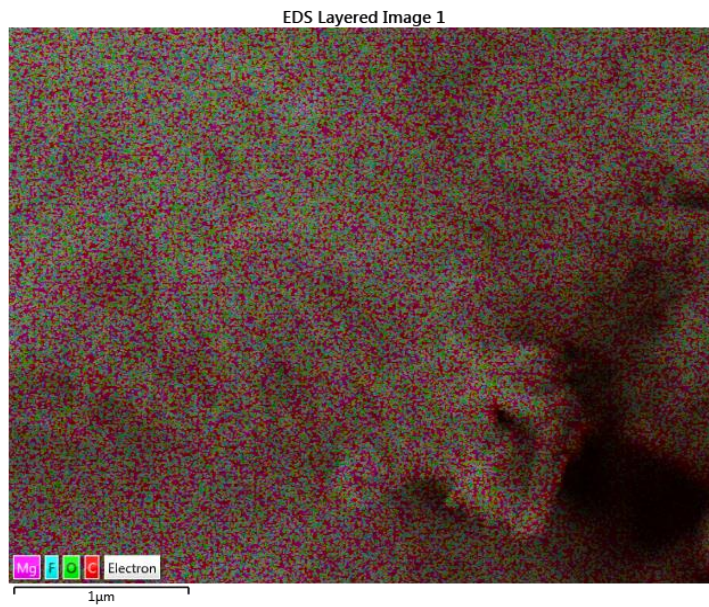


Fig. 8 EDS images of Mg@BTC.

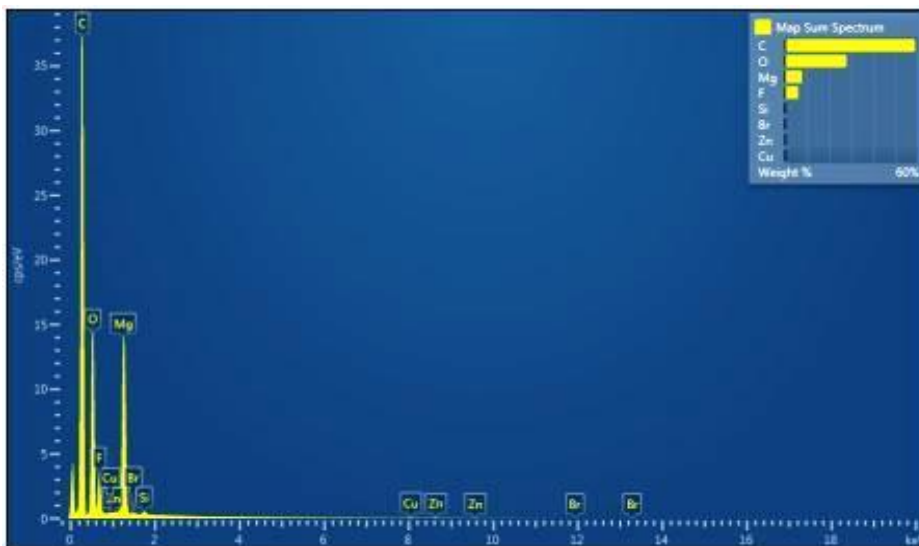


Fig. 9 EDS images of Mg@BTC.

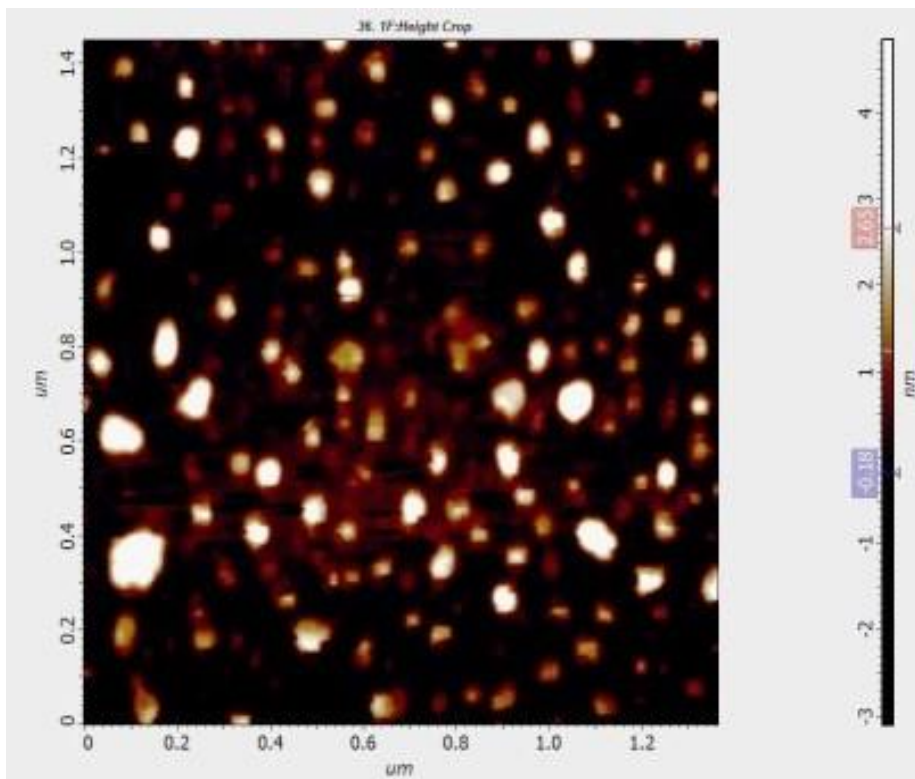


Fig. 10 AFM images of nano-sized Mg@BTC.

AFM images of nano-sized Mg@BTC are shown in Fig. 10. Based on AFM tapping mode images, Mg@BTC nanoparticles are filamentous-spherical in shape with homogeneous and regular distribution, and their sizes range from 30 to 100 nm.

### 3.1. Loading and release of ibuprofen into Mg@BTC

Concentration of loaded and released ibuprofen were calculated by the absorbance data obtained from UV-Vis spectroscopy. The UV-Vis spectra of ibuprofen in n-hexane is shown Fig. 11. The maximum wavelength at 220 nm was used for determining the concentration of loaded ibuprofen in the structure. The normal healthy body temperature  $36 \pm 0.5$  °C and high body temperature  $40 \pm 0.5$  °C were chosen for detected release behavior of ibu@[Mg@BTC].

The ibuprofen is loaded to the Mg@BTC 1:1 ratio with the amount of 99.8%. The PBS at the physiological pH was used for the *in vitro* drug release study. Maximum wavelength observed at the 228 nm is shown in Fig. 12. Ibuprofen loaded Mg@BTC showed a slow release over 100 h at  $36 \pm 0.5$  °C. After 100 hours, the release ratio yields 36 % as shown in Fig. 13 and Fig. 14. As shown in Fig. 13, loaded ratio have slow release profile as compared with pure release and better holding capacity. The ibuprofen was loaded to the Mg@BTC 1:1 ratio with the amount of 112,5 mg was tested at  $40 \pm 0.5$  °C. System showed a rapid release after 100 hours, the release ratio yield 72.29 % shown in Fig. 15 and Fig. 16.

These data indicate that Mg@BTC is effective nanocarrier and possess the slow released of ibuprofen. Drug could stay in the blood circulation very long time with slow release at  $36 \pm 0.5$  °C. Thus, it could effect on the disease efficiently.

System showed a rapid release after 100 hours at  $40 \pm 0.5$  °C. Which may be related to solubility of ibuprofen in aqueous solvents. Entropy, enthalpy, and Gibbs energy of the aqueous environment can be affected the solubility of ibuprofen at different temperature conditions. As was known, the solubility of ibuprofen are related to aqueous media [34]. Our results showed that ibuprofen possess rapid and control release under heat stoke conditions.

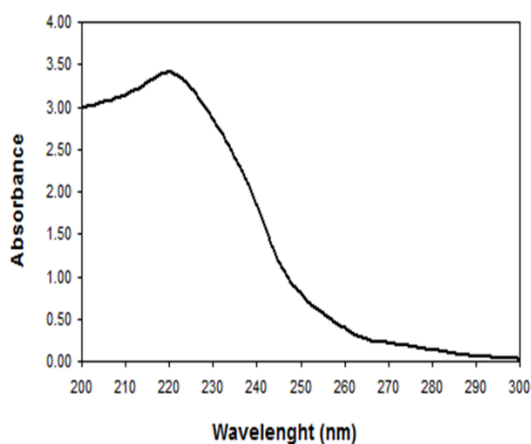


Fig. 11 UV-Vis spectra of ibuprofen in n-hexane.

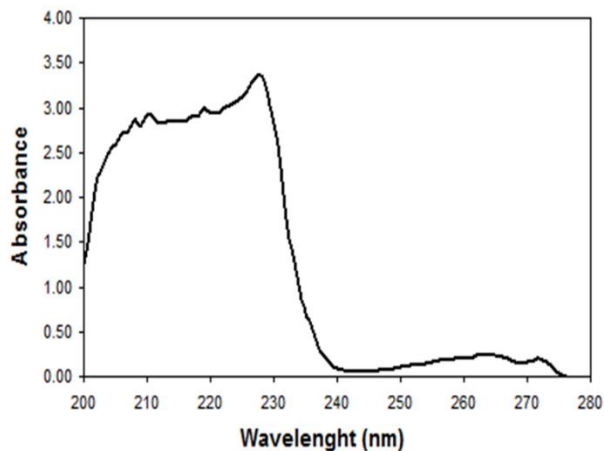


Fig. 12 UV-Vis spectra of ibuprofen in PBS and tween 20.

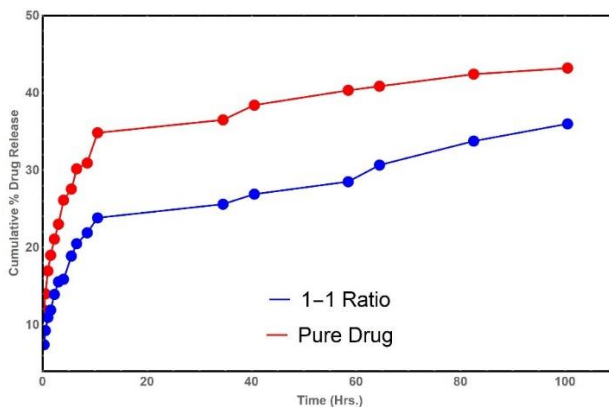


Fig. 13 Comparison of the release profiles.

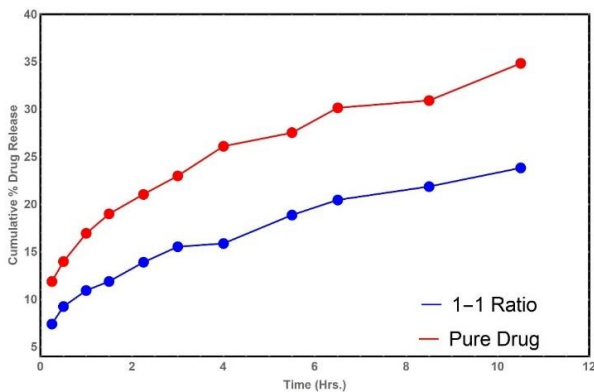


Fig. 14 Comparison of release profiles for short term.

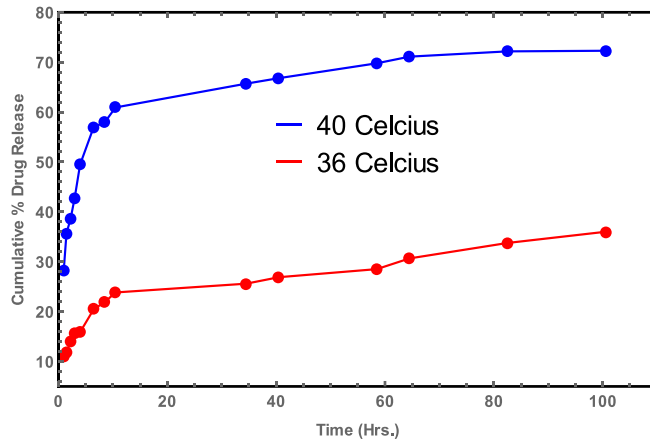


Fig. 15 Comparison of 1:1 ratio loaded drug release for 36 and 40 Celsius.

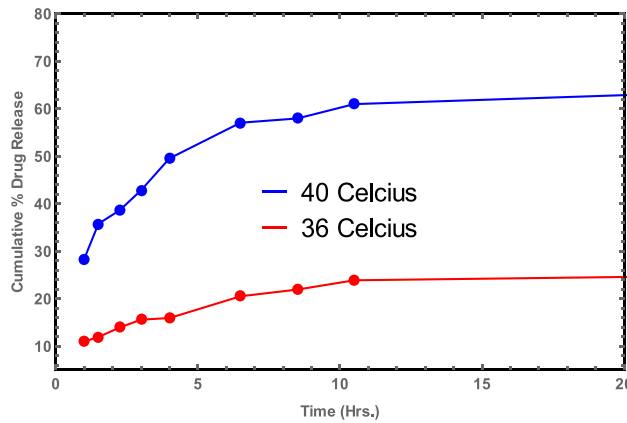


Fig. 16 Comparison of 1:1 ratio loaded drug release for 36 and 40 Celsius for short term.

#### 4. Modeling

Mathematical modeling is essential for the comparison of the experimental results [25-27, 35-44]. They give us both graphical interference which gives us to chance for the prediction and numerical comparison to estimate the strength of the models. It is also obvious that graphical profile is the best way to generate comments on the dynamics of the system.

For the experiment described above, five mathematical models used. First two models are Zero Order Model and First Order Model from the reaction kinetics of the chemistry because these models represent the most basic release profile of the drug and from the nature of the generated equations, they can applied to release system easily. For the third model, it is decided to use Higuchi Model [1], because the Higuchi Model is the most famous mathematical representation of the drug release profile. And both its pure form and its modified form are used extensively to describe to drug release profile [2-4]. Also Peppas [27] and Hixon [28] models are added to the studies for their strong representations and usage frequency in the field. Solutions of these five models are respectively as;

$$C_t = C_0 \pm K_0 t \tag{1}$$

$$\log(C_t) = \log(C_0) - \frac{K_1 t}{2.303} \tag{2}$$

$$Q = K_2 \sqrt{t} \tag{3}$$

$$Q = K_3 t^n \tag{4}$$

$$W_0^{1/3} - W_t^{1/3} = K_4 t \tag{5}$$

Where  $C_t$  is the amount of drug released at time  $t$  (and percent of drug remaining for the first order model),  $C_0$  is the initial concentration of drug at time  $t = 0$ ,  $K_0$  is the zero-order rate constant,  $K_1$  is the first order rate equation expressed in  $\text{time}^{-1}$  or per hour,  $Q$  is the cumulative amount of drug released in time  $t$  per unit area (and fraction of drug released at time  $t$  for Peppas model),  $K_2$  is the Higuchi dissolution constant,  $K_3$  is the Peppas release rate constant,  $W_0$  is the amount of drug remaining at time  $t$ ,  $W_t$  is the remaining amount of drug,  $K_4$  is the Hixon constant describing surface volume relaxation.

For the fitting procedure of the models into the experimental data shouldn't ignored for the model functions dependence. Otherwise fits are going to yield false results. For the Zero Order model it does not needed to make any change data matrix for the function is simple and the function varies with time only. For the First Order Model one should observe logarithmic percentage of the remaining drug because of the equation. So, the data matrix should be converted into logarithmic axes. For the Higuchi Model, drug release is pure function, but the time is increasing with the power of  $1/2$ . So, the time part of the data matrix should be converted into the SQRT. Same kind of arrangements has been performed for other models as well. This is the only way to for generating meaningful results.

As it is seen from the graphs of the drug release profiles (Fig. 17, Fig. 18, Fig. 19, Fig. 20, Fig. 21), fit results are expressed according to their proper axes'. According to generated fit functions, the parameters of the functions are shown in Table 1

Table 1. The parameters of the fitted functions. Where C is the amount of drug released at time t (and percent of drug remaining for the first order model, K is the rate constant and n is the empirical parameter respectively.

Model	Parameters		
	C	K	n
Zero Order	14.65350	0.24091	-
First Order	85.14300	0.00316	-
Higuchi	-	11.24320	-
Peppas	-	11.97880	0.48056
Hixon	-	0.00826	-

In consideration to the derived parameters and fit strength table (Table 1), Peppas Model might be chosen for the best fit results and the better holding capacity to generate a predictive function as,

$$Q = 11.97880t^{0.48056} \tag{6}$$

which gives the 100% release after about 3.5 Days (82.74 hours). The reason of this surprising result comes from the difference between long and short term prediction. For the short time prediction, one may observe regular release up to 9 hours (Fig. 16) because the sink acts like a perfect sink and keeps the diffusion continuous state which is reasonable for the theoretical modeling studies, but it doesn't represent the experimental conditions appropriate way. After 9 hours, it is seen another release order which can be called long term release because according to experimental conditions the sink does not act like a perfect sink anymore. For the proper representation of the long term release this difference should not be ignored.

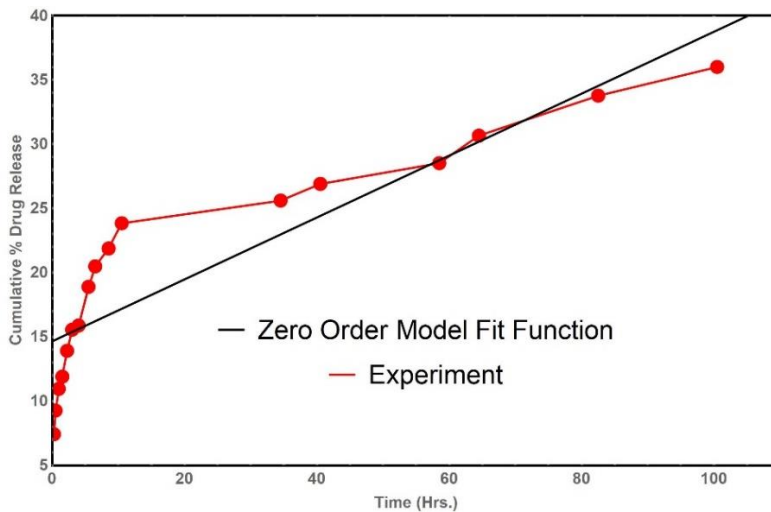


Fig. 17 1:1 Ratio release profile with Zero Order Model fit.

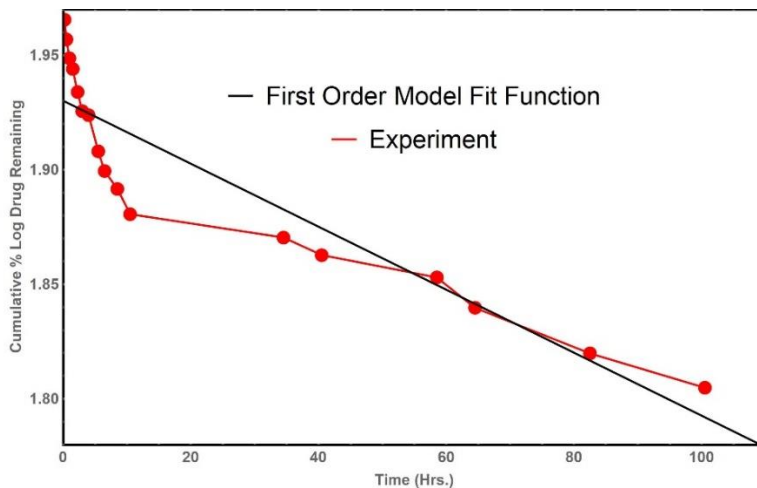


Fig. 18 1:1 Ratio release profile with First Order Model fit.

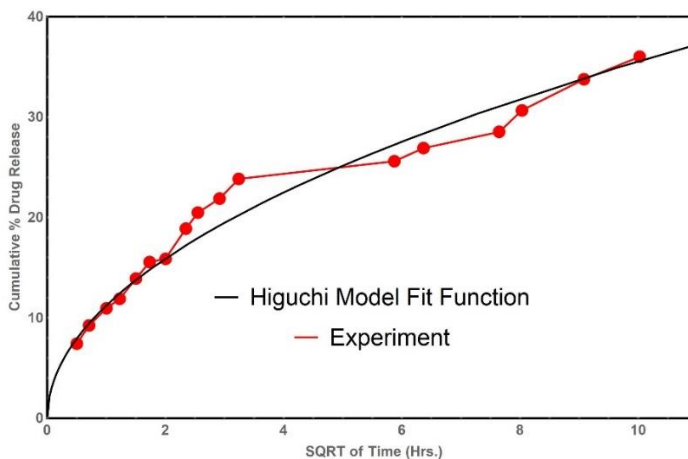


Fig. 19 1:1 Ratio release profile with Higuchi Model fit.

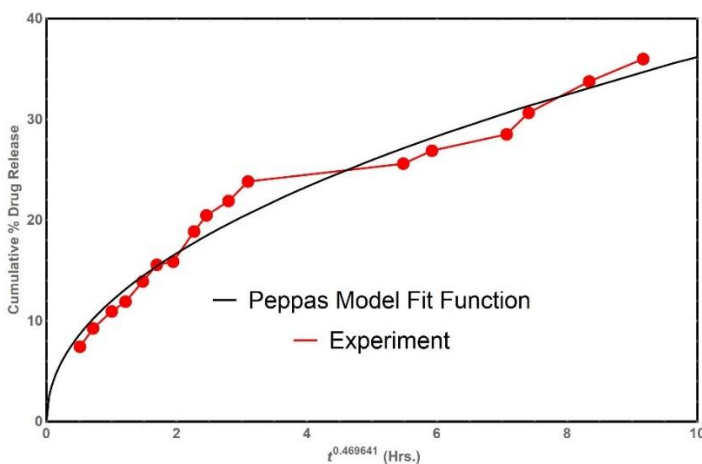


Fig. 20 1:1 Ratio release profile with Peppas Model fit.

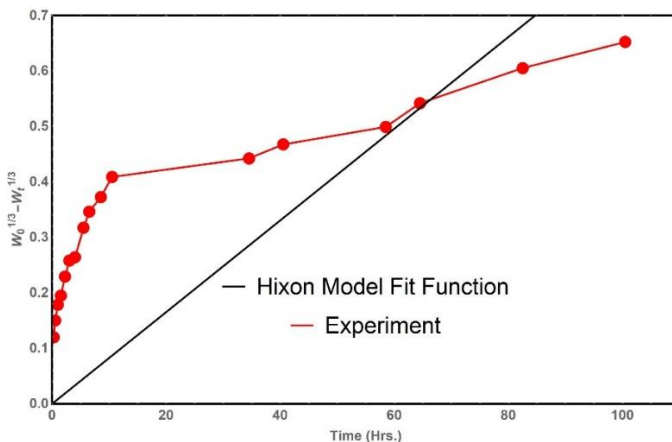


Fig. 21 1:1 Ratio release profile with Hixon Model fit.

Besides, for the comparison of the strength of the models Watson’s U-Squared Method is used for the convenience of the data set. Which yields to two parameters as *statistic* and *P-Value*. For a strong model statistic should close to 0 and P-Value should close to 1. Statistic equals zero and P-Value equals 1 is mean perfect fit [29]. According to Watson’s U-Squared test results, model parameters are shown in Table 2.

Table 2. Comparison of the fit results of the models according to Watson’s U-Squared Method.

Model	Statistic	P-Value
Zero Order Model	0.125204	0.168768
First Order Model	0.125204	0.168768
Higuchi Model	0.038901	0.858828
Peppas Model	0.031981	0.929518
Hixon Model	0.371082	0.001180

According to the results it seems that it is needed to long hours to 100 % of pure drug release for experiment described above which is not make sense. The reason of the unexpected result is the difference between long- and short-term prediction. Short term predictions are only valid for sink conditions which the concentration is always zero. This phenomenon is also eligible for drug loaded nanocarriers.

For the thermodynamic analysis, the experimental results are shown in Fig. 24 and Fig. 25

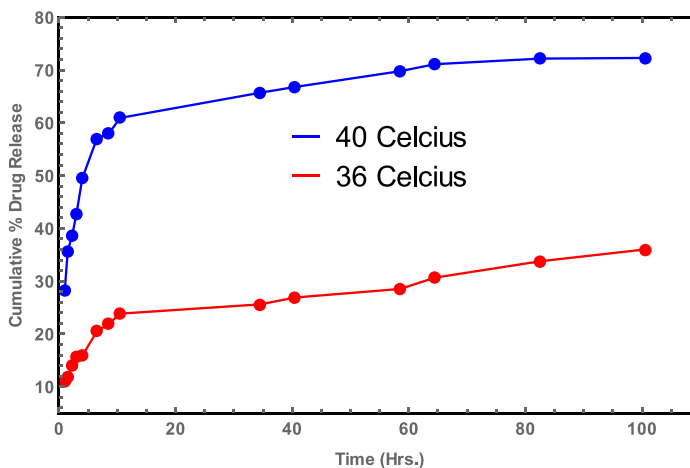


Fig. 22 Drug release profiles for 36 and 40 Celsius.

It is expected that faster release for higher temperature obviously. For finding activation energy, constant *K* is needed. In this study it is chosen Higuchi model (Eqn. 3) for evaluating that constant. Fitting results are shown in Table 3.

Table 3. K parameters for different temperatures

T (Kelvin)	K (hours <sup>-1</sup> )
309	4.18826
313	9.82826

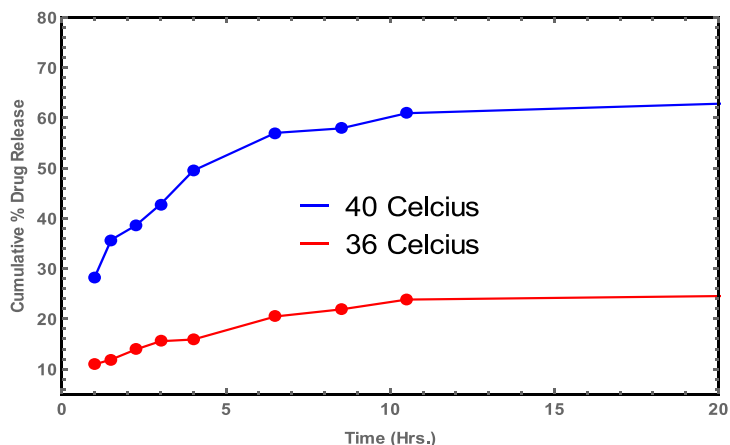


Fig. 23 Drug release profile for 36 and 40 Celsius up to 20 hours.

Arrhenius Equation [30] is used for evaluating activation energy.

$$K = Ae^{E_a/RT} \tag{7}$$

Where  $E_a$  is the activation energy ( $kJ.mol^{-1}$ ),  $R$  is the universal gas constant ( $8314 j/mol.K$ ),  $T$  is the temperature (Kelvin).  $K$  is the reaction constant. Converting the Eqn. (7) into the  $y = mx + n$  formation to get activation energy by slope, Fig. 24, it is found  $E_a = 171636 j/mol$ .

$$\ln(k) = -\frac{E_a}{R} \left(\frac{1}{T}\right) + \ln(A) \tag{8}$$

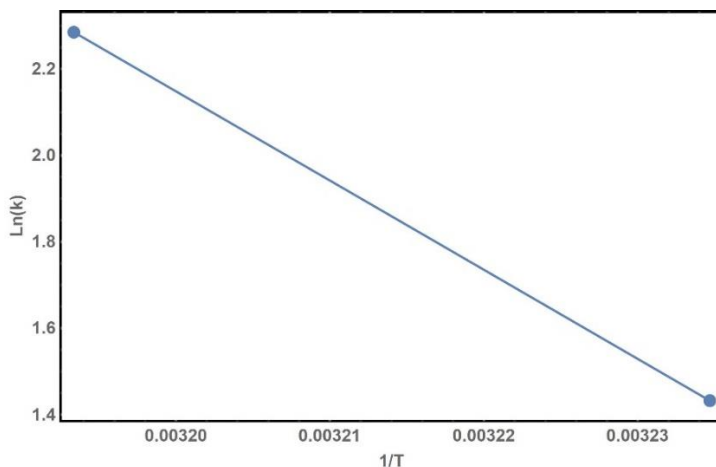


Fig. 24 Arrhenius slope.

Also, the Eyring equation is used to get a thermodynamic parameters of the system [30].

$$\ln\left(\frac{K}{T}\right) = \left[ \ln\left(\frac{K_b}{h}\right) + \frac{\Delta S}{R_g} \right] - \frac{\Delta H}{R_g} \times \frac{1}{T} \tag{9}$$

Where,  $K_b$  is the Boltzmann constant,  $h$  is the Plank constant,  $R_g$  is the universal gas constant,  $K$  is the reaction constant and  $T$  is the temperature (Kelvin). Converting the Eqn. (9) into  $y = mx + n$  formation to get thermodynamic parameters by slope, Fig. 25, enthalpy is found  $\Delta H = 169049 \text{ j/mol}$ , and entropy is found  $\Delta S = 313.514 \text{ j/kg.K}$

$$\ln\left(\frac{K}{T}\right) = -\frac{\Delta H}{R} \times \frac{1}{T} + \left[ \ln\left(\frac{K_b}{h}\right) + \frac{\Delta S}{R} \right] \tag{10}$$

Gibbs free energy is found by the Eqn. (11) for both temperatures [30] Table 4. Also, behavior of the system can observed by the Fig. 26 and Fig. 27

$$\Delta G = \Delta H - T \times \Delta S \tag{11}$$

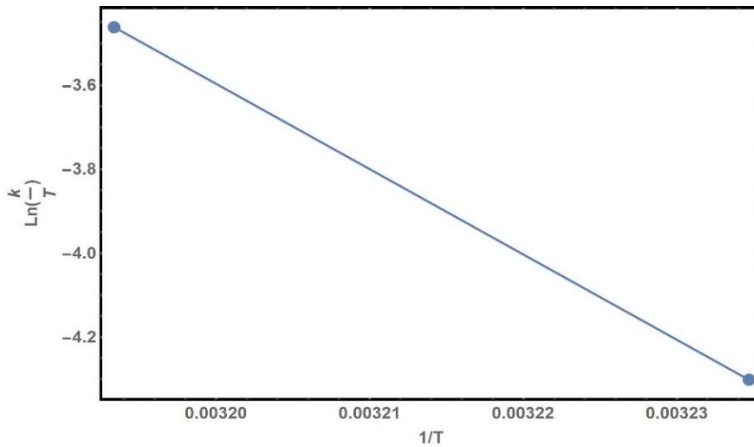


Fig. 25  $\Delta H$  Slope.

Table 4. Gibbs free energy values and reaction constants for different temperatures.

$T$ (Kelvin)	$K$ ( $s^{-1}$ )	$\Delta G$ ( $j/mol$ )
309	4.18826	72.1264
313	9.82826	70.8724

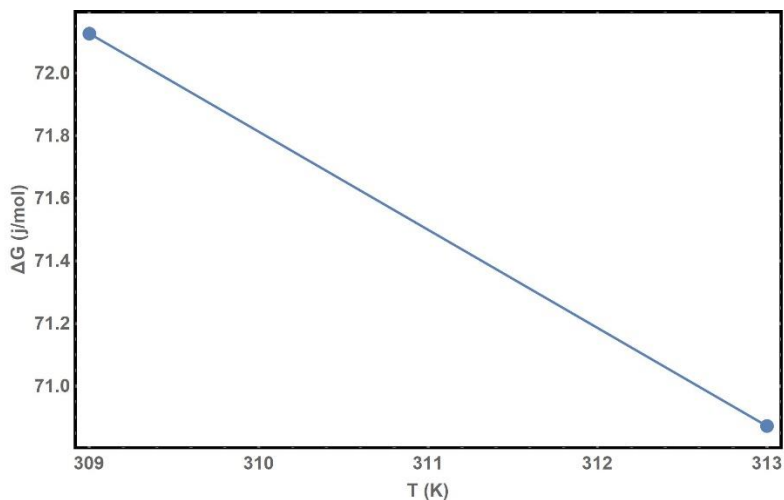


Fig. 26 Free energy change for different temperatures.

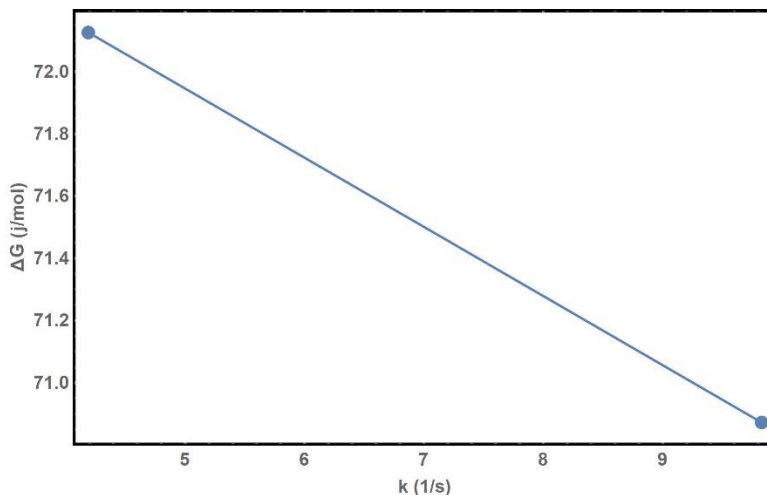


Fig. 27 Free energy change for different reaction constants.

### 5. Conclusions

In this study, nanosized Mg@BTC, synthesized by electrochemical method was used as a nanocarrier for ibuprofen first time. The ibuprofen was loaded to the Mg@BTC successfully. After long term release, the obtained release ratio was 36 % for 1:1. Mg@BTC could be afforded as a carrier for the slow-released of drug. Releasing of drug concentration for a specific period of time can be achieved by the Mg@BTC. Thus, it could effect on the disease efficiently. Besides, side effects can be eliminated in the bloodstream with the slow release.

Also, the release profile of the Mg@BTC is tested in the frame of mathematical models to get observation and prediction of the release patterns. Data sets are arranged for model suitable form thanks to the software. Five popular model functions are fitted to the release profiles. Watson's U-Squared Method is used to test the fit strength of the models.

According to the fit results for release profile are demonstrated that Peppas Model is the strongest one and predicted approximately 3.5 days of fully release. The short term dissolution profile of drug is different than the long term profile for that reason the used models have a limitation for the prediction of long term drug release pattern. Also, in thermodynamic studies, Fig. 26 showed that the increasing temperature results the free energy decrease, which means the loss of stability and holding capacity of the system is decreased. So, in further studies the temperature dependence should not be ignored.

The theoretical predictions have been foreseeing the better experiment conditions by avoiding waste of time and work power. In future studies, increasing the drug holding capacity will be studied thanks to the model fit results.

### Acknowledgements

This study was completed as a part of BAP research project founded by the University of Ondokuz Mayıs (Project Number: PYO.FEN.1901.18.008).

### References

- [1] Gangu KK., et al. A review on contemporary Metal-Organic Framework materials. *Inorganica Chimica Acta*, 2016; 446:61-74. <https://doi.org/10.1016/j.ica.2016.02.062>
- [2] Amir Reza Abbasi MR. Influence of the ultrasound-assisted synthesis of Cu-BTC metal-organic frameworks nanoparticles on uptake and release properties of rifampicin. *Journal of Molecular Structure* 2017; 36e42:1131.
- [3] Lestari WW., et al. Green and facile synthesis of MOF and nano MOF containing zinc(II) and benzen 1,3,5-tri carboxylate and its study in ibuprofen slow-release. *Materials Chemistry and Physics*, 2018; 204:141-146. <https://doi.org/10.1016/j.matchemphys.2017.10.034>
- [4] Alizadeh S, Nematollahi D. Electrochemically Assisted Self-Assembly Technique for the Fabrication of Mesoporous Metal-Organic Framework Thin Films: Composition of 3D Hexagonally Packed Crystals with 2D Honeycomb-like Mesopores. *J Am Chem Soc*, 2017; 139:13 4753-4761. <https://doi.org/10.1021/jacs.6b12564>
- [5] Alinaghi Langari AA., et al. Efficient extraction of aromatic amines in the air by the needle trap device packed with the zirconium based metal-organic framework sorbent. *RSC Advances*, 2020; 10:23 13562-13572. <https://doi.org/10.1039/D0RA00687D>
- [6] Firoozichahak A., et al. UIO-66-NH<sub>2</sub> Packed Needle Trap for Accurate and Reliable Sampling and Analysis of the Halogenated Volatile Organic Compounds in Air. *International Journal of Environmental Analytical Chemistry*, 2019; 1-18. <https://doi.org/10.1080/03067319.2019.1664497>
- [7] Firoozichahak A., et al. Development of a needle trap device packed with titanium-based metal-organic framework sorbent for extraction of phenolic derivatives in air. *J Sep Sci*, 2020; 43:5 1011-1018. <https://doi.org/10.1002/jssc.201900938>
- [8] Pirmohammadi Z., et al. Determination of urinary methylhippuric acids using MIL-53-NH<sub>2</sub> (Al) metal-organic framework in microextraction by packed sorbent followed by HPLC-UV analysis. *Biomed Chromatogr*, 2020; 34:1 e4725. <https://doi.org/10.1002/bmc.4725>
- [9] Saedi N., et al. A needle trap device packed with MIL-100(Fe) metal organic frameworks for efficient headspace sampling and analysis of urinary BTEXs. *Biomed Chromatogr*, 2020; 34:4 e4800. <https://doi.org/10.1002/bmc.4800>
- [10] Soury S., et al. Development of a needle trap device packed with zinc based metal-organic framework sorbent for the sampling and analysis of polycyclic aromatic hydrocarbons in the air. *Microchemical Journal*, 2019; 148:346-354. <https://doi.org/10.1016/j.microc.2019.05.019>
- [11] Zhou JM, Shi W, Li HM, Li H, Cheng P. *Phys. Chem. C*, 2014; 118 416. <https://doi.org/10.1021/jp4097502>

- [12] Yao Q., et al. Series of Highly Stable Isoreticular Lanthanide Metal-Organic Frameworks with Expanding Pore Size and Tunable Luminescent Properties. *Chemistry of Materials*, 2015; 27:15 5332-5339. <https://doi.org/10.1021/acs.chemmater.5b01711>
- [13] K. Jihoon YS, Deok J, Seung YK. *Microporous Mesoporous Mater*, 2015; 202 8.
- [14] Hu ZJ, Jian Z, Xiu FY, Xiao PS, Ai HY. *Inorg. Chem. Commun*, 2015; 54 54.
- [15] Rao CNR., et al. Hybrid inorganic-organic materials: a new family in condensed matter physics (vol 20, art no 083202, 2006). *Journal of Physics-Condensed Matter*, 2008; 20:15. <https://doi.org/10.1088/0953-8984/20/8/083202>
- [16] Yao Q, Gómez AB, Su J, Pascanu V, Yun Y, Zheng H, Chen H, Liu L, Abdelhamid HN, Martín-Matute B, Zou X. *Chem. Mater*, 2015; 27 5332. <https://doi.org/10.1021/acs.chemmater.5b01711>
- [17] Blundell SJ, Pratt FL. Organic and molecular magnets. *Journal of Physics-Condensed Matter*, 2004; 16:24 R771-R828. <https://doi.org/10.1088/0953-8984/16/24/R03>
- [18] Sheldon RA, Arends IWCE, Hanefeld U. *Green Chemistry and Catalysis*. Wiley-VCH, 2007. <https://doi.org/10.1002/9783527611003>
- [19] Lucena FRS, de Araújo LCC, Rodrigues MD, da Silva TG, Pereira VRA, Militão GCG, Fontes DAF, Rolim-Neto PJ, da Silva FF, Nascimento SC. Induction of cancer cell death by apoptosis and slow release of 5-fluoracil from metal-organic frameworks Cu-BTC. *Biomedicine & Pharmacotherapy*. Silene C. Nascimento, 2013; 67 707-713. <https://doi.org/10.1016/j.biopha.2013.06.003>
- [20] Lazaro IA, Forgan RS. Application of zirconium MOFs in drug delivery and biomedicine. *Coordination Chemistry Reviews*, 2019; 380:230-259. <https://doi.org/10.1016/j.ccr.2018.09.009>
- [21] Silva EDV., et al. Solvent-free synthesis of acetylated cashew gum for oral delivery system of insulin. *Carbohydrate Polymers*, 2019; 207:601-608. <https://doi.org/10.1016/j.carbpol.2018.11.071>
- [22] Vasconcelos IB, Wanderley KA, Rodrigues NM, da Costa Jr. NB, Freire RO, Junior SA. Host-guest interaction of ZnBDC-MOF  $\beta$  doxorubicin: A theoretical and experimental study. *Journal of Molecular Structure*, 2017; 1131 36e42. <https://doi.org/10.1016/j.molstruc.2016.11.034>
- [23] Bushra R, Aslam N. *Oman Med. J.*, 2010; 25 (3) 155e1661. <https://doi.org/10.5001/omj.2010.49>
- [24] Moss Jr WM, Bendel Lp, Et Al. A multicenter, randomized, double-blind placebo-controlled, single dose trial of the safety and efficacy of intravenous ibuprofen for treatment of pain in pediatric patients undergoing tonsillectomy. *Paediatr Anaesth*, 2014; 9:24 483. <https://doi.org/10.1111/pan.12381>
- [25] Gouda R. Baishya H, Qing Z. Application of Mathematical Models in Drug release Kinetics of Carbidopa and Levodopa ER Tablets. *Journal of Developing Drugs*, 2017; 6:2.
- [26] Higuchi T., et al., *Pharmaceutical analysis*, Interscience Publishers, New York,, 1961.
- [27] Ritger PL, Peppas NA. Transport of Penetrants in the Macromolecular Structure of Coals .7. Transport in Thin Coal Sections. *Fuel*, 1987; 66:10 1379-1388. [https://doi.org/10.1016/0016-2361\(87\)90185-2](https://doi.org/10.1016/0016-2361(87)90185-2)
- [28] Hixon AW, Crowell JH. Dependence of Reaction Velocity upon Surface and Agitation. *Industrial and Engineering Chemistry*, 1931; 923-931. <https://doi.org/10.1021/ie50260a018>
- [29] Batschelet E. United States. Office of Naval Research., *Statistical methods for the analysis of problems in animal orientation and certain biological rhythms*, American Institute of Biological Sciences, Washington, 1965.
- [30] Freire LMC., et al. Understanding Drug Release Data through Thermodynamic Analysis. *Materials*, 2017; 10:6. <https://doi.org/10.3390/ma10060651>

- [31] Wang Z., et al. Self-Supported Catalysts. *Chemical Reviews*, 2009; 109:2 322-359. <https://doi.org/10.1021/cr800406u>
- [32] Gaffney JS, Marley NA, Jones DE. Fourier Transform Infrared (FTIR) Spectroscopy. Characterization of Materials, 2012. <https://doi.org/10.1002/0471266965.com107.pub2>
- [33] Bella F., et al. Light cured networks containing metal organic frameworks as efficient and durable polymer electrolytes for dye-sensitized solar cells. *Journal of Materials Chemistry A*, 2013; 1:32 9033-9036. <https://doi.org/10.1039/c3ta12135f>
- [34] Garzon LC, Martinez F. Temperature Dependence of Solubility for Ibuprofen in Some Organic and Aqueous Solvents. *Journal of Solution Chemistry*, 2004; 33:11 1379-1395. <https://doi.org/10.1007/s10953-004-1051-2>
- [35] Langer R, Peppas N. Chemical and Physical Structure of Polymers as Carriers for Controlled Release of Bioactive Agents - a Review. *Journal of Macromolecular Science-Reviews in Macromolecular Chemistry and Physics*, 1983; C23:1 61-126. <https://doi.org/10.1080/07366578308079439>
- [36] Plackett RL. Pearson, Karl and the Chi-Squared Test. *International Statistical Review*, 1983; 51:1 59-72. <https://doi.org/10.2307/1402731>
- [37] Ju RTC., et al. Drug-Release from Hydrophilic Matrices .1. New Scaling Laws for Predicting Polymer and Drug-Release Based on the Polymer Disentanglement Concentration and the Diffusion Layer. *Journal of Pharmaceutical Sciences*, 1995; 84:12 1455-1463. <https://doi.org/10.1002/jps.2600841213>
- [38] Fick A. On Liquid Diffusion (Reprinted from the London, Edinburgh, and Dublin Philosophical Magazine and Journal of Science, Vol 10, Pg 30, 1855). *Journal of Membrane Science*, 1995; 100:1 33-38. <https://doi.org/10.1080/14786445508641925>
- [39] Narasimhan B, Peppas NA. Molecular analysis of drug delivery systems controlled by dissolution of the polymer carrier. *J Pharm Sci*, 1997; 86:3 297-304. <https://doi.org/10.1021/js960372z>
- [40] Langer MB. *Drugs and the pressure to be perfect*, Rosen Pub. Group, New York, 1998.
- [41] Siepmann J., et al. A new model describing the swelling and drug release kinetics from hydroxypropyl methylcellulose tablets. *Journal of Pharmaceutical Sciences*, 1999; 88:1 65-72. <https://doi.org/10.1021/js9802291>
- [42] Siepmann J., et al. HPMC-matrices for controlled drug delivery: A new model combining diffusion, swelling, and dissolution mechanisms and predicting the release kinetics. *Pharmaceutical Research*, 1999; 16:11 1748-1756.
- [43] Siepmann J, Peppas NA. Modeling of drug release from delivery systems based on hydroxypropyl methylcellulose (HPMC). *Advanced Drug Delivery Reviews*, 2001; 48:2-3 139-157. [https://doi.org/10.1016/S0169-409X\(01\)00112-0](https://doi.org/10.1016/S0169-409X(01)00112-0)
- [44] Grassi M., et al. Modeling of drug release from partially coated matrices made of a high viscosity HPMC. *International Journal of Pharmaceutics*, 2004; 276:1-2 107-114. <https://doi.org/10.1016/j.ijpharm.2004.02.016>



Research Article

## Impact of multi-walled carbon nanotube and graphene oxide on abrasive wear performance of polypropylene

Salih Hakan Yetgin

*Department of Mechanical Engineering, Faculty of Engineering, Tarsus University, Mersin, Turkey*

### Article Info

### Abstract

#### Article history:

Received 18 Jan 2020

Revised 29 May 2020

Accepted 12 June 2020

#### Keywords:

*Graphene oxide;*

*Multi-walled carbon nanotube;*

*Taguchi analysis;*

*Tribological properties;*

*Coefficient of friction*

In this study, the abrasive wear behavior of multi-walled carbon nanotube (MWCNT) and graphene oxide (GO) filled polypropylene (PP) nanocomposites without using compatibiliser were investigated. The effects of material type, sliding distance, and emery paper number on the abrasive wear of PP nanocomposites were investigated by adopting a statistical approach. The tribological tests were performed in dry condition using pin-on-disc at 1.0m/s sliding speed and 10N load. The optimization of signal-to-noise ratio (S/N) and degree of significance of the control variables to minimize the wear volume and coefficient of friction was carried out. As a result of the study, wear volume and coefficient of friction increased with increasing sliding distance, while decreased with increasing emery paper number for all tested materials. The coefficient of friction of the MWCNT and GO filled PP nanocomposites decreased by 19% and 23% compared to unfilled PP polymer, respectively. GO filled PP nanocomposites was found to be approximately 95% less wear volume than MWCNT filled PP nanocomposites. The minimized coefficient of friction and wear volume was obtained at 0.3%wt GO filled PP nanocomposite with the parameters of 100m sliding speed and 1200 grid emery paper number with a value of 0.2716 and 3.07 mm<sup>3</sup>, respectively.

© 2021 MIM Research Group. All rights reserved.

## 1. Introduction

Polymer materials are widely used as engineering materials for automotive, electronics, construction, home furnishings, and similar industries because of their low density, easy processability, low cost, and reasonable mechanical strength. However, their usage areas are restricted because of low impact resistance, low service temperature range, and high coefficient of friction (except UHMWPE and PTFE) under dry sliding conditions [1,2]. Traditionally, micro-size fillers and reinforcements have been used to increase the mechanical and tribological properties of the polymer materials. However, in recent years, carbon-based nanoparticles (carbon nanotube and graphene oxide) have become the most important material group for improving the mechanical and the tribological properties of polymers because of their superior thermal, electrical, mechanical properties and large surface area [1, 3-6]. Barretta et al. [7] examined the size-dependent structural response and constitutive behavior of carbon nanotubes (CNTs) by exploiting the modified nonlocal strain gradient elasticity. The structural response of CNTs is modeled by Timoshenko beam and the modified nonlocal strain gradient elasticity theory. Based on the flexural analysis of Timoshenko nano-beam, a novel reduced Euler-Young elastic modulus is introduced for CNTs and calibrated by Molecular Dynamics (MD) simulations results. Mertens and Senthilvelan [1] investigated the mechanical and tribological properties of PP-CNT (carbon nanotube) (0.5, 1.0, 3.0, and 5.0wt%) composites prepared using the melt compounding

\*Corresponding author: [shvetgin@gmail.com](mailto:shvetgin@gmail.com)

<sup>a</sup> [orcid.org/0000-0002-6068-9204](https://orcid.org/0000-0002-6068-9204)

DOI: <http://dx.doi.org/10.17515/resm2020.176na0118>

Res. Eng. Struct. Mat. Vol. 7 Iss. 1 (2021) 157-171

process. As the CNT content increased, the tensile strength and Young's modulus of the PP composites increased. The addition of the CNTs to the PP did not significantly increase the wear resistance of the composite. Shim and Park [8] investigated the viscoelastic properties of the glycidyl methacrylate (GMA) grafted MWCNTs filled PP. Storage modulus, loss modulus, and shear viscosity increased with GMA-MWCNT addition to the PP. Golchin et al. [9] have studied the tribological properties of multi-walled carbon nanotubes (MWCNT) and graphene oxide reinforcement added into the Ultra High Molecular Weight Polyethylene (UHMWPE) polymer. As a result of the study, they have reported that the coefficient of friction and wear ratio values decreased with the addition of multi-walled carbon nanotubes and graphene oxide into the UHMWPE polymer. Liu et al. [10] studied the tribological properties of thermoset polyimide (PI)/graphene oxide nanocomposites. Experimental studies have indicated that the friction and abrasion properties of the polyimide polymer are improved by the addition of graphene oxide. The reason for this is attributed to the uniform transfer film layer formed and the increased load-carrying capacity. Padenko et al. [11] investigated the tribological properties of functionalized graphene reinforced poly-tetra-fluoro-ethylene (PTFE) polymer at 0-4% by weight. As a result of the study, it has been determined that the friction coefficient decreases with the addition of graphene oxide reinforcement into the PTFE polymer. They determined that the wear rate increased up to 1% graphene oxide reinforcement addition into the PTFE and decreased after this addition. The reason for this explained by the transfer film layer. They have indicated that they have an important influence on the friction and abrasion properties of the resulting transfer film layer. Bastiurea et al. [12] prepared the graphene oxide and graphite filled polyester composites by using conventional melt-mixing methods to improve the tribological performance of polyester. Hassan et al. [13] investigated the tribological properties of unfilled Low-Density Polyethylene (LDPE), Polyamide-12 (PA-12), and graphene nanoplatelets (GNPs) filled polymers by a pin-on-disc tester. Tribological properties showed that LDPE/GNPs and PA12/GNPs nanocomposites have lower coefficients of friction, and wear rates compared with pure LDPE and PA-12. Pan et al. [14] investigated the mechanical and tribological properties of monomer casting (MC) nylon/graphene oxide nanocomposites. The results showed that graphene oxide of very low content had a notable effect on reinforcing the MC nylon matrix. The incorporation of graphene oxide into MC nylon largely reduced wear and friction under dry sliding. The nanocomposites have lower wear rates in comparison with neat MC nylon and the greater the difference, the greater are the loads and the sliding velocities. Shen et al. [15] investigated the effect of the hybrid of multi-wall carbon nanotubes (MWCNTs) and graphene oxide (GO) nanosheets on the tribological performance of epoxy composites. Friction and wear tests against smooth steel showed that the introduction of 0.5 phr MWCNTs into the epoxy matrix increases the friction coefficient and decreases the specific wear rate. When testing the tribological performance of MWCNT/GO hybrids, it is shown that at a high GO amount of 0.5 phr, the friction coefficient is decreased below that of the neat matrix whereas the wear rate is increased above that of the neat matrix. At an optimal hybrid formulation, i.e., 0.5 phr MWCNTs and 0.1 phr GO, a further increase in the friction coefficient and a further reduction in the specific wear rate are observed. There have been a lot of investigations related to the test conditions such as normal load, sliding speed, temperature, and environment on the tribological behavior of polymers. In recent years, analytical methods are extensively employed for the optimization and prediction of these test conditions for a wide range of engineering fields. This has the benefit of optimizing several experiments and essential variables. In this view, one of the most effective methods is the Taguchi method. Firojkhan et al. [16] investigated the influence of load, sliding speed, sliding distance, amount of glass fiber on friction coefficient and wear ratio of PTFE composites by using the Taguchi method. Sudheer et al. [17] investigated the effect of test parameters on the wear behavior of potassium-titanate-whiskers (PTW) reinforced epoxy

composites using the Taguchi method. Sudeepan et al. [18] studied the tribological behavior of micron-sized kaolin filler filled with acrylonitrile-butadiene-styrene (ABS) using Taguchi method. Taguchi design techniques were applied to investigate the significant influence of various operating and design parameters, such as contact load, rotational sliding speed, carbon nanotubes (CNTs) concentration on the tribological properties of UHMWPE nanocomposites by Lawal et al. [19]. The applied normal force was found to be the dominant parameter controlling the wear ratio and friction coefficient. The significance of CNTs concentration on both the coefficient of friction and wear rate closely follows that of the applied load.

In the literature, there are lots of studies that examined wear and friction behaviors by using different types of polymers with filled graphene oxide and MWCNT. In these studies, generally, the effects of the environment (dry, aqueous) and the amount of the GOs and MWCNTs were investigated. According to the authors' knowledge, there are no studies on the tribological properties of graphene oxide and MWCNT filled PP polymers at abrasive conditions. At the same time, in this study, besides the effects of the amount of GO and MWCNT on the friction and wear behavior, the effects of sliding distance and emery paper numbers are also investigated by using Taguchi method.

## 2. Experimental Details

### 2.1. Materials

Commercial Polypropylene (PP) (ExxonMobil Chemical Company, commercial code:PP3374E3) with a specific gravity of  $0.9 \text{ g/cm}^3$ , a melt flow index (MFI) of  $1.3\text{g}/10 \text{ min.}$  (at  $230 \text{ }^\circ\text{C}$  and  $2.16\text{kg}$ ) was used as a matrix material. Graphene oxide (GO) was purchased from Nanografen Co (Turkey) with a bulk density, average number of layers and oxygen content of  $0.022\text{g/mL}$ , 27 and 4.1%, respectively, and multi-walled carbon nanotubes (MWCNT) were purchased from Detsan Company (Turkey). The purity of MWCNTs was declared to be higher than 97% by the manufacturer. The average outer-diameter and length of MWCNTs are about  $10\text{-}20\text{nm}$  and  $10\text{-}30\mu\text{m}$ , respectively and its surface area is higher than  $200\text{m}^2/\text{g}$ . Figure 1 represents the scanning electron microscope (SEM) images of as-received GO sheets and MWCNT.

### 2.2. Fabrications

Carbon-based nanostructure reinforced nanocomposites were fabricated with a constant filler concentration. MWCNT filled PP nanocomposite specimens were produced with the two-step mixing process. In the first step, PP-MWCNTs pellets were prepared by using a co-rotating twin-screw extruder operated with a screw speed of 350 rpm and barrel temperature of  $160\text{-}200^\circ\text{C}$  from the main feeder to die. In the second step, an injection molding method was utilized to produce nanocomposite laminates. The barrel temperature ranged  $215\text{-}230^\circ\text{C}$  and the mould temperature was kept at  $30^\circ\text{C}$ . A similar route was followed to fabricate GO/PP nanocomposites. Before the production of the 0.3%wt. GO filled PP nanocomposite, the GO was mixed with distilled water in an ultrasonic mixer to separate the layers. The obtained mixture was mixed with the PP polymer and dried at  $100^\circ\text{C}$  for 2 hours before the extrusion process. PP nanocomposite granules with graphene oxide were produced in a twin-screw extruder at a temperature range of  $185\text{-}210^\circ\text{C}$ . Injection temperatures were determined to be  $190\text{-}220^\circ\text{C}$ . The mold temperature is fixed at  $30^\circ\text{C}$ . Figure 2 shows the production scheme of graphene oxide filled PP nanocomposite.



Fig. 1 SEM images of the graphene oxide layers and MWCNT

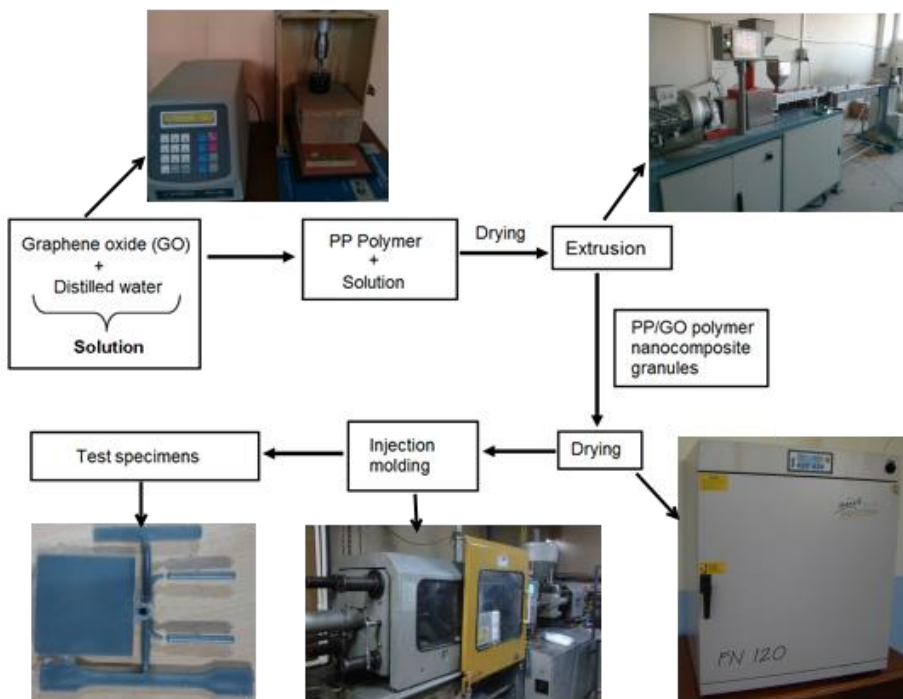


Fig. 2 Production process of graphene oxide filled PP nanocomposite

### 2.3. Abrasive wear test

Abrasive wear tests were performed using a pin-on-disc machine (Figure 3) equipped emery papers with grit grades of 400, 800 and 1200. The emery paper was fixed on the rotating disc surface. Samples with a diameter of 5mm and a length of 50mm were used for tests. Before each test, samples were cleaned by alcohol and dried in air. Abrasive wear tests were run at the sliding distance of 100, 200 and 400m and, under 1.0m/s sliding speed and 10N load. The wear volume (WV) was computed from the mass loss of the pin.

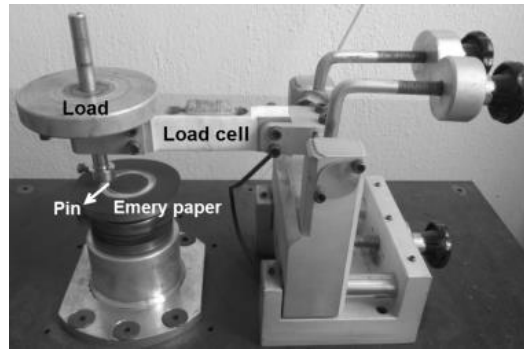


Fig. 3 Wear test device.

### 2.4. Experimental Plan and statistical analysis

In this study, the Taguchi model and statistical analysis process were carried out using MINITAB 17. The most important stage in the design of the experiment lies in the selection of the experimental parameters [20]. Three parameters, namely, material type (A), sliding distance (B) and emery paper number (C) each at three levels, were considered in this study following  $L_{27}$  ( $3^3$ ) orthogonal array design. The experimental parameters are indicated in Table 1.

Table 1. Experimental parameters

Parameters	Levels		
	I	II	III
A: Material type	PP	PP/0.3MWCNT	PP/0.3GO
B: Sliding distance, m	100	200	400
C: Emery paper number	400	800	1200

The results are transformed into a signal-to-noise ratio, which has been used to measure the quality characteristics deviating from the desired values. In the analysis of the S / N ratio, there are three categories of quality features: smaller is the best, nominal is the best, and larger is the best. In this work, “smaller is the best” is used to measure the quality characteristics of the coefficient of friction ( $\mu$ ) and WV. The S/N ratio is calculated from equation 1:

$$S / N = -10 \times \log \left( \frac{y_1^2 + y_2^2 + \dots + y_n^2}{n} \right) \quad (1)$$

Where, ‘n’ is the number of observations and ‘yi’ is the observed data result of the *i*th test. Furthermore, a statistical analysis of variance (ANOVA) is performed to identify the statistically significant process parameters. With the S/N and ANOVA analyses, the optimum parameters combination can be predicted to a useful level of accuracy. Finally, a confirmation experiment is performed to verify the optimum parameters.

### 3. Results and Discussion

#### 3.1. Control Factors

The calculated values of the S/N ratio were given in Table 2. The average S/N ratio for the coefficient of friction ( $\mu$ ) and wear volume (WV) was obtained as 9.42dB and -16.81dB from Table 2. The main effects plots of S/N for  $\mu$  and WV were given in Figure 4-a and 4-b. Generally, these figures show that S/N ratio values differ with material type, sliding distance, and emery paper number values. The optimal process conditions of experimental parameters could be easily decided from these graphs. The highest S/N value is represented that the optimal level of the process factors. It could be seen in Fig. 4-a and 4-b that the optimized process condition for PP nanocomposites became A<sub>3</sub>B<sub>1</sub>C<sub>3</sub> for main control factors as for PP/0.3GO with the sliding distance of 100m, and the emery paper number of 1200. The friction coefficient of the PP and its composites were increased with the increase in sliding distance and decreased with the increase in the emery paper number. Minimum  $\mu$  values were obtained with the material type of PP/0.3GO. It is known that graphene, as filler with high strength and high thermal conductivity, can improve the load-carrying capacity and transmission of frictional heat of the composites [11]. Rafiee et al. [21, 22] stated that the graphene structure provides better stress transfer than CNT during the applied load. Padenko [23] also explained that the reduction in the coefficient of friction is due to the self-lubrication behaviors of graphene oxide and the formation of the transfer film on the disc surface under dry sliding conditions. Polymer nanocomposites have superior friction properties because graphene oxide has small dimensions, thin layer structure and excellent self-lubrication properties. This plays an important role during friction tests in reducing the shear force and in the formation and preservation of low friction [24]. The WV of the PP and its composites were decreased with the increase in the emery paper number and increased with the increasing sliding distance. Minimum WV values were obtained with the material type of the PP/0.3GO because of the GO can be readily released from the PP to form a third-body transfer film, which leads to reduce the direct contact between the PP and emery paper counterface. The graphene could work as a solid lubricant material between the two contacted surfaces and prevent direct contact between them, thereby reduce the  $\mu$  and increase the WV [4].

Analysis of the impact of each parameter on the coefficient of friction and wear volume was carried out with the S/N response table. The control factors were classified with different values. The response for the coefficient of friction and wear volume of the PP nanocomposite materials are also presented in Table 3. It can be seen that the strongest effect was obtained as factor material type for  $\mu$  and sliding distance for WV in these tables.

Table 2. Experimental results and S/N ratios

Material type	Sliding distance, m	Emery paper number	Coefficient of friction, $\mu$		Wear volume (mm <sup>3</sup> )	
			Measured	S/N	Measured	S/N
PP	100	400	0,3861	8,2660	5,52	- 14,8454
PP	100	800	0,3509	9,0963	4,62	- 13,2972
PP	100	1200	0,3344	9,5147	3,72	- 11,4118
PP	200	400	0,3921	8,1321	8,68	- 18,7713
PP	200	800	0,3691	8,6571	7,33	- 17,2998

PP	200	1200	0,3431	9,2916	6,09	-	15,6894
PP	400	400	0,4132	7,6768	1,03	-	20,2224
PP	400	800	0,3951	8,0659	9,81	-	19,8319
PP	400	1200	0,3693	8,6524	8,12	-	18,1882
PP/0.3MWCNT	100	400	0,3365	9,4603	9,10	-	19,1819
PP/0.3MWCNT	100	800	0,3061	10,2827	6,97	-	16,8600
PP/0.3MWCNT	100	1200	0,2804	11,0444	4,94	-	13,8813
PP/0.3MWCNT	200	400	0,3526	9,0544	1,08	-	20,6576
PP/0.3MWCNT	200	800	0,3343	9,5173	8,54	-	18,6285
PP/0.3MWCNT	200	1200	0,3041	10,3397	7,42	-	17,4031
PP/0.3MWCNT	400	400	0,3841	8,3111	1,30	-	22,3014
PP/0.3MWCNT	400	800	0,3605	8,8619	1,13	-	21,0986
PP/0.3MWCNT	400	1200	0,3335	9,5381	9,10	-	19,1819
PP/0.3GO	100	400	0,3153	10,0255	4,66	-	13,3660
PP/0.3GO	100	800	0,2955	10,5889	3,86	-	11,7399
PP/0.3GO	100	1200	0,2716	11,3214	3,07	-	-9,7376
PP/0.3GO	200	400	0,3421	9,3169	7,84	-	17,8873
PP/0.3GO	200	800	0,3175	9,9651	6,02	-	15,5959
PP/0.3GO	200	1200	0,2943	10,6242	5,57	-	14,9143
PP/0.3GO	400	400	0,3621	8,8234	8,86	-	18,9522
PP/0.3GO	400	800	0,3245	9,7757	7,05	-	16,9582
PP/0.3GO	400	1200	0,3089	10,2036	6,48	-	16,2278

Table 3. Response table for S/N ratios (dB) and means.

Control Factors	Coefficient of friction, $\mu$				Wear volume, $\text{mm}^3$			
	1	2	3	Delta	1	2	3	Delta
<b>S/N ratio (dB)</b>								
Material type	8.595	9.601	10.072	1.477 <sup>1</sup>	-	-	-	3.76 <sup>2</sup>
Sliding distance	9.956	9.433	8.879	1.077 <sup>3</sup>	13.81	17.43	19.22	5.40 <sup>1</sup>
Emery paper number	8.785	9.423	10.059	1.274 <sup>2</sup>	-	-	-	3.28 <sup>3</sup>
<b>Means</b>								
Material type	0.3726	0.3325	0.3146	0.0579 <sup>1</sup>	7.128	9.026	5.934	3.092 <sup>2</sup>
Sliding distance	0.3196	0.3388	0.3612	0.0416 <sup>3</sup>	5.163	7.586	9.339	4.176 <sup>1</sup>
Emery paper number	0.3649	0.3393	0.3155	0.0494 <sup>2</sup>	8.750	7.283	6.056	2.694 <sup>3</sup>

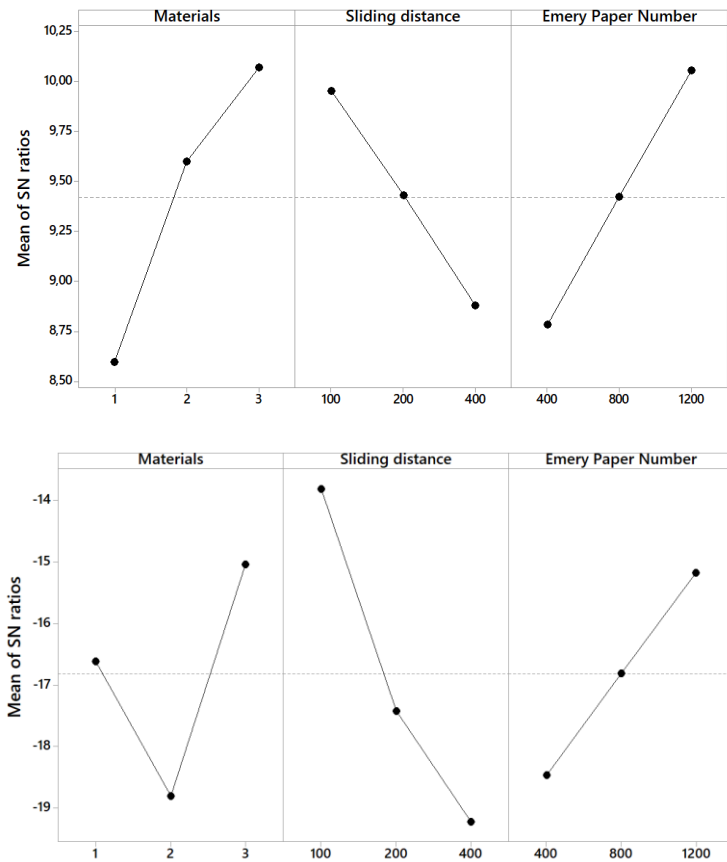


Fig. 4 Main effect plots, a)  $\mu$ , b) WV.

The interaction effect plots were given in Fig. 5. The relationship between experimental parameters and levels and results can be derived from the interaction plots. It is well known that interactions do not occur when the lines on the interaction plots are parallel and strong interactions occur between parameters when the lines cross [25]. The coefficient of friction and wear volume decreases with the increasing emery paper number. The coefficient of friction for PP polymer decreased by 15%, for PP/0.3MWCNT polymer by 20% and for PP/0.3GO polymer by 16% with increasing emery paper number. Also, the coefficient of friction and wear volume increased with increasing sliding distance. The coefficient of friction increased by 7% for PP polymer, 14.1% for PP/0.3MWCNT polymer and 14.8% for PP/0.3GO polymer with increasing the sliding distance from 400 to 1200. Similar results are obtained by Suresha et al. [26]. Suresha et al. [26] stated that the wear volume tends to increase near linearly with increasing abrading distance and strongly depends on the grit size of abrasive paper. The lowest wear volume was obtained for PP/0.3GO while the highest wear volume was obtained for PP/0.3MWCNT. The minimum wear volume of PP/0.3GO composite is nearly 25% and 40% less than that of unfilled PP polymer and PP/0.3MWCNT at the same test conditions, respectively.

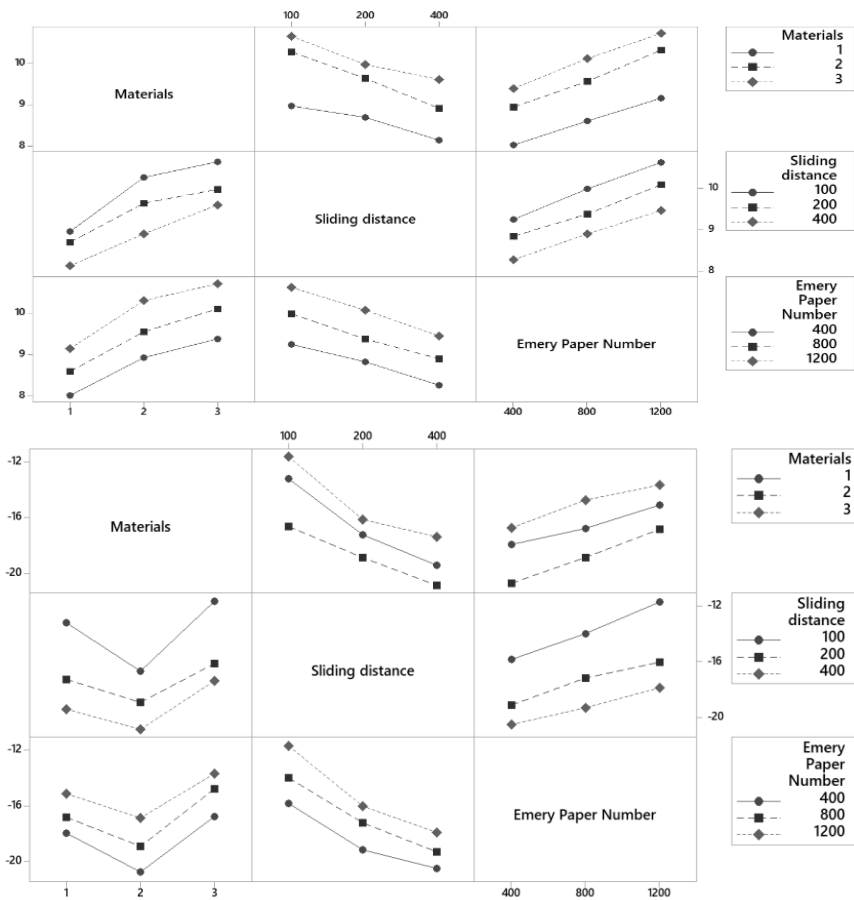


Fig. 5 Interaction effect plots; a)  $\mu$ , b) WV.

### 3.2. Analysis of variance (ANOVA)

ANOVA is a method most widely used and aims at determining significant parameters on response and measuring their individual effects. The ratio of percentage (PCR %) of experimental parameters is used to determining the corresponding effect on the results. When 'P' is less than the '5%' column value the assigned factor is statistically and significant. Table 4 presents the ANOVA for the  $\mu$  and WV.

One can observe from Table 4 that material type has greater statistically influence of 44.84%, emery paper number has an influence of 31.02% and sliding distance has an influence of 22.01% on  $\mu$ . However, the interaction between material type\*sliding distance (P=0.035), material type\*emery paper number (P=0.775), and lastly sliding distance\*emery paper number (P=0.793) show less significance of contribution on the coefficient of friction. In Table 4, when PCR values of the WV were evaluated, the material types (PCR=27.01%), the sliding distance (PCR=48.84%), emery paper number (PCR=20.21%) influence on the WV. The interactions material type\*sliding distance, material type\*emery paper number and sliding distance\*emery paper number were for WV PCR=1.24%, PCR=2.00%, PCR=0.24%, respectively. These interactions are very minimum and can be neglected. The error was a small value of 0.46. This result was supported successful of the ANOVA.

Table 4. ANOVA results of means for  $\mu$  and WV.

Source	DF	Sum of Squares (SS)	Mean of Squares (MS)	F ratio	P value	PCR (%)
<b>Coefficient of friction, (<math>\mu</math>)</b>						
Material type	2	0.015856	0.007928	372.08	0.000*	44,84
Sliding distance	2	0.007804	0.003902	138.12	0.000*	22,01
Emery paper number	2	0.010982	0.005491	257.70	0.000*	31,02
Material type*Sliding distance	4	0.000378	0.000094	4.43	0.035	0,83
Material type*Emery paper number	4	0.000038	0.000009	0.44	0.775	0
Sliding distance*Emery paper number	4	0.000036	0.000009	0.42	0.793	0
Residual Error	8	0.000170	0.000021			
Total	26			0.035264		
S = 0,004616 R-Sq = 99,5% R-Sq(adj) = 98,4%						
<b>Wear Volume, (WV)</b>						
Material type	2	43.765	21.8823	235.60	0.000*	27,01
Sliding distance	2	79.151	39.5756	426.10	0.000*	48,84
Emery paper number	2	32.755	16.3777	176.33	0.000*	20,21
Material type*Sliding distance	4	2.002	0.5006	5.39	0.021	1,24
Material type*Emery paper number	4	3.248	0.8119	8.74	0.005	2,00
Sliding distance*Emery paper number	4	0.381	0.0954	1.03	0.449	0,24
Residual Error	8	0.743	0.0929			0.46
Total	26			162.046		
S = 0,3048 R-Sq = 99,5% R-Sq(adj) = 98,5%						

\* is significant parameter at 95% confidence level.

### 3.3. Confirmation tests

The final step of the Taguchi method is to perform a confirmatory experiment for examining the quality characteristic. The two approaches to confirmation are multiplied. In the first one, S/N values are compared with the second one, and confirmation is made according to Means values. In this study, confirmation tests will be evaluated considering Means values. The confirmation test was performed with an optimized factor set of factors A3B1C3 to predict the  $\mu$  and WV. The estimated means for the  $\mu$  and WV can be calculated from equation 2, where, T the overall experimental average, and A3, B1, and C3 is the mean response for the factors:

$$\begin{aligned} \mu &= T + (A3 - T) + (B1 - T) + (C3 - T) \\ \mu &= 0.27 \\ WV &= 2.433 \end{aligned} \tag{2}$$

A confidence interval for the predicted mean of the confirmation run can be calculated using equation 3 and 4 [27];

$$CI = \sqrt{F_{\alpha;1;v2} \times V_e \times \left( \frac{1}{n_{eff}} + \frac{1}{r} \right)} \tag{3}$$

where  $F_{\alpha;1;v2}$  = The F value from the F Table at a required confidence level at DOF 1 and error DOF v2,  $V_e$  is the variance of the error term,  $r$  is the replication number,  $n_{eff}$  is the number of valid measurement results [28];

$$n_{eff} = \frac{T_{den}}{1 + dof} \tag{4}$$

Where;  $T_{den}$  is the total number of the experiment,  $dof$  is the total degree of freedom of the factors used for prediction [29]. The confidence interval for the  $\mu$  and WV calculated from equation 3 and 4, and the results are given in Table 5. Furthermore, a comparison of the results of the confirmation test which was performed according to the optimum levels of the variables was given in Table 5. It can be seen from Table 5, the result values of the conducted confirmation test for the responses are obtained in the confidence interval with a 95% confidence level. Thus, the system optimization for  $\mu$  and WR was achieved using the Taguchi method at a significance level of 0.05.

Table 5. Comparisons the results of confirmation tests and predicted values by the Taguchi method.

Response	Optimal conditions			Confirmation test results	Predicted value	Confidence interval (CI)	Differences	Results
	Material type	Sliding distance	Emery paper number					
$\mu$	PP/0.3G O	100	1200	0.2716	0.27	$\pm 0.0137$	$ +0.0016 $	0.0016 < 0.0137 successful
WV				3.07	2.433	$\pm 0.9176$	$ +0.637 $	0.637 < 0.9176 successful

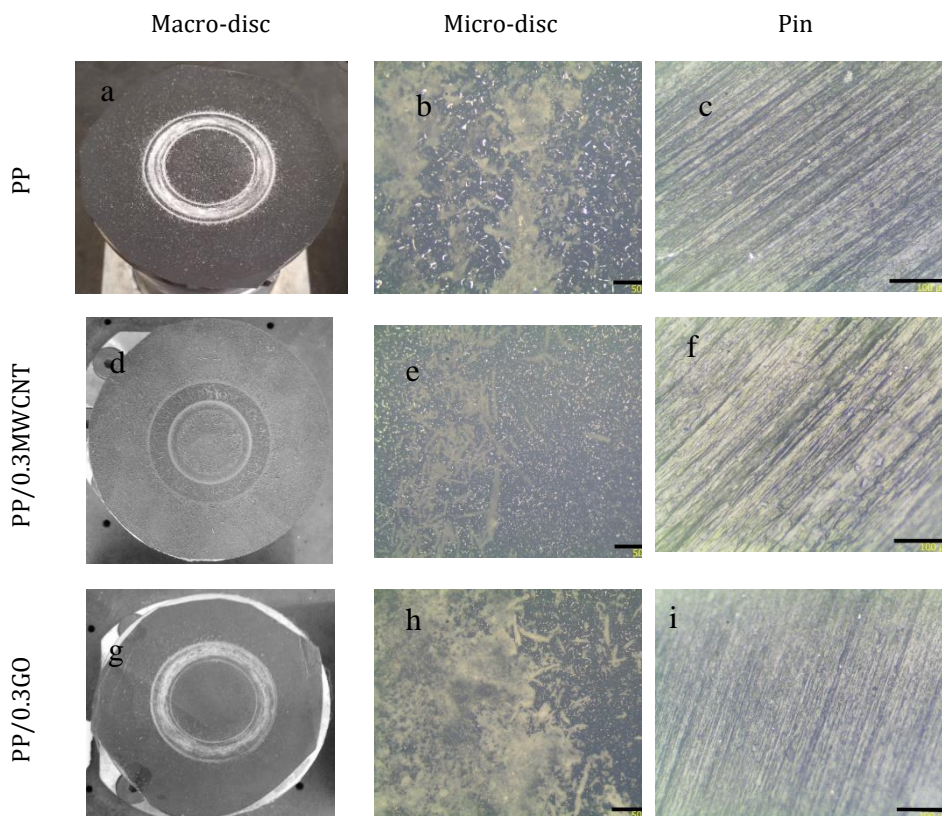


Fig. 6 Optical microscope of worn surfaces of disc and pin surfaces for PP and PP nanocomposites

The macro and micro-optical microscopy examination of the worn disc and pin surfaces of pure PP polymer, PP/0.3GO and PP/0.3MWCNT composites against emery paper with grit grade of 400 and sliding distance of 400m is given in Figure 6 a-i. It is seen that from the macro and micro disc images, the transfer film layer is formed on the abrasive disc surface. The transfer film layer prevented the contact between the polymer and the disc surface and caused to decrease in the coefficient of friction. For pure PP polymer, the worn surface of the pin showed sliding with wider and deeper grooves due to ploughing action by sharp abrasive particles (Fig 6 c). A smoother worn pin surface is observed for PP/0.3GO and PP/0.3MWCNT nanocomposites under the same conditions see Fig 6 f and i. This is explained as the particles are transferred more easily out of the contact area and regions of smooth matrix materials are visible. Therefore, the mechanism is a combination of adhesive and abrasive wears.

#### 4. Conclusions

The results of the abrasive wear tests of GO and MWCNT filled PP composites are as follows:

The addition of the GO and MWCNT fillers in the PP polymer increases the WV and  $\mu$  of the PP composites. WV and  $\mu$  increased with increasing sliding distance, while decreased with increasing emery paper number for all tested materials. The coefficient of friction of the MWCNT and GO filled PP nanocomposites decreased by 19% and 23% compared to

unfilled PP polymer, respectively. GO filled PP nanocomposites was found to be approximately 95% less wear volume than MWCNT filled PP nanocomposites. The optimal condition for  $\mu$  and WV is the material type at level 3 (PP/0.3GO), the sliding distance at level 1 (100m), and the emery paper number at level 3 (1200). It can also be concluded that the design factor material type has a major effect on the  $\mu$  while sliding distance has a major effect on the WV. The experimental results approved the accuracy of the Taguchi method for enhancing the tribological properties and optimizing the tribological parameters under abrasive conditions. Graphene oxide can be used as an effective modifier to improve the wear performance of PP polymer under harsh tribological conditions.

## References

- [1] Mertens AJ, Senthilvelan S. Mechanical and tribological properties of carbon nanotube reinforced polypropylene composites. *Journal of Materials: Design and Applications*. 2018;232(8):669-680. <https://doi.org/10.1177/1464420716642620>
- [2] Ravi Kumar BN, Suresh B, Venkataramareddy M. Effect of Abrasives on Three-Body Abrasive Wear Behaviour of Particulate-Filled Polyamide66/Polypropylene Nanocomposites. *Composite Interfaces*. 2010;17:113-126. <https://doi.org/10.1163/092764410X490536>
- [3] Yuanshi X, Fanglin X, Mingming W, Tongsheng L. Synergistic Effects of Carbon Nanotube/Nano-MoS<sub>2</sub> Hybrid on Tribological Performance of Polyimide Nanocomposite Films. *Tribology Letters*. 2018; 66(25):1-18. <https://doi.org/10.1007/s11249-017-0977-7>
- [4] Hassan A. El-Sayed M, EiD A.I, El-Sheikh M, Ali WY. Tribological properties of Low Density Polyethylene and Polyamide 12 as polymer matrix nanocomposites, *Journal of the Egyptian Society of Tribology*. 2017;14(4):40-53.
- [5] Yuanshi X, Tongsheng L, Dafei G, Fanglin X, Mingming W. Preparation and tribological properties of graphene oxide/nano-MoS<sub>2</sub> hybrid as multidimensional assembly used in the polyimide nanocomposites. *RSC Advances*. 2017;7:6323-6335. <https://doi.org/10.1039/C6RA27108A>
- [6] Beibei C, Xiang L, Yuhan J, Lin X, Hongyu L, Xiaofang L, Jin Y, Changsheng L, Fengyuan Y. Fabrication of ternary hybrid of carbon nanotubes/graphene oxide/MoS<sub>2</sub> and its enhancement on the tribological properties of epoxy composite coatings. *Composites Part A*. 2018;115:157-165. <https://doi.org/10.1016/j.compositesa.2018.09.021>
- [7] Barretta R, Ali Faghidian S, Marotti de Sciarra F, Pinnola F. P. Timoshenko nonlocal strain gradient nanobeams: Variational consistency, exact solutions and carbon nanotube Young moduli. *Mechanics of Advanced Materials and Structures*. 2019;1-15. <https://doi.org/10.1080/15376494.2019.1683660>
- [8] Shim YS, Park SJ. Influence of glycidyl methacrylate grafted multiwalled carbon nanotubes on viscoelastic behaviors of polypropylene nanocomposites. *Carbon Letters*. 2010;11:311-315. <https://doi.org/10.5714/CL.2010.11.4.31>
- [9] Golchin AAW, Nazann E. An investigation into tribological behaviour of multi-walled carbon nanotube/graphene oxide reinforced UHMWPE in water lubricated contacts. *Tribology International*. 2016;95:156-161. <https://doi.org/10.1016/j.triboint.2015.11.023>
- [10] Liu Y, Qihua W, Tingmei W, Guangqin P. Preparation and tribological properties of graphene oxide/nitrile rubber nanocomposites. *Journal of Materials Science*. 2012;47:730-738. <https://doi.org/10.1007/s10853-011-5846-4>
- [11] Padenko E, Van Rooyen LJ, Wetzel B, Karger-Kocsis J. "Ultralow" sliding wear polytetrafluoro ethylene nanocomposites with functionalized graphene. *Journal of Reinforced Plastics and Composites*. 2016;1-10. <https://doi.org/10.1177/0731684416630817>

- [12] Bastiurea M, Dumitru D, Gabriel A. Effect of Graphene Oxide and Graphite on Dry Sliding Wear Behavior of Polyester Composites. *Materiale Plastice*. 2018;55(1):102-110. <https://doi.org/10.37358/MP.18.1.4973>
- [13] Hassan A. El-Sayed M, Alaa I. EiD, El-Sheikh M, Ali WY. Effect of graphene nanoplatelets and paraffin oil addition on the mechanical and tribological properties of Low-Density Polyethylene nanocomposites. *Arabian Journal for Science and Engineering*. 2018;43:1435-1443. <https://doi.org/10.1007/s13369-017-2965-5>
- [14] Pan B, Shupeng Z, Wenzhong L, Jing Z, Jinlong L, Yuqing Z, Yongzhen Z. Tribological and mechanical investigation of MC nylon reinforced by modified graphene oxide. *Wear*. 2012;294-295:395-401. <https://doi.org/10.1016/j.wear.2012.07.032>
- [15] Shen XJ, Xian-Qiang P, Yu L, Shao-Yun F. Tribological performance of carbon nanotube-graphene oxide hybrid/epoxy composites. *Composites: Part B*. 2014;57:120-125. <https://doi.org/10.1016/j.compositesb.2013.09.050>
- [16] Firojkhan P, Hemant G, Sonam G. Optimization for Tribological Properties of Glass Fiber-Reinforced PTFE Composites with Grey Relational Analysis. *Journal of Materials*. 2016;1-7. <https://doi.org/10.1155/2016/8981746>
- [17] Sudheer M, Ravikantha P, Raju K, Thirumaleshwara B. Optimization of Dry SlidingWear Performance of Ceramic Whisker Filled Epoxy Composites Using Taguchi Approach. *Advanced Tribology*. 2012;1-9. <https://doi.org/10.1155/2012/431903>
- [18] Sudeepan J, Kumar K, Barman TK, Sahoo P. Study Of Tribological Properties Of ABS/Kaolin Polymer Composite Using Taguchi Technique. *International Journal of Applied Engineering Research*. 2014;9(26):8755-8758.
- [19] Lawal D, Annas BA, Abdul Samad M. Tribological investigations of carbon nanotube-reinforced polymer (UHMWPE) nanocomposites using Taguchi methodology. *Journal Applied Polymer Science*. 2016;44018-44030. <https://doi.org/10.1002/app.44018>
- [20] Mahapatra SS, Amar P. Study on mechanical and erosion wear behavior of hybrid composites using Taguchi experimental design. *Materials and Design*. 2009;30:2791-2801. <https://doi.org/10.1016/j.matdes.2009.01.037>
- [21] Rafiee MA, Lu W, Thomas AV, Zandiatashbar A, Rafiee J, Tour JM, Koratkar NA. Graphene nanoribbon composites. *ACS Nano*. 2010;4(12):7415-7420. <https://doi.org/10.1021/nn102529n>
- [22] Rafiee MA, Rafiee J, Wang Z, Song H, Yu Z-Z, Koratkar N. Enhanced mechanical properties of nanocomposites at low graphene content. *ACS Nano*. 2009;3(12):3884-3890. <https://doi.org/10.1021/nn9010472>
- [23] Padenko E., van Rooyen L.J. and Karger-Kocsis J. Transfer Film Formation in PTFE/Oxyfluorinated Graphene Nanocomposites During Dry Sliding. *Tribology Letters*. 2017; (65):36-47. <https://doi.org/10.1007/s11249-017-0821-0>
- [24] An Y., Zhixin T., Yuanyuan Q., Xingbin Y., Bin L., Qunji X. and Jinying P. Friction and Wear Properties of Graphene Oxide/Ultrahigh-MolecularWeight Polyethylene Composites Under the Lubrication of Deionized Water and Normal Saline Solution. *Journal Applied Polymer Science*. 2014;39640-39651.
- [25] Deprez P, Hivart P, Coutouly JF, Debarre E. Friction and wear studies using taguchi method: application to the characterization of carbon-silicon carbide tribological couples of automotive water pump seals. *Advances in Materials Science and Engineering*. 2009:1-10. <https://doi.org/10.1155/2009/830476>
- [26] Suresha B, Kunigal N, Shiva K. Investigations on mechanical and two-body abrasive wear behaviour of glass/carbon fabric reinforced vinyl ester composites. *Materials and Design*. 2009;30:2056-2060. <https://doi.org/10.1016/j.matdes.2008.08.038>
- [27] Ross PJ. *Taguchi Techniques for Quality Engineering*, McGraw-Hill Education (India) Pvt Limited, 2005. ISBN 0070598800.
- [28] Kacal A. Determination of optimal cutting conditions in finish turning of austempered ductile iron using Taguchi design method, *Journal of Scientific & Industrial Research*. 2011;70:278-283.

- [29] Roy RK. A Primer on the Taguchi Method. Competitive Manufacturing Series, 1st ed., Van Nostrand Reinhold; 1990.



# Research on Engineering Structures & Materials

## In This Issue

Editorial Note

1 **Hayri Baytan Ozmen**

A view on how to mitigate earthquake damages in Turkey from a civil engineering perspective

Research Article

13 **İlker Bekir Topçu, Arda Uzunömeroğlu**

Experimental investigation of utilizing chemical additives and new generation corrosion inhibitors on reinforced concrete

35 **Samson Olalekan Odeyemi, Omolola Titilayo Odeyemi, Adewale George Adeniyi, Zainab Tolu Giwa, Ademola Kamorudeen Salami, Adeyemi Adesina**

Prediction of chloride ingress for palm kernel shell concrete

Research Article

51 **Anas M. Fares**

The impact of RC shear wall openings at the lateral stiffness of the cantilever shear walls

Research Article

65 **Ercan Işık, İbrahim Baran Karaşin**

The mutual interaction between the structural footprint and number of floors in steel structures

Research Article

87 **Stephen John Hardy, Harvir Satsavia**

Experimental low cycle fatigue testing of circular bars with radial through-holes subjected to tension-compression loading

Research Article

97 **Tanay Karademir**

Micro-mechanical properties of geotextile fibers: measurement and characterization at cold environmental conditions

Research Article

121 **Baran Sarac**

Influence of sub-glass transition heat-treatment on physical and structural properties of Cu<sub>46</sub>Zr<sub>44</sub>Al<sub>8</sub>Hf<sub>2</sub> metallic glass

Research Article

135 **Güliz Akyüz, Aykut Elmas, Müberra Andaç, Ömer Andaç**

Evaluation of nano sized Mg@BTC metal organic framework as a drug carrier: A long term experimental and predictive theoretical study

Research Article

157 **Salih Hakan Yetgin**

Impact of multi-walled carbon nanotube and graphene oxide on abrasive wear performance of polypropylene

C  
O  
N  
T  
E  
N  
T



Research Group